Dipl.-Ing. Judith Maja Biedermann, BSc

Synthesis and Electrochemical Studies of Aryl-Substituted Group 14 Compounds

DOCTORAL THESIS

to achieve the university degree of

Doktorin der technischen Wissenschaften

submitted to

Graz University of Technology

Supervisor

Univ.-Prof. Dipl.-Chem. Dr.rer.nat. Frank Uhlig

Institute of Inorganic Chemistry

Dr. Ilie Hanzu

Institute for Chemistry and Technology of Materials

Faculty of Technical Chemistry, Chemical and Process Engineering and Biotechnology

Graz, June 2018

AFFIDAVIT

I declare that I have authored this thesis independently, that I have not used other than the declared sources/resources, and that I have explicitly indicated all material which has been quoted either literally or by content from the sources used. The text document uploaded to TUGRAZonline is identical to the present doctoral thesis.

Date	Signature

"In the beginning there was nothing, which exploded."

— Sir Terry Pratchett

Danksagung

An dieser Stelle möchte ich mich bei all jenen bedanken, die mich in den letzten Jahren begleitet, unterstützt und gefordert haben.

Ein großer Dank gilt Prof. Frank Uhlig, der mir die Gelegenheit gab, selbstständig zu arbeiten und damit zu meiner wissenschaftlichen und persönlichen Weiterentwicklung beigetragen hat. Vielen Dank, Frank, dass du mir die nötigen Freiheiten gelassen hast und mich mit deinen Ideen, deinem Rat und vor allem deiner Menschlichkeit zurück auf Kurs geführt hast, wenn ich mich verirrt hatte. Dr. Ilie Hanzu möchte ich auch herzlich danken für seine tatkräftige Unterstützung, seinen Optimismus, seinen beinahe unerschöpflichen Ideenreichtum sowie sein immer offenes Ohr für alle Anliegen. Danke, Ilie, dass ich durch deine Hilfe immer auch das Positive an scheinbar misslungenen Experimenten erkennen und auch menschlich viel von dir lernen konnte.

Des Weiteren gilt mein Dank all jenen, ohne die diese Arbeit nicht möglich gewesen wäre. Ein großes Dankeschön an unsere «guten Feen» Astrid, Barbara und Monika, dass ihr mir wo immer möglich zu Messergebnissen, Laborbedarf oder guten Ratschlägen verholfen habt. Prof. Roland Fischer und Dr. Ana Torvisco danke ich für ihre Unterstützung mit kristallografischen oder chemischen Anliegen. Prof. Klaus Reichmann und Dr. Angela Chemelli möchte ich für diverse TGA/DSC beziehungsweise SAXS und DLS Messungen sowie der Hilfe mit deren Interpretation danken. Auch bei meinen studentischen Helfern sowie unserem Lehrling möchte ich mich für die tatkräftige Unterstützung im Labor bedanken.

Vielen Dank an meine Institutskollegen, die die letzten Jahre mit diversen Diskussionen, gemeinsamen Projekten, lustigen Geschichten, Ausflügen und guter Feierlaune bereichert haben. Ihr seid super, danke für die Zusammenarbeit. Auch außerhalb des AC Instituts genoss ich viele Freiheiten, vor allem mit und dank «Team Kellerassel» sowie deren Ehrenmitgliedern. Ohne euch wären mir viele Möglichkeiten verborgen geblieben; ob Verstecken im Keller, gemeinsame Mittagspausen oder Pläne schmieden, es hätte mir ohne euch bei Weitem nicht so viel Spaß bereitet. Herzlichen Dank!

Besonderer Dank soll auch meinen Freunden zu Gute kommen, die mich wo immer nur möglich mit Rat und Tat unterstützt haben. Danke, dass ihr immer ein offenes Ohr für mich habt, mir Flausen und neue Ziele in den Kopf setzt, euch mit mir über alles Mögliche freut und auf mich achtet wenn's nötig ist. Liebe Rahel, vielen Dank für deine herzliche Unterstützung in allen Belangen und die Freude, die du mir immer wieder bereitest. Danke Betti und Luki, dass ihr in jeder Lebenslage zu mir haltet, nie müde werdet, mir neue Dinge beizubringen und mich auch manchmal zu meinem Glück zwingt. Danke Moni und Yassi, dass ihr mir mit eurer Art auch leidige Situationen erleichtert. Mika und Dave, danke, dass ihr für jegliche nicht-chemiebezogenen Schandtaten zu haben seid. Thanks, Pennyless Players, for distracting me every now and then.

Auch bei meiner Familie möchte ich mich herzlich bedanken. Susanna und Rolf, bessere Eltern hätte ich mir nicht wünschen können. Vielen Dank für euren Rückhalt und die Unterstützung, die mir dieses Studium ermöglicht haben. Christina, herzlichen Dank, dass ich mit dir schon jede Menge Unfug und spontane Reisen erleben durfte. Deine sensible Art hilft mir immer wieder zurück auf meinen Weg.
Der größte Dank gilt jedoch meinem (zukünftigen) Ehemann Daniel. Über das gesamte Studium hinweg hast du mich liebevoll unterstützt, mir die Richtung gewiesen, mich abgelenkt und mich wo nötig ergänzt. Ich freue mich auf unsere gemeinsame Zukunft.

Abstract

Organosilicon and -tin compounds are already used in various industries ranging from surface modifying silicones, thin films for electronic transistors and opto-electronic devices. Future consumer electronics and electric vehicles could also rely on high-performance Li-ion batteries with silicon or tin-based anodes. Their fully lithiated phases $Li_{4.4}E(IV)$ boast theoretical capacities of 4200 mAh g^{-1} for silicon and 990 mAh g^{-1} for tin. So far, however, such anodes still suffer from immense volume expansions of up to 400%vol which eventually fractures the material and thus limits cycle-life. These complications are mitigated when the silicon or tin are nanostructured or embedded in carbon (Si/C or Sn/C).

In this work, novel and previously published aryl-substituted silanes and stannanes were synthesised, comprehensively characterised and processed in order to develop nanostructured Si/C or Sn/C anode materials for Li-ion batteries. The silanes and stannanes were substituted with aryl groups such as phenyl, *o*-tolyl, 2,5-xylyl and 1-naphthyl or, hitherto uncharacterised, mixtures thereof. The effects of substituent bulk on the ^{29}Si chemical shifts, the solid-state interactions in single crystals and the electrochemical properties are discussed. Electrochemical characterisation of aryl silanes was carried out in non-aqueous environment in a purpose-built, optimised cyclic voltammetry cell. Subsequently, the aryl silanes were pyrolysed and the arylstannanes coupled to form Si/C and Sn/C anode materials, respectively. These materials displayed specific capacities exceeding the capacities of state-of-the-art graphite anodes by up to 20% and excellent cyclic stability.

Kurzfassung

Organosilicium- und Organozinnverbindungen werden bereits in unterschiedlichsten Industrien eingesetzt. Dazu gehören Silicone zur Oberflächenmodifizierung, dünne Schichten für elektronische Transistoren und opto-elektronische Geräte. Zukünftige Unterhaltungselektronik und Elektrofahrzeuge könnten ebenfalls auf Hochleistungs-Lithium-Ionen-Batterien mit silicium- oder zinnbasierten Anoden zurückgreifen. Deren vollständig lithiierten Phasen $Li_{4.4}E(IV)$ können theoretische Kapazitäten von 4200 mAh g^{-1} für Silicium und 990 mAh g^{-1} für Zinn erreichen. Solche Anoden leiden jedoch noch immer unter einer immensen Volumenausdehnung von bis zu 400%vol, welche zum Bruch des Materials führt und somit die Lebensdauer der Elektrode begrenzt. Diese Komplikation wird gemildert, wenn Silicium oder Zinn in nanostrukturierter Form eingesetzt oder in Kohlenstoff eingebettet werden (Si/C oder Sn/C).

Im Zuge dieser Arbeit wurden neuartige und bereits bekannte aryl-substituierte Silane und Stannane synthetisiert, umfassend charakterisiert und verarbeitet, um nanostrukturierte Si/C oder Sn/C-Anodenmaterialien für Lithium-Ionen-Batterien zu entwickeln. Die Silane und Stannane wurden mit Arylgruppen wie Phenyl, *o*-Tolyl, 2,5-Xylyl und 1-Naphthyl oder bislang nicht charakterisierten Gemischen davon substituiert. Es werden die Auswirkungen der Größe und Menge der Substituenten auf die chemischen Verschiebungen im ^{29}Si NMR, die Wechselwirkungen im Festkörper anhand von Einkristallen und die elektrochemischen Eigenschaften der Verbindungen untersucht und diskutiert. Die elektrochemische Charakterisierung von Arylsilanen und -stannanen wurde in nicht-wässriger Umgebung in einer speziell dafür entwickelten und optimierten Cyclovoltammetriezelle durchgeführt. Anschließend wurden die Arylsilane pyrolysiert und die Arylstannane gekoppelt, um Si/C beziehungsweise Sn/C-Anodenmaterialien herzustellen. Die so erhaltenen Materialien weisen spezifische Kapazitäten auf, die diejenigen von kommerziellen Graphitanoden um bis zu 20% übertreffen und eine ausgezeichnete Zyklenstabilität besitzen.

List of Abbreviations

acetone d_6	deuterated acetone
BuLi	butyl lithium
C_6D_6	deuterated benzene
$CDCl_3$	deuterated chloroform
CE, RE, WE	counter, reference and working electrode
CV	cyclic voltammetry
D_2O	deuterated water
DCM	dichloromethane
DEPT	distortionless enhancement by polarization transfer
DLS	dynamic light scattering
EA	elemental analysis
EDX	electron dispersive X-ray spectroscopy
Et_2O	diethyl ether
EtOH	ethanol
eq	equivalent(s)
Fc	ferrocene
GC-MS	gas chromatography-mass spectroscopy
GCPL	galvanostatic cycling with potential limitation
HOMO, LUMO	highest occupied and lowest unoccupied molecular orbital
HSQC/HMBC	heteronuclear single quantum coherence/heteronuclear multiple bond correlation
J	coupling constant
$LiAlH_4$	lithium aluminium hydride
MeCN	acetonitrile
mp	melting point
Naph	naphthyl
NMP	*N*-methyl pyrrolidone
NMR	nuclear magnetic resonance
PEEK	polyether ether ketone
Ph	phenyl
ppm	parts per million
PTFE	polytetrafluorethen, Teflon
PVdF	polyvinylidene difluoride
pyPz	3,6-(2-dipyridinyl)-1,4-dihydropyridazine / pyridine pyridazine
pyTz	3,6-(2-dipyridinyl)-1,2,4,5-tetrazine / pyridine tetrazine
SAXS	small angle X-ray scattering
SEI	solid electrolyte interphase
SEM	secondary electron microscope
TBACl	tetrabutylammonium chloride
TBAF	tetrabutylammonium hexafluorophosphate
THF (d_8)	(deuterated) tetrahydrofuran
TMEDA	*N,N,N',N'*-tetramethylethylene diamine
TMS	tetramethyl silane
UV-Vis	ultra violet-visible
δ	chemical shift

Numbering of Compounds

Table 1 Numbering of silanes and stannanes.

N°	*Compound*	*N°*	*Compound*
1	2,5-xylyl$SiCl_3$	**34**	*o*-tolyl$_4$Sn
2	1-naphthyl$SiCl_3$	**35**	1-naphthyl$_4$Sn
3	2,5-xylyl$_2SiCl_2$	**36**	phenyl$SnCl_3$
4	1-naphthyl(phenyl)$SiCl_2$	**37**	*o*-tolyl$SnCl_3$
5	1-naphthyl$_2SiCl_2$	**38**	1-naphthyl$SnCl_3$
6	2,5-xylyl$_3$SiCl	**39**	phenyl$_2SnCl_2$
7	1-naphthyl(phenyl)$_2$SiCl	**40**	1-naphthyl$_2SnCl_2$
8	1-naphthyl$_2$(phenyl)SiCl	**41**	phenylSnH_3
9	1-naphthyl$_3$SiCl	**42**	*o*-tolylSnH_3
10	phenylSiH_3	**43**	1-naphthylSnH_3
11	2,5-xylylSiH_3	**44**	phenyl$_2SnH_2$
12	1-naphthylSiH_3	**45**	1-naphthyl$_2SnH_2$
13	phenyl$_2SiH_2$		
14	2,5-xylyl$_2SiH_2$		
15	1-naphthyl(phenyl)SiH_2		
16	1-naphthyl$_2SiH_2$		
17	phenyl$_3$SiH		
18	2,5-xylyl$_3$SiH		
19	1-naphthyl(phenyl)$_2$SiH		
20	1-naphthyl$_2$(phenyl)SiH		
21	1-naphthyl$_3$SiH		
22	phenyl$_3$(allyl)Si		
23	1-naphthyl(phenyl)$_2$(allyl)Si		
24	1-naphthyl$_2$(phenyl) (allyl)Si		
25	1-naphthyl$_3$(allyl)Si		
26	3,6-(2-pyridinyl)$_2$-4-((phenyl$_3$silyl)methyl)pyridazine		
27	3,6-(2-pyridinyl)$_2$-4-((1-naphthyl(phenyl)$_2$silyl)methyl)pyridazine		
28	3,6-(2-pyridinyl)$_2$-4-((1-naphthyl$_2$ (phenyl) silyl)methyl)pyridazine		
29	3,6-(2-pyridinyl)$_2$-4-((1-naphthyl$_3$silyl)methyl)pyridazine		
30	(1-naphthyl)phenyl$_3$Si		
31	(1-naphthyl)$_2$phenyl$_2$Si		
32	(1-naphthyl)$_3$phenylSi		
33	phenyl$_8Si_4$ (**a**)/phenyl$_{10}Si_5$ (**b**)		

Index

Introduction

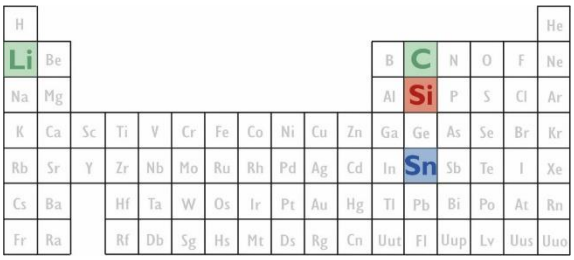

1 Introduction and Objective

Silicon and organosilicon compounds are already broadly applied in modern technology and have become valuable materials in different industries. While organo(halo)silanes are versatile precursor materials for diverse organosilicon derivatives *via* a large range of substitution reactions, their hydrogenated counterparts display many attractive properties such as air and moisture stability and low toxicity. The applications of organosilanes range from protecting groups in organic chemistry to surface modifications and preparation of ceramics. Both organo(halo)silanes and organosilanes are also frequently used as precursors for inorganic polymers or silicon-enriched materials. These may be used in opto-electronics,[1] solar cell technology[2] or as silicon thin films in advanced electronic devices.[3] Organotin compounds, as well, have manifold uses in organic chemistry, *e.g.* in hydrostannolysis or hydrostannation reactions by radical chain mechanisms.[4,5]

Despite the wide-spread application possibilities and the corresponding research interest, a lack of characterisation is still evident. For instance, only few information on the electrochemical reduction and oxidation potentials of hydrogen-bearing organosilanes and -stannanes is available, especially considering aryl-substituted species. With respect to organosilanes, the NMR spectroscopic data of literature-known compounds is often restricted to ^{1}H and ^{13}C spectra, even though ^{29}Si NMR has been established as a conventional characterisation method in the 1980s. The effects of bulky substituents of aryl silanes have recently been studied considering ^{29}Si NMR shifts and crystal structures in our research group by Binder *et al.*.[6–8] The present work extends these previous results by adding novel compounds or completing the characterisation sets of several literature-known compounds. Furthermore, electrochemical characterisation of aryl silanes and -stannanes obtained in a purpose-built cyclic voltammetry cell in non-aqueous environment is provided.

In the last decades, organosilicon and -tin compounds have also become interesting for the use as electrode materials in Li-ion batteries.[9,10] This is owed to their high theoretical capacities in the fully lithiated alloy phase $Li_{4.4}E(IV)$ with values of 4200 mAh g^{-1} for silicon and 990 mAh g^{-1} for tin, respectively. However, the pure elements suffer a large drawback: upon formation of the alloy, a mostly irreversible expansion of up to 400%vol occurs, which causes contact loss after only a few cycles. Since the employment of nano-structured or composite materials was proposed to be able to circumvent this issue,[11] a large portion of research was dedicated to obtain such materials.

This work aims for the development of Si/C and Sn/C materials starting from novel and literature-known aryl silanes and -stannanes for the use as anodes in Li-ion batteries. Therefore, the focus was set on the synthesis, comprehensive characterisation, reactivity, processing and electrochemical testing of the pure materials.

2 Literature

2.1 Organometallic Group 14 Compounds

2.1.1 Organosilanes

Organosilanes are generally prepared from other organometallic compounds reacted with a silicon halide. Friedel and Crafts developed the first organosilane, methyl$_4$Si, in 1863 by reduction of $SiCl_4$ with methylzinc.[12] In 1901, Grignard[13] reported the activated magnesium reagents RMgX (R = organyl, X = halide) prepared from the respective organohalides. Shortly after this, Kipping[14] and Dilthey[15] reported first organo(chloro)silanes prepared from methyl or phenyl Grignard reagents, respectively, reacted with $SiCl_4$ in 1904. The reaction yields in a mixture of mono-, di-, tri- and tetraorgano silanes. In Grignard reactions magnesium is oxidatively inserted into the carbon-halogen bond.[16] A change in polarisation of this bond is caused by the Grignard reagent and the resulting carbanion forms a new σ-bond (*cf.* Scheme 1). Alternative to Grignard reactions, organic groups may be transferred onto silicon by a reaction of tetrachlorosilane with other alkali metal organics. The most frequently used reactions employ butyl lithium to react with an organohalide. Similar to the Grignard reaction, a nucleophilic carbanion forms a new σ-bond, only here the carbanion is created by a halogen-metal exchange.

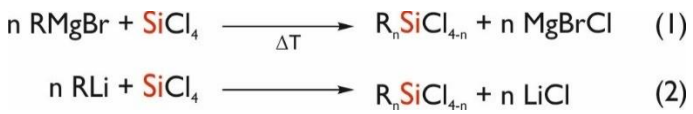

Scheme 1 General reaction scheme for the preparation of organo(chloro)silanes *via* Grignard and lithiation reactions. R = organyl, n = 1-4.

The product distribution depends on stoichiometry between $SiCl_4$ and the respective Grignard reagent/lithiated species as well as on the bulkiness of the substituents. Organolithium reagents are highly reactive towards silicon tetrachloride, which makes them often harder to control than the respective Grignard reagents. Since the latter are sensitive towards the substituent bulkiness and are overall less reactive, they show a higher reaction selectivity. Therefore, the Grignard reagent is preferred for the selective introduction of one organic group while lithiation is mostly employed for two or more organic moieties.[6,17]

The reactive organochlorosilanes offer a wide range of possible reactions, including amination, oligo-/polymerisation and specific hydrolysis with water or alcohols.[18] Furthermore, they are convenient intermediates in the production of organosilanes. The reduction of organo group 14 chlorides with $LiAlH_4$ developed by Finholt[19] leads conveniently to the respective hydrogen rich silanes, germanes or stannanes (see Scheme 2). These materials are widely used in hydrosilylation,[20,21] reduction,[22,23] cyclisation[24] or cross-coupling reactions.[25,26]

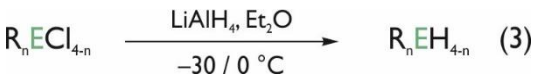

Scheme 2 General reaction conditions for the hydrogenation of organo group 14 halides using $LiAlH_4$ (E = Si, Sn; R = organyl)

Tetraorganosilanes with terminal olefins, such as R_3(allyl)Si, have found a wide-spread set of applications as well: they are applied in a variety of addition/elimination or annulation reactions as well as in the allylation of suitable electrophiles.[27] Generally, the reactivity of organosilanes is determined by the sizes of their substituents. While alkyl moieties tend to be more reactive, their aryl counterparts are able to stabilise certain intermediates.

2.1.2 Organostannanes

Tin hydrides are more sensitive towards oxygen and temperature than the respective silanes or germanes due to the dissociation energy of the Sn–H bond.[28] The sensitivity of E(IV) hydrides may be lowered by gradual replacement of the hydrogen atoms by organic groups, *e.g.* alkyl or aryl moieties. Along with a rising number of organic substituents the sensitivity decreases immensely – for example SnH_4 decomposes slowly at ambient conditions whereas mesityl$_3$SnH is stable at room temperature for an indefinite amount of time.[29] Furthermore, tin hydrides react readily with atmospheric oxygen to form poorly in organic solvents soluble precipitates.[30]

Paneth and his co–workers succeeded in the preparation of stannane *via* different routes including the cathodic reduction of tin sulphate at lead electrodes. Even though this route resulted in comparatively high yields compared to other procedures known at the time, it was still highly inefficient by delivering only 2-3 mg per hour of electrolysis.[31–33]

Both chlorides and hydrides suffer from low yields, inconvenient preparation methods, and instability. This led to a neglect of further investigations on synthesis, characterisation and reactivity of tin hydrides. More recently, a more convenient route to group 14 metal hydrides and their organic derivatives was developed by Finholt and co-workers (see Scheme 2).[19] The preparation method consisted of the reduction of the corresponding chlorides with lithium aluminium hydride ($LiAlH_4$) in diethyl ether. Following this procedure, they were able to generate stannane as well as methylstannane, dimethylstannane and trimethylstannane. A variety of other reducing agents has been used since, including R_2AlH, $NaBH_4$, NaBHCN, B_2H_6, LiH, polymethylhydrosiloxane ($(MeSiOH)_n$, PMHS) and Et_3SiH.[5,34,35] However, the convenient and straight forward procedure using $LiAlH_4$ as hydrogenation agent is still widely used in the successful synthesis of mono-, di- and triorganotin hydrides ($RSnH_3$, R_2SnH_2 and R_3SnH) in high yields and purities.[5,19]

In organic chemistry, organotin hydrides have found numerous applications including compounds designed especially to facilitate the separation of tin residues *via* adsorption on activated carbon, *via* formation of water soluble derivatives, or by support on polystyrene in order to avoid toxic residues.[5]

2.1.3 Organometallic Oligo- and Polymers of Group 14 Compounds

2.1.3.1 Organosilicon Polymers

Industrial polymers based on inorganic main chains often consist of alternating silicon and oxygen atoms (silicones) or alternating phosphorous and nitrogen atoms (phosphazenes) in the backbone. While cyclic and linear polysilanes with backbones of covalently linked silicon atoms were presumably first synthesised by Kipping[36,37] in the 1920s, the first clear description of a

polysilane was given by Burkhard in 1949.[38] Linear chains of organosilanes were first reported by Kumada *et al*. who synthesised methyl(methyl$_2$Si)$_{12}$methyl.[39] Boberski and Allred were able to extend the chain length to 24 consecutive silicon atoms in the backbone.[40] A general scheme of linear organometallic polymer chains is given in Scheme 3, a).

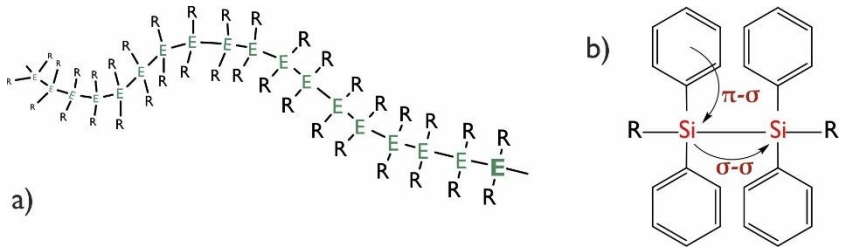

Scheme 3 a) Schematic structure of linear organometallic polymer chains (E = Si, Sn; R = organyl). b) π–σ and σ–σ conjugation in silylarene units as well as in the main polymer chain. R = organyl and/or silylarene units.[1]

Linear and cyclic per(methyl)polysilanes were found to show strong electron absorption bands in the ultraviolet region[41,42], caused by a delocalisation of σ-electrons along the Si–Si backbone, which gives them unique optoelectronic properties.[43] In aryl-substituted linear polysilanes, a so-called σ-π conjugation is generated by silylarene units in the main chain (*cf*. Scheme 3, b)). These result from interactions between Si–Si σ-orbitals and C=C π-orbitals and lead to a bathochromic shift of the absorption maximum, indicating lowered optical band gaps.[2]

The aromatic behaviour of the cyclic arylated organosilanes ($R_{2n}Si_n$) led to extensive studies by West, Gilman as well as Hengge *et al*..[42,44–53] Additional to the aromaticity of these cyclic compounds, they are able to (electro)chemically create highly reactive radical anions, *e.g.* [phenyl$_2$Si]$_4^{\bullet-}$ from octaphenylcyclotetrasilane.[54]

The pure phenyl$_8$Si$_4$ and phenyl$_{10}$Si$_5$ have been investigated as possible candidates for the generation of nano-structured silicon by abstraction of the aromatic leaving groups *via* pyrolysis in our research group (see section 2.1.4).[6,55] Cyclopentasilane, derived from phenyl$_{10}$Si$_5$, undergoes ring opening polymerisation upon cleavage of the Si–Si bonds by UV irradiation and deposit the products in form of thin films.[56] Such silicon-enriched, nano-structured materials are interesting candidates for the use in Si/C composite anodes in Li-ion batteries owing to the high theoretical capacity of silicon which amounts to 4200 mAh g^{-1}.

2.1.3.2 Organotin Polymers

The most widely spread form of organotin polymers are the linear polystannanes which are usually formed from diorganotin dihydrides (R_2SnH_2). Generally, polystannanes consist of a backbone of covalently bound tin atoms which may be labelled as molecular wires embedded in an organic jacket as depicted in Scheme 3.[57] A remarkable feature of these compounds is the σ–delocalisation of the sp^3 orbitals of the Sn atoms, which in addition to very low band gaps leads to an increased degree of electron delocalization with catenation.[58] Polystannanes display a characteristic yellow to orange colour depending on the substituent on the metal: absorption bands of dialkylstannanes are found around 400 nm, which is in agreement with the $\sigma \rightarrow \sigma^*$

transition of delocalized σ–electrons of the alkyl groups whereas diarylstannanes absorb around 470 nm due to σ–π delocalization of the monomer units.[59] The thermal stability up to 200 °C, results in easy processability, and together with a straight forward synthesis, makes these potentially highly conductive metal–bearing materials interesting for a variety of applications. These include plastic electronics where it is envisioned for the production of flexible polymer displays (electronic paper).[60,61]

These materials are accessible *via* electrochemical synthesis or catalysed dehydropolymerisation of the monomeric dihydrides. Metal complexes based on Pd, Pt, Zr, Rh, lanthanides or, less common, Fe and Mo are used as catalysts.[62–67] Only in recent years the use of amine bases such as *N,N,N′,N′*-tetramethylethylenediamine (TMEDA) or pyridine have been introduced to catalyse polymerisation reactions leading to poly(diaryl)stannanes.[68]

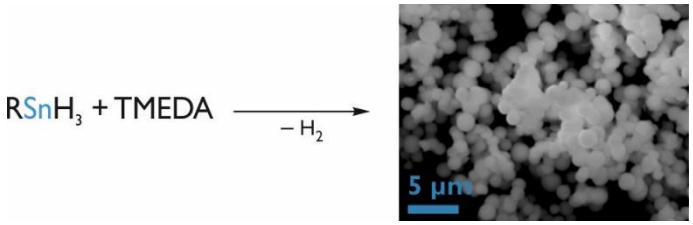

Figure 1 Example of a base-assisted dehydrogenative coupling reaction of organotin trihydrides. R = aryl group.

The investigations on amine bases as catalysts in the dehydrogenative coupling have not been restricted to tin dihydrides, however: the formation of Sn-Sn bonds under the abstraction of hydrogen of organotin monohydrides assisted by pyridine was already described by Neumann in 1962.[69] Recently, Sindlinger and co-workers reported the formation of an aryltin(II) species by the treatment of a highly sterically hindered aryltin trihydride with different amine bases, using 2,6-bis(2′,4′,6′-triisopropylphenyl)phenyl as aryl moiety.[70,71] Concurrently, Zeppek investigated the TMEDA assisted dehydrogenative coupling of monoaryl stannanes with less sterically demanding substituents such as phenyl, *o*-tolyl and 1-naphthyl. These reactions lead to hitherto unknown insoluble, aryl "decorated" Sn based materials (Sn@aryl) whose nano-morphologies are tuneable by the use of different solvents: donating ones such as diethyl ether (Et_2O) or dimethoxy ethane (DME) lead to the formation of spherical particles, whereas apolar solvents such as cyclohexane (CH) or toluene lead to nano rods or branched structures.[72] The versatility in shape and a high theoretical capacity of tin (990 mAh g^{-1}) make these tin enriched nano-materials another promising candidate enhancing the anode capacity in Li-ion batteries.

2.1.4 Pyrolysis

Pyrolysed (organo)silanes have a wide area of applications. Since the 1960s, polymer-derived ceramics (PDCs) were produced directly by pyrolysis of organosilicon polymers, *e.g.* polysiloxanes or polycarbosilanes.[73] The thermal treatment of the latter results in SiC formation, which is widely used in ceramic fibres for high-temperature applications, fibre-reinforced composite materials and coatings.[74]

The complex process of organosilane pyrolysis involves at least three stages: the condensation of the material (1), elimination of small fragments, *e.g.* hydrogen or volatile organic groups such as methane or benzene (2), and the elimination of oxygen as carboxides as well as the crystallisation of β-SiC (3).[75]

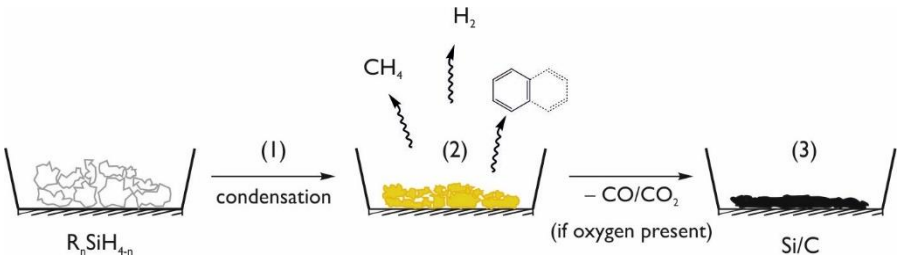

Figure 2 General depiction of the pyrolysis process, displaying condensation (1), cleavage of volatile components (2) and the generated Si/C product (3).

Generally, Si–H bonds are cleaved at approximately 400 °C and release H_2, while Si–C bonds usually cleave at approximately > 650 °C.[76] The cleavage temperature of Si–C is influenced by the structure of the precursor material; in cross-linked polymers, a complete depolymerisation is not possible.[75] The decomposition temperature, solubility as well as the yield of the products appear to be dependent on their molecular structure $(R_1R_2Si)_n$. The pyrolysis products are usually not solely crystallised SiC but rather complex structures caused by radical reactions, in which it is not possible to identify each intermediate.[77] With respect to organo(mono)silanes, pyrolysis sometimes even leads to a Si=C double bond and radical species, as was reported by Ring *et al.* at the example of trimethylsilane and -germane.[78]

Coleman *et al.*[79] reported the formation of silicon nanowires from arylated silanes, using a process with supercritical solvents. Even though the exact mechanism could not be fully elucidated and not all intermediates could be identified, they showed that silanes bearing aromatic residues are promising precursor materials. Pyrolysis of monosilane (SiH_4) leads to the cleavage of H_2 and thus formation of the radical SiH_2, which is often employed for film deposition *via* chemical vapor deposition (CVD) methods.[80] Such radical intermediates could also be detected in pyrolysis experiments involving ethyl- and *tert*-butylsilane.[81]

Experiments conducted by Binder[6,55] with different aryl-substituted mono- and oligosilanes confirmed that these materials are suitable candidates for the formation of nano-structured silicon under elimination of aryl moieties and cleavage of Si–Si bonds. Such nano-structured silicon-rich materials are particularly interesting for an implementation in Li-ion battery anodes, which encouraged further research on the pyrolysis of arylsilanes carried out in this work.

2.1.5 Electrochemistry of Organometallic Group 14 Compounds

2.1.5.1 Organosilicon Compounds

Silicon offers interesting electrochemical properties, peculiarly when present as a silyl substituent of an organic moiety. Halogenated silanes are well-known in literature. For instance, they are useful precursors for generating hydrogen-rich silanes[82–88] and, in combination with reactive metal electrodes, Si–Si bonds. The latter reaction leads to different linear or cyclic polysilanes. The Si–Si bonds themselves act as unique electron pools, making them interesting for electrochemical research.[89–91] While the oxidation/reduction potentials of halogenated and polymeric silane species are well documented, only few information on the electrochemical potentials of arylsilicon hydrides is available.[92,93] Therefore, we investigated the redox potentials of arylsilicon hydrides.

Considering an aryl-substitution on the silicon, the silicon exerts a strong influence on the chemical reactions and the redox properties of π-systems, which is known as the silyl effect.[94] Depending on their position on the aromatic ring system, silyl groups display different properties: upon substitution in α-position they act as acceptors, while in β-position they act as donors. This dual donor/acceptor behaviour enhanced the interest in electrochemical reactions with arylsilanes.[95]

In this work, the main focus is on aromatic systems in α-position with aromatic substituents such as phenyl, 1-naphthyl or 2,5-xylyl. When a silyl group is introduced in such systems the π*-(LUMO) level decreases due to an interaction of a low-lying silicon-based unoccupied orbital, *e.g.* an empty *d* orbital, and the π* orbital of the organic moiety in form of d_π-p_π interactions. Alternatively, the decrease in the LUMO level may be explained by the interaction between Si–R σ* orbitals and the π system.[96] Such orbital interactions further enhance the electron accepting character of the π system, which consequently leads to less negative reduction potentials than the unsubstituted parent π systems.[95]

Another intriguing property of silyl substituents on aromatic rings is the stabilization of negative or positive charges in α-position, including radical anions. This is possible due to d_π-p_π interactions between the half-filled π* orbital of the anion radical and the empty low-lying silicon orbital, which enables a partial electron donation of the π-system to the silicon atom and which eventually stabilises the anion radical. The effects of α-silyl substitution on anion radicals was demonstrated by O'Brien *et al.* by ESR spectroscopy at the example of phenylsilanes.[97] Anodic oxidation of arylsilanes also leads to radical cations on the anode surface. In the absence of water, these radical species are relatively stable. However, in the presence of residual water, the electrolysis leads to black coatings of the anode, consisting mainly of conjugated aromatic polymers.[95]

In general, silicon displays unique properties. It is able to activate organic molecules, specifically aromatic groups. The position of the silyl substituent causes different effects: in α-position the substituent lowers the LUMO of the molecule and consequently facilitates reduction while in β-position it elevates the HOMO and facilitates oxidation.

2.1.5.2 Organotin Compounds

Despite a widespread set of applications, very little is known about the electrochemical properties of organotin hydrides. Similar to their silicon analogues, the focus in electrochemical research of organotin compounds was in the anodic reduction of organotin halides to form the respective hydrides or the preparation of poly(organo)stannanes from the respective chloride monomers.[62,63] The lack of information on the electrochemical potentials as well as their prospective use in anodes for Li-ion batteries provided a motivation for synthesis, characterisation and electrochemical testing of a series of organotin di- and trihydrides.

2.2 Li-Ion Batteries

2.2.1 General Aspects

Innovative technologies and their rapid development in modern times demand for new and efficient power source systems. Particularly electric vehicles and handheld consumer electronics require ever higher energy density and capacity. Since their introduction in 1990 by Sony and Sanyo,[98,99] the Li-ion batteries have become the most widely used battery type for everyday technology.

Generally, the lithium-ion battery consists of anodes with low and cathodes with high voltages *vs.* Li^+/Li, which are soaked in a lithium-rich electrolyte and parted by a glass-fibre separator. Most anodes consist of carbonaceous materials such as graphite. For cathodes, on the other hand, mostly transition metal oxides such as $LiCoO_2$ or $LiMn_2O_4$ are used.[100] Liquid electrolytes of typical Li-ion batteries consist of solutions of $LiPF_6$ in carbonate-based solvents such as ethylene carbonate and dimethyl carbonate. Both electrodes undergo reversible intercalation reactions during (dis)charge of the cell.[101–103] Considering the full battery anodes, cathodes, separator material and electrolytes may be tuned to optimise the performance of the cell.

Rechargeable lithium batteries based on intercalation were suggested by Armand in the late 1970s as so-called *rocking chair* batteries.[104] Due to safety aspects, the use of metallic lithium for anodes has been replaced by carbonaceous materials and later alloys with silicon or tin.[105] However, some of these carbonaceous materials were prone to co-intercalation of propylene carbonate (PC), which was used as electrolyte solvent. To avoid co-intercalation, Sony employed coke as anodes in their first commercial cells.[99] Later, PC was replaced with ethylene carbonate which does not co-intercalate and thus permits graphite anodes.[106,107] Graphite bears a long list of advantages: it is highly abundant, has low voltage hysteresis, good rate capability, low irreversible capacity, high Coulombic efficiency, good electronic conductivity and displays stable lithium storage performances.[10] Despite these excellent properties of graphite, its electrochemical performance is limited by its theoretical capacity of 372 mAh g^{-1} for LiC_6. Therefore, a considerable part of research on Li-ion batteries has been dedicated to the development of novel high capacity materials, which may enhance the capacity of graphite or eventually replace it in anodes altogether.

2.2.2 Anodes Containing Group 14 Compounds

Enhancing the capacity of lithium ion batteries is an on-going chase for new materials. Focusing on the anode, the capacity may only be increased by employing materials with high theoretical capacities. Group 14 elements, for instance, display some of the highest theoretical capacities of the fully lithiated phased $Li_{4.4}Si$ (4200 mAh g^{-1}), $Li_{4.4}Ge$ (1620 mAh g^{-1}), and $Li_{4.4}Sn$ (990 mAh g^{-1}), making them appealing candidates for anode materials. This high capacity, however, comes at the cost of low cycle-life. The lithiation of group 14 elements results in volume expansion of up to 400%. This process is illustrated in Figure 3.

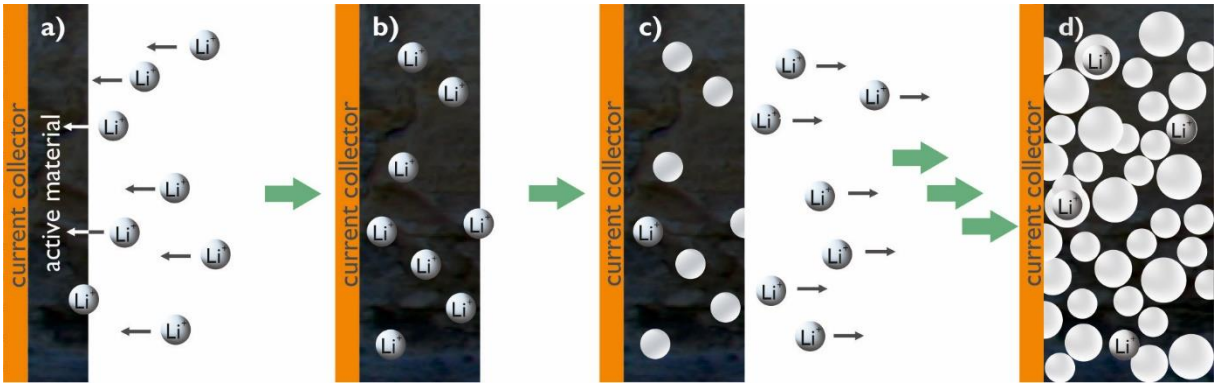

Figure 3 Schematic illustration of lithium intercalation into a group 14 element electrode followed by volume expansion. a) Lithium intercalation into Si or Sn, b) swelling of the metals caused by lithium ion insertion, c) generation of holes upon delithiation, d) trapped lithium ions in a sponge-like structure of Si or Sn after several cycles.

In a) the lithium intercalates into an unused group 14 metal electrode attached to a copper current collector, b) the formation of a Li–E(IV) alloy leads to the expansion of the active material under cleavage of host atom bonds.[9] This step is followed by delithiation of the electrode, which is not able to return to its initial packing structure. Therefore, upon re-charging of the electrode, the lithium ions again form alloys with the pristine parts of the electrode, which after repetition of the delithiation results in a sponge-like structure as depicted in d). The brittleness of the group 14 metal causes a collapse of the matrix and consequently a contact loss to the current collector. Since the use of pure bulk metal leads to these effects, a work-around needed to be developed. It was found that a reduction in metal size could delay the contact loss caused by volume expansion, yet not fully avoid it.[103] Additionally, it was found that the expansion could possibly be mitigated by embedding the metals in a carbonaceous matrix, preferably graphite.[103] Since graphite consists of parallel stacked graphene sheets coordinated by Van-der-Waals forces, the distance between the layers is flexible enough to allow for a certain expansion without destroying the overall structure.[108]

Most research focused on silicon and its derivatives due to its abundance and high theoretical capacity of the fully lithiated phase $Li_{4.4}Si$. However, germanium and tin represent additional candidates for enhancing the capacity of lithium ion batteries, with tin remaining the more economic option.

There are two main approaches towards materials matching the criteria for anodes in Li-ion batteries: top-down processes use elemental group 14 elements which are milled until a suitable size is reached and/or coated by a carbonaceous layer, whereas the bottom-up process starts the development of the material from a molecular level. In this work, the latter approach was followed by the synthesis of different aryl-substituted silanes and stannanes, which were either pyrolysed, polymerised or both.

2.2.2.1 Silicon-Based Compounds

The lithiation mechanism of silicon is complex and highly dependent on voltage limits, temperature, initial silicon structure, particle size and morphology.[10] In the late 1970s, the formation of binary crystalline Li–Si phases matching the Li–Si phase diagram could be shown in electrochemical studies at 400 °C.[109,110] According to the phase diagram and the equilibrium Coulometric titration at 415 °C, $Li_{22}Si_5$ (= $Li_{4.4}Si$) represents the most lithium rich phase of the Li–Si alloy possible, corresponding to a theoretical capacity of 4200 mAh g^{-1}. The behaviour of silicon at room temperature, however, shows significantly different voltage curves.[111] Obrovac and Christensen studied the structural changes of silicon during lithiation *via ex-situ* XRD powder diffraction. They found that at potentials of < 50 mV *vs*. Li/Li^+ a highly lithiated amorphous Si crystallises unexpectedly to form the metastable phase $Li_{15}Si_4$.[112] In this phase, the silicon atoms are isolated and exhibit equivalent crystallographic sites, where each silicon atom is surrounded by 12 lithium neighbours.[113] The full lithiation mechanism is widely discussed in literature and summarised in several reviews.[9,10]

Even though the full lithiation phase $Li_{22}Si_5$ may not be reached at room temperature and therefore its full theoretical capacity is not available, the $Li_{15}Si_4$ phase still amounts to a theoretical capacity of 3580 mAh g^{-1}, which is approximately 10 times higher than the one of graphite.[112] While in several publications initially higher capacities than 3580 mAh g^{-1} are reported for experiments at room temperature, additional capacity can be attributed to surface reactions stemming from either SEI formation of lithiation of surface oxides.[10] The $Li_{15}Si_4$ phase has been found in bulk silicon,[112,114] silicon thin films[115] and nano-structured silicon[116] *via* TEM and XRD experiments. Thus, the theoretical capacities do not seem to differ at different morphologies. However, in order to avoid the problematic volume expansion, most interest has been directed to nano-silicon, in form of nanoparticles, nanotubes, nanowires, Si thin flakes, nanopillars, nanospheres or combinations of nanoparticles and nanowires. The electrochemistry of nano-silicon is very similar to bulk silicon, yet the nano-sizing helps considerably in $Li_{15}Si_4$ formation, SEI growth, packing density and in mitigating the particle fracture.[10]

Therefore, this work also aimed for the generation of nano-structured silicon/carbon materials *via* the pyrolysis of aryl-substituted polysilanes or hydrogen-rich monosilanes.

2.2.2.2 Tin-Based Compounds

Compounds based on tin represent promising materials for the replacement of graphite as high–capacity anodes for Li-ion batteries. Despite the metallic tin being able to electrochemically alloy with lithium to form $Li_{4.4}Sn$ and yielding a maximum theoretical capacity of 990 mAh g^{-1}, the problem of the volume expansion of approximately 300% upon the lithiation process still remains. A great portion of research was dedicated to tin (IV) oxides which lead in the first cycle to the formation of a Li_2O matrix suitable for the accommodation of the volume changes caused by lithium insertion into the tin particles. The high reversible capacity of such materials (782 mAh g^{-1}), however, is accompanied by an almost equally high irreversible capacity (711 mAh g^{-1}) stemming from the decomposition of tin dioxide into metallic tin (and Li_2O), restricting commercial use.[117–120] Further materials investigated for the use in anodes for high capacity Li-ion batteries include SnSb alloys or nano crystalline Sn as well as Sn@C materials.[121–125]

Sn@aryl particles created from aryltin trihydrides offer the advantage of a tin core decorated with aromatic moieties thus combining the high theoretical capacity with built-in electron-rich attack sites for lithiation/delithiation. Additionally, the nano-structure should be more resilient to volume expansion, as was suggested by Besenhard.[11] Another advantage is the possibility to form mixtures with graphite *in-situ*, thereby facilitating a possible capacity boost of the negative electrode (anode). However, very little information on electrochemical reduction or oxidation potentials of either the precursor material (organotin hydrides) or the polymeric particles has been reported.

2.3 Reactivity

2.3.1 Inverse Electron Demand Diels-Alder (iEDDA) Reactions

Diels-Alder reactions, including the iEDDA, are generally [4+2] cycloadditions of dienes with suitable dienophiles. The reactions advance *via* bicyclic, uncharged intermediates which eliminate nitrogen, rearrange into dihydropyridazines and finally oxidise to the respective pyridazines. A general reaction scheme with the well-established reaction partners 1,2,4,5-tetrazines and olefins is displayed in Scheme 4. In contrast to a classic Diels-Alder reaction, the electron withdrawing groups are placed at the diene instead of on the dienophile, which lowers the $HOMO_{dienophile}$-$LUMO_{diene}$-gap and allows for a fast reaction.

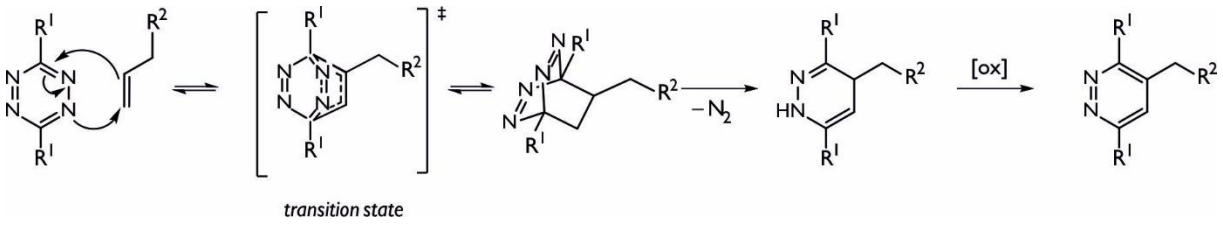

Scheme 4 Inverse electron demand Diels-Alder (iEDDA) reaction leading to the formation of pyridazines.

Using tetrazines as dienes, the reactions have been determined to match the criteria of *click-chemistry* as established by Sharpless in 2001[126–128] and offer several advantages: catalysts or excesses of educts are not necessary and they usually undergo only few side-reactions,[129–131] whose products are effectively removed by chromatographic methods.[132] Furthermore, they belong to some of the fastest *click* reactions, whose reaction rates are tuneable by exchange of the residues R^1 (*e.g.* phenyl or pyridyl) and R^2 (*e.g.* norbornenes or styrene), the use of different solvents such as methanol, tetrahydrofuran or toluene, or application of temperature. Lastly, a large advantage is given by the possibility to optically detect the full conversion of the tetrazine educts by a colour change from bright pink to yellow, hence no elaborate determination of the reaction progress is necessary.

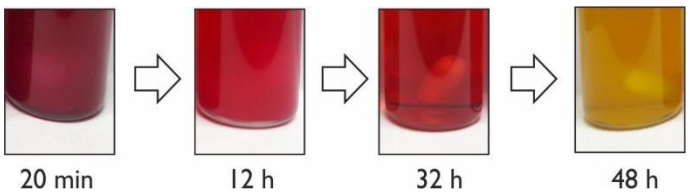

Figure 4 Colour change of the reaction solution upon consumption of pyTz at the example of $phenyl_3(allyl)Si$ in THF at room temperature.

The most frequently used dienes include bicyclic norbornenes, which enhance the reaction rates with their ring-strain. However, also olefins without ring strain such as hexene or styrene were found to fully convert the tetrazine educt, albeit at a slower rate. The products open up a set of interesting possibilities, such as the targeted functionalisation of macro-porous foams,[133] the synthesis of block-copolymers[134,135] or the modification of materials[126]. Most of these applications based on the cycloaddition of two purely organic educts, which encouraged us to extend the research on olefin-substituted silanes as dienophiles for the use in iEDDA reactions.

Silanes

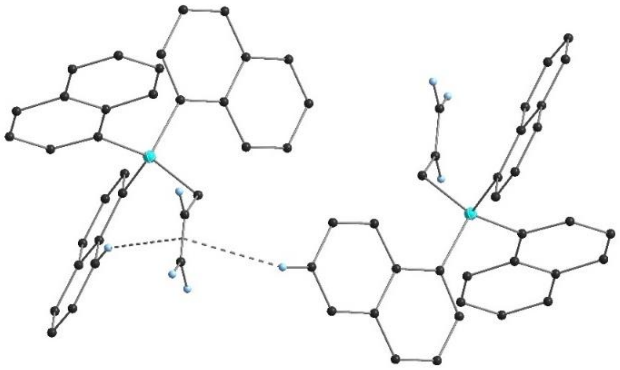

3 Results and Discussion

3.1 Synthesis

Over the course of this work various aryl-substituted silanes were synthesized and comprehensively characterised. The substituents were chosen considering a potential application in Li-ion anodes, where enrichment of the most commonly used graphite with silicon was aimed at by intercalation of monomeric silanes or by introducing silicon enriched particles gained by pyrolysis into the active material. Therefore, planar, aromatic residues with a sp^2 hybridised carbon on the silicon atom were chosen which are similar to the graphite matrix, could embed lithium ions during the charging step of a Li-ion battery and doubled as target leaving-groups when thermally treated. Additional focus was set on the effects of steric bulk on synthetic aspects as well as the spectroscopic, electrochemical and solid-state properties. With respect to all of the mentioned reasons phenyl, 1-naphthyl and 2,5-xylyl, were employed.

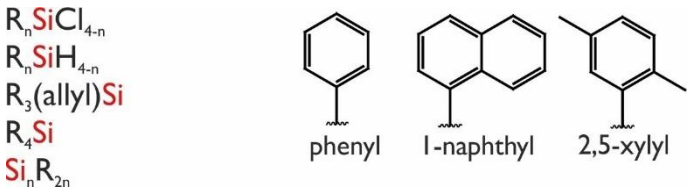

Figure 5 General formulations of organosilane target molecules (R = aryl substituent) and the investigated aryl moieties (right).

Aryl(chloro)silanes were synthesised as educts for further functionalised arylsilicon compounds. Their synthesis follows two typically employed reaction pathways with varying stoichiometry of the aryl bromide towards $SiCl_4$, $phenylSiCl_3$ or $phenyl_2SiCl_2$ (Figure 6). It was found that for the introduction of more than one aryl moiety onto the silicon a reaction *via* the lithiation route led to only minor by-products whereas the cleanest aryl trichlorosilanes resulted from Grignard-type reactions with a large excess of $SiCl_4$.[6]

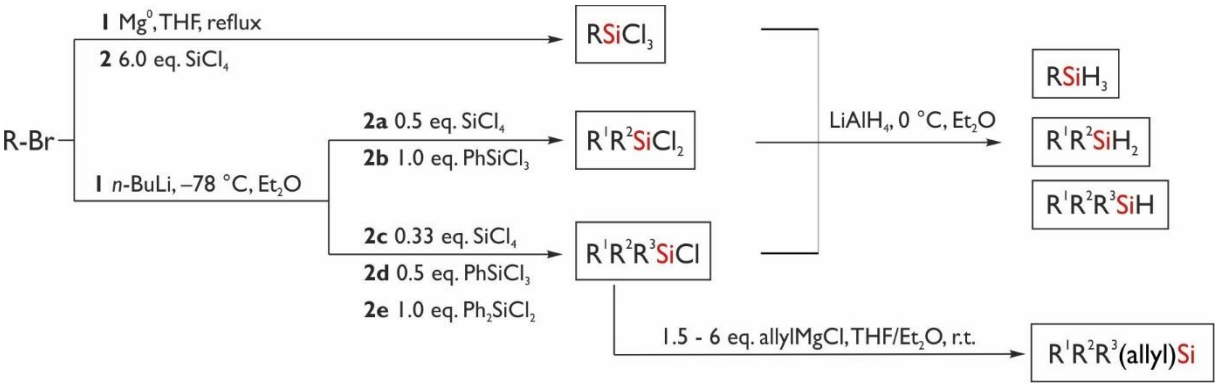

Figure 6 General synthetic procedures towards R_nSiZ_{4-n} (R = phenyl, 1-naphthyl, 2,5-xylyl; Z = Cl, H, allyl).

Additionally, perarylated silanes were synthesised for comparison. Cyclic compounds, *i.e.* $phenyl_8Si_4$ and $phenyl_{10}Si_5$, and tetraarylsilanes R_4Si with R = phenyl, 1-naphthyl were prepared according to literature procedures.[37,136,137] A list of all synthesised compounds along with the numbering scheme (Table 1) may be found on page V of this work.

3.1.1 Aryl-Substituted Chlorosilanes (R_nSiCl_{4-n})

$RSiCl_3$ (1-3): Aryltrichlorosilanes were prepared *via* reaction of the respective aryl Grignard reagent with $SiCl_4$ in THF, as reported in literature.[138] In a previous study performed in our working group it was established that employment of large excesses of $SiCl_4$ (8 equivalents) could reduce the formation of by-products.[6] However, in the present work it was found that also smaller excesses, *i.e.* 4-6 equivalents, lead to the desired effect, yielding in 76% of 2,5-xylyl$SiCl_3$ (**1**) and 90% of 1-naphthyl$SiCl_3$ (**2**). Purification of the products by distillation resulted in crystals suitable for single crystal X-ray diffraction.

R_2SiCl_2 (4,5): For the synthesised diaryldichlorosilanes a lithiation reaction was preferred over the Grignard route due to comparatively less by-products. In a typical reaction the aryl bromide was lithiated at –78 °C in Et_2O and subsequently transferred onto a solution of 0.5 equivalents $SiCl_4$ at 0 °C (Figure 6, route **2a**). After stirring at room temperature (room temperature), filtration of the formed salts and evaporation of the solvent, the products were purified by distillation or recrystallisation from THF, toluene or ethyl acetate. The compounds 2,5-xylyl$_2SiCl_2$ (**3**) and 1-naphthyl$_2SiCl_2$ (**5**) could be obtained in satisfactory yields of 65%. In case of the mixed substituent compound
1-naphthyl(phenyl)$SiCl_2$ (**4**) the procedure was optimised by transferring the lithiated aryl species onto a solution of 2.0 equivalents phenyl$SiCl_3$ at –20 °C (Figure 6, route **2b**). Thereby the formation of side-products could be minimised and the yield of the desired product could be elevated to 62% as compared to the standard procedure yielding in approximately 40%.

R_3SiCl (6-9): Triaryl chlorosilanes were prepared according to literature procedures[6,137] *via* lithiation of the respective aryl bromide with *n*-butyl lithium (*n*-BuLi) in Et_2O at –78 °C and subsequent reaction with a chlorosilane at 0 °C. While 2,5-xylyl$_3SiCl$ (**6**) and 1-naphthyl$_3SiCl$ (**9**) were prepared with 0.33 eq of $SiCl_4$ each (Figure 6, route **2c**), phenylated chlorosilanes were employed for the formation of 1-naphthyl/phenyl mixed substituent monosilanes, namely 1.0 eq phenyl$_2SiCl_2$ (Figure 6, route **2d**) for 1-naphthyl(phenyl)$_2SiCl$ (**7**) and 0.5 eq phenyl$SiCl_3$ (Figure 6, route **2e**) for 1-naphthyl$_2$(phenyl)$SiCl$ (**8**). The solid products were purified by recrystallization in THF, toluene or ethyl acetate resulting crystals suitable for single crystal X-ray diffraction studies.

3.1.2 Aryl-Substituted Silanes (R_nSiH_{4-n})

The preparation of all reported aryl silanes based on a reaction of the precursor aryl chlorosilanes with lithium aluminium hydride ($LiAlH_4$) in Et_2O at 0 °C. Phase separation with diluted, degassed sulfuric acid, removal of salts over aqueous, degassed sodium tartrate solution and evaporation of the solvent resulted in the colourless hydride species.

$RSiH_3$ (10-12): The primary silanes phenylSiH_3 (**10**), 2,5-xylylSiH_3 (**11**) and 1-naphthylSiH_3 (**12**) were purified by distillation resulting in air- and moisture sensitive colourless oils.

R_2SiH_2 (13-16): The secondary silanes phenyl$_2SiH_2$ (**13**) and 1-naphthyl(phenyl)SiH_2 (**15**) were purified by distillation resulting in colourless oils. Compounds 2,5-xylyl$_2SiH_2$ (**14**) and 1-naphthyl$_2SiH_2$ (**16**) were purified by recrystallization from toluene or THF, affording crystals suitable for single crystal X-ray diffraction. In contrast to the known air- and moisture sensitivity of phenylated secondary silanes, no hydrolysis was observed for compounds **14-16** when stored

under air for several weeks. The sterically more demanding substituents offer a shielding of the silicon centre atom which slows down the reactivity and thus provides higher stability to ambient conditions.

R_3SiH (17-21): Purification of the tertiary silanes phenyl$_3$SiH (**17**), 2,5-xylyl$_3$SiH (**18**), 1-naphthyl(phenyl)$_2$SiH (**19**), 1-naphthyl$_2$(phenyl)SiH (**20**) and 1-naphthy$_3$SiH (**21**) was carried out by recrystallisation from THF, toluene or ethyl acetate. For compounds **19**-**21** the hydrogenation reaction was performed in a mixture of Et_2O and THF due to the decreasing solubility caused by the introduction of the sterically demanding 1-naphthyl groups.

3.1.3 Triaryl(allyl)silanes

The triaryl(allyl)silanes (**22**-**25**) were obtained *via* Grignard reaction of allyl chloride in Et_2O and subsequent reaction with a triaryl chlorosilane in Et_2O solution at room temperature. A mixture of Et_2O and THF was necessary for compounds containing more than one 1-naphthyl moiety (1-naphthyl$_2$(phenyl)(allyl)Si (**23**) and 1-naphthyl$_3$(allyl)Si (**24**)) due to low solubility. Extraction of the organic phase with diluted hydrochloric acid (approximately 3%) yielded in 67-95% of the desired products. However, such yields could only be obtained, when an excess of 1.8 to 6.5 equivalents of the Grignard reagent was employed. Otherwise, larger amounts of unreacted triaryl(chloro)silanes were observed. The concentration of the Grignard reagent was determined by titration against 0.1 M hydrochloric acid with phenolphthalein as indicator. In contrast to usual Grignard reagents, which are liquid or easily soluble in donating solvents, the allylMgCl species forms a colourless, hardly soluble gel. Therefore, instead of filtrating the reagent to remove excessive Mg^0 and adding it to the chloride solution, the procedure was reversed since the selectivity was neglectable for the targeted compounds. The reactions led to colourless, easily in donating solvents soluble compounds. All triaryl(allyl)silanes were purified by recrystallisation from THF and afforded crystals suitable for X-ray diffraction.

3.1.4 Reactivity Studies

Triorgano(allyl)silanes are frequently used in organic chemistry for elimination/addition, annulation reactions or as allylation agent for suitable electrophiles.[27] While alkyl moieties tend to be more reactive, their aryl counterparts are able to stabilise certain intermediates.[27,139] Thus far, mostly phenyl moieties were used as aryl substituents since they are easily available. However, the use of differently sized aryl substituents is a promising route towards stereo-controlled reactions as shown by Knölker and co-workers who used a *tert*-butyl and phenyl substituted allylsilane for Lewis acid promoted formal [3+2] cycloaddition reactions.[140,141]
This encouraged further investigations in the direction of cycloadditions of arylated allylsilanes.

3.1.4.1 iEDDA Reactions

iEDDA reactions of 1,2,4,5-tetrazines with olefins have found a wide-spread set of applications in "click chemistry" and are very convenient due to their mild reaction conditions where neither an excess of reagent nor a catalyst is required.[142] However, hitherto no reactions of 1,2,4,5-tetrazines

with double-bond bearing organosilanes have been reported. Thus, the triaryl(allyl)silanes synthesised in this work (**22**-**25**) were reacted with 3,6-(2-pyridinyl)$_2$-1,2,4,5-tetrazine (**pyTz**) and the influence of the substituent sizes on the kinetics was determined by a literature known procedure.[127] The assumed reaction path is displayed in Scheme 5.

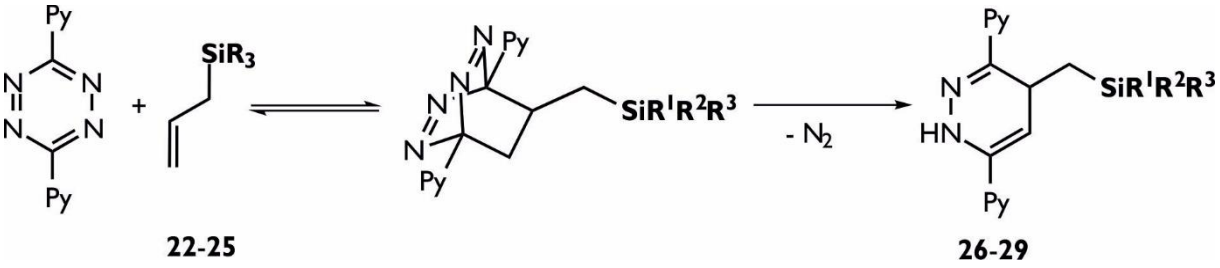

Scheme 5 Inverse electron demand Diels-Alder (iEDDA) reactions leading to silylated dihydropyridazines (compounds **26**-**29**). Py = pyridyl, pyPz = pyridine 1,4-dihydropyridazine.

PyTz was prepared according to a Pinner type reaction as described in literature.[133,143] In a typical reaction **pyTz** was reacted with 1.0 eq of a triaryl(allyl)silane in THF at room temperature. The conversion of the **pyTz** was observable by the typical colour change from pink to yellow and additional clearing up of the reaction suspension upon consumption of the tetrazine (Figure 7, right). ^{29}Si NMR shifts as well as ^{1}H NMR confirmed almost complete conversion of the **pyTz** after 48-160 h (**26**-**29**) resulting in isolated yields of typically 35-40% after column chromatography. The identity of the 1,4-dihydropyridazine (pyPz) products, as shown in Scheme 5, could further be confirmed by 2D HSQC and HMBC NMR spectra as well as by X-ray crystallography in case of **29** (*cf.* section 3.3.4, Figure 27). The crystal structure shows an implementation of the silane into the central ring-system of the **pyTz** under elimination of N_2 resulting in a non-planar six-membered ring-structure. In many cases the herein obtained **pyPz** derivatives are not the final products since usually exposure to air leads to oxidation of the dihydropyridazine system yielding the corresponding pyridazine derivatives.[133] However, in case of the triaryl(allyl)silanes, the hyperconjugation of the silicon atom over two bonds as well as the bulky nature of the substituents seems to be responsible for the stabilisation of the 1,4-dihydropyridazine product. No sign of oxidation could be retrieved upon storage of **26**-**29** at room temperature under ambient conditions for weeks.

The reaction kinetics was studied under pseudo-first order conditions using UV-Vis spectroscopy in toluene as the solvent. Second order rate constants ranging from 3.95×10^{-3} (**13**) to 9.01×10^{-4} M^{-1} s^{-1} (**16**) were obtained. Expectedly, the reaction rate is decreasing along with increasing bulk-size provided by the aryl-moieties. Nevertheless, the rate constants are unexpectedly high when compared to those for smaller, sterically less encumbered alkenes like styrene (3.0×10^{-3} M^{-1} s^{-1} measured in MeOH) or 1-hexene (1.0×10^{-3} M^{-1} s^{-1} measured in MeOH).[127] Polar-protic solvents like MeOH are known to accelerate iEDDA reaction in comparison to nonpolar like toluene used here.[127] The use of MeOH was prevented by the low solubility of **23**-**25** in this solvent. However, the solubility of **22** was sufficient to perform the kinetic experiment which resulted in a second order rate constant approximately two times higher ($7.35 \times 10^{-3}M^{-1}$ s^{-1}) in comparison to the experiment in toluene. Accordingly, **22** reacts more than 7 times faster than 1-hexene under the

same reaction conditions. Consequently, the triarylsilyl group in allylic position exerts an activating effect on the double bond.

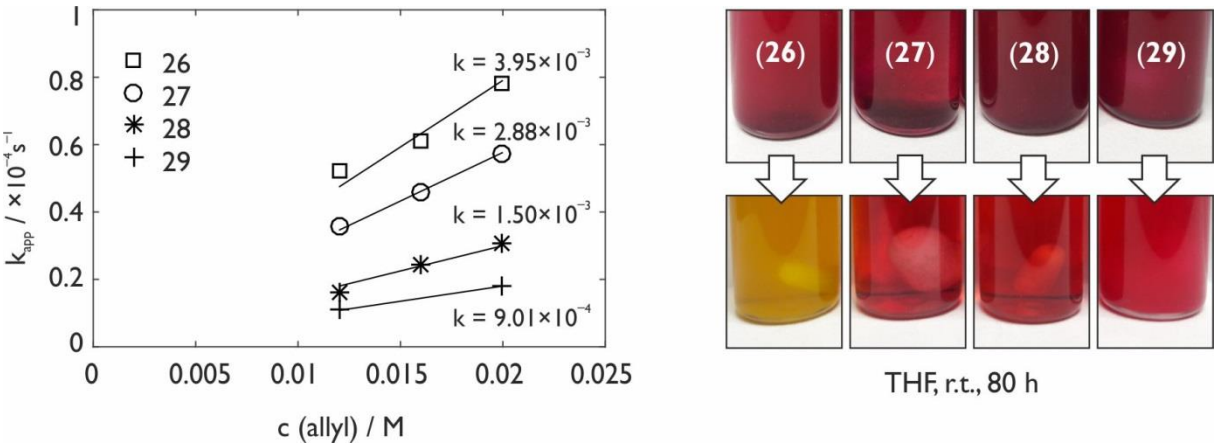

Figure 7 Linear dependence of second order reaction rate constants on the alkene concentration for **26**-**29** (left), color change during the iEDDA reaction (right).

To further elucidate this effect, the iEDDA of trimethylallylsilane and **pyTz** was studied in toluene and a second order rate constant of 6.15 × 10^{-3} $M^{-1}s^{-1}$ was determined, meaning that this transformation is about 1.5 times faster than the reaction of **22** and the activating effect is not specific for triarylsilyl groups but is also present for trialkylsilyl groups. However, it is worth to note that the corresponding 1,4-dihydropyridazine derivative featuring the trimethylsilyl group is not stable and decomposes into two still unidentified follow-up products. This behaviour is in strong contrast to clean formation of **26**-**29** from **22**-**25**.

A possible effect caused by the electron-withdrawing nature of the substituents was tested by reaction of methoxy$_3$(allyl)Si. The reaction in THF resulted in conversion of approximately 90% of the silane after 70 h. However, when the same experiment was carried out in toluene instead, the reaction rate was slowed down drastically (210 h).

Overall, the reactivity of the terminal double bond in triaryl(allyl)silanes in iEDDA reactions revealed an activating effect of the silyl group. The second order rate constants for the reaction of triaryl(allyl)silanes are higher than for 1-hexene.

3.1.5 Perarylated Silanes

In order to complete the row of homologues, a series of tetraaryl silanes with 1-naphthyl and phenyl as substituents was synthesised according to adapted literature procedures.[137,144] 1-napthyl(phenyl)$_3$Si (**30**) could be obtained by reaction of phenyl$_3$SiCl with an excess of freshly prepared 1-naphthyl lithium at 0 °C (*cf.* Figure 8). The product was worked up analogous to the triaryl chlorosilanes and purified by recrystallisation from toluene. 1-naphthyl$_2$(phenyl)$_2$Si (**31**) and 1-naphthyl$_3$(phenyl)Si (**32**), however, could not be obtained by the same reaction with a phenyl chlorosilane. Instead, these compounds were successfully synthesised in moderate yields by employing the 1-naphthyl-containing educts 1-naphthyl(phenyl)$_2$SiCl (**7**) and 1-naphthyl$_3$SiCl (**9**), respectively.

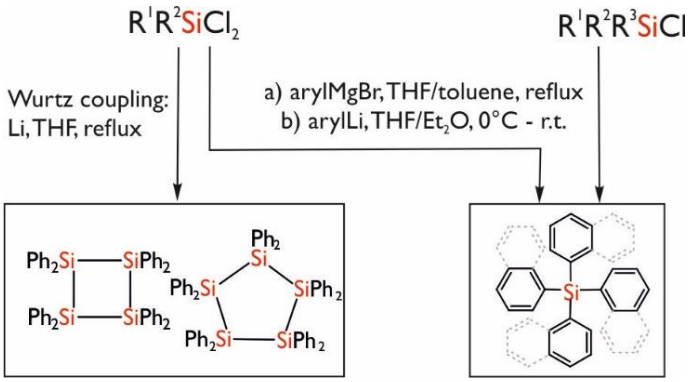

Figure 8 Synthetic procedures towards perarylated silanes.

The synthesis of 1-naphthyl$_4$Si was attempted *via* different routes, always involving either the Grignard reagent 1-naphthylMgBr or its lithiated species 1-naphthylLi. The reactions were carried out employing different ratios of the 1-naphthyl reagent with either $SiCl_4$ (4-8 equivalents), 1-naphthyl$_3$SiCl (4-10 equivalents), 1-naphthyl$_2$$SiCl_2$ (4 equivalents) or 1-naphthyl$_2$$SiF_2$ (2 equivalents). THF and/or toluene were used as solvents, the reactions were carried out at 0 °C, room temperature or at reflux. However, all of the attempted routes resulted in 1-naphthyl$_3$SiX (X = Cl, F). DFT calculations conducted by Prof. M. Flock stated that the desired product could theoretically exist; however, the thermodynamic conditions could not yet be met with the conducted experiments. A detailed summary of the reaction conditions is given in section 5.2.1 of this work.

With the prospect of an application in Li-ion battery anodes, also arylated oligosilanes were considered. Synthesis was carried out according to literature procedures *via* Wurtz-type coupling of phenyl$_2$$SiCl_2$ with lithium.[36,48,145,146] These compounds offer the intriguing property of σ-delocalisation along the Si–Si backbone, which is close to aromatic behaviour. While linear phenyl-substituted silanes are mostly insoluble in organic solvents, their well-established cyclic counterparts with the general formula phenyl$_{2n}$Si$_n$ (n = 4-6) are soluble in solvents such as toluene. Additionally, the latter are especially interesting due to their ability to electrochemically form radical anions[54] with the delocalised extra electron within the silicon skeleton. In combination with the aryl substituents, the influence of the radical anions is likely to contribute to a higher capacity of graphite anodes.

3.2 ^{29}Si-NMR

Functionalised organosilanes are considered for a wide variety of applications *e.g.* in ceramics or surface modification materials. Despite a recent interest in organosilicon chemistry, there is still a considerable lack in experimental data, especially regarding aryl-substituted silanes. For instance, information on ^{29}Si–NMR shifts of organosilicon compounds is only partially reported. This stems from the fact that ^{29}Si–NMR spectroscopy was established in the early 1960s but only became a conventional characterisation method two decades later. In our working group, the effects of the bulkiness of aryl substituents on the NMR behaviour were investigated with focus on mono- and diaryl (chloro)silanes.[6] The present work enhances previous investigations by focusing on different substituents as well as on asymmetrically substituted species. Additionally, the effects of non-aromatic functionalities *i.e.* Cl, H, allyl and pyridine pyridazine (pyPz), on the NMR behaviour are discussed.

Considering the experiments established within our working group,[6] ^{29}Si–NMR experiments were carried out with relaxation delay times adjusted to the sterical hindrance of the compounds. The relaxation times ranged from 20-60s, whereas 1-naphthyl$_3$(phenyl)Si (**32**) required the longest delay. For compounds **22**-**29** bearing a proton on the α-positioned carbon in *ortho* configuration to the silicon, a DEPT (Distortionless Enhancement by Polarisation Transfer) sequence was used.

The experimental ^{29}Si-NMR shifts for compounds **1**-**9** as well as comparable literature-known shifts are summarised in Table 2. The shifts of herein synthesised products are given in $CDCl_3$. However, some shifts of previously published compounds are reported in C_6D_6. Nevertheless, since the solvent influences the ^{29}Si shift in a range of ±1 ppm, some trends may be determined. If not marked otherwise, the chemical shifts were determined with compounds prepared during this work.

Table 2 ^{29}Si–NMR of synthesised and literature-known aryl chlorosilanes in $CDCl_3$. *Shifts reported in C_6D_6.

№	***RSiCl$_3$***	*δ ^{29}Si [ppm]*	№	***R$_2$SiCl$_2$***	*δ ^{29}Si [ppm]*	№	***R$_3$SiCl***	*δ ^{29}Si [ppm]*
	SiCl$_4$	–18.0[147]						
	phenylSiCl$_3$	–0.6		*phenyl$_2$SiCl$_2$*	5.9		*phenyl$_3$SiCl*	1.2
	o-tolylSiCl$_3$	–1.0		*o-tolyl$_2$SiCl$_2$*	6.2		*2,4-xylyl$_3$SiCl*	4.6*
	2,4-xylylSiCl$_3$	–0.4*		*2,4-xylyl$_2$SiCl$_2$*	7.2*	**6**	*2,5-xylyl$_3$SiCl*	2.9
1	*2,5-xylylSiCl$_3$*	–0.9	**3**	*2,5-xylyl$_2$SiCl$_2$*	6.4	**7**	*1-naphthyl(phenyl)$_2$SiCl*	2.4
2	*1-naphthylSiCl$_3$*	–0.8	**4**	*1-naphthyl(phenyl)SiCl$_2$*	6.9	**8**	*1-naphthyl$_2$(phenyl)SiCl*	3.1
	2-naphthylSiCl$_3$	–0.9[17]*	**5**	*1-naphthyl$_2$SiCl$_2$*	7.3	**9**	*1-naphthyl$_3$SiCl*	3.7

All novel chlorosilanes (compounds **1**-**9**) display chemical shifts fitting to values reported in literature. Comparing monoarylated chlorosilanes to their di- and triarylated counterparts, the well-known "sagging" behaviour is observable, leading to a bell-shaped curve when the chemical shifts are plotted against the sum of electronegativities. The shape of the curve is influenced by the shielding of the silicon atom by the substituents; a detailed discussion is provided by Ernst *et al.*.[148]

Regarding the substitution pattern of the chlorosilanes a consistent low-field shift is noticeable along with the increasing number of sterically demanding substituents, *e.g.* 1-naphthyl. As expected, all of the chlorosilanes with mixed substituents display ^{29}Si NMR shifts between the ones of the purely phenyl- or 1-naphthyl-substituted silanes.

With respect to the hydride species, an almost linear trend of a low-field shift is observed along with an increasing number of aryl-substituents (Figure 9). The influence of the aryl moiety on the chemical shift lessens with increasing substituent numbers. Considering 2,5-xylyl-substituted compounds, for instance, the largest high-field shift is provided by the mono-arylated species (**11**) with –62.9 ppm, followed by the diaryl silane (**14**) with –39.5 ppm and finally the triaryl silane (**18**) with the largest low-field shift of –20.7 ppm. The same trend is mirrored also in the substituent bulkiness, as the strongest low-field shifts are observed for the most sterically shielded silanes, *i.e.* mesityl$_3$SiH.[149] It becomes evident that the substitution in *ortho* position of the aryl moiety, such as the methyl groups of 2,5-xylyl or mesityl, as well as the extended ring-system of 1-naphthyl, cause this effect by providing a steric shielding of the silicon core.

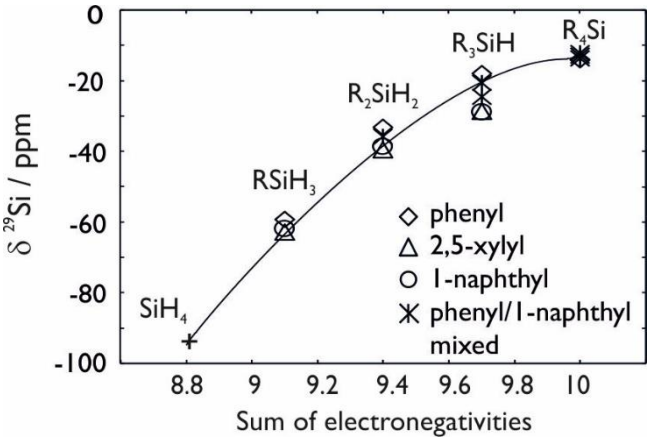

Figure 9 ^{29}Si NMR shifts of differently aryl-substituted silanes *vs.* the sum of substituent electronegativities according to Allred-Rochow.

All of the presented silanes **10**-**21**, again, are in agreement with previously published values. Additionally, the $^{1}J_{Si-H}$ coupling constants range between 195-203 Hz and are therefore also within the expected range (Table 3).[8]

Table 3 ^{29}Si-NMR and hydride (^{1}H) shifts of synthesised and literature-known arylsilanes. * Shifts reported in C_6D_6 ** Shifts reported in THF d_8.

No	R_nSiH_{4-n}	δ ^{29}Si [ppm]	δ ^{1}H (hydride) [ppm]	$^{1}J_{Si-H}$ [Hz]
	SiH_4	–95.8[147]**	3.14	203.0
10	*phenylSiH$_3$*	–59.2	4.24	199.6
	o-tolylSiH$_3$	–62.8	4.24	200.1
	2,4-xylylSiH$_3$	–63.9[6]*	4.27	197.8
11	*2,5-xylylSiH$_3$*	–62.9	4.25	200.2
12	*1-naphthylSiH$_3$*	–61.9	4.59	201.3
	mesitylSiH$_3$	–77.6[93]*	4.25	198.1

№	R_nSiH_{4-n}	δ ^{29}Si [ppm]	δ ^{1}H (hydride) [ppm]	$^{1}J_{Si-H}$ [Hz]
13	*phenyl$_2$SiH$_2$*	–33.3	4.99	199.2
	o-tolyl$_2$SiH$_2$	–39.7[150]	4.97	—
	2,4-xylyl$_2$SiH$_2$	–40.4[6*]	5.21	195.4
14	*2,5-xylyl$_2$SiH$_2$*	–39.5	4.93	197.2
15	*1-naphthyl(phenyl)SiH$_2$*	–35.9	5.39	199.6
16	*1-naphthyl$_2$SiH$_2$*	–38.7	5.56	200.9
17	*phenyl$_3$SiH*	–18.1	5.56	200.0
18	*2,5-xylyl$_3$SiH*	–20.7	5.93	199.0
19	*1-naphthyl(phenyl)$_2$SiH*	–24.5	5.92	196.5
20	*1-naphthyl$_2$(phenyl)SiH*	–28.7	6.40	197.6
21	*1-naphthyl$_3$SiH*	–28.9	6.84	196.6
	mesityl$_3$SiH	–44.1[149*]	5.72	—

Clear trends are also evident considering species of the general formula aryl$_3$SiZ where aryl = phenyl, 1-naphthyl and Z = allyl, pyridine pyridazine (pyPz) or another aryl moiety. All of these tetraorgano silanes show peaks in the range of –7.6 to –18.7 ppm (Table 4), which is consistent with values reported in literature for similar compounds. Since compounds **26**-**29** decomposed when exposed to CDCl$_3$, the NMR shifts were obtained in acetone d$_6$. In order to directly compare them to their educts (compounds **22**-**25**), the latter were also measured in acetone d$_6$.

Table 4 ^{29}Si–NMR shifts for triaryl(allyl)silanes, silylated pyridazines and tetraarylsilanes in CDCl$_3$. * Shifts are reported in acetone d$_6$.

№	*Compound*	δ ^{29}Si [ppm]
22	*phenyl$_3$(allyl)Si*	–13.8 / –13.8*
23	*1-naphthyl(phenyl)$_2$(allyl)Si*	–12.9 / –13.1*
24	*1-naphthyl$_2$(phenyl) (allyl)Si*	–11.5 / –11.3*
25	*1-naphthyl$_3$(allyl)Si*	–7.6 / –8.3*
	1-naphthyl(2,4,6-mesityl)(phenyl)(allyl)Si	–14.5[151]
	mesityl$_3$(allyl)Si	–18.7[152]
26	*phenyl$_3$SipyPz*	–13.2*
27	*1-naphthyl(phenyl)$_2$SipyPz*	–12.4*
28	*1-naphthyl$_2$(phenyl)SipyPz*	–10.9*
29	*1-naphthyl$_3$SipyPz*	–9.1*
	phenyl$_4$Si	–14.0[153]
30	*1-naphthyl(phenyl)$_3$Si*	–13.7
31	*1-naphthyl$_2$(phenyl)$_2$Si*	–12.9
32	*1-naphthyl$_3$(phenyl)Si*	–12.2

An interesting behaviour was observed for triaryl(allyl)silanes: compounds **22**–**25** show a progressing high-field shift along with increasing substituent sizes with values between –13.8 ppm (**22**) and –7.6 ppm (**25**). However, the values deviate for the sterically more demanding literature-known compounds 1-naphthyl(2,4,6-mesityl)(phenyl)(allyl)Si[151] and mesityl$_3$(allyl)Si.[152] This could indicate the effects of two *ortho* positioned methyl groups in the 2,4,6-mesityl moiety on the symmetry and electronic structure of the molecule. The overlapping orbitals of these methyl-group containing aryl moieties may cause such a high-field shift.

With respect to triaryl silanes substituted with phenyl and 1-naphthyl groups, solely linear correlations of the ^{29}Si shifts were observed. Depending on the nature of the fourth substituent, the trends were directed towards low-field shifts with increasing substituent bulk (Figure 10). The only exception was posed by the hydride species, which shift towards high-field instead. This is in agreement with literature.[6,8]

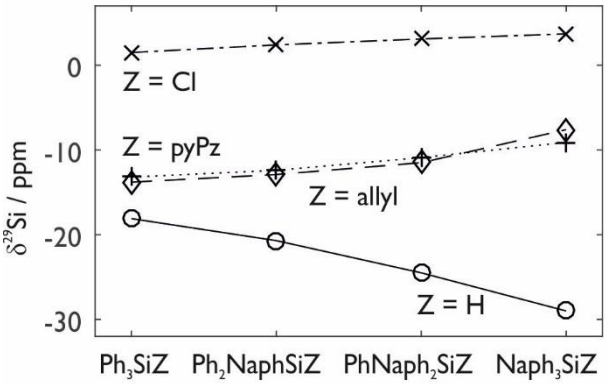

Figure 10 Linear dependence of ^{29}Si NMR shifts on increasing substituent bulk-sizes of phenyl/1-naphthyl substituted silanes R$_3$SiZ (Z = Cl, H, allyl, pyPz) in differently functionalised triaryl silanes.

Considering the triaryl silanes substituted with a fourth organic moiety it becomes evident that the chemical shift is mostly dependent on the nature of the adjacent carbon atoms instead of on the bulk-size of the respective substituents. Thus, the terminal olefin of the allyl group is affecting the electronical shielding in the same way as the extended hetero-cycle attached to the silicon atom All R$_3$SipyPz derivatives were measured in acetone d$_6$ instead of CDCl$_3$ due to stability issues with the latter solvent. However, a direct comparison is deemed possible since the respective allyl derivatives were measured in both solvents and close to no deviation of the ^{29}Si could be detected.

3.2.1 Summary of ^{29}Si-NMR

In conclusion, it was possible to extend the existing database of ^{29}Si NMR shifts with a series of differently substituted arylsilanes as well as their chloride, allyl and pyridine pyridazyl derivates. The presented compounds displayed shifts in the expected range and agree with values reported for similar species in literature. The effects of increasing bulk-size of the aryl moieties consist of a continuous low-field shift for chloride and tetraorgano species, whereas hydride species display a high-field shift.

3.3 Solid State Structures

Despite an increasing interest in aryl-substituted (chloro)silanes in recent years, only few crystal structures have been published.[6–8,149,152,154–162] In our working group the influence of the substitution pattern on solid state structures of arylsilanes and especially on the secondary interactions of the aryl moieties was previously investigated.[6] Most commonly, electrostatic interactions in form of π-π stacking and edge to face interactions stemming from the aromatic sustbituents are found in arylsilicon chlorides and hydrides, along with Van-der-Waals contacts in form of CH···Cl, CH_3···π or Si-H···Si.

Since in the previous study the focus was foremost laid on diaryl species, the dataset is herein expanded by some yet unreported solid-state structures of symmetrically and asymmetrically substituted di- and triaryl (chloro)silanes. Furthermore, the structures of triaryl(allyl)silanes and interactions leading to their stabilisation are discussed.

3.3.1 Aryl-Substituted Chlorosilanes (R_nSiCl_{4-n})

Mono- and Diaryl Chlorosilanes

This section summarises the crystallographic data of synthesised mono- and diaryl chlorosilanes (compounds **1**, **3** and **4**, Figure 11) and compares them to previously reported structures. The silicon atom is found in a near tetrahedral environment in each of the investigated chlorosilanes. Crystallographic data as well as details of measurements and refinement for the presented compounds may be found in the appendix. Averaged bond lengths and angles of herein presented as well as of comparable compounds reported in literature are summarised in Table 5.

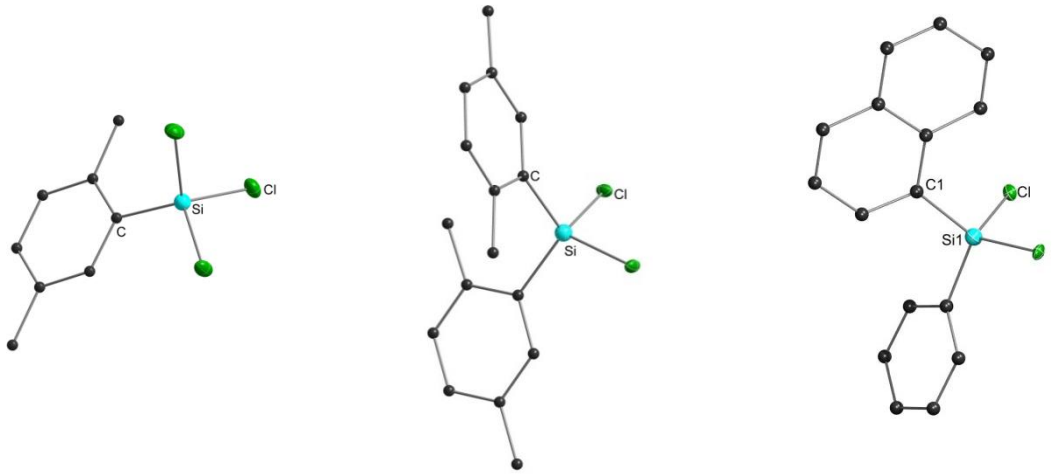

2,5-xylylSiCl$_3$ (**1**) 2,5-xylyl$_2$SiCl$_2$ (**3**) 1-naphthyl(phenyl)SiCl$_2$ (**4**)

Figure 11 Crystal structures of presented mono- and diaryl chlorosilanes. All non-carbon atoms are displayed as 50% shaded ellipsoids. Hydrogen atoms are omitted for clarity.

2,5-xylylSiCl$_3$ (**1**) crystallises in the monoclinic space group $P2_{1/m}$ and displays an average Si–C bond length of 1.844(12) Å as well as an average Si–Cl distance of 2.039(3) Å. These values are very close to the ones reported for 1-naphthylSiCl$_3$ and differ only slightly from 2,6-xylylSiCl$_3$ and 2,4,6-mesitylSiCl$_3$ (*cf.* Table 5). The found C–Si–C and C–Si–Cl angles of 106 and 112°, respectively, are also in accordance with values reported for comparable structures.

Both of the presented di-arylated chlorosilanes, compounds 2,5-xylyl$_2$SiCl$_2$ (**3**) and 1-naphthyl(phenyl)SiCl$_2$ (**4**) (Figure 11), crystallise in the monoclinic space group P2$_{1/c}$ and display similar Si–C and Si–Cl bond lengths of 1.861(3)/2.063(3) Å (**3**) and 1.859(3)/2.062(9) Å (**4**) which are comparable with reported structures (see Table 5). An influence of the steric bulk is seen in the C–Si–C angles, as an expected narrowing of the angles between the aryl moieties with an increasing steric demand from 118° (2,4-xylyl$_2$SiCl$_2$) to 113° (**4**) is observed. The angle between the chlorine residues reflects the influence of substituents in *ortho* position of the aromatic system. While 2,6-xylyl$_2$SiCl$_2$ with two *ortho*-positioned methyl groups on the phenyl ring displays the narrowest angle of 102°, the 2,4- and 2,5-xylyl substituted silicon dichlorides with only one *ortho* methyl group show angles of 104°. The trend is continued by compound **4** (106°), which is substituted with a plain phenyl group and a 1-naphthyl group accounting for the steric bulk.

Table 5 Selected bond lengths and angles for mono- and diaryl chlorosilanes.

N°	Compound	Space Group	Si–C$_{aryl}$ [Å] (avg.)	Si–Cl [Å] (avg.)	C–Si–C [°] (avg.)	Cl–Si–Cl [°] (avg.)	C–Si–Cl [°] (avg.)
1	2,5-xylylSiCl$_3$ ‡	P2$_{1/m}$	1.844(12)	2.039(3)	—	106.39(7)	112.39(2)
	2,6-xylylSiCl$_3$[159]	Pnma	1.860(4)	2.048(4)	—	105.35(7)	113.37(7)
	2,4,6-mesitylSiCl$_3$[159]	P-1	1.861(2)	2.043(9)	—	105.19(3)	113.33(3)
	1-naphthylSiCl$_3$[6]	P2$_{1/c}$	1.841(2)	2.034(8)	—	106.9(4)	111.9(7)
	2,4-xylyl$_2$SiCl$_2$[7]	P-1	1.858(3)	2.059(2)	118.15(9)	104.95(4)	108.24(9)
3	2,5-xylyl$_2$SiCl$_2$	P2$_{1/c}$	1.861(3)	2.063(3)	116.11(4)	104.667(5)	108.86(3)
	2,6-xylyl$_2$SiCl$_2$[7]	P-1	1.877(2)	2.069(2)	113.72(7)	102.66(3)	110.09(3)
4	1-naphthyl(phenyl)SiCl$_2$ ‡	P2$_{1/c}$	1.859(3)	2.062(9)	113.03(12)	106.57(4)	109.24(9)
	1-naphthyl$_2$SiCl$_2$ [7]	P2$_{1/n}$	1.859(3)	2.063(2)	116.84(10)	106.18(4)	110.01(8)

‡ Hitherto, no crystal structures were reported for the literature-known compounds **1**[163–165] and **4**[166].

2,5-xylylSiCl$_3$ (**1**) displays mainly two types of intermolecular interactions: CH$_3$···π contacts with a distance of 2.95 Å and CH$_3$···Cl contacts with distances ranging from 3.02 – 3.20 Å (Figure 12, left). The same type of packing with similar distances has been reported for 2,6-xylylSiCl$_3$, 2,4,6-mesitylSiCl$_3$ and 1-naphthylSiCl$_3$, as well (Table 6). The introduction of a second 2,5-xylyl group onto the silicon atom (compound **3**) results in less symmetrical packing of the crystals in which additional stabilisation by edge to face interactions with lengths of 2.73 Å are present (Figure 12, right). There, *meta*-positioned hydrogen atoms of the aryl moiety interact with the aromatic system of an adjacent molecule. Overall, a comparatively large range (3.17-3.38 Å) is found for the CH$_3$···π contacts while CH$_3$···Cl contacts remain in the same range as in the mono-arylated species (Table 6).

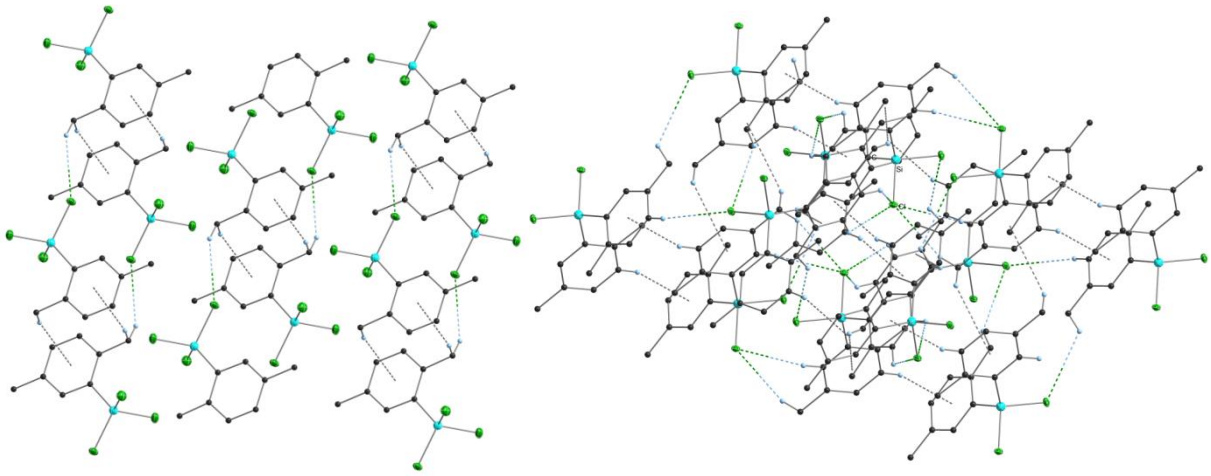

2,5-xylylSiCl$_3$ (**1**) 2,5-xylyl$_2$SiCl$_2$ (**3**)

Figure 12 Crystal packing diagram of 2,5-xylyl substituted chlorosilanes. Edge to face interactions as well as CH···Cl are highlighted by dashed lines. All non-carbon atoms are displayed as 50% shaded ellipsoids. Hydrogen atoms not involved in intermolecular interactions are omitted for clarity.

Table 6 List of non-covalent interactions for presented mono- and diaryl chlorosilanes.

N°	*Compound*	*π-π Stacking [Å]*		*Edge to Face [Å]*	*CH$_3$···π [Å]*	*C–H···Cl [Å]*
		d	*R*			
1	*2,5-xylylSiCl$_3$* ‡	—	—	—	2.95	3.02 – 3.20
	2,6-xylylSiCl$_3$[159]	—	—	—	2.94	3.07 – 3.22
	2,4,6-mesitylSiCl$_3$[159]	—	—	—	2.65	3.01 – 3.29
	1-naphthylSiCl$_3$[6]	3.41	1.72	2.94	—	3.01 – 3.19
	2,4-xylyl$_2$SiCl$_2$[7]	—	—	3.26	2.99	—
3	*2,5-xylyl$_2$SiCl$_2$*	—	—	2.73	3.17 – 3.38	3.08 – 3.33
	2,6-xylyl$_2$SiCl$_2$[7]	3.45	1.46	—	3.24	2.99
4	*1-naphthyl(phenyl)SiCl$_2$* ‡	3.42	2.2	2.73, 3.39	—	2.97 – 3.19
	1-naphthyl$_2$SiCl$_2$ [7]	3.58, 3.69	1.54, 1.23	2.95	—	2.91

‡ Hitherto, no crystal structures were reported for the literature-known compounds **1**[164,165,167], **4**[166].

In the asymmetrically substituted 1-naphthyl(phenyl)$SiCl_2$ (**4**), a layer formation by stacking of the 1-naphthyl moieties is observed (Figure 13). The aromatic moieties are displaced parallel in specific distances of 3.42 Å (d) and an off-set of 2.2 Å (R). Additionally, edge to face interactions between a hydrogen atom of an aromatic ring and the plane of another are found for both, phenyl to naphthyl (3.39 Å) and vice versa (2.73 Å). Compared to 1-naphthyl$_2$$SiCl_2$, compound **4** displays shorter distances and a larger off-set in the π–π stacking interactions, which is the result of the asymmetric substitution pattern.

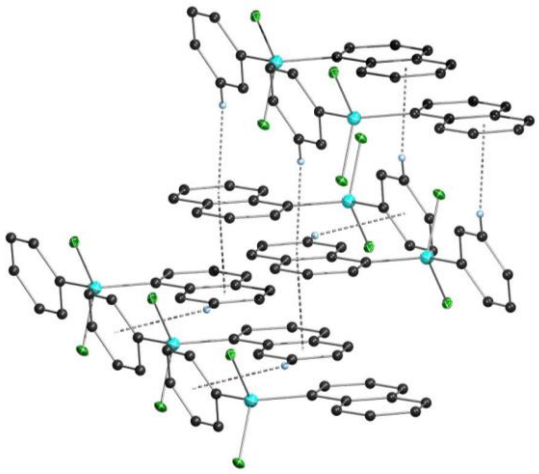

1-naphthyl(phenyl)$SiCl_2$ (**4**)

Figure 13 Crystal packing diagram of 1-naphthyl(phenyl)$SiCl_2$ (compound **4**). Edge to face interactions are highlighted by dashed lines. All non-carbon atoms are displayed as 50% shaded ellipsoids. Hydrogen atoms not involved in intermolecular interactions are omitted for clarity.

Triaryl Chlorosilanes

All triaryl chlorosilanes (**6**-**9**, Figure 14) are comparable to previously reported compounds and exist in a distorted tetrahedral environment with an average C–Si–C and C–Si–Cl angle of 111° and 107°, respectively (Table 7). The averaged Si–C bond lengths fall within the narrow range of 1.858(3) Å to 1.874(3) Å and are seemingly not affected by the degree of bulkiness afforded by the aryl substituent on the silicon atom. However, the successive exchange of a phenyl group with a bulkier 1-naphthyl residue results in a gradual elongation of the Si-Cl bond from 2.079(2) Å for phenyl$_3$SiCl[168] and 1-naphthyl(phenyl)$_2$SiCl (**7**) to 2.089(2) Å for 1-naphthyl$_3$SiCl[6].

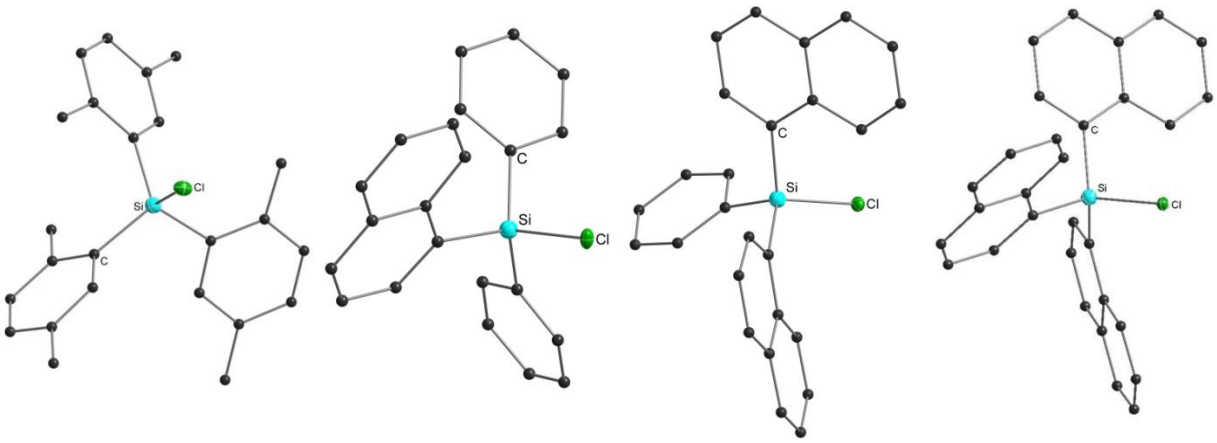

2,5-xylyl$_3$SiCl (**6**) 1-naphthyl(phenyl)$_2$SiCl (**7**) 1-naphthyl$_2$(phenyl)SiCl (**8**) 1-naphthyl$_3$SiCl (**9**)

Figure 14 Crystal structures of presented triaryl chlorosilanes. All non-carbon atoms are displayed as 50% shaded ellipsoids. Hydrogen atoms are omitted for clarity.

Table 7 Selected bond lengths and angles for triaryl chlorosilanes.

N°	Compound	Space Group	Si–C_{aryl} [Å] (avg.)	Si–C_{Ph} [Å] (avg.)	Si–Cl [Å] (avg.)	C–Si–C [°] (avg.)	C–Si–Cl [°] (avg.)
	phenyl$_3$SiCl[168]	$P2_{1/c}$	—	1.861(2)	2.079(2)	111.57(3)	107.27(3)
	p-^{i}propyl(phenyl)$_3$SiCl[169]	*P*-1	1.858(3)	—	2.084(3)	111.17(6)	107.71(3)
6	2,5-xylyl$_3$SiCl	$P2_{1/c}$	1.872(2)	—	2.096(6)	112.31(7)	106.43(5)
7	1-naphthyl(phenyl)$_2$SiCl ‡	$P2_{1/c}$	1.868(2)	1.859(2)	2.079(2)	111.25(10)	107.61(8)
8	1-naphthyl$_2$(phenyl)SiCl	*P*-1	1.869(3)	1.863(2)	2.086(3)	110.86(9)	107.99(7)
	1-naphthyl$_3$SiCl[6]	*P*-1	1.874(3)	—	2.089(2)	111.23(6)	107.66(5)
9	1-naphthyl$_3$SiCl · naph.	*P*-1	1.872(2)	—	2.078(2)	110.78(9)	108.12(6)

‡ No crystal structure was reported for compound **7**[170,171] so far.

Regarding the crystal packing, all synthesised triaryl chlorosilanes display different patterns. 2,5-xylyl$_3$SiCl (**6**) is mainly stabilised by edge to face interactions between a proton of the methyl groups and an adjacent aromatic ring system with distances of 3.08-3.38 Å (Figure 15). Analogous to its mono- and diaryl derivatives, CH···Cl interactions are found for hydrogen atoms of the methyl group as well as of the aromatic system at distances between 3.11 and 3.21 Å.

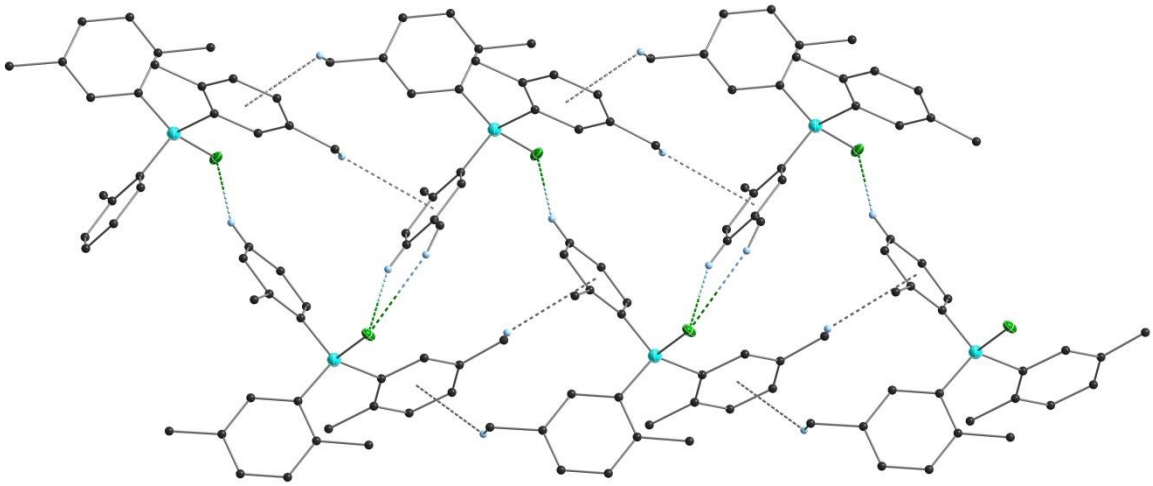

Figure 15 Crystal packing diagram of 2,5-xylyl$_3$SiCl (**6**). Edge to face interactions are highlighted by dashed lines. All non-carbon atoms are displayed as 50% shaded ellipsoids. Hydrogen atoms not involved in interactions are omitted for clarity.

1-naphthyl(phenyl)$_2$SiCl (**7**) crystallises in a symmetrical alignment of phenyl residues forming a column (Figure 16). However, these moieties are not located close enough to interact in π–π stacking but are lined up by the aid of edge to face and CH···Cl interactions. The edge to face interactions are all taking place between two hydrogen atoms of a phenyl residue and the aromatic plane of a naphthyl moiety. The hydrogen atoms of the latter in turn stabilise the structure by interacting with an adjacent chlorine atom. This type of alignment has not been found in any other presented structure.

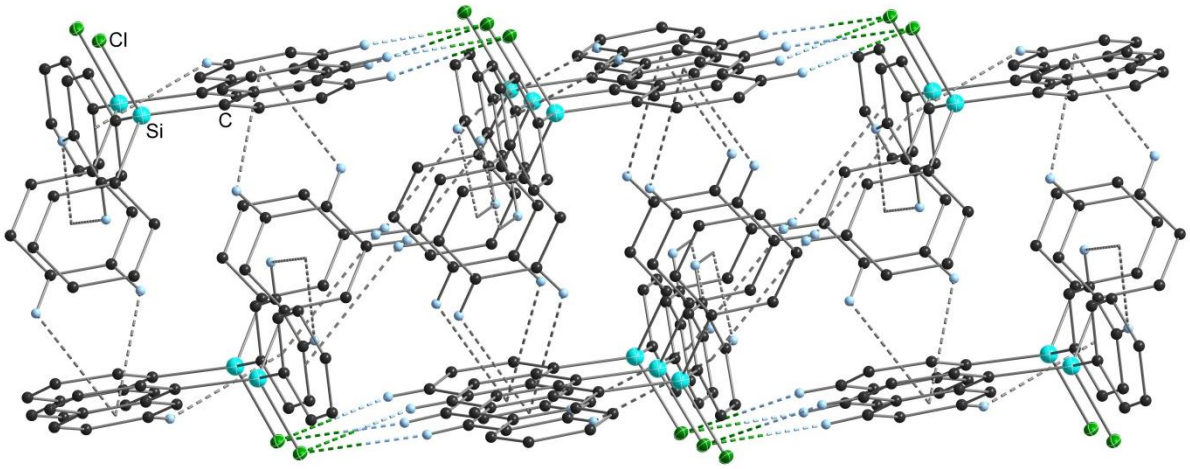

Figure 16 Crystal packing diagram of 1-naphthyl(phenyl)$_2$SiCl (**7**). Edge to face interactions as well as CH···Cl interactions are highlighted by dashed lines. All non-carbon atoms are displayed as 50% shaded ellipsoids. Hydrogen atoms not involved in interactions are omitted for clarity.

When one phenyl group is replaced by a naphthyl residue, the main stabilizing interactions consist of CH···Cl and CH···π, both emanating from *para*-positioned hydrogen atoms of a naphthyl moiety (Figure 17). Both asymmetrically substituted phenyl/naphthyl chlorosilanes (compounds **7** and **8**) display very similar alignments with average CH···Cl distances in the range of 2.95-3.15 Å and edge to face interactions at distances of 2.69-3.39 Å. These distances are comparable to the ones reported for p-^{i}propyl(phenyl)$_3$SiCl[169] (2.92 and 3.17 Å).

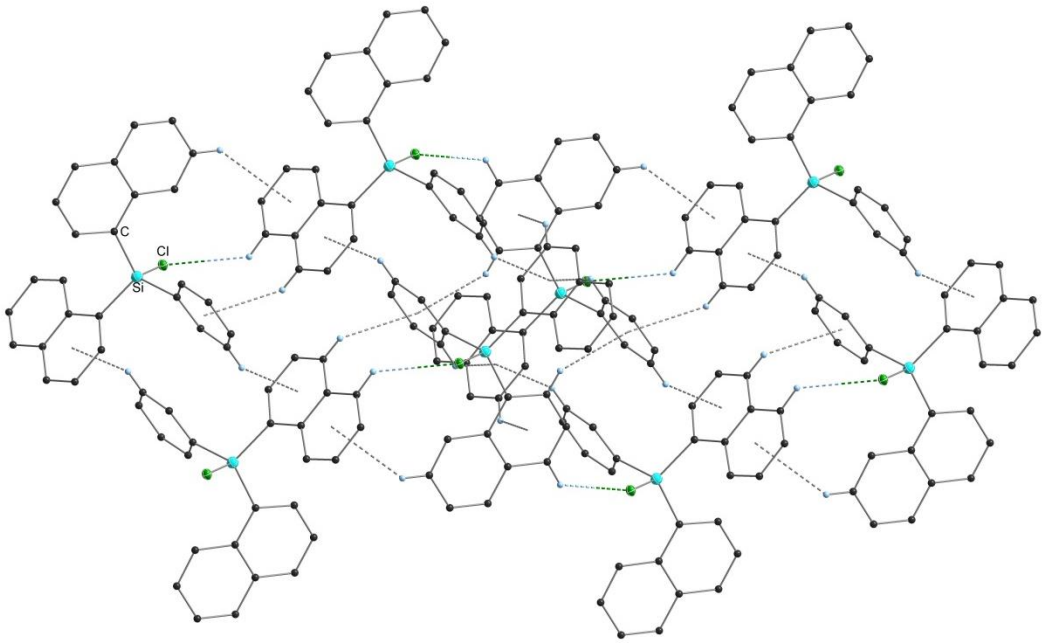

Figure 17 Crystal packing diagram of 1-naphthyl$_2$(phenyl)SiCl (**8**). Edge to face interactions are highlighted by dashed lines. All non-carbon atoms are displayed as 50% shaded ellipsoids. Hydrogen atoms not involved in intermolecular interactions are omitted for clarity.

Due to the planar nature of the naphthalene residue, 1-naphthyl$_3$SiCl (**9**) exhibits π-π stacking interactions. In this work 1-naphtyl$_3$SiCl was found to co-crystallise with naphthalene which provides stabilisation *via* edge to face interactions additional to the parallel displaced π-π stacking between two naphthyl groups from neighbouring molecules with a specific distance (*d*) of 3.67 Å and an off-set (*R*) of 2.92 Å (Figure 18). However, no similar behaviour for other 1-naphthyl containing species was observed.

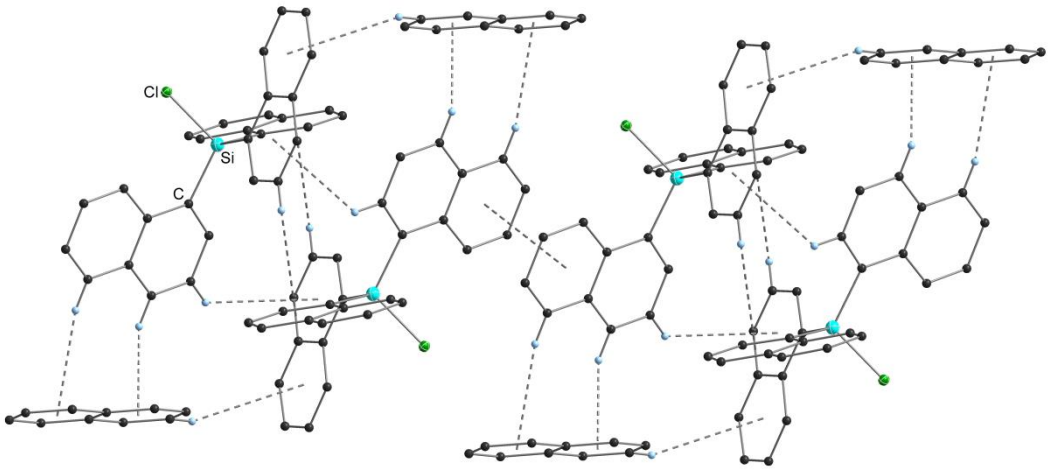

Figure 18 Crystal packing diagram of 1-naphthyl$_3$SiCl (**9**). Edge to face interactions are highlighted by dashed lines. All non-carbon atoms are displayed as 50% shaded ellipsoids. Hydrogen atoms not involved in intermolecular interactions are omitted for clarity.

Table 8 List of non-covalent interactions for presented triaryl chlorosilanes.

N°	*Compound*	*π-π Stacking [Å]*		*Edge to Face [Å]*	*C–H···π [Å]*	*C–H···Cl [Å]*
		d	*R*			
	p-^{i}propylphenyl$_3$SiCl[169]	—	—	2.92	—	3.17
6	*2,5-xylyl$_3$SiCl*	—	—	3.08 – 3.35	2.51 – 3.29	3.11 - 3.21
7	*1-naphthyl(phenyl)$_2$SiCl*‡	—	—	2.87 – 3.37	—	2.95 – 3.15
8	*1-naphthyl$_2$(phenyl)SiCl*	—	—	2.69 – 3.39	—	3.10 – 3.12
	1-naphthyl$_3$SiCl[6]	3.45	1.61	2.79 – 3.20	—	3.08 – 3.19
9	*1-naphthyl$_3$SiCl · naph.*	3.67	2.92	2.59 – 3.38	—	—

‡ No crystal structure was reported for compound **7**[170,171] so far.

3.3.2 Aryl-Substituted Silanes (R_nSiH_{4-n})

Di- and Triaryl Silanes

2,5-xylyl substituted silanes (Figure 19) display average Si–C bond lengths of 1.872(18) Å (**14**) and 1.889(2) Å (**18**). These bond lengths are slightly elongated in comparison to their chlorinated counterparts (1.844(12) Å (**1**) and 1.861(3) Å (**3**)). In comparison to other reported xylyl-substituted silanes, the Si–H bonds of compound **14** are notably longer (*cf.* Table 9). This is possibly caused by crystallisation in a different solvent than the reported compounds, resulting

in the lower symmetry. Further, the C–Si–C angle is unexpectedly closer to the one reported for 2,6-xylyl$_2$SiH$_2$ (114°) where the two methyl substituents on the phenyl ring are both located in *ortho* position than to the one for 2,4-xylyl$_2$SiH$_2$ (117°).

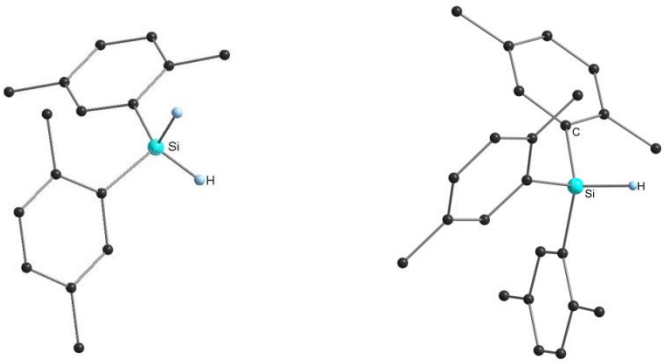

2,5-xylyl$_2$SiH$_2$ (**14**) 2,5-xylyl$_3$SiH (**18**)

Figure 19 Crystal structures of 2,5-xylyl substituted silanes. All non-carbon atoms are displayed as 50% shaded ellipsoids. Hydrogen atoms are omitted for clarity.

Compound **18** displays Si–C (1.889(2) Å) and Si–H (1.464(2) Å) bond lengths that fit nicely into the trend seen for increasingly larger substituents (Table 10). The observed average C–Si–C angles of 110° are slightly narrower than the ones reported for phenyl$_3$SiH (111°) caused by the methyl substituent on the ring system. Consequently, the C–Si–H angles widen by the same increment as compared to the phenylated species. Interestingly, the C–Si–H angles for both, compounds **14** and **18**, were found to be 108.8°.

Table 9 Selected bond lengths and angles as well as non-covalent interactions for di- and triaryl silanes.

N°	*Compound*	*Space Group*	*Si–C$_{Aryl}$ [Å] (avg.)*	*Si–H [Å] (avg.)*	*C–Si–C [°] (avg.)*	*C–Si–H [°] (avg.)*
	2,4-xylyl$_2$SiH$_2$[8]	*P2$_1$/c*	1.869(2)	1.389(2)	117.18(6)	109.0(7)
14	*2,5-xylyl$_2$SiH$_2$*	*P-1*	1.873(2)	1.427(2)	114.15(8)	108.8(8)
	2,6-xylyl$_2$SiH$_2$[8]	*P2$_1$/c*	1.885(2)	1.354(2)	114.05(7)	110.9(10)
	1-naphthyl$_2$SiH$_2$[8]	*Pbca*	1.869(3)	1.385(2)	109.90(6)	109.2(6)
18	*2,5-xylyl$_3$SiH*	*P2$_1$/c*	1.889(2)	1.464(2)	110.10(9)	108.83(7)

N°	*Compound*	*Edge to Face [Å]*	*CH···π [Å]*	*Si–H···Si [Å]*
	2,4-xylyl$_2$SiH$_2$[8]	3.18	2.83	—
14	*2,5-xylyl$_2$SiH$_2$*	—	2.80	3.19
	2,6-xylyl$_2$SiH$_2$[8]	2.95	2.76	—
	1-naphthyl$_2$SiH$_2$[8]	2.79 – 2.83	—	—
18	*2,5-xylyl$_3$SiH*	—	2.76 – 3.01	3.78

In contrast to the respective chloride derivatives (compounds **1**, **2** and **6**), 2,5-xylyl$_2$SiH$_2$ (**14**) and 2,5-xylyl$_3$SiH (**18**) crystallise in linear chains of molecules propagated by CH$_3$···π interactions

(Figure 20). As a result of maximising these interactions, all Si–H bonds face in the same direction and consequently allow for an orientation of Si–H towards a neighbouring silicon atom with Si-H···Si distances of 3.19 Å for 2,5-xylyl$_2$SiH$_2$ (**14**) at an angle of 177° and 3.78 Å for 2,5-xylyl$_3$SiH (**18**) at 178°. The elongation of these distances results from the enhanced steric demand afforded by a third aryl residue onto the silicon centre atom.

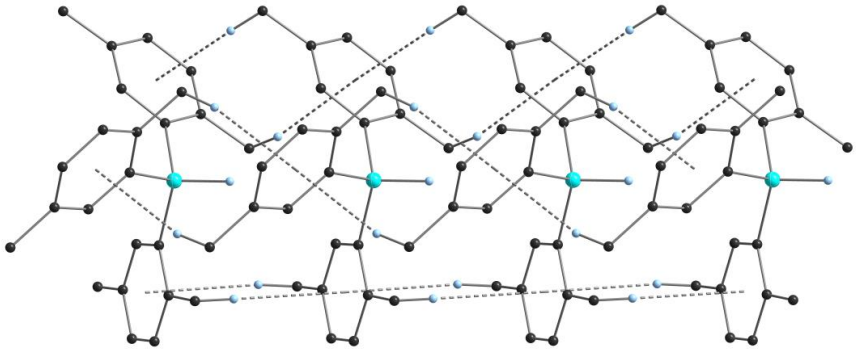

Figure 20 Crystal packing diagram of 2,5-xylyl$_3$SiH (**18**). Edge to face interactions are highlighted by dashed lines. All non-carbon atoms are displayed as 50% shaded ellipsoids. Hydrogen atoms not involved in intermolecular interactions are omitted for clarity.

Triaryl Silanes Containing 1-naphthyl Residues

Compared to the phenyl$_3$SiH (**17**) (1.851(2) Å),[172] a slight increase in the average Si–C$_{Ph}$ distances is observed for both, 1-naphthyl(phenyl)$_2$SiH (**19**) (1.874(3) Å) and 1-naphthyl$_2$(phenyl)SiH (**20**) (1.874(4) Å) due to the introduction of the bulkier substituent 1-naphthyl (Table 10, Figure 21). Even though the number of bulkier substituents does not seem to have an influence on the C–Si–C angles, a widening of the C–Si–H angles along with the introduction of one or two 1-naphthyl moieties (**19** with 108.5° and **20** with 109.2°) is observed. The C–Si–H angle for phenyl$_3$SiH and 1-naphthyl$_3$SiH are the same (107.8°). Contrary to an expected increase of the Si-H bond length by a higher number of 1-naphthyl moieties due to the +I effect of the aryl residues, the Si-H distances decrease from 1.490(2) Å for **17** over 1.437(3) Å for **19** to the shortest length of 1.36(3) Å for **20**.

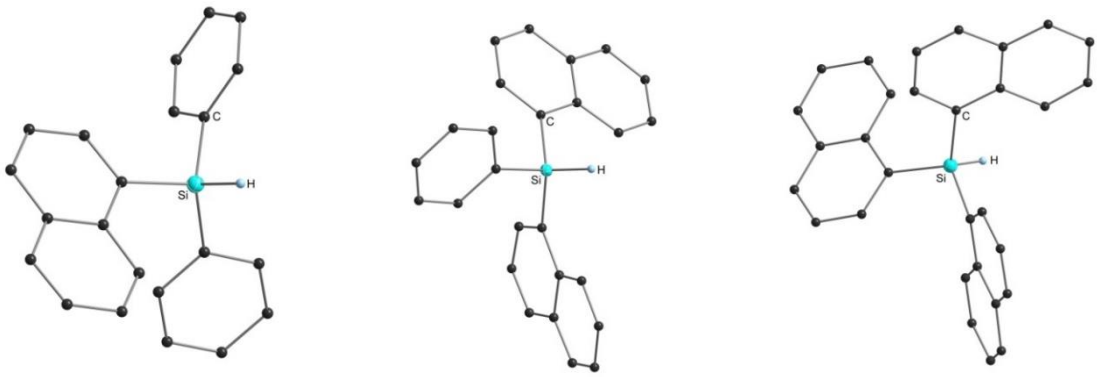

1-naphthyl(phenyl)$_2$SiH (**19**) 1-naphthyl$_2$(phenyl)SiH (**20**) 1-naphthyl$_3$SiH (**21**)

Figure 21 Crystal structures of presented triaryl silanes. All non-carbon atoms are displayed as 50% shaded ellipsoids. Hydrogen atoms are omitted for clarity.

Table 10 Selected bond lengths and angles for triaryl silanes.

N°	Compound	Space Group	Si–C_{Aryl} [Å] (avg.)	Si–C_{Ph} [Å] (avg.)	Si–H [Å] (avg.)	C–Si–C [°] (avg.)	C–Si–H [°] (avg.)
	phenyl$_3$*SiH*[172]	$P2_{1/c}$	—	1.851(2)	1.490(2)	111.03(5)	107.87(5)
18	*2,5-xylyl*$_3$*SiH*	$P2_{1/c}$	1.889(2)	—	1.464(2)	110.1(9)	108.83(7)
19	*1-naphthyl(phenyl)*$_2$*SiH* ‡	$P2_{1/n}$	1.884(3)	1.874(3)	1.437(3)	110.36(5)	108.57(5)
20	*1-naphthyl*$_2$*(phenyl)SiH*	*Pbca*	1.869(4)	1.874(4)	1.36(3)	109.69(17)	109.23(12)
21	*1-naphthyl*$_3$*SiH*	$Pna2_1$	1.872(6)	—	1.39(3)	111.07(3)	107.83(4)
	2,4,6-mesityl$_3$*SiH*[152]	Cc	2.02	—	—	105.23	—
	(methyl$_5$*phenyl)*$_3$*SiH*[173]	*P*-1	1.963(4)	—	1.000(2)	105.87(2)	105.41(2)

‡ Hitherto, no crystal structures were reported for the literature-known compounds **19**[170,174–177] and **21**[6,137,178,179].

Edge to face interactions are predominant in 1-naphthyl containing aryl silanes (compounds **19**-**21**). In case of 1-naphthyl(phenyl)$_2$SiH (**19**), the interacting phenyl group is aligned in a close to perpendicular angle to the adjacent naphthyl moiety, maximising the interactions between hydrogen atoms and the aromatic plane (Figure 22).

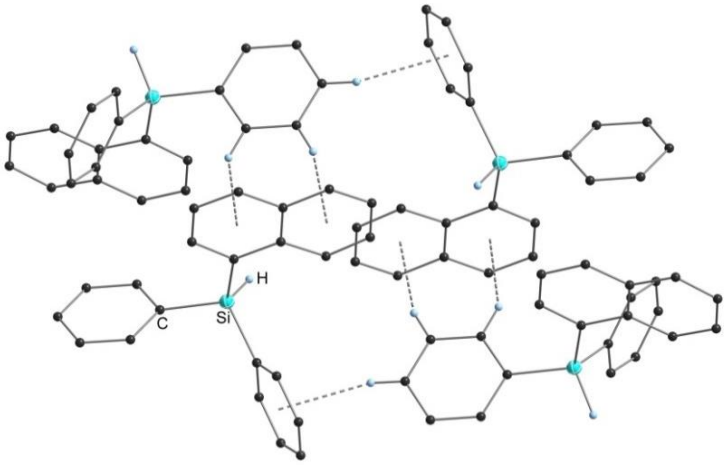

Figure 22 Crystal packing diagram of 1-naphthyl(phenyl)$_2$SiH (**19**). Edge to face interactions are highlighted by dashed lines. All non-carbon atoms are displayed as 50% shaded ellipsoids. Hydrogen atoms not involved in intermolecular interactions are omitted for clarity.

Similar to the 2,5-xylyl$_3$SiH (**18**), 1-naphthyl$_2$(phenyl)SiH (**20**) and 1-naphthyl$_3$SiH (**21**) crystallise with the Si–H bonds facing in the same direction, allowing for Si-H···Si interactions with the exposed sides of a neighbouring silicon atom (Figure 23). The resulting distances are listed in Table 11.

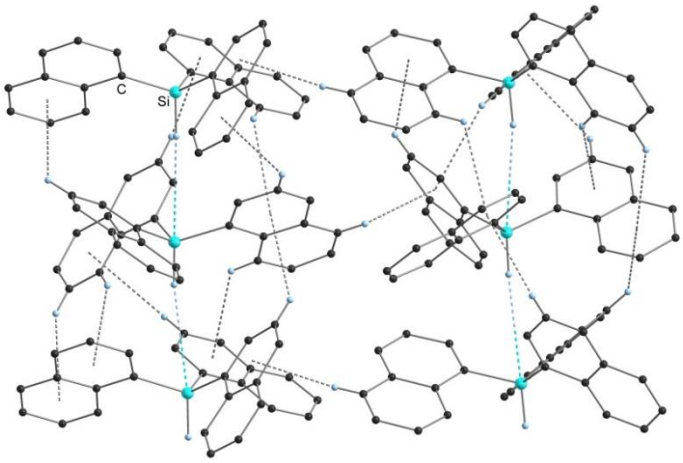

Figure 18 Crystal packing diagram of 1-naphthyl$_3$SiH (**21**). Edge to face interactions are highlighted by dashed lines. All non-carbon atoms are displayed as 50% shaded ellipsoids. Hydrogen atoms not involved in intermolecular interactions are omitted for clarity.

Comparing the presented interaction distances, different effects are notable. While 1-naphthyl$_3$SiH (**21**) displays the shortest distances of 3.49-3.51 Å, the spans extend to 3.63 Å for 1-naphthyl$_2$(phenyl)SiH (**20**) and 3.78 Å for 2,5-xylyl$_3$SiH (**18**). These elongations stem from asymmetry of the substituent pattern (**20**) as well as the spatial extent of the *ortho* and *meta* substituted 2,5-xylyl group (compound **18**). Although no Si–H···Si interactions are reported for similar compounds their presence may be reasonably assumed.

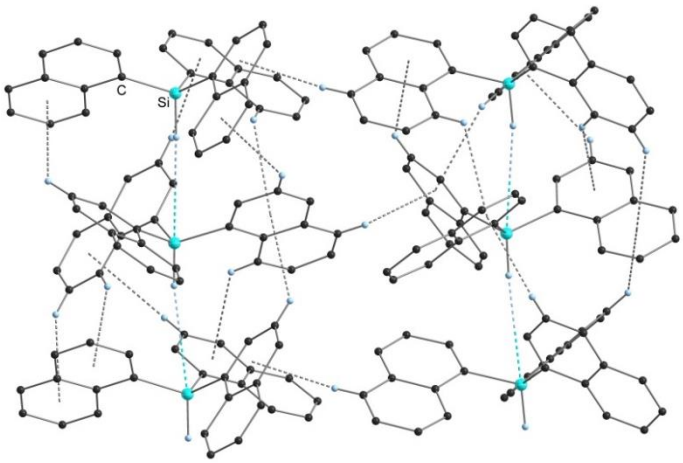

Figure 23 Crystal packing diagram of 1-naphthyl$_3$SiH (**21**). Edge to face interactions are highlighted by dashed lines. All non-carbon atoms are displayed as 50% shaded ellipsoids. Hydrogen atoms not involved in intermolecular interactions are omitted for clarity.

Table 11 List of non-covalent interactions for triaryl silanes.

N°	*Compound*	*Edge to Face [Å]*	*CH···π [Å]*	*Si–H···Si [Å]*
	phenyl$_3$SiH[172]	2.82 – 3.09	—	—
18	*2,5-xylyl$_3$SiH*	—	2.76 – 3.01	3.78
19	*1-naphthyl(phenyl)$_2$SiH* ‡	2.65 – 2.93	—	—
20	*1-naphthyl$_2$(phenyl)SiH*	2.88 – 3.18	—	3.63
21	*1-naphthyl$_3$SiH* ‡	2.98 – 3.39	—	3.49 – 3.51
	(methyl$_5$phenyl)$_3$SiH[173]	—	2.82 – 3.32	—

‡ Hitherto, no crystal structures were reported for the literature-known compounds **19**[170,174–177] and **21**[6,137,178,180].

3.3.3 Triaryl (allyl)silanes

This section summarises crystallographic data of the synthesised triaryl(allyl)silanes (compounds **22**- **25**) and compares them to previously reported structures. In each case the silicon atom is found in a near tetrahedral environment (Figure 24). Averaged bond lengths and angles are summarised in Table 12, a more detailed list may be found in section 6.

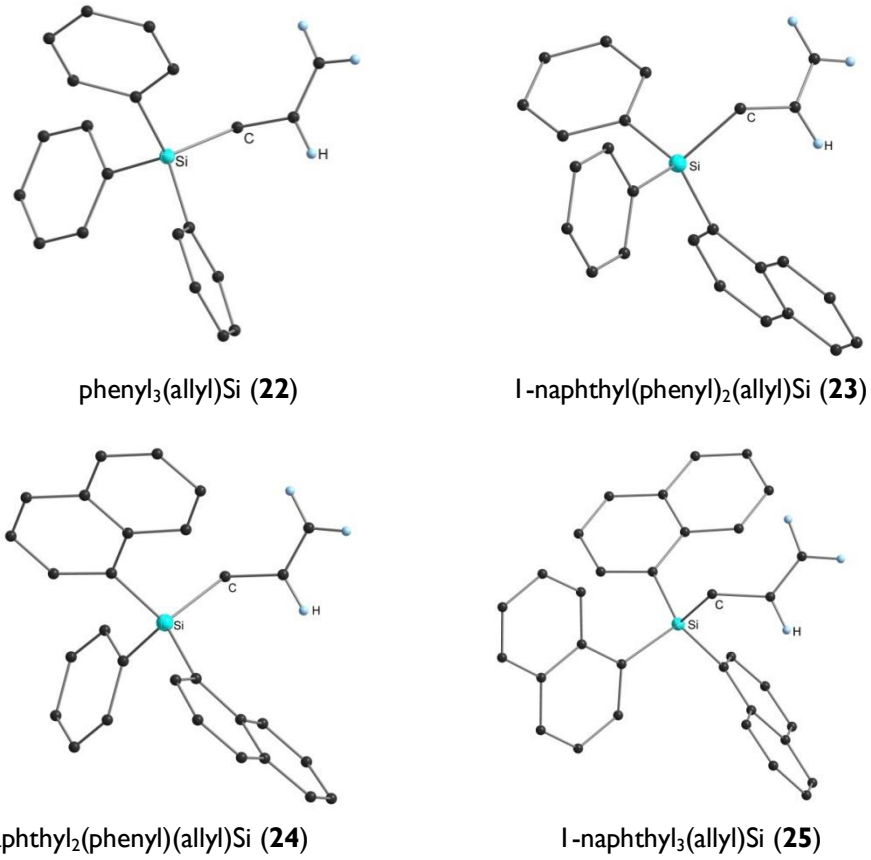

phenyl$_3$(allyl)Si (**22**) 1-naphthyl(phenyl)$_2$(allyl)Si (**23**)

1-naphthyl$_2$(phenyl)(allyl)Si (**24**) 1-naphthyl$_3$(allyl)Si (**25**)

Figure 24 Crystal structures of presented triaryl(allyl)silanes. All non-carbon atoms are displayed as 50% shaded ellipsoids. Aromatic hydrogen atoms are omitted for clarity.

All triaryl(allyl)silanes (**22**-**25**) display average Si–C_{Naph} and Si–C_{Ph} bond lengths in the range 1.87-1.89 Å. Regarding the distances of the silicon atom to the first carbon of the allyl group (C_1), a slight elongation is visible when two (1-naphthyl$_2$(phenyl) (allyl) (**24**)) (1.920(3) Å) or three 1-naphthyl moieties are introduced (1-naphthyl$_3$(allyl)Si (**25**)) (1.918(3) Å) compared to phenyl$_3$(allyl)Si (**22**) (1.892(3) Å), caused by the increased steric demand of the 1-naphthyl substituents.

Along the same trend of increasing 1-napthyl residues, a narrowing of the C–Si–C angles between aryl residues and a thereby resulting widening of the C–Si–C_{allyl} angles of 108.9° (phenyl$_3$(allyl)Si (**22**)) to 110.3° (1-naphthyl$_3$(allyl)Si (**25**)) is notable.

Table 12 Selected average bond lengths and angles of triaryl(allyl)silanes.

N°	Compound	$Si–C_{Naph}$ [Å] (avg.)	$Si–C_{Ph}$ [Å] (avg.)	$Si–C_{1'}$ [Å] (avg.)
22	phenyl$_3$(allyl)Si	—	1.872(3)	1.892(3)
23	1-naphthyl(phenyl)$_2$(allyl)Si	1.891(3)	1.881(3)	1.899(3)
24	1-naphthyl$_2$(phenyl) (allyl)Si	1.890(3)	1.881(3)	1.920(3)
25	1-naphthyl$_3$(allyl)Si	1.892(3)	—	1.918(3)
	1-naphthyl(2,4,6-mesityl)(phenyl) (allyl)Si[151]	1.873(2)	1.877(2)	1.888(2)
	2,4,6-mesityl$_3$Si[152]	—	1.909(2)	1.919(3)
N°	Compound	$C_{aryl}–Si–C_{aryl}$ [°] (avg.)	$C_{aryl}–Si–C_{allyl}$ [°] (avg.)	$Si–C_{1'}–C_{2'}$ (allyl) [°]
22	phenyl$_3$(allyl)Si	110.01(6)	108.93(6)	115.14(9)
23	1-naphthyl(phenyl)$_2$(allyl)Si	110.21(7)	108.69(7)	117.49(12)
24	1-naphthyl$_2$(phenyl)(allyl)Si	109.00(6)	109.89(6)	117.21(10)
25	1-naphthyl$_3$(allyl)Si	108.61(5)	110.32(6)	118.00(9)
	1-naphthyl(2,4,6-mesityl)(phenyl)(allyl)Si[151]	109.65(6)	109.26(2)	114.52(1)
	2,4,6-mesityl$_3$(allyl)Si[152]	112.87(1)	105.81(2)	124.71(2)

Compounds **22**-**25** exhibit both, inter- and intramolecular edge to face interactions of hydrogen atoms of an aryl residue with the double bond of the allyl group, an example is displayed in Figure 25. The distances of these interactions decrease with increasing bulk-size of the aryl substituents, lying in the range of 2.92-2.65 Å (intra) and 2.82-3.32 Å (inter) and are thereby in accordance with values for 1-naphthyl(2,4,6-mesityl)(phenyl)(allyl)Si (2.96, 3.09 Å).[151]

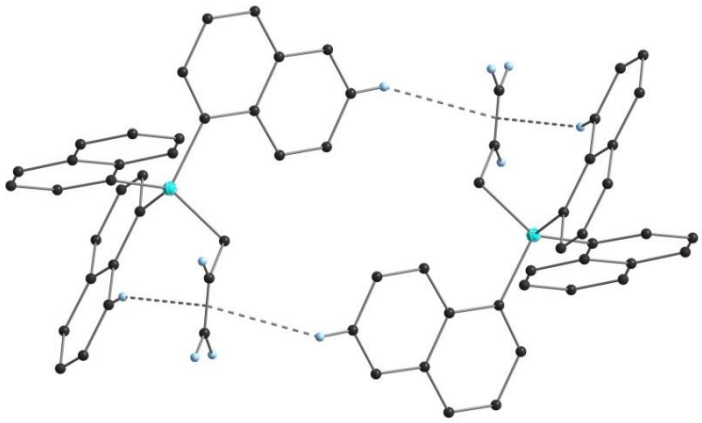

Figure 25 Crystal packing diagram of 1-naphthyl$_3$(allyl)Si (**25**). Edge to face interactions are highlighted by dashed lines. All non-carbon atoms are displayed as 50% shaded ellipsoids. Hydrogen atoms not involved in intermolecular interactions are omitted for clarity.

Among the synthesised allylsilanes phenyl$_3$(allyl)Si (**22**) is the least sterically crowded species. The Si–C$_{1'}$–C$_{2'}$ bond angle is noticeably narrower 115° as opposed to the average 117.5° for **23**-**25**, owing to the lower spatial extent of the residues. This bond angle allows for an orientation in which a hydrogen atom of the methylene group (C$_{1'}$H$_2$) may interact with an adjacent molecule, displaying Van-der-Waals contacts (CH···π) of 3.28 Å (Figure 26, a)). The molecules of arylated allylsilanes arrange themselves in order to maximise these interactions leading to crystals in form of large, colourless blocks (Figure 26, b)).

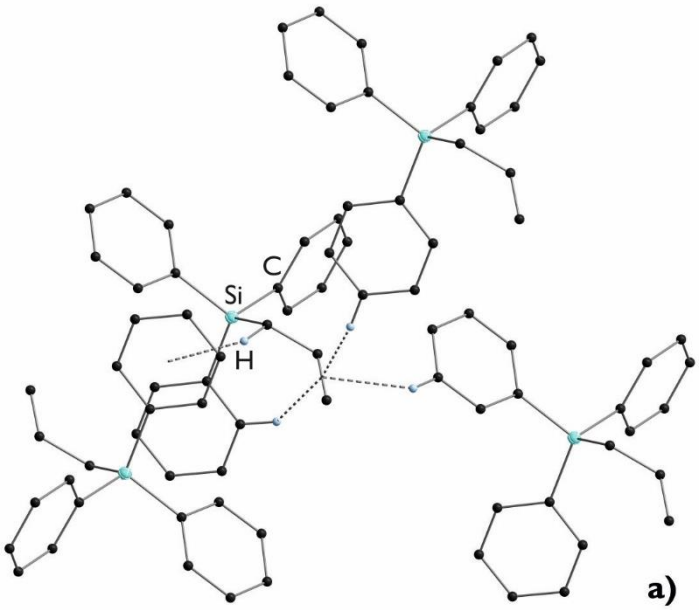

Figure 26 a) Crystal packing diagram of 1-naphthyl(phenyl)$_2$(allyl)Si (**23**). Edge to face interactions are highlighted by dashed lines. All non-carbon atoms are displayed as 50% shaded ellipsoids. Hydrogen atoms not involved in intermolecular interactions are omitted for clarity. b) Phenyl$_3$(allyl)Si (**22**) crystals grown from Et$_2$O.

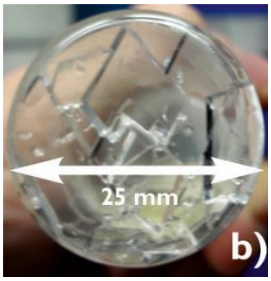

Table 13 Inter- and intramolecular interactions of triaryl(allyl)silanes.

N°	*Compound*	*Edge to Face [Å]*	*CH ··π [Å]*	*CH$_2$ (allyl) ··π [Å]*	*CH=CH$_2$(π) (allyl) ··H [Å]*	
					intra	inter
22	*phenyl$_3$(allyl)Si*	2.81 – 3.34	3.28 (methylene-pi)	—	2.92	2.94, 3.02
23	*1-naphthyl(phenyl)$_2$(allyl)Si*	2.81 – 3.41	—	—	2.90, 3.31	2.95, 3.34
24	*1-naphthyl$_2$(phenyl) (allyl)Si*	3.21 – 3.74	—	—	2.72	2.89
25	*1-naphthyl$_3$(allyl)Si*	2.66 – 3.28	—	—	2.65	2.82
	1-naphthyl(2,4,6-mesityl)(phenyl) (allyl)Si[151]	2.84 – 2.94	2.85	3.25	2.81	2.96, 3.09
	2,4,6-mesityl$_3$(allyl)Si[152]	—	3.12 – 3.31	3.49	3.23 methyl	3.29 methyl

3.3.4 3,6-(2-pyridinyl)$_2$-4-((1-naphthyl$_3$silyl)methyl)pyridazine (**29**)

The silylated dihydropyridazine **29** (Figure 27) displays average Si–C$_{Naph}$ bond lengths of 1.891(18) Å and remains therefore unchanged in comparison to the educt 1-naphthyl$_3$Si(CH$_2$CH=CH$_2$) (**25**). The Si–C$_{1'}$ bond length at 1.905(17) Å, however, is slightly shorter than for compound **25** (1.918(3) Å). Compared to the educt, the C$_{aryl}$–Si-C$_{aryl}$ angle is found to widen by one degree (108.6° (**25**) to 109.7° (**29**)) while the C$_{aryl}$-Si-C$_{allyl}$ angle narrows by the same increment (110.3° (**25**) to 109.2° (**29**)) and the angle between Si–C$_{1'-2'}$ remains the same at 118°. These slight changes result from the addition of the allylic double bond to the pyridazine ring system. In the product, C$_{2'}$ is implemented into the central ring at an angle of 33° out of plane.

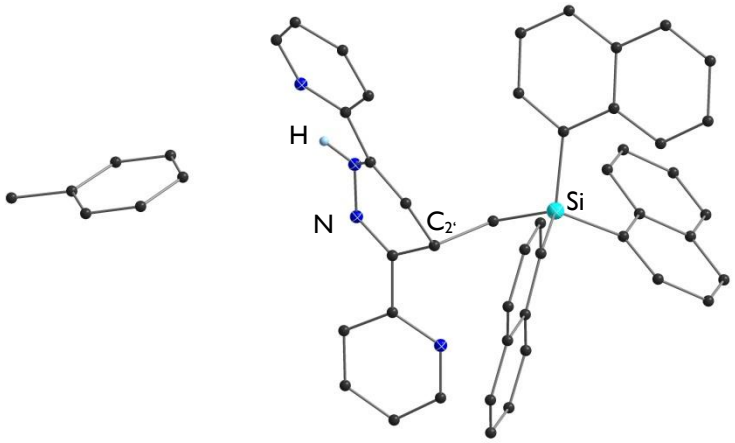

Figure 27 Crystal structure of compound **29**. All non-carbon atoms are displayed as 50% shaded ellipsoids. Aromatic hydrogen atoms are omitted for clarity.

The structure is stabilised by π–π stacking interactions of a naphthyl group with an adjacent pyridine moiety at a distance of 3.46 Å and an offset of 1.57 Å. Furthermore, edge to face interactions are found between the co-crystallising solvent (toluene) and neighbouring molecules, as well as from hydrogens of the naphthyl moiety to the pyridine ring system, ranging from 2.23-2.87 Å.

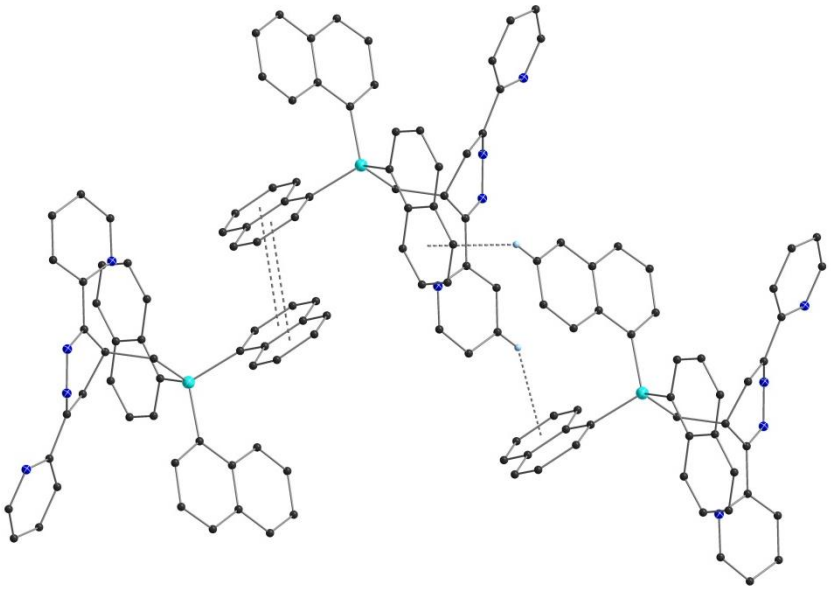

Figure 28 Crystal packing diagram of compound **29**. Edge to face interactions are highlighted by dashed lines. All non-carbon atoms are displayed as 50% shaded ellipsoids. Hydrogen atoms not involved in intermolecular interactions are omitted for clarity.

3.3.5 Summary of Crystallography

A series of symmetrically and asymmetrically substituted aryl chlorosilanes, arylsilanes and triaryl(allyl)silanes were characterised by X-ray crystallography. The effects of residue bulk and substitution patterns on the environment around the silicon atom have been discussed. All of the herein described structures display at least one residue with a substituent in *ortho*-position of the aryl moiety and hence display slightly elongated average Si–C bond lengths in comparison to un- or *para*-substituted aryl groups. This is consistent with crystallographic data reported by Binder[6–8]. However, the bond lengths are seemingly unaffected by the exchange of a phenyl with a 1-naphthyl group in asymmetrically substituted silanes (**4**, **7**, **8**, **19**, **20**, **23**, **24**). Electrostatic interactions in the form of π-stacking stem from the aromatic substituents (π–π stacking, edge to face and CH_3···π interactions) as well as Van-der-Waals contacts from the halogenide substituent and adjacent hydrogens (C–H···Cl) or from the hydrogen functionality of a silane and adjacent exposed silicon atoms (Si–H···Si). They offer an overall stabilising effect to these molecules in the solid state and aid in their crystallisation. The types of non-covalent interactions present in these systems are directly dependent on the nature of the aryl substituent. Edge to face interactions are prevalent as stabilising factors in most of the reported aryl silicon compounds. However, solely CH_3···π interactions were observed for silanes substituted with 2,5-xylyl residues (**14**, **18**) which lead to the formation of linear chains. This is consistent with 2,4-xylyl$_2$SiCl$_2$.[7] All aryl chlorosilanes exhibit Van-der-Waals contacts (C–H···Cl) in the range of 2.95-3.13 Å, which are in accordance with the previously reported p-^{i}propyl(phenyl)$_3$SiCl[169] (3.17 Å) and in the range of other reported species e.g. 1-naphthyl$_2$SiCl$_2$ (2.91 Å) or 2,6-xylyl$_2$SiCl$_2$ (2.99 Å).[7] Furthermore, all reported aryl silanes (**14**, **18–21**) exhibit hitherto unreported Si–H···Si contacts in the range of 3.19-3.78 Å. Triaryl(allyl)silanes feature both, inter- and intramolecular stabilisation *via* Van-der-Waals contacts of the allylic double bond with adjacent hydrogen atoms. Considering mixed-substituent triarylsilanes, no clear trend could be observed by stepwise replacing phenyl by 1-naphthyl moieties.

Anticipated π–π stacking interactions of naphthyl residues in 1-naphthyl substituted silicon derivatives (**7**-**9**, **19**-**21**, **23–25**, **29**), as seen at the example of 1-naphthyl$_3$SiCl,[6] were prevented by the bulkiness of three aromatic substituents. However, parallel displaced π–π stacking interactions were observed for 1-naphthyl(phenyl)SiCl$_2$ (**4**), which shows additional edge to face interactions, leading to a layered structure. Furthermore, π–π stacking was found between naphthyl and pyridine groups in the novel compound **29**.

3.4 Pyrolysis Experiments

Pyrolysis of (organo)silanes has gained attention during the last decades, as its products may be widely used in ceramics, fibre-reinforced composite materials, coatings and photovoltaics.[74,181,182] The thermal treatment of alkylated silanes results in silicon carbide, which may be used for most of the aforementioned applications. Considering the recent interest in Li-ion batteries and the concurrent demand for high capacity components such as Si/C composite electrodes, pyrolysis products of organosilanes could provide suitable materials. The present work extends preliminary investigations on the pyrolysis of 1-naphthyl$_2$SiH$_2$ and phenyl$_{10}$Si$_5$ thin films conducted in our working group[6] by studying the bulk pyrolysis behaviour of phenyl$_{2n}$Si$_n$ as well as di- and triaryl silanes leading to silicon enriched (nano)particles.

The silanes used in our investigations were chosen according to different criteria: aryl groups were preferred over alkyl substituents to avoid the formation of the electrochemically inert silicon carbide. Furthermore, the aryl moieties function as good leaving groups upon heat treatment *via* Si–C bond cleavage and residual groups double as possible storage sites for lithium ions. The respective arylsilanes were chosen considering their high melting points and substitution patterns. Therefore, 1-naphthyl$_2$SiH$_2$ (**16**), 1-naphthyl(phenyl)$_2$SiH (**19**), 1-naphthyl$_2$(phenyl)SiH (**20**), 1-naphthyl$_3$SiH (**21**) and the perphenylated cyclosilanes phenyl$_8$Si$_4$ and phenyl$_{10}$Si$_5$ (**33a/b**) were tested. Details on the elemental composition and the respective melting points may be found in Table 14.

Table 14 Elemental composition of compounds **16**, **19-21** and **33a/b**.

	*1-naphthyl$_2$SiH$_2$ (**16**)*	*1-naphthyl(phenyl)$_2$SiH (**19**)*	*1-naphthyl$_2$(phenyl)SiH (**20**)*	*1-naphthyl$_3$SiH (**21**)*	*phenyl$_8$Si$_4$/phenyl$_{10}$Si$_5$ (**33**)*
M_w [g mol^{-1}]	284.43	310.47	360.53	410.59	729.19 / 911.48
mp [°C]	150	92	169	237	321 / 462
Element	*%wt*	*%wt*	*%wt*	*%wt*	*%wt*
Si	9.9	9.1	7.8	6.8	15.4
C	84.4	85.1	86.6	87.8	79.1
H	5.7	5.8	5.6	5.4	5.5

3.4.1 Differential Scanning Calorimetry/Thermogravimetric Analysis (DSC/TGA)

The chosen compounds were subjected to differential scanning calorimetry/thermogravimetric analysis (DSC/TGA) measurements before pyrolysis in order to determine the temperature at which a bond cleavage of either Si–C or Si–Si occurs. The latter is relevant for compounds **33a** and **b**, where the cleavage of the silicon backbone is aided by the ring-strain. Resulting curves are discussed at the example of compounds **33a** and **b** (*cf.* Figure 29).

The marked peaks represent endothermic reactions such as melting. In case of phenyl$_8$Si$_4$ (**33a**) a peak at 84 °C indicates the evaporation of residual ethyl acetate used for recrystallisation of the sample, which also accounts for the initial mass loss of –7%wt. Both silanes display a clear peak at their melting points. However, the melting of phenyl$_{10}$Si$_5$ sets in at 402 °C, indicating slight impurities, most probably in form of the respective six-membered ring. Nevertheless, a clear peak at 493 °C is visible. The following shoulder of the curve could indicate the cleavage of an Si–Si

bond of the ring systems. Both samples display additional peaks at higher temperatures caused by the step-wise cleavage of the phenyl groups.

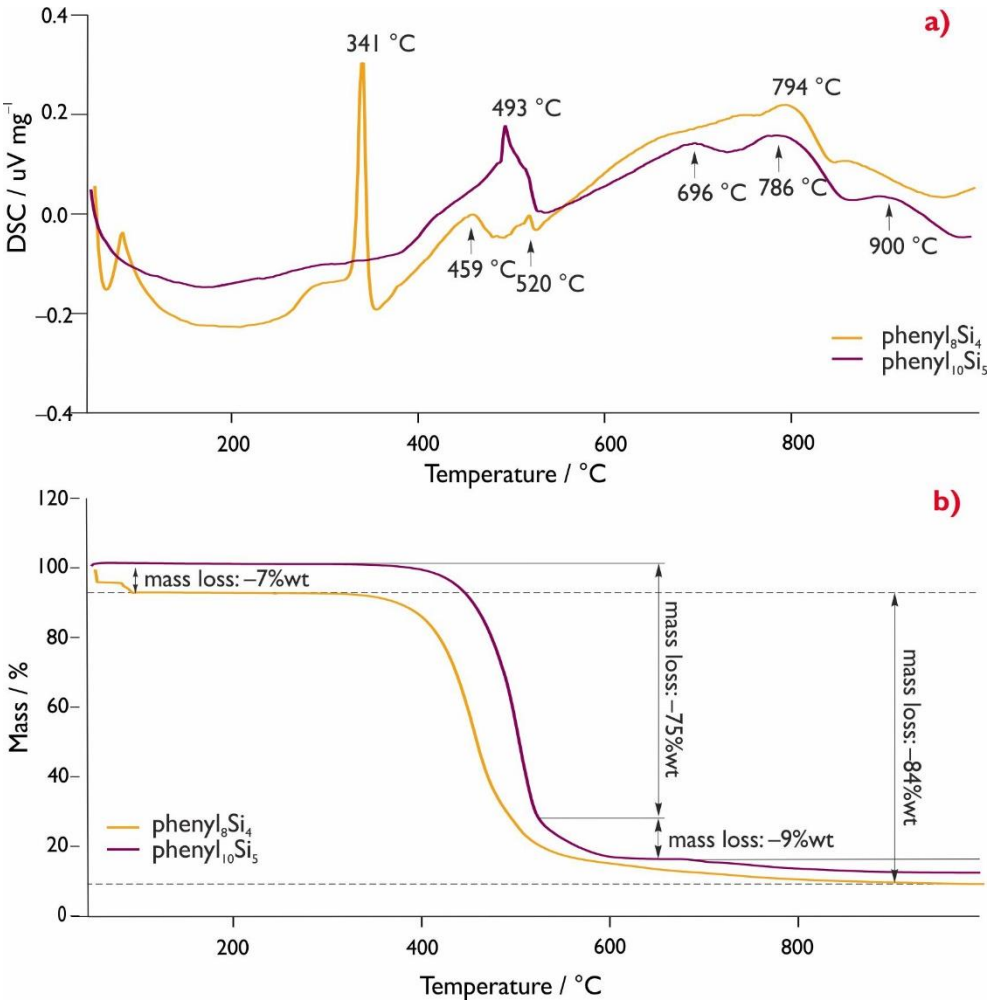

Figure 29 a) DSC curves of phenyl$_{2n}$Si$_n$ (n = 4, 5) and b) the respective TGA curves. Samples were heated up to 1000 °C under argon atmosphere with 10 °C min^{-1}.

For both compounds **33a** and **b**, the main mass loss step sets in concurrently with the inset of the melting in the range of 290-533 °C (**33a**) and 347-525 °C (**33b**), respectively. The step-wise cleavage of the phenyl groups is more pronounced for compound **33b**, again caused by slight impurities with the six-membered moiety. The overall mass loss of 84-87%wt corresponds to the abstraction of all phenyl groups, leaving pure silicon.

Similar to the samples discussed above, a mass loss corresponding to the cleaved substituents was found for compounds **16** (89%wt), **19** (91%wt), **20** (92%wt) and **21** (94%wt) as well. The temperatures employed in pyrolysis experiments were chosen with respect to the results of the DSC/TGA analysis.

3.4.2 Characterisation of the Pyrolysis Products

The morphology and material properties of the pyrolysed products are influenced by different parameters: the surrounding atmosphere (inert or atmospheric, still or agitated/flowing), heating rate, dwell temperature, dwell time and application technique (loose powder or thin films). This work focused on the bulk pyrolysis of arylsilanes under argon atmosphere, varying the remaining parameters. Experiments conducted in a horizontal tube furnace (*Carbolite* GHA 12/600) showed that for each compound an individual pyrolysis protocol was necessary in order to gain (nano) Si/C materials, hence all insights are purely empirical.

The pyrolysis protocols for the most promising samples resulting in Si/C materials are summarised in Table 15. An overview over all pyrolysis experiments conducted during this work as well as the typical procedures are given in the *Experimental* part (*cf.* section 5.3). The pyrolysed materials were characterised by elemental analysis (CHN) and SEM/EDX.

Table 15 Most promising pyrolysis protocols for arylated mono- and oligosilanes tested in this work.

N°	Compound	temp. [°C]	Rate [°C min^{-1}]	gas flow [L min^{-1}]	dwell time [min]
16	1-naphthyl$_2$SiH$_2$	700	20	2	120
19	1-naphthyl(phenyl)$_2$SiH	600	50	2	30
20	1-naphthyl$_2$(phenyl)SiH	700	50	2	30
21	1-naphthyl$_3$SiH	700	50	0.1	60
33a	phenyl$_8$Si$_4$	850	20	2	120
33b	phenyl$_{10}$Si$_5$	800	20	2	120

Typically, the silane precursors were heaped loosely in an aluminium oxide shuttle for bulk pyrolysis. The thermal treatment led to pumice-like macro-structures and a colour change of the originally colourless silanes (*cf.* Figure 30). The discolouring is directly dependent on the pyrolysis temperature, finally leading to black, insoluble residues, as was described by Binder.[6,55] Elemental analysis of the displayed samples (**33b**) gave residual carbon/hydrogen amounts of 80.2/1.7%wt and 73.1/0.9%wt for the samples pyrolysed at 500 and 800 °C, respectively. These findings confirm the initial assumption that the pyrolysis temperature is directly related to the amount of cleaved aryl moieties from the silicon centres.

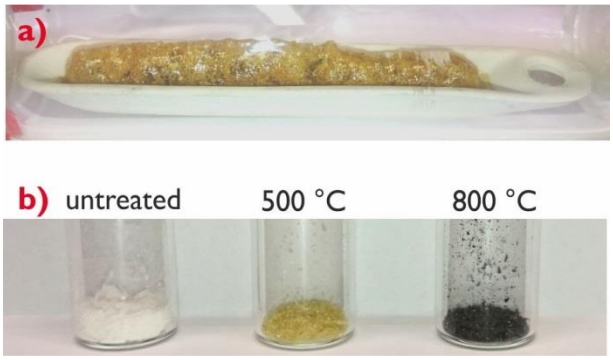

Figure 30 Pyrolysed phenyl$_{10}$Si$_5$ a) Sample taken directly from the oven (pyrolysed at 500 °C) displaying similarities to pumice. b) Colour change of the silane at different temperatures. Samples were roughly minced in a mortar.

Preliminary studies conducted in our working group[6,55] came to the conclusion, that the formed products consist mainly of oxygen and silicon. Since the precursor materials do not contain covalently bound oxygen and the experiments are carried out under inert atmosphere, the oxygen content observed in these studies is assumed to stem from adsorption when the samples are handled at ambient conditions. Therefore, the particles produced in this work were transferred directly into an argon filled glovebox *via* a glass tube with two NS 29 joints and a gas inlet valve which was directly connected to the glass-tube of the oven. Thereby, the exposure to oxygen was minimised to the few seconds needed for the transfer of the samples to the vacuum chamber of the SEM. This transfer resulted in comparably low oxygen contents of the samples of max. 11%wt as determined by EDX. A schematic depiction of the pyrolysis setup is given in the *Experimental* part of this work (*cf.* section 5.3, Figure 81).

*3.4.2.1 Cyclic Phenylsilanes (phenyl$_{2n}$Si$_n$, n = 4 or 5; Compounds **33a**/**b**)*

In the following sections, the morphologies of particles prepared by employing different temperatures, heating rates and gas flows are discussed. The most extensive investigations were conducted for the cyclic perphenylated silanes due to their comparatively high silicon content as well as their thermal decomposition behaviour (*cf.* Figure 29).

Initially, an established pyrolysis protocol consisting of a heating rate of 20 °C min^{-1}, a gas flow rate of 2 L min^{-1} and a dwell time of 120 min was applied to compound **33a** at temperatures of 500, 700 and 850 °C. In all cases, a porous macro-structure remained in the ceramic sample holder, which was roughly minced with a mortar before optical characterisation. All components based on phenyl$_8$Si$_4$ resulted in similar morphologies, as determined by SEM/EDX investigations. An example is given in Figure 31.

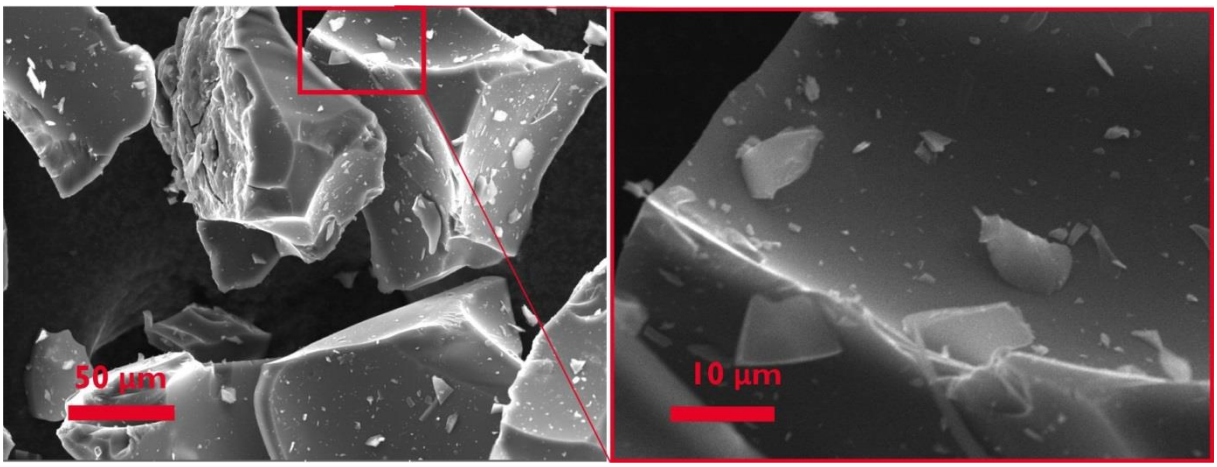

Figure 31 SEM images of phenyl$_8$Si$_4$, pyrolysed at 850 °C (heat rate 20 °C min^{-1}, gas flow 2 L min–1, dwell time 120 min; EDX: 23%wt Si, 72%wt C).

Larger chunks of the material (50-250 µm) were found to be covered with splinters ranging in sizes from 10 µm to 200 nm. A main feature of the bulk material, next to its smooth surface is its brittleness, which may be seen in Figure 31 (left) in form of cracks in the structure. This indicates that the particles consist at least partially of an amorphous phase created by the heat treatment. Considering the use of such materials in Li-ion batteries, the cracking behaviour resulting in layered structures with smooth surfaces could provide intercalation sites for lithium ions.

Additionally, the surface of the particles is dented, indicating the formation of gas bubbles trapped in the bulk. These bubbles are caused by the evaporation of benzene originating from cleaved off phenyl substituents.

EDX measurements determined that the larger particles consist mainly of carbon (87%wt C, 10%wt Si). Interestingly, parts of the sample, especially the splinters, were found to contain higher amounts of silicon, amounting to approximately 19%wt Si, 79%wt C. This could be caused by the heat transfer which induces a higher cleavage rate at the surface than inside the bulk. These findings are in agreement with the work of Binder.[6]

Similar results were gained for the pyrolysis of compound **33b**, following the same protocol at temperatures of 500, 700, 800 and 900 °C. An example of these pyrolysis products gained from experiments at 800 °C is displayed in Figure 32.

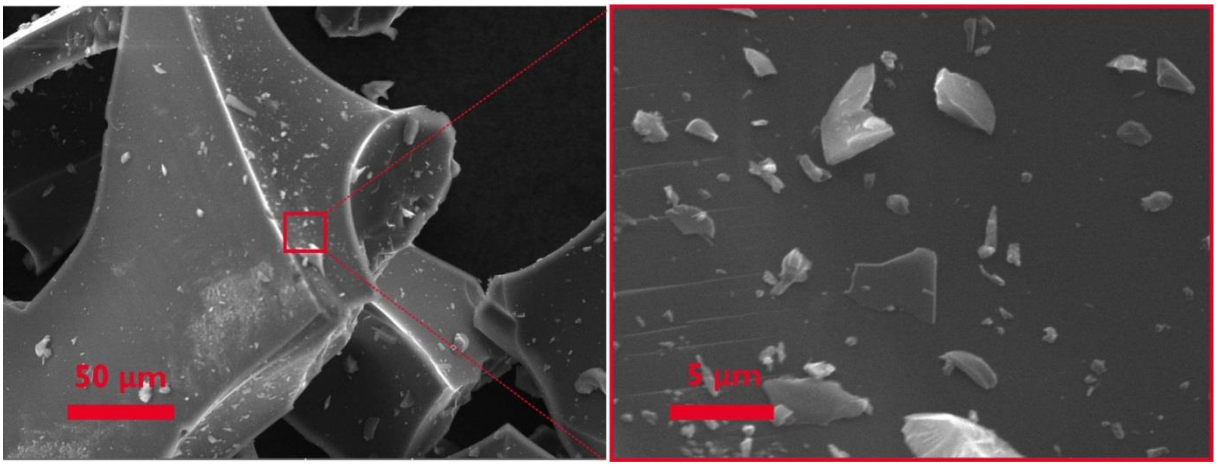

Figure 32 SEM images of phenyl$_{10}$Si$_5$ pyrolysed at 800 °C (20 °C min^{-1}, 2 L min^{-1}, 120 min; 22%wt Si, 71%wt C), displaying sheet-like particles.

In this example, the layered structure is visible in form of welts at the edge (break site) of a larger particle. EDX measurements determined a silicon content of 22%wt and a carbon content of 71%wt for the highlighted area. These values agree in principle with the CHN analysis resulting in 73.4%wt carbon and 0.7%wt hydrogen, where the residual mass of 25.9%wt is attributed to silicon. Since the samples are exclusively handled under argon atmosphere for the elemental analysis, an adsorption of oxygen in these samples may be excluded.

Further experiments included the variation of gas flow, heating rate and temperature steps. Therefore, the samples were subjected to the pyrolysis protocols summarised in Table 16. Experiments a) and b) followed the usual heating procedure and varied only in the gas flow. The flow rate for approach b) was set to 0.1 L min^{-1}, which is close to a standing atmosphere and nevertheless able to transport evaporated components from the residual bulk. In experiments c) and d) the samples were introduced into a pre-heated oven under argon counterflow and were exposed to one- or two-step pyrolysis. The heating rate between the temperature steps in approach d) was set to 50 °C min^{-1}, which corresponds to the fastest heating possible with the equipment used.

Table 16 Pyrolysis protocols used for phenyl$_{10}$Si$_5$ samples.

	pyrolysis temp. [°C]	*rate [°C min^{-1}]*	*pre-heated*	*gas flow [L min^{-1}]*	*dwell time [min]*
a)	800	20	—	2	120
b)	800	20	—	0.1	120
c)	800	—	✓	2	60
d)	450/800	50	✓	2	30/30

The morphology of the corresponding samples is displayed in Figure 33. Comparing approaches, a) and b), the morphologies deviate only slightly by the smoothness of the surface. With respect to the elemental composition determined by EDX and CHN analyses, close to no deviations could be detected, either (*cf.* Table 17). The only difference was found in the mass loss of the sample: in experiment a) the overall mass was reduced by 84%, in experiment b) by 80%. The faster gas flow causes an increased transport of the evaporated components consisting of benzene, mono-, di- and triphenyl silane. A preliminary transport of the precursor powder off the sample holder may not be excluded under these circumstances.

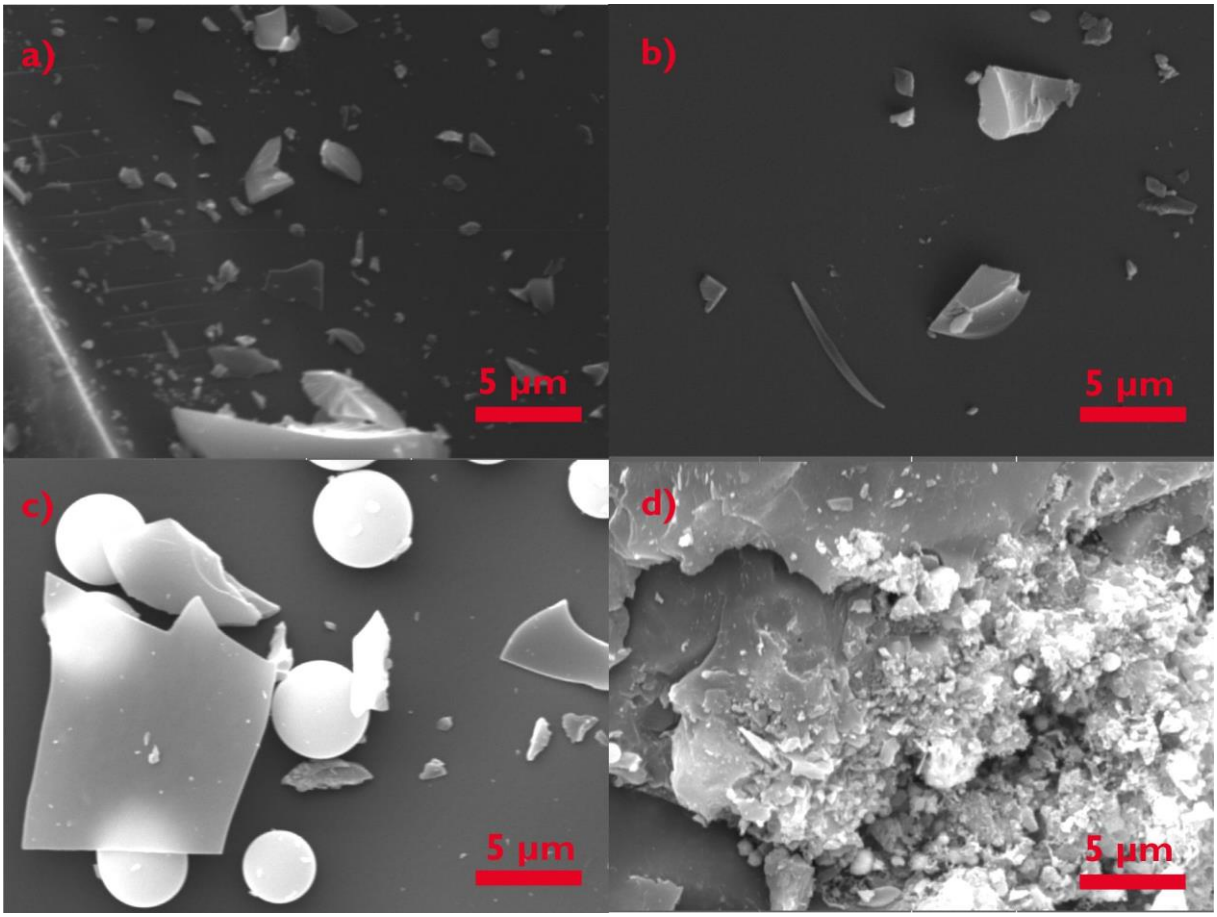

Figure 33 SEM images of phenyl$_{10}$Si$_5$ pyrolysed at 800 °C. a) 20 °C min^{-1}, 2 L min^{-1}, 120 min. b) 20 °C min^{-1}, 0.1 L min^{-1}, 120 min. c) pre-heated, 2 L min^{-1}, 60 min. d) pre-heated, 2 L min^{-1}, 450/800 °C, 30 min, each.

Table 17 Composition of differently pyrolysed phenyl$_{10}$Si$_5$ samples determined by EDX and CHN elemental analysis.

	EDX		CHN		
	Si [%wt]	*C [%wt]*	*Si [%wt]**	*C [%wt]*	*H [%wt]*
a)	22	71	25.7	73.4	0.7
b)	20	80	25.8	73.1	0.9
c)	30	70	24.9	72.5	1.4
d)	37	51	25.0	72.8	1.1

* Difference to 100%, judged by C and H contents.

An interesting behaviour was observed in experiment c): the surface of the materials was covered with spherical particles and thin sheets consisting of 76%wt carbon, 16%wt silicon, 6%wt oxygen and 2%wt nitrogen, according to EDX analysis. These structures formed due to the sudden temperature change of the sample from room temperature to 800 °C, bypassing the usual acclimation and melting phase. The nitrogen and oxygen content stem from the storage of the sample under air before introducing it into the oven. Similar results were gained by Binder, who found spherical particles of high silicon content in the gas-stream of the apparatus, and no residual silicon in the powdered samples.[6]

Similar spheres were detected in the two-step treatment of experiment d). These structures, however, were not only considerably smaller (approximately 500 nm) than the ones found in experiment c) (approximately 4 µm) but were also embedded in a frayed irregular surface. This is the result of the initial exposure of the sample powder to a temperature close to its melting point of 462 °C. The subsequent fast heating of the nearly molten sample causes the cleavage of Si–Si as well as Si–C bonds which in turn leads to the observed formations. Despite the frayed surface, also in this example the layered basic structure is preserved.

The layered nature of the materials is an appealing property, especially regarding a possible application in Li-ion battery anodes. Considering this application, a homogeneous distribution of the silicon is necessary and its volume expansion upon lithiation should not be neglected. Thus, the materials were homogenised *via* ball-milling. The resulting powder is displayed in Figure 34.

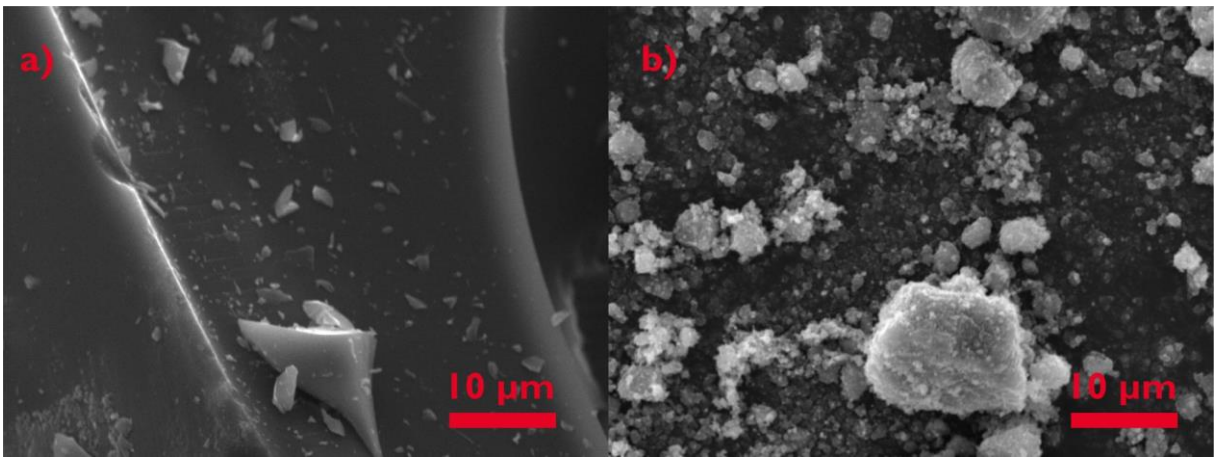

Figure 34 SEM images of phenyl$_{10}$Si$_5$.pyrolysed at 800 °C, 20 °C min^{-1}, 2 L min^{-1}, 120 min. a) pyrolysed particles. b) particles after ball-milling (600 rpm, 4 x 15 min).

Compared to the untreated pyrolysis product, the particle sizes were immensely reduced. However, no fully homogeneous size distribution could be obtained. Furthermore, the formerly smooth surfaces appear frayed and are thus losing some of their layered character. Despite this draw-back, the homogeneous distribution of silicon in a graphite composite material should be facilitated by using the ball-milled samples.

*3.4.2.2 Di- and Triaryl silanes (Compounds **16, 19-21**)*

Di- and triaryl silanes bearing at least one 1-naphthyl group, *i.e.* 1-naphthyl$_2$SiH$_2$ (**16**), 1-naphthyl(phenyl)$_2$SiH (**19**), 1-naphthyl$_2$(phenyl)SiH (**20**) and 1-naphthyl$_3$SiH (**21**), were also subjected to pyrolysis experiments. Similar to the oligo-silanes the pyrolysis protocols were determined empirically. These compounds offer comparatively smaller amounts of silicon (7-10%wt) and thus tend to a larger mass-loss when the organic residues are cleaved off. However, Binder already showed that the formation of pure silicon is possible with 1-naphthyl$_2$SiH$_2$ thin films on a molybdenum foil when it is treated at 700 °C with the max. possible heating rate of the *Carbolite* furnace.[6]

Following the goal to create silicon enriched Si/C particles, several approaches were necessary for each compound. In preliminary work it was determined that 1-naphthyl groups tend to cleave off between 264 and 327 °C, accounting for a mass loss of –77% for compound **16**.[6] Initial experiments with this compound were conducted by an established two-step pyrolysis at 450/700 °C (20 °C min^{-1}, 2 L min^{-1}, 30 min, each). The resulting material is displayed in Figure 35, a). In contrast to the previous work, the compound was pyrolysed in bulk rather than on a substrate. Additionally, the sample was handled solely under argon atmosphere. This resulted in an overall silicon and carbon content of 17%wt and 82%wt, respectively. Similar to the cyclic oligosilanes phenyl$_{2n}$Si$_n$, the materials consisted of larger bulk with smooth surfaces which were covered with smaller particles. The two-step experiment showed additionally frayed structures as expected of a congealed melt.

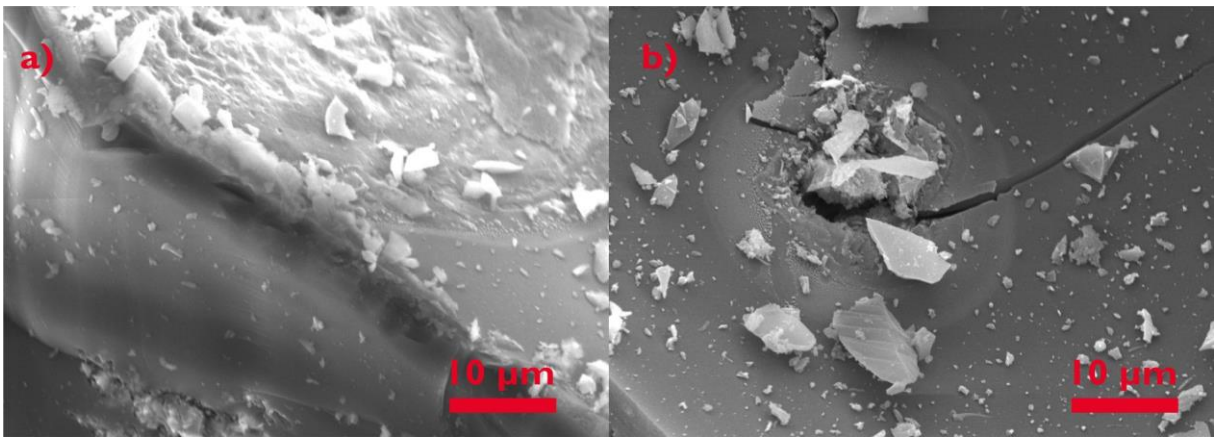

Figure 35 SEM images of 1-naphthyl$_2$SiH$_2$ pyrolysed at different temperatures. a) 450/700 °C (30 min, each; 17%wt Si, 82%wt C). b) 700 °C (30 min, 32%wt Si, 68%wt C)

In a second experiment the compound was heated directly to 700 °C, all other parameters were kept the same (*cf.* Figure 35 b)). These samples show a much smoother surface and crack similar to the ones obtained for compounds **33a** and **b**, again indicating a layered structure. EDX of the particles situated on the surface of the layered Si/C material determined them to consist solely of

silicon, while the overall silicon content amounts to 32%wt. The dispersion of silicon and carbon was determined by EDX elemental mapping (Figure 36) and shows a homogeneous distribution of both elements.

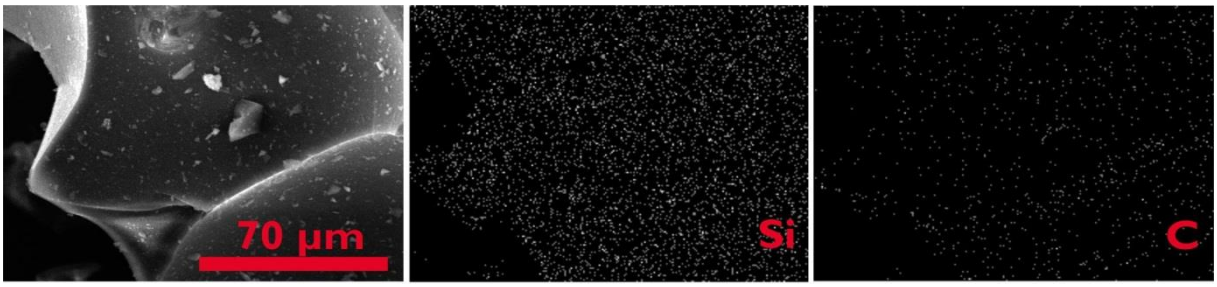

Figure 36 EDX Elemental mapping of 1-naphthyl$_2$SiH$_2$ pyrolysed at 700 °C.

The same pyrolysis protocols were applied to the triaryl silanes **19**-**21**. However, in all cases close to no Si/C residues were detected in the sample holder. Residual substances in the quartz-glass tube along the gas-stream consisted mainly of naphthalene and different evaporated monosilanes. Therefore, the protocols were adapted for each compound with respect to the corresponding melting points until a solid residue could be retrieved (*cf.* Table 15).

In case of 1-naphthyl$_3$SiH (**21**) the most promising results were gained by applying 700 °C at the highest possible heating rate (50 °C min^{-1} or pre-heated) with gas flow rates of 2 or 0.1 L min^{-1}. Similar to compounds **33**a and **b**, the lowered gas flow resulted in the familiar pumice-like structures covered with spherical particles (*cf.* Figure 37, a)). In contrast to the cyclic silanes, however, these structures appeared to agglomerate to larger, round shapes (approximately 10-40 µm) in compound **21**, while the spheres themselves range from 3-8 µm. EDX analysis gave a composition of 84%wt C and 8%wt Si. Thus, the structures are likely consisting of the molten precursor compound. When a gas flow of 2 L min^{-1} was applied, no similar agglomerations were observed but solely the layered structures as discussed for **33b**. This is most likely due to the slight cooling of the samples provided by the gas stream in addition to a distribution of the molten phase to form another layer.

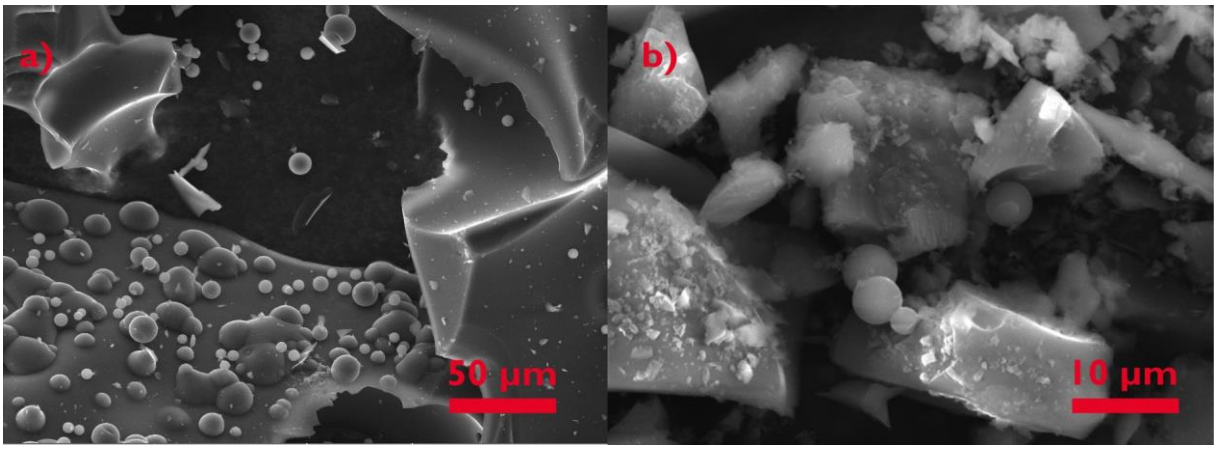

Figure 37 SEM images of pyrolysed triaryl silanes. a) 1-naphthyl$_3$SiH **21** (700 °C, 50 °C min^{-1}, 0.1 L min^{-1}, 30 min; 21%wt Si, 78%wt C), b) 1-naphthyl(phenyl)$_2$SiH **19** (600 °C, 50 °C min^{-1}, 2 L min^{-1}, 30 min; 19%wt Si, 79%wt C).

The triaryl silanes containing mixed substituents were pyrolysed at 600 (**19**) and 700 °C (**20**), respectively, with a gas flow rate of 2 L min^{-1}, a heating rate of 50 °C min^{-1} and dwell time of 30 min, each. These experiments resulted in the expected structures as seen in previous examples

(Figure 37, b)). However, despite a higher gas flow rate, spherical particles could be detected for compounds **19** and **20** as well. This might stem from the mixed nature of the substituents, displaying different cleaving temperatures (1-naphthyl 264-327 °C, phenyl 290-533 °C) and therefore a different arrangement-behaviour.

3.4.3 Summary of Pyrolysis Experiments

The bulk-pyrolysis of differently substituted mono- and oligosilanes was tested. Therefore, the parameters of pyrolysis temperature, heating rate, gas flow rate and dwell-time were varied with respect to the corresponding melting points as well as DSC/TGA results. The products were characterised by SEM/EDX and CHN elemental analysis.

All samples resulted in layered structures formed by arrangement of the aryl-moieties. Overall, elemental composition of the samples accounted to 19-32%wt silicon and 68-81%wt carbon, respectively. Pyrolysis of 1-naphthyl$_2$SiH$_2$ at 700 °C resulted in flakes of pure silicon placed on the surface of the Si/C composite materials, which is in agreement with previous research performed by Binder, who investigated the pyrolysis of arylsilane thin films.[6]

The heating and gas flow rates were determined to greatly influence the formation of Si/C composite materials and their resulting morphology. Pyrolysis of aryl-substituted silanes results in a homogeneous distribution of silicon as well as a layered array of the residual aryl groups, making them interesting candidates for intercalation materials in Li-ion battery anodes.

3.5 Electrochemical Characterisation of Arylsilicon Hydrides

Several intriguing properties make arylsilicon compounds interesting for electrochemistry. When an aromatic compound is substituted with a silyl group in α-position, the HOMO energy level of its π-electron system rises. In contrast, the LUMO energy level is lowered which facilitates reduction. Furthermore, silyl-substituents are good leaving groups acting as "super protons", especially when cathodic intermediates are formed in β-position. A further advantage lies within their ability to generate and stabilize α-anions.[183]

During the last decades, the focus was on the electrochemical synthesis of organosilicon compounds, especially on organosilicon halides and polysilanes.[82,84–86,184–186] The electrochemical reduction potentials of triorganohalosilanes[187] have been investigated while, on the other hand, information on aryl silanes bearing hydrogen remains sparse.[85] The influence of size and nature of the aryl substituents is largely unknown as well.[93,188]

Since hydrogen-rich aryl silanes are promising candidates for various applications including precursors for composite materials for *e.g.* ceramics, protecting groups in organic chemistry and materials for surface modification,[189–191] a deeper knowledge of electrochemical stability and reactions of this compound class could contribute to the development of new materials.

In this chapter, the anodic potentials of a series of novel and literature-known mono-, di- and triaryl silanes bearing hydrogen are investigated, and trends about the influence of the aryl moieties are assessed. The products formed during electrolysis are characterized by GC-MS measurements and the products identified.

3.5.1 Cyclic Voltammetry Experiments

Cyclic voltammetry experiments were conducted with arylated silanes in acetonitrile (MeCN) at different current rates of 50, 100 and 1000 mV s^{-1} in a purpose-built CV cell (see section 3.5.2). The electrochemical stability window was determined to lie between -2.0 and 2.5 V *vs.* non-aqueous Ag/AgCl by employing linear sweep voltammetry on a blank electrolyte solution (0.1 M TBAF/MeCN). Since no significant differences in the shape of the curves were observable at different rates, only results for 100 mV s^{-1} are discussed.

In this series of measurements, silanes with the general formula R_nSiH_{4-n}, where R = phenyl, 1-naphthyl, 2,5-xylyl and n = 1-3, were tested. While in all cases no reduction could be detected within the measurable range (Figure 38, a)), irreversible anodic oxidation behaviour was observed for most samples within the range of 1.9-2.5 V *vs.* Ag/AgCl. For discussion, the area of interest (1.5 - 2.5 V *vs.* Ag/AgCl) is shown at an enlarged scale (Figure 38, b)).

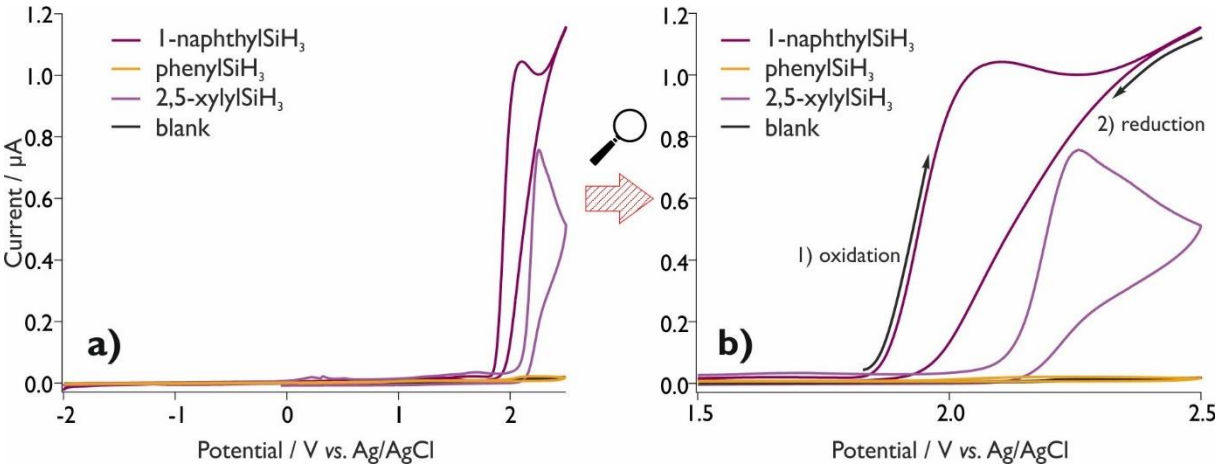

Figure 38 CV of $RSiH_3$ (R = phenyl, 1-napththyl, 2,5-xylyl) in 0.1 M TBAF/MeCN solution *vs.* Ag/AgCl in MeCN at 100 mV s^{-1} with a 20 µm diam. Pt microelectrode as WE and a non-aqueous Ag/AgCl RE. a) Spectrum of the full range of the $RSiH_3$ measurements within the electrochemical stability window of MeCN; b) Oxidation peaks of the measured compounds in a smaller segment of the measurable range. The direction of the CV experiments is indicated with arrows. All experiments were carried out equally.

Regarding the arylsilicon trihydride samples, the influence of bulky aromatic ring systems is evident: while for $phenylSiH_3$ neither reduction nor oxidation peaks were detected, oxidation peaks are observed for $2,5\text{-}xylylSiH_3$ (**11**) and $1\text{-}naphthylSiH_3$ (**12**) at 2.25 V and 2.08 V *vs.* Ag/AgCl, respectively. The shift of the peaks indicates a dependence of the oxidation potential on the aryl substituents. This effect has been described for silylarenes $R(SiH_3)_n$ by Becker *et al.*[93] who found that the introduction of methyl groups into the phenyl substituent caused an inductive effect which leads to lower peak potentials. An extension of the phenyl ring system lowers the peak potentials, too, which is likely to be caused by a negative inductive effect towards the ring stemming from the polar Si–C bond.[93] In case of $1\text{-}naphthylSiH_3$ (**12**) an additional peak is hinted at the edge of the stability window (2.5 V), which has also been described for pure naphthalene.[192] In general, different mechanisms for the electrochemical reaction of aromatic systems were considered. The prevalent mechanism suggests that the oxidation peaks may be attributed to the extraction of an electron from the E_{HOMO} of the aromatic system. This leads to radical cations which have an unpaired spin and positive charge at the same time according to Equation 4.[192]

$$AH_2 = [AH_2]^{+\cdot} + e^- \qquad (4)$$

In our research we investigated the influence of the number of aromatic substituents on the silicon atom. Compared to the monoaryl silanes, the CV experiments for diaryl silanes (R_2SiH_2) display broader oxidation peaks while the currents decline drastically from approximately 1.2 µA (*e.g.* $1\text{-}naphthylSiH_3$ (**12**)) to 60 nA (*e.g.* $1\text{-}naphthyl_2SiH_2$ (**16**)) (Figure 39). Compounds substituted with 2,5-xylyl groups oxidise at lower potentials when a second substituent is introduced, whereas for 1-naphthyl-substituted compounds the potential remains roughly the same (2.09 V) even though the response broadens strongly most likely due to much slower kinetics. While the $phenyl_2SiH_2$, again, did not oxidise within the measured range, the asymmetrically substituted 1-naphthyl(phenyl)SiH_2 showed a shoulder similar to the curve of $1\text{-}naphthyl_2SiH_2$ (**16**), but slightly shifted to positive potentials (2.15 V).

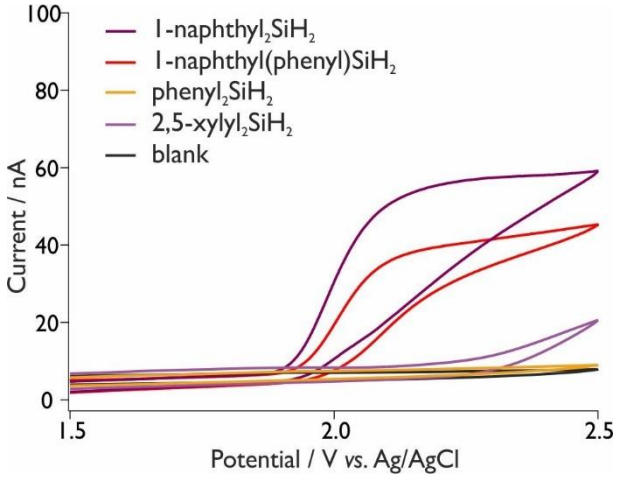

Figure 39 CV of R_2SiH_2 (R = phenyl, 1-naphthyl, 2,5-xylyl) in 0.1 M TBAF/MeCN *vs.* Ag/AgCl at 100 mV s^{-1}.

The same trend is seen for asymmetrically substituted triaryl silanes (Figure 40, left). When more phenyl groups are introduced, the oxidation potential shifts to higher voltages and the currents are lowered. The exact oxidation potentials of triaryl silanes are masked by broadened curves. However, judging from onset, shape and slope of the curve, the potentials change only slightly compared to the 1-naphthyl2SiH2.

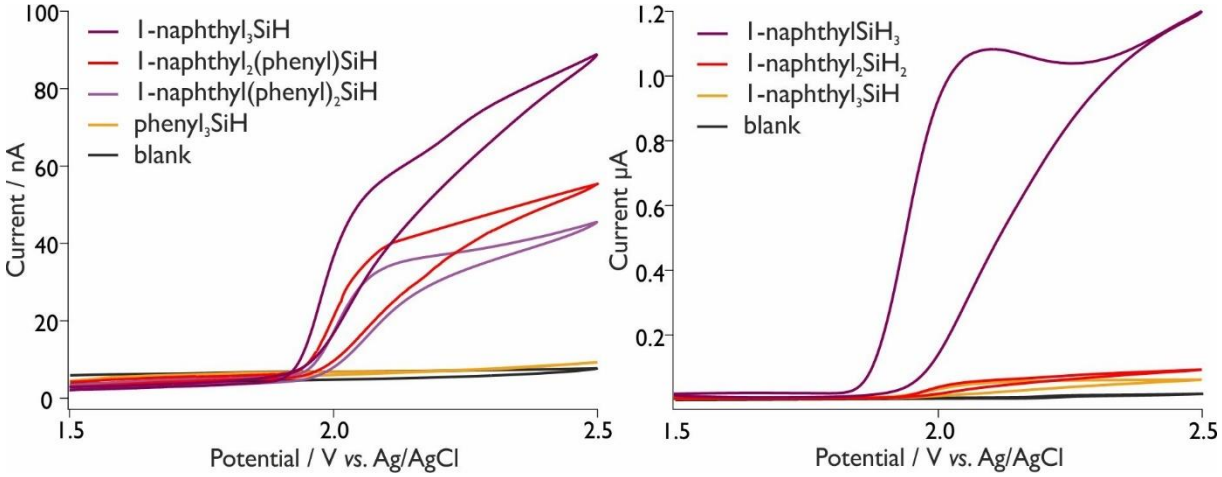

Figure 40 CV of R_3SiH (R = phenyl, 1-naphthyl) (left) and 1-naphthylsilicon mono-, di- and trihydride (right) in 0.1 M TBAF/MeCN at 100 mV s^{-1}.

Overall a substitution of the silicon atom with more than one aryl moiety leads to a significant loss in current and consequently in reactivity. This result is expected due to shielding by the sterically demanding substituents. However, the introduction of a second aryl group displays a larger influence than the successive third aryl moiety.

Additional information was gained when the electrode processes were monitored over the course of several cycles. Independent on the number of substituents, successively lower currents were recorded for every subsequent cycle. An example is shown in Figure 41. This behaviour strongly indicates that the microelectrode passivates due to electrochemical reactions. Since it was proven for organosilicon halides that an electrochemical generation of radicals is followed by halogenation or recombination and leads to oligomers, an analogous reaction path for the silicon hydride species may be reasonably assumed.[82,86,193]

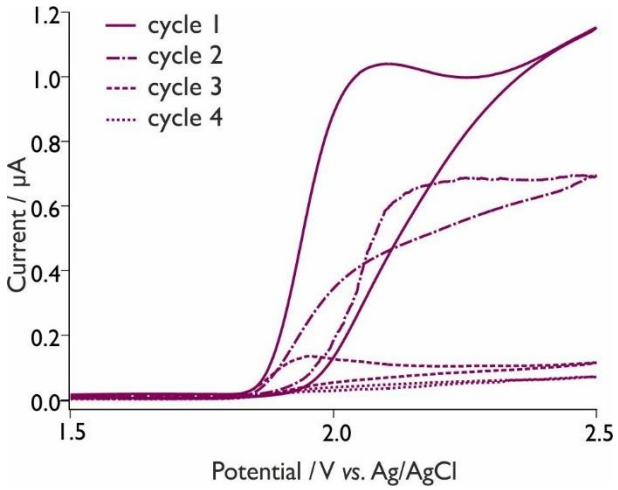

Figure 41 Passivation of the WE during CV of 1-naphthylSiH$_3$ in 0.1 M TBAF in MeCN.

The formation of a solid residue on the microelectrode surface, however, was not visible to the unaided eye. Further investigations on the passivation of the WE included chronoamperometry (CA) experiments at 2.3 V *vs.* Ag/AgCl for 15 min, using Pt macro-electrodes as WE and CE. In case of the liquid silanes *i.e.* RSiH$_3$, phenyl$_2$SiH$_2$ and 1-naphthyl(phenyl)SiH$_2$ (**15**), a concentration of 25 mM was employed which corresponds to a saturated solution of the most soluble compound (phenyl$_3$SiH (**17**)) in the electrolyte. The experiments showed that the currents initially drop and subsequently stabilise (Figure 43). Except of 2,5-xylyl-substituted compounds, the aryl silanes show a fast reaction within the first second which consumes the educts molecules close to the electrode. The CA curves stabilise at different currents indicating an ongoing reaction throughout the measured timeframe. Due to the fact that the samples were not stirred during the measurements all reactions are likely limited by diffusion. The stabilisation of the reaction curves signifies the formation of soluble products, most likely to be oligomeric silanes. In case of the 2,5-xylyl-substituted silanes, the educts near the WE are consumed very slowly and a stable reaction rate is reached after approximately 7 min.

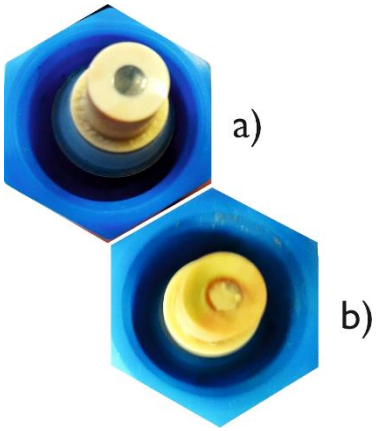

Figure 42 a) unused Pt WE b) Residue on the Pt WE after the chronoamperometry experiment of 1-naphthyl(phenyl)$_2$SiH.

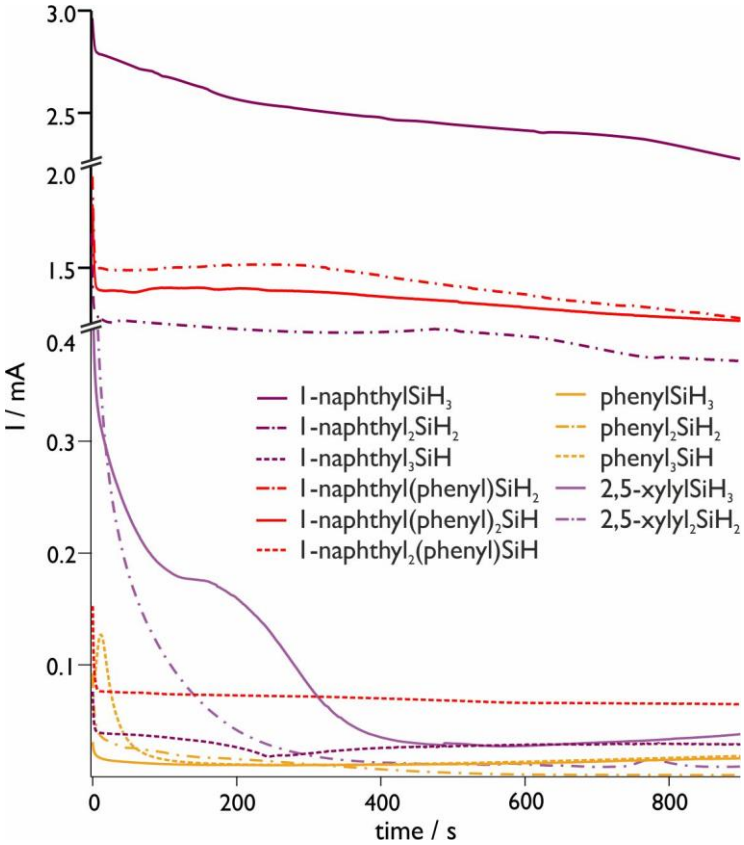

Figure 43 Chronoamperometry curves of R_nSiH_{4-n} with R = phenyl, 1-naphthyl, 2,5-xylyl and n = 1-3 in 0.1 M TBAF in MeCN *vs.* Ag/AgCl.

The cell was disassembled after the experiments and the sample solutions were recovered. The samples with fast reaction rates had changed in colour whereas the slowly reacting silanes remained colourless with an occasional dark precipitate (Figure 44). The colour change is the product of soluble silane oligo-/polymers formed during the reaction. The Si–Si backbones of these oligo-/polymers are known to be chromophores depending on conformation and σ-delocalisation along the Si–Si chain, as reported on the example of polydimethylsilanes.[194,195]

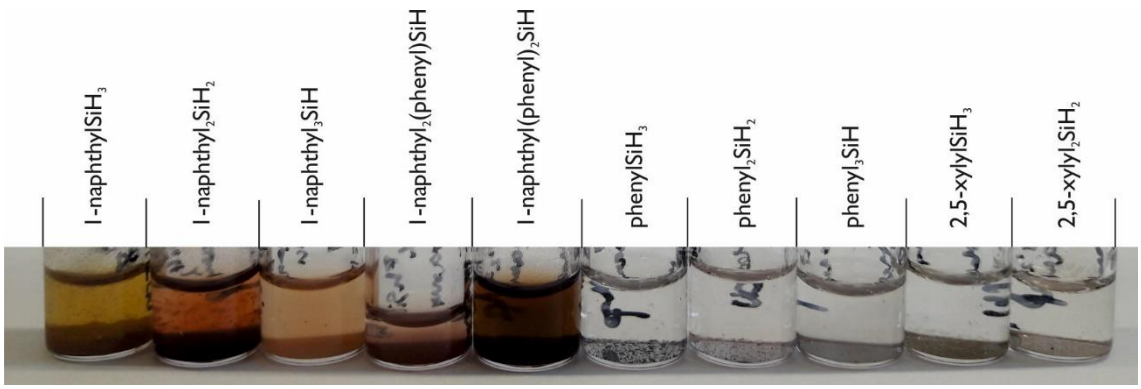

Figure 44 Recovered silane solutions after chronoamperometry (15 min, 0.1 M TBAF, Pt WE & CE, 2.3 V *vs.* Ag/AgCl).

The reactivity monitored by CA agrees with cyclic voltammetry experiments and follows the trend $RSiH_3$ > R_2SiH_2 > R_3SiH, as expected. Regarding the reactivity of triaryl silanes no clear trend can be deduced from chronoamperometry experiments since the currents measured for 1-naphthyl(phenyl)$_2$SiH (**19**) (1.4 mA) exceed the ones for the other triaryl silanes ranging between 0.03 and 0.08 mA by far.

GC-MS measurements of the resulting solutions gave an overview over the soluble products which are summarised in Table 18. For samples with one aryl residue, *i.e.* compounds **10**-**12**, only the educts could be detected. In case of di- and triarylated silanes (compounds **13**-**21**) the electrochemical treatment resulted in partial fluorination of the educt silanes caused by reactions with the electrolyte salt. The residual educts accounted to 60-80% of the soluble silane components. A full conversion of the silane to its fluorinated derivatives could be achieved by prolonging the reaction times. Compounds **19** and **20** yielded traces of the rearrangement products phenyl$_2$SiF$_2$ and phenyl$_3$SiF, indicating an abstraction of a naphthyl group. The presence of a dark, in MeCN insoluble, precipitate in all samples suggests the formation of oligosilanes as observed for the halogenated organosilicon compounds.[86,95]

Table 18 Selected examples of electrochemically formed soluble products determined by GC-MS. % are given with respect to the overall content of detected silanes.

Educt		*Soluble Product(s)*	%
11	*2,5-xylylSiH$_3$*	—	—
12	*1-naphthylSiH$_3$*	—	—
15	*1-naphthyl(phenyl)SiH$_2$*	1-naphthyl(phenyl)SiF$_2$	29
16	*1-naphthyl$_2$SiH$_2$*	1-naphthyl$_2$SiF$_2$	14
19	*1-naphthyl(phenyl)$_2$SiH*	1-naphthyl(phenyl)$_2$SiF phenyl$_2$SiF$_2$	26 <1
20	*1-naphthyl$_2$(phenyl)SiH*	1-naphthyl$_2$(phenyl)SiF phenyl$_3$SiF	7 <1
21	*1-naphthyl$_3$SiH*	1-naphthyl$_3$SiF	2

3.5.1.1 Summary of Electrochemical Characterisation of Arylsilicon Hydrides

In conclusion, with exception of the seemingly unreactive phenylated species, irreversible oxidation processes could be observed for mono-, di- and triaryl silanes. The oxidation processes may be ascribed to the withdrawal of an electron from the E_{HOMO} of the respective aryl-moiety. However, the attack seems to take place close to the silicon atom, which is shielded with increasing bulk and number of the substituents. As a consequence, the electroactivity of the monitored compounds decreases due to steric and electronic shielding of the silicon centre atom. The oxidation potentials are lowered along with increasing steric demand given by aryl substituents. This is induced by the polarity of the Si–C bond causing a negative inductive effect towards the ring system.[93] Analysis of the electrochemically generated soluble products revealed the main reaction to be a fluorination of the hydride functionality along with oligomerisation of the arylated silanes.

3.5.2 Optimising a CV Setup

Arylsilanes and arylstannanes pose interesting candidates for an application in Li-ion batteries due to their high theoretical capacities and the electron density stemming from the aromatic ring-systems of the substituents. These compound classes, however, have not yet been fully characterised. Especially the electrochemical properties were neglected thus far. Over the course of this work a characterisation by cyclic voltammetry was pursued in order to gain insights into the redox-behaviour of mono-, di- and triaryl silanes and stannanes. The investigated compounds are prone to hydrolysis and, in case of aryltin trihydrides, decomposition through exposition to air, moisture, temperatures above –30°C and UV irradiation. Thus, even the synthesis and storage of such products is difficult let alone electrochemical investigations where some more critical requirements have to be met. Therefore, a cyclic voltammetry electrochemical cell was designed to fit, wherever possible, the strict requirements of such an investigation.

Previously, the electrochemical reactivity of arylsilicon and aryltin halides was reported in literature in the context of the generation of either hydrides, fluororgano-species or polymers.[62,83,184,185,196] Usually, a three-electrode setup in a 10-100 mL undivided cell filled with 0.1 M solutions of a supporting electrolyte salt in solvents such as tetrahydrofuran (THF), 1,2-dimethoxyethane (DME) or acetonitrile (MeCN) is used. These solvents were chosen considering the solubility of the investigated compounds and their electrochemical stability windows. The most common supporting electrolyte salts are tetrabutylammonium salts with different anions, *e.g.* hexafluorophosphate (TBAF), perchlorate (TBAP), chloride (TBACl), tetrafluoroborate ($TBABF_4$) or tetraphenylborate ($TBABPh_4$). Typically, the working and counter electrodes consist of a variation of Pt (wire, grid, macro-/micro disk or rotating disk electrode), whereas different types of reference electrodes were used in literature: saturated calomel (SCE), Ag/AgI or Ag/AgCl are under the most commonly reported ones.[85,87,187,197–200]

The difficulty of the synthesis and storage of larger amounts of aryltin trihydrides makes a cell requiring only small sample volumes necessary. Therefore, based on the modular setup used for Li-ion half-cells, a *Swagelok*® PFA 620-3 union tee connector with an inner diameter of ⅜ inch was chosen as the cell body part. Perfluoralkoxy polymers (PFA) offer the advantage of being solvent resistant and in general (electro-) chemically inert. Platinum and glassy carbon (GC) disk electrodes with a diameter of 3 mm in a mantle made of polyether ether ketone (PEEK) were purchased from *Metrohm*, the mantle was mechanically adjusted to fit into the PFA body and used as either working or counter electrodes.

In order to design a reference electrode suitable for the characterisation of organosilicon and organotin hydrides several aspects need to be taken into account: the used materials need to withstand the organic solvents and electrolyte salts, should be airtight, fit seamlessly into the *Swagelok*® body part and offer connectivity with the rest of the cell as well as with the potentiostat. The desire for an airtight cell stems from the observation that potentiostat channels installed in glove-boxes suffer problems with shielding resulting in high noise levels of the CV curves during the measurements. The shielding issue is aggravated by the relatively small currents that are measured.

Thus, a modular system for a versatile reference electrode based on commonly used multiple joints with a Haber-Luggin capillary was developed. Therefore, conjoining parts were manufactured from PEEK as shown in Figure 46. Porous glass frits (*CoralPor*™, frit diameter 2.8 mm, specific surface area 212 $m^2\ g^{-1}$, pore diameter 7.8 nm) were attached using a heat shrink Teflon® (PTFE) tube following the example of Bühlmann and co-workers.[201] The created reference electrode was able to be adapted to and used with different solutions – either with a silver chloride coated silver wire in TBACl/AgCl (sat.) solution in MeCN or as redox reference electrode with a platinum wire in a solution of 4 mM (equimolar) ferrocene/ferrocenium hexafluorophosphate ($Fc/Fc^+PF_6^-$) solution in THF with an additional salt bridge, the latter set-up being inspired by Compton and co-workers.[202]

One of the greatest challenges was posed by the introduction of the metal wire into the system. The most important aspect was the sealing of the wire. Nearly all commercially available reference electrodes consist of glass bodies to which the connecting metal wire is glued with epoxy resin or similar adhesives. However, this is only feasible for aqueous systems, as organic solvents such as MeCN or THF are dissolving or swelling the adhesive over time and thereby introducing impurities into the reference. In order to circumvent this problem, HPLC fittings made of PEEK with bores according to the wire thickness, *i.e.* 0.25 mm for the Pt and 0.5 mm for the Ag wire, and an outer diameter of 1/16 inch were used. In order to seal the wires tightly, additional PTFE tubing was applied at two distances which was fastened together *via* a respective conical inset (Figure 45). In this way, an airtight sealing could be provided, although this was in fact an interim solution until a setup with less joints became available. Nevertheless, it still has the advantage of being customisable.

Figure 45 Setup for the metal wire sealing (interim solution) with 2 HPLC fittings and connecting PTFE tubing.

Initial experiments were run with the redox reference electrode in THF as stated above. Therefore, the frits were conditioned with the respective electrolyte solutions for at least 48 h. The PEEK part **A** was filled with an $Fc/Fc^+PF_6^-$ solution in THF and the Pt wire was immersed. Following the example of Compton,[202] PEEK part **B** was filled with a 0.1 M TBAP solution and connected to part **A** to form the full redox reference electrode. Pt and GC macro-electrodes were used as working- and counter-electrodes, respectively (Figure 46). Despite several attempts at assembling this setup and replacing individual parts, ionic contact through the reference electrode was poor, this leading to a high impedance of the reference electrode. Very likely, this can be traced to the less than optimal performance of the glass frits that were either defective or clogged by impurities during assembly. However, when omitting the salt-bridge (part **B**), the reference worked adequately and some CVs could be measured without further ado.

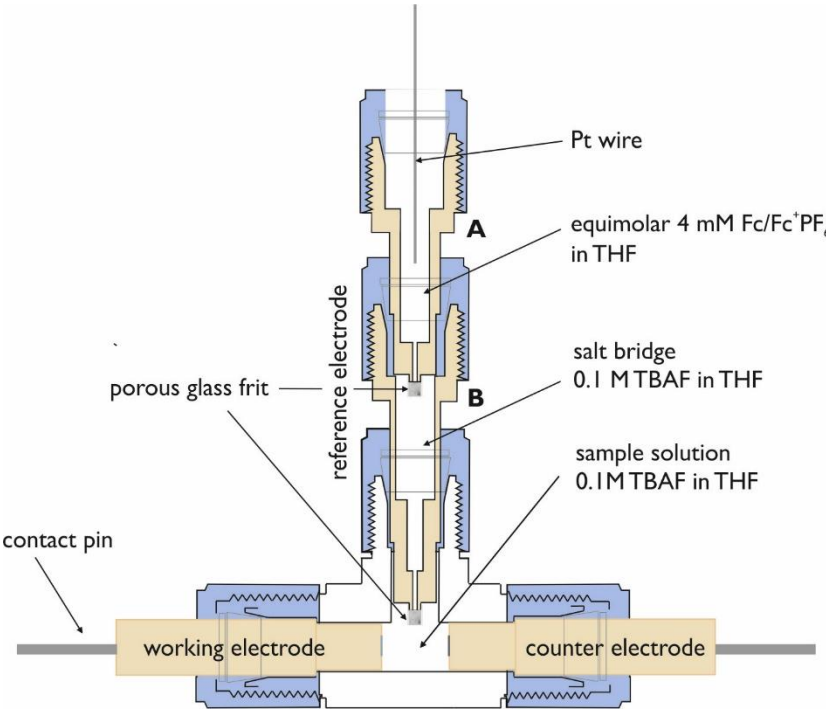

Figure 46 Modular CV cell setup for the use with a redox reference electrode basing on $Fc/Fc^+PF_6^-$ in THF. The sealing of the Pt wire is omitted for clarity.

With this setup, a first overview over the electrochemical behaviour of aryl-substituted silanes could be gained. Besides the insights into the role of size and number of aryl residues on group 14 metals, the limitations of the chosen solvent became evident: the observed oxidations take place at the edge of the electrochemical stability window of THF at 0.5 V *vs.* Fc/Fc^+. In order to enlarge the oxidative region of the CV, MeCN was chosen as solvent. The initial decision to use THF as solvent was based on the solubility of the aryl-substituted group 14 compounds; resorting to MeCN came along with a considerably lower solubility of the samples.

The measurements, however, revealed other interesting facts. First, all CV curves showed irregularities on the upper oxidation limit in form of small current pulses. These irregular current pulses may be an indication of a passive layer that develops cracks or delaminates from the surface of the electrode during the CV scan. Second, a behaviour similar to nucleation loops for all measured samples was recorded close to the oxidation onset potentials as well as close to the potential upper limit (Figure 47). This is consistent with new phase formation, although in the two regions completely different electrochemical processes may take place. Third, the potential difference between the anodic and the cathodic sweep (the return curve) points strongly towards a dominant electrode passivation phenomenon. Fourth, the oxidation peak recorded during the cathodic (return) scan is intriguing. Such a feature may nevertheless occur whenever an electrochemical reaction is coupled with a chemical reaction that may lead to a second electroactive species. Therefore, the role of the diffusion to and from the electrode surface is likely to play a role in shaping the curves.

To complicate matters even more, at a closer inspection, it could not be excluded that the frontally aligned macro-electrodes were spatially not sufficiently separated leading to direct interactions between working- and counter-electrode. Consequently, in order to minimise such interactions, a Pt microelectrode with a diameter of 20 µm embedded in a glass mantle was used. Since the glass mantle of the microelectrode was too slender to fit seamlessly into the cell, a PTFE

sleeve was designed to seal the electrode tightly into the cell and to adjust the distance to the counter electrode if needed. Together with the use of the microelectrode a utilisation of a Faraday cage became mandatory.

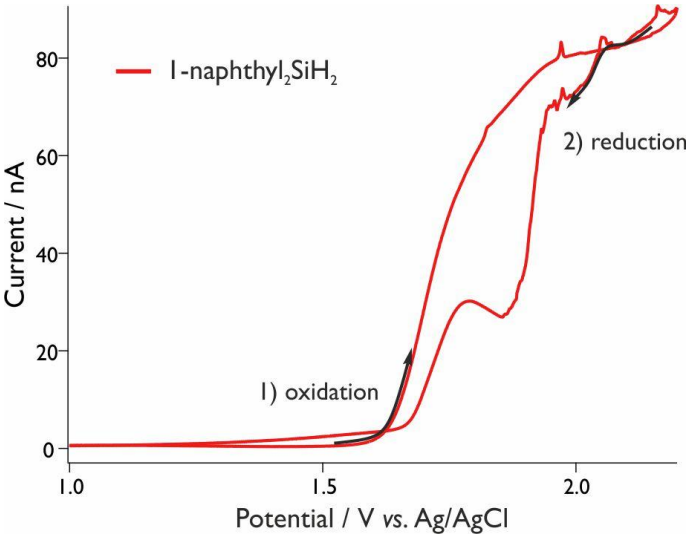

Figure 47 Typical CV measurements of 2 mM 1-naphthyl$_2$SiH$_2$ in 0.1 M TBAF solution in MeCN *vs.* Ag/AgCl at 100 mV s^{-1}. Two "nucleation loop domains" are visible at approximately 1.5 and 2.1 V. Also, small irregular current pulses recorded at higher potentials as well as indications of a passive layer build-up are present. See test for further explanations.

In order to assemble a good Ag/AgCl reference electrode, the silver wire needed to be coated with AgCl, while, in order to increase the AgCl surface, the wire was formed into a spiral before coating. Therefore, the electrode was assembled as described above, the wire was cleaned with concentrated nitric acid and deionised water, was subsequently dipped into an aqueous 0.05 M KCl solution and 3 V were applied for 10 min *vs.* a Pt counter electrode. The coated wire was washed with deionised water and subsequently dried thoroughly *in vacuo* until its use. The PEEK container was filled with 0.1 M TBACl solution saturated with AgCl and the coated silver wire was immersed (Figure 48). Using this reference electrode, several of the aryl-substituted silanes and stannanes prepared over the course of this work could be characterised.

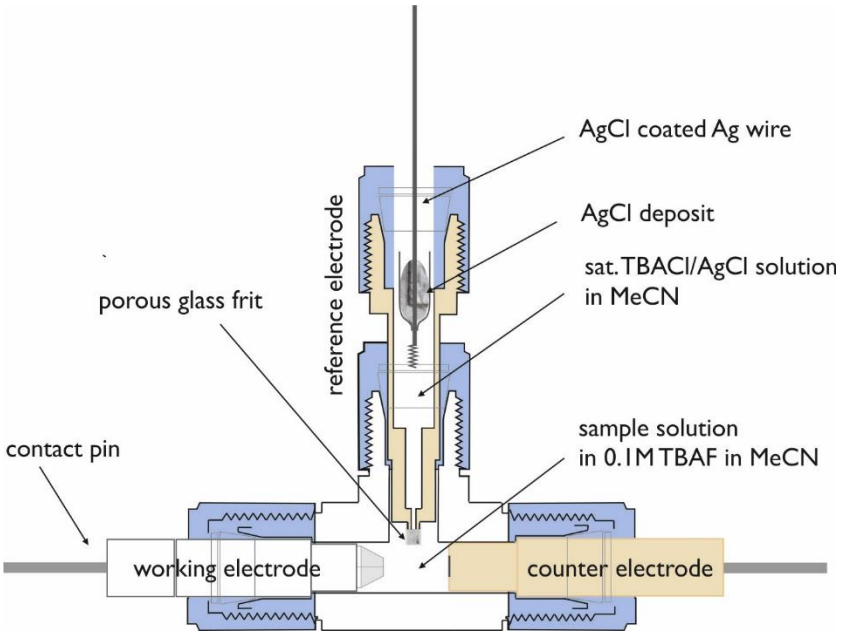

Figure 48 Modular CV cell setup with a Pt microelectrode (WE), a glassy carbon macroelectrode (CE) and a Ag/AgCl reference electrode in MeCN. The sealing of the Ag wire is omitted for clarity.

During the measurements a further problem emerged, resulting in a sloping of the base-line. Ohmic drops caused by the low conductivity of the silanes solution as well as a slow dissolving of the AgCl coating in the MeCN solution were suspected. However, the same problems recurred when the distance between the electrodes was adjusted and a freshly coated silver wire in newly prepared electrolyte solution was used. To assure a sufficient provision of Cl^- ions and contact to the former, a glass vessel was attached to the silver wire, in which AgCl was provided. Additionally, another way of sealing the silver wire was attempted: the wire was threaded into a cylindrical piece of PEEK with an outer diameter of 1/16 inch which was subsequently shrunk by heating to 120 °C and sealed tightly. Despite these efforts, no improvement of the measurements could be achieved. There are nevertheless indications that the glass frits used are unsuitable for these measurements as they clog all too easily. For instance, only after few uses the glass frits show yellow discolouration on the exposed side, a tell-tale of clogging with impurities. Nevertheless, for any future developments a compromise must be found between the leakage through the frit, which must be kept low to ensure reproducible results, and the risk of clogging, which should be, the worst case, kept moderate, if a low risk of clogging is not achievable.

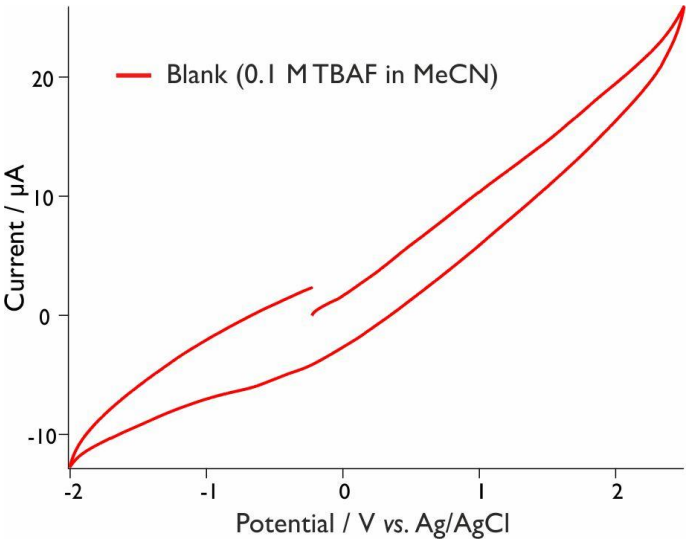

Figure 49 Sloping of the base line at the example of a 0.1 M TBAF in MeCN blank solution *vs.* Ag/AgCl at 100 mV s^{-1}.

Hereafter, a suitable Ag/AgCl reference electrode for non-aqueous systems consisting of a polychlorotrifluoroethylene (PCTFE) container, equipped with a ceramic frit, filled with AgCl and contacted with a silver wire was found and purchased from *Metrohm*. Solvent/electrolyte contact is assured by a ceramic diaphragm, the electrolyte solution may be chosen at will. We chose to use a saturated solution of TBACl and AgCl in MeCN. In order to fit into the cell, a PTFE sleeve was designed and manufactured, doubling as salt-bridge. A porous glass frit was attached to the latter with a PTFE shrink-tube and soaked in 0.1 M TBAF solution in MeCN for several days before use. Intermittently, measurements were attempted to assure the compatibility of all cell parts. However, even after one week of soaking the frit in the electrolyte and also exchanging the frit as well as the solution, no sufficient ionic contact was achievable. The most probable part to cause these issues was identified to be again the frit, which was of the same Vycor glass like the ones used before. The problems with the frit consisted of different factors, as briefly described above, one being a tendency to clog easily. In our case the slow process of dissolving AgCl from the coated wire during use and storage of the electrode led to an oversaturation of AgCl in the electrolyte solution. The therefrom resulting finely precipitating salt consequently blocked the

pores of the frit. Another factor is the brittleness of the material: the frit tends to break upon weak impacts which may occur during the assembly, leading to hard-to-clean patterns which in turn cause impurities. Despite cleaning every frit with different organic solvents before use, *i.e.* acetone, isopropanol, toluene and acetonitrile, some residues of an undisclosed surface coating seem to remain, which may be observed by a colour change to slightly yellowish when dried for several days after cleaning. Due to all of the mentioned reasons, the frit was removed for further tests and another type of diaphragm should be considered for future uses of the designed cell.

Upon removal of the frit, the reference electrode was assembled like a Haber-Luggin capillary and finally proved to work flawlessly. A scheme of the optimised cell design is shown in Figure 50. Measurements with the optimised cell were carried out in 0.1 M TBAF solution in MeCN with sample concentrations of 2 mM, each, limited by the low solubility of triaryl silanes in the organic solvent.

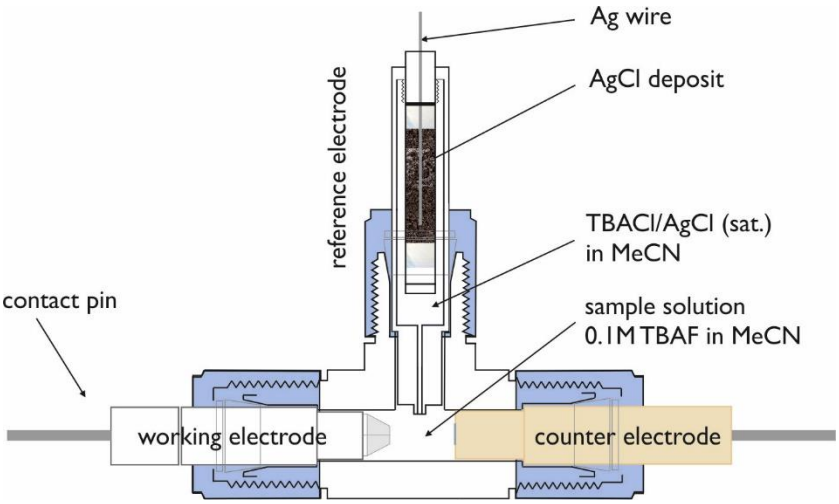

Figure 50 Optimised CV cell setup with a Pt microelectrode (WE), a glassy carbon macro-electrode (CE) and a non-aqueous Ag/AgCl reference electrode.

3.5.2.1 Summary of Cell Optimisation

In conclusion: a system consisting of a Pt micro-electrode as working electrode, a glassy carbon macro-electrode as counter electrode and a non-aqueous Ag/AgCl reference electrode using saturated TBACl and AgCl solution in MeCN housed in a *Swagelok*® PFA body was developed and successfully tested (Figure 50). The main issues in the design stemmed from complications in the sealing of the reference metal wire and from the use of nano-porous glass frits. The designed cell offers several advantages: the modular nature of the cell makes it versatile in terms of electrode choice and easy to handle, only small sample volumes of 0.6 mL are needed, it is (electro-)chemically inert, airtight, transportable and could be easily used with a cooling mantle to carry out reactions at lower temperatures.

3.6 Li-Ion Batteries

As aryl silanes are electro-active and Si has a high theoretical capacity of 4200 mAh g^{-1}, these compounds are interesting candidates for an application as anode materials in Li-ion batteries. The main focus of these investigations was on the pyrolysis products due to their particle sizes, structures and elevated silicon contents. Nevertheless, their precursor aryl silanes were tested as well.

3.6.1 Electrode Preparation

Electrode preparation is crucial for reproducible battery data. An ideal electrode consists of a current collector which is homogeneously coated with active material at even, defined film-thicknesses. Since many active materials lack sufficient adhesive properties to stick on the metal foil, an (electro-)chemically inert binder material is added to the samples. Most frequently used binder materials are composed of fluorinated polymers, *e.g.* polyvinylidene difluoride (PVdF). In order to ensure conductivity, also a certain percentage of carbon black (*i.e.* typically 4-10%wt Super C65) is added to the mixture. All components are usually dispersed in a solvent, the most common being *N*-methyl pyrrolidone (NMP), to form viscous slurries which are cast on the current collector.

In this work, different electrode preparation methods were tested and optimised for the use with organometallic compounds containing elements of group 14, *i.e.* Si and Sn. The tested methods comprised different slurry compositions as well as homogenisation techniques. The latter was tested at model graphite slurries. Reproducible data was obtained by employing previously ball-milled graphite (400 rpm, 60 min with tungsten carbide milling balls) and homogenising the slurry in a planetary ball-mill with stabilised ZrO_2 balls at 300 rpm for a total of 45 min. Electrodes prepared by this procedure deviated by approximately 6%, thus lying in an acceptable range, while the electrodes prepared from stirred slurries (12 h at 600 rpm) deviated by 25%. To prepare composite anodes from the insoluble pyrolysed silanes, the black silane component was roughly milled in a mortar and subsequently homogenised with the planetary ball-mill. Since the casting step is critical to produce homogeneous electrodes, it is discussed in detail in section 4.3.1. In a typical procedure, the silane and/or PVdF were dispersed in NMP before adding carbon black and/or graphite and milling of the slurry. Thereby, better dispersions (slurries) were obtained and the binder material was distributed more evenly.

Furthermore, the composition of the slurries varied in the aspects of active material to additive (carbon black/binder) as well as in silane to graphite ratio. Details to the tested compositions are summarised in Figure 51. The aim of this work was to enhance the capacity of the currently used graphite anode standard by using a blend of a silicon-rich phase with graphite. It was hoped that a composite might overcome the hurdle of volume expansion, while still delivering higher capacities. Therefore, graphite blanks were prepared accordingly in order to compare the composite anodes to the reference materials.

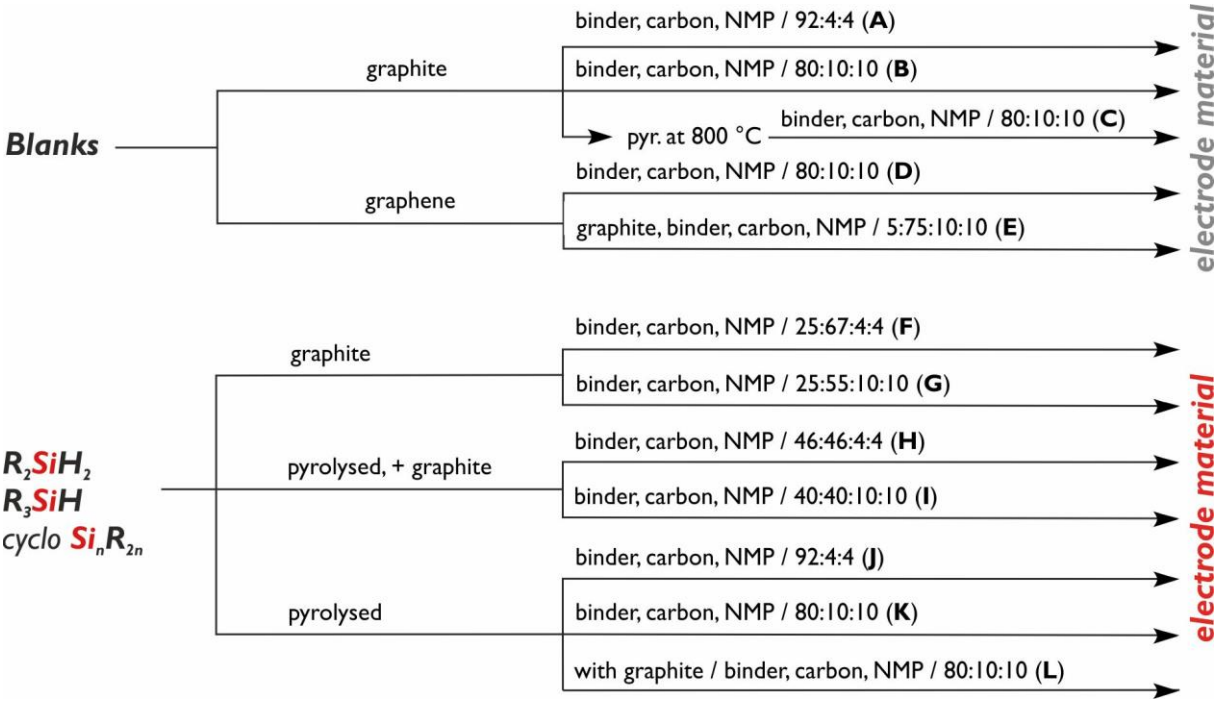

Figure 51 Routes towards electrode materials: blanks and silanes as starting materials. Hereafter, the preparation methods are referred to this figure and indicated with the respective letters.

3.6.2 Cyclic Voltammetry

Pyrolysed silanes appear as black, silicon enriched micro- or nano-sized particles with residual carbon content which are insoluble in common organic solvents (*cf.* section 3.4). Thus, an electrochemical characterisation in a classical setup was not feasible. Therefore, the electrochemical properties of these materials were determined by testing them as anodes in Li-ion battery half-cells. Therefore, composite anodes were prepared from the pyrolysed samples either with or without the addition of graphite.

Cyclic voltammetry measurements were conducted in Li-ion battery half-cells with lithium hexafluorophosphate ($LiPF_6$) in an ethylene carbonate (EC):dimethyl carbonate (DMC) 1:1 (vol.) solution as electrolyte. A potential range of 0-2 V *vs.* Li was applied. In order to monitor both fast and slow reactions occurring during the CV experiments, different scan rates, *i.e.* 0.05, 0.1, 0.2, 0.5, 1, 2, and 5 mV s^{-1}, were applied. Typical experiments started with two cycles at 1 mV s^{-1}, followed by a resting period of 12 h at open circuit voltage (OCV) and subsequent cycling at scan rates given above with two consecutive scans, each. Hereafter, all cyclic voltammetry curves are displayed normalised to the respective mass of active material.

The effect of the scan rates on the resulting CV curves is displayed in Figure 52 at the example of a graphite blank electrode. Peaks appear most distinct at the slowest applied scan rate of 0.05 mV s^{-1}, where three reversible (de-)intercalation steps are visible in the highlighted area between 0.05 and 0.25 V *vs.* Li/Li^+. This corresponds to the classical staging mechanism leading to the formation of graphite intercalation compounds. With increasing scan speeds, higher currents are observed. The aforementioned oxidation and reduction peaks broaden and overlap, leading to a single broad peak with shoulders hinting at the original peaks. Additionally, the oxidation

and reduction peaks shift apart from each other – oxidation peaks towards higher, reduction peaks towards lower potentials.

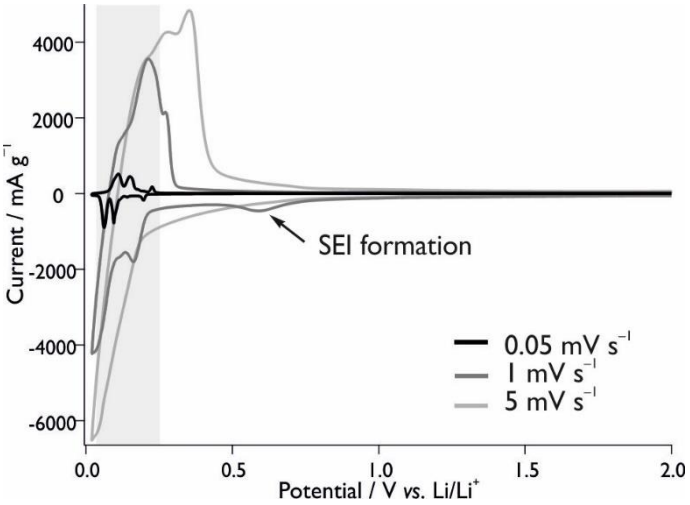

Figure 52 Effect of different scan rates on the shape of cyclic voltammetry curves at the example of graphite blanks prepared by method (**B**). Cyclic voltammetry was measured in $LiPF_6$ in EC:DMC 1:1 (vol.) *vs.* Li.

A solid electrolyte interphase (SEI) formed in all tested samples during the first cycle, at a scan rate of 1 mV s^{-1}. The respective peaks are found in the range of 0.52-0.59 V *vs.* Li/Li^+ and appear more distinct in graphite containing samples while pure silane samples display a broad shoulder.

Since the subsequent cycles lack any electrochemical response at potentials over 0.3 V *vs.* Li and no additional information could be gained from scans at faster rates, cyclic voltammetry data of the range between 0-0.3 V *vs.* Li at the slowest rate of 0.05 mV s^{-1} are used for discussion.

The graphite blank displays reversible reduction and oxidation peaks which may be assigned to the different saturation stages of the graphite with lithium ions during charge and discharge (Figure 53, black line). In total three distinct peaks are found at 0.2, 0.10 and 0.6 V (reduction/charge) and 0.10, 0.15 and 0.23 V (oxidation/discharge), along with small shoulders.

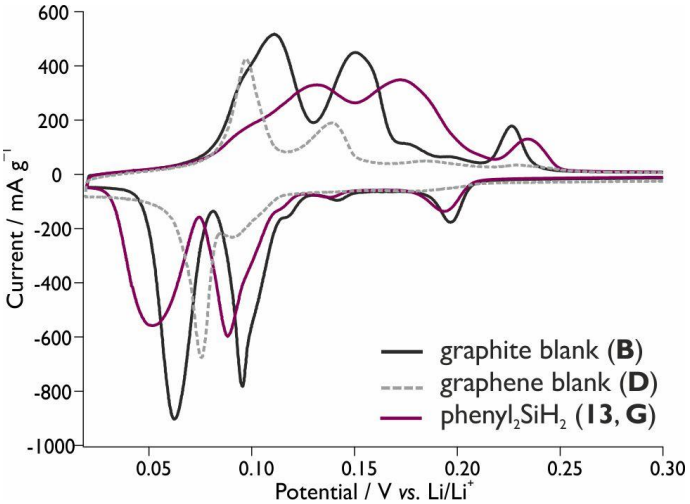

Figure 53 CV of a silane precursor composite anode compared to graphite and graphene blanks at 0.05 mV s^{-1}. Cyclic voltammetry was measured in $LiPF_6$ in EC:DMC 1:1 (vol.) *vs.* Li. The graphite and graphene blanks were prepared with 80%wt of the active materials. Preparation method **G** (*cf.* Figure 51) consisted of a 25:55%wt ratio of the arylsilane to graphite.

As expected, the same peaks are found for graphite/silane composite anodes, displayed at the example of phenyl2SiH2 (Figure 53, purple line), showing the effect of silane on the graphite

system. The influence of the silane component, however, is seen as a shift of the peaks towards lower potentials during the reduction step and towards higher potentials during oxidation, indicating a higher over-potential.

Additionally, the distinct oxidation peaks of the graphite are blurred and broadened by the silane, possibly caused by the inductive effect of the silane as discussed in section 0 or by coating of the graphite with the less electroactive silane component.

Regarding the graphene blank (Figure 53, grey dotted line), fewer peaks are determined than for the graphite blank. During reduction only a shoulder hinting at the comparable graphite peak at 0.10 V and one distinct peak at 0.08 V are present, while peaks in the region of 0.20-0.25 V are missing completely. This is possibly caused by the reduced symmetry of the graphene lattice upon recombining after the exfoliating in an organic solvent (*cf.* Figure 53). Typically, intercalation of lithium ions into the graphite lattice of an anode during the charging step occurs at the edges and imperfections of the substrate, after which a redistribution takes place. Thereby, defined LiC_x phases are formed, namely LiC_{72}, LiC_{12} and the (ideally) fully lithiated phase LiC_6.

A different substituent pattern on the silicon atom has some effects on the electrochemical potentials (Figure 54). In contrast to the results found in section 0, the successive exchange of phenyl with 1-naphthyl groups did not result in consequent lowering of the oxidation potentials as seen in the classic CV approaches. While the oxidation peaks of 1-naphthyl$_2$SiH$_2$ (**16**) are shifted towards lower potentials as compared to phenyl$_2$SiH$_2$ (**13**), the peaks of 1-naphthyl(phenyl)SiH$_2$ (**15**) are shifted slightly towards higher potentials (*e.g.* 0.17 V (**13**) → 0.16 V (**16**) → 0.18 V (**15**)).

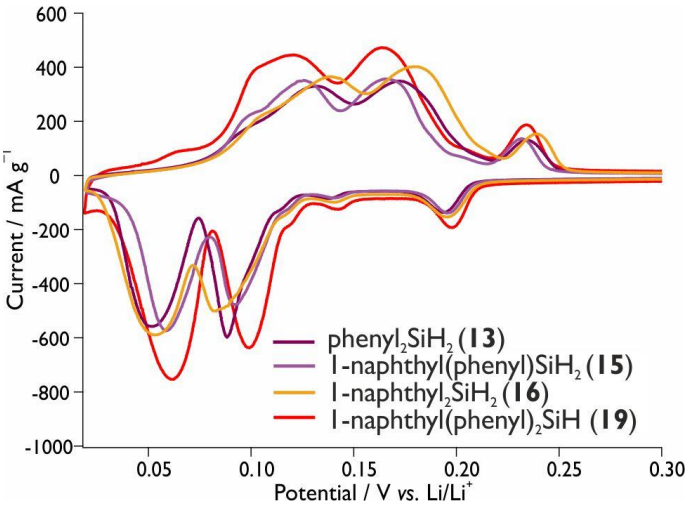

Figure 54 CV of differently aryl-substituted diarylsilane composite anodes compared to an asymmetrically substituted triarylsilane composite anode at 0.05 mV s^{-1}. Cyclic voltammetry was measured in $LiPF_6$ in EC:DMC 1:1 (vol.) *vs.* Li. All samples were prepared with a 25:55%wt of silanes to graphite ratio (*cf.* Figure 51, method **G**).

The asymmetrical nature of compound **15**, was compared to the equally asymmetrical 1-naphthyl(phenyl)$_2$SiH (**19**). The latter displays the anticipated shift of the oxidation peaks towards lower potentials, as well as clearly broadened peaks caused by the increased steric demand of the aromatic substituents. Since the observed peaks correspond to the ones found for pure graphite, a complete blocking of graphite active sites inhibiting its storage capacity of lithium ions can be excluded. The effect of the silanes, however, is seen by broadening and blurring of the prevalent reduction/oxidation peaks in the range of 0.05-0.18 V. Considering that

the pure silanes are electricall insulating compounds, this effect is unsurprising. The anomalous behaviour of compound **15** remains to be fully understood.

The particles formed by pyrolysis of the precursor silanes were tested as composite anodes with or without adding graphite. Some examples of the resulting curves are displayed in Figure 55. When embedded in a graphite matrix, the same effects as for the precursor materials are evident with oxidation/reduction peaks stemming mainly from the (de-)intercalation of lithium ions into graphite (Figure 55, a)). With respect to the different temperatures at which the samples in **a)** were treated, only marginal differences are noticeable. A slight shift of the reduction peaks assigned to phenyl$_{10}$Si$_5$ pyrolysed at 800 °C towards higher potentials as well as overall higher currents found for this sample are possibly caused by the morphology of the particles or their distribution within the electrode.

Examples for the electrochemical behaviour of the silanes without addition of graphite is displayed in Figure 55, b). All of the pyrolysed samples undergo a reduction close to 0 V and show partial reversibility in form of an oxidation peak at 0.12 V emerging for the pyrolysed 1-naphthyl$_3$SiH and broader shoulders for other samples. Of all tested silane particles, the ones obtained from the cyclic silane phenyl$_{10}$Si$_5$ treated at 800 °C displayed the highest electroactivity.

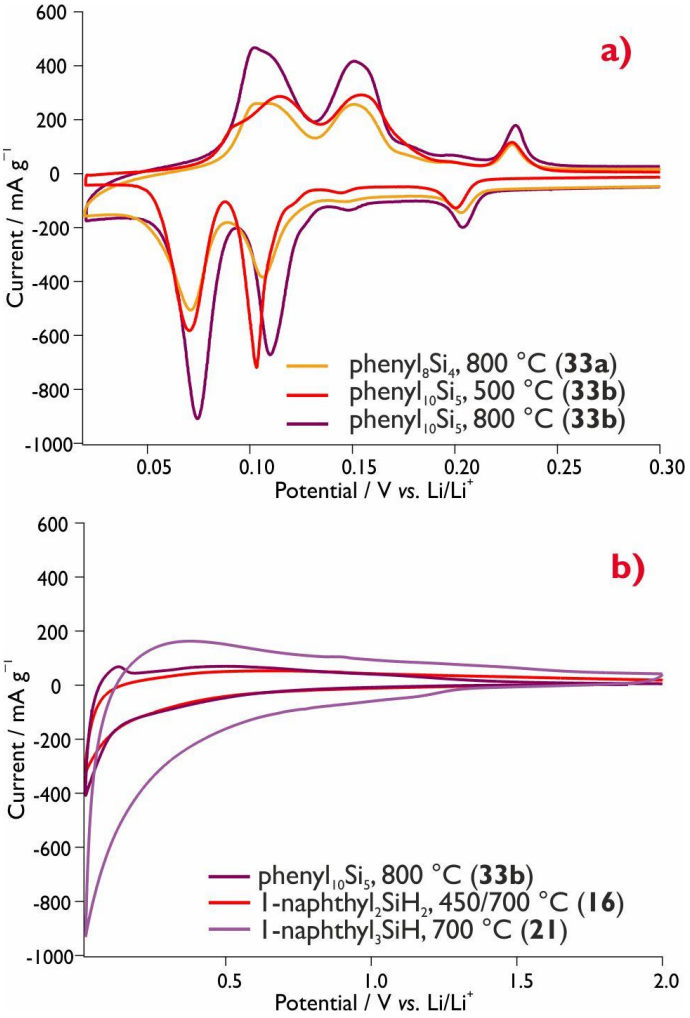

Figure 55 CV of pyrolysed silane composite anodes with (a)) and without (**b)**) addition of graphite at 0.05 mV s^{-1}. Cyclic voltammetry was performed in $LiPF_6$ in EC:DMC 1:1 (vol.) *vs.* Li. Electrodes used in these experiments were prepared **a**) with a pyrolysed silanes-to-graphite ratio of 46:46%wt (*cf.* Figure 51, method **H**) and b) with 80%wt of the pyrolysed silanes (method **K**). Residual percentage up to 100%wt consisted of equal parts carbon black and binder.

In conclusion: all of the tested silanes are affecting the electrochemical potentials of a graphite anode by means of potential shifts and broadening of the specific reduction/oxidation peaks. The effects on the cycling behaviour are less distinct as in classical cyclic voltammetry (*cf.* section 3.5.1). Anodes prepared from pyrolysed silanes without addition of graphite display only partial reversibility. However, when mixed with graphite the oxidation/reduction processes of the latter are not impaired.

3.6.3 Galvanostatic Cycling with Potential Limitation (GCPL)

Encouraged by the CV results also constant current cycling experiments (GCPL) were performed with which the specific anodic capacities could be determined.

In a typical experiment, a half-cell was cycled at a C-rate of C/2 for 100 cycles. The active material consisted of either the silane component or mixtures of silanes with graphite. Details for the electrode compositions are summarised in Figure 51. At least three electrodes of the respective compositions were tested in order to assure the reproducibility. Regular experiments recorded 100 cycles to determine the long–term stability of the specific capacities reached. The capacities were compared to those of a graphite composite electrode, further referred to as blank.

3.6.3.1 Graphite and Graphene Blanks

Blank graphite anodes were prepared for optimising of the electrode preparation as well as for reference purposes. Therefore, two different compositions were chosen, consisting of graphite:binder:carbon black ratios of 92:4:4%wt (**A**) and 80:10:10%wt (**B**), respectively. In a series of experiments 10 electrodes, each, were tested in order to determine reproducibility. All slurries were prepared by the aforementioned method and the maximum error between all of the tested electrodes was determined to be 6%, therefore lying within an acceptable range.

Electrodes prepared according to method **B** (Figure 56) gave specific anodic capacities of averagely 360 mAh g^{-1} which is remarkably close to the maximum theoretical capacity of fully lithiated graphite with 375 mAh g^{-1}. Additionally, a coulombic efficiency of averagely 99% was achieved. These excellent results were reproduced at two different occasions and are therefore deemed reliable.

Similar results could be obtained for a series of graphene blanks obtained by exfoliated graphite in THF. However, the graphene capacity decays in the observed cycling range, which leads to an overall coulombic efficiency of 97% (Figure 56).

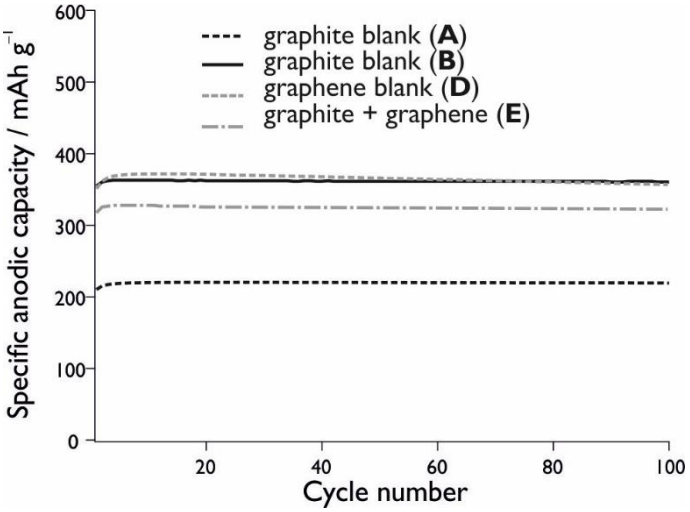

Figure 56 Specific anodic capacities of graphite and graphene blank electrodes determined by GCPL experiments. Measurements were carried out in $LiPF_6$ in EC:DMC 1:1 (vol.) *vs.* Li. (**A**) was prepared with 92%wt, (**B**) with 80%wt graphite. For sample (**D**) the electrodes contained 80%wt of pyrolysed graphite. In (**E**) 5%wt graphene were added to 75%wt graphite. A more detailed overview of the preparation methods is given in Figure 51.

Considering the introduction of a silane into the anode materials, partial coating of the graphite component by the silane may not be excluded as seen in the cyclic voltammetry. Therefore, another attempt aimed at the incorporation of the silane between graphene sheets by mixing exfoliated graphite sheets in a suspension of THF with the silane and subsequently mixing the dried composite with graphite. The accordingly prepared blank (method **E**) is displayed in Figure 56, amounting to average specific anodic capacities of 325 mAh g^{-1} and displaying coulombic efficiencies of up to 99%.

3.6.4 Precursor Materials

Di- and triaryl silanes (**13**, **15**, **16**, **19** and **20**) as well as the cyclic perphenylated silanes (**33a/b**) were tested as additives to graphite anodes in different ratios. Preliminary works in our group found that a ratio of 4%wt binder/carbon black yielded the most reproducible cells. Therefore, initial experiments were carried out with silane:graphite:binder:carbon black ratios of 25:67:4:4%wt (preparation method **F**). The resulting specific anodic capacities for differently substituted silane precursor materials are shown in Figure 57, a). Compared to the respective graphite blank, the tested precursor materials display lower capacities with deviations between 23% (phenyl$_2$SiH$_2$, **13**) and 40% (phenyl$_{10}$Si$_5$, **33b**). The only exceptions are anodes containing 1-naphthyl(phenyl)SiH$_2$ (**15**), which exceed the blank by 12%, amounting to 246 mAh g^{-1}.

Considering this unexpected result, the influence of compound **15** was tested in another composition. Therefore, 10%wt binder/carbon black, each, was taken into account. The amount of silane remained the same and the one of the graphite component was reduced (25:55:10:10%wt, preparation method **G**). The resulting capacities are shown in Figure 57, b). Compared to the respective blank, the specific anodic capacities of 1-naphthyl(phenyl)SiH$_2$ deviate by 11% and amount to 322 mAh g^{-1}. Even though the silane did not emerge as the desired capacity enhancing material, overall higher capacities and lower deviations (7-17%) could be achieved by employing preparation method **G**, as shown in Figure 57, c).

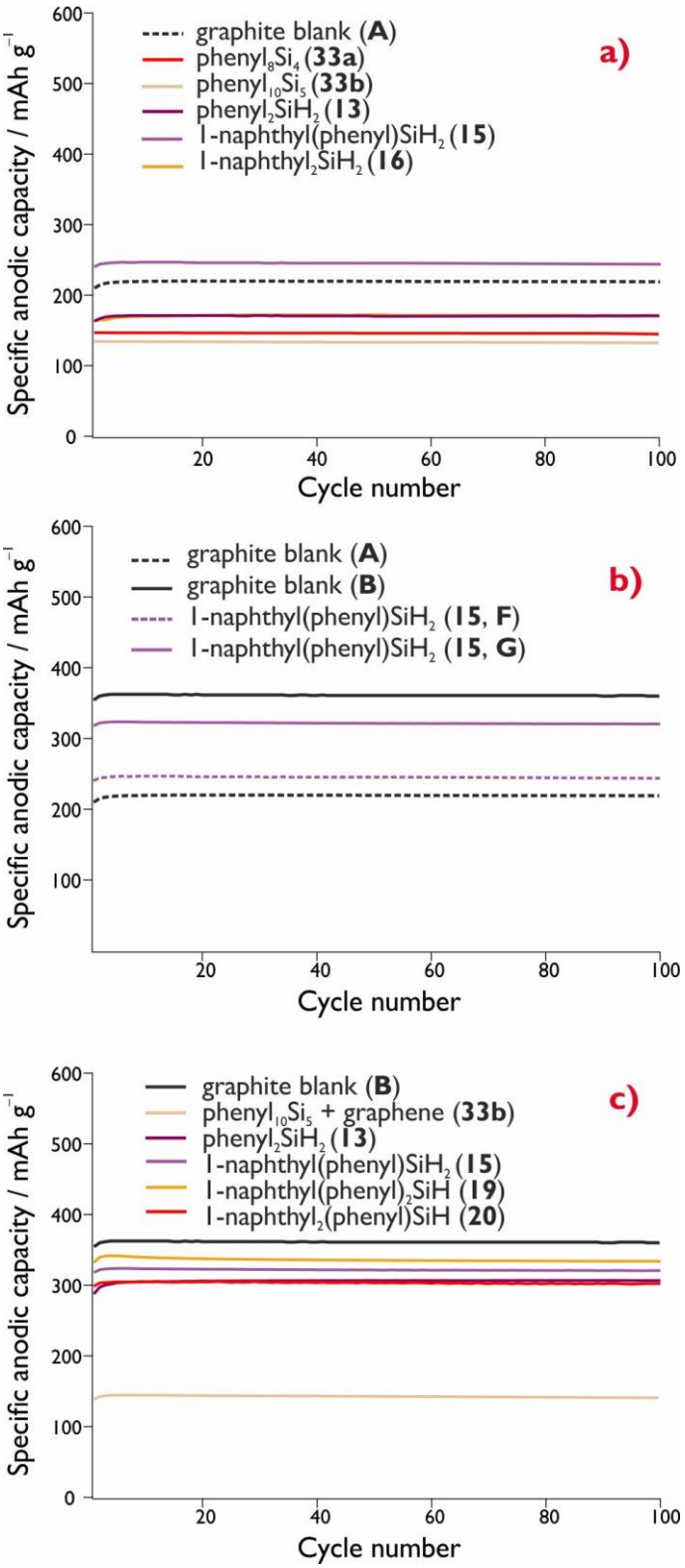

Figure 57 Specific anodic capacities (reversible capacity) of precursor silanes determined by GCPL experiments. Measurements were carried out in $LiPF_6$ in EC:DMC 1:1 (vol.) *vs.* Li.
a) Active material ratios of 25%wt silane, 67%wt graphite and 4%wt binder and carbon black, each, were employed (method **F**, *cf.* Figure 51). (**A**) represents a blank with 92%wt graphite.
b) Comparison of specific capacities of 1-naphthyl(phenyl)SiH_2 at different active material ratios (methods **F** and **G**) (determined by GCPL experiments. (**B**) represents a blank with 80%wt graphite.
c) Active material ratios of 25%wt silane, 55%wt graphite and 10%wt binder and carbon black, each, were employed (**G**).

When graphene was added to compound **33b**, however, the capacity dropped to 143 mAh g^{-1}. In order to investigate this occurrence, electrodes prepared by method **F** were subjected to SEM-EDX as well as Raman-SEM spectroscopy. The resulting pictures, shown inFigure 58, shed light on the issues: despite several attempts to distribute the precursor material homogeneously in the graphite, crystalline junks of silane are found on and near the electrode surface. These cause an insulating effect on the graphite overall by blocking attack sites for lithium intercalation.

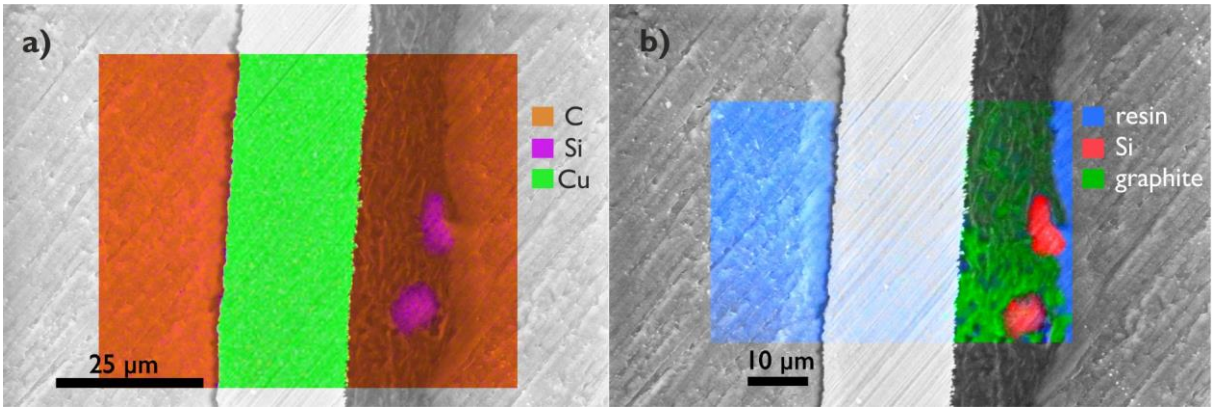

Figure 58 a) SEM-EDX b) Raman-SEM pictures of a resin-embedded silane anode (phenyl$_{10}$Si$_5$ (25%wt), graphite (67%wt), binder/carbon black (4%wt, each)).

3.6.4.1 Pyrolysed Materials

3.6.4.1.1 Pyrolysed Materials with Graphite

An objective of this work was the investigation of silicon enriched particles created by pyrolysis of precursor silanes. Therefore, different silanes were pyrolysed at different conditions, varying in temperature, dwell time as well as gas-flow and heating rate during pyrolysis (*cf.* section 3.4). The resulting particles were tested in Li-ion battery anodes. In this section, the different approaches to create composite anodes with pyrolysed silanes are summarised.

The main focus was set on the pyrolysed cyclic compounds phenyl$_8$Si$_4$ and phenyl$_{10}$Si$_5$ (**33a/b**), due to their comparably high silicon content (28%wt) as well as their facile synthesis and handling. Nevertheless, also pyrolysed monosilanes, *i.e.* 1-naphthyl$_2$SiH$_2$ (**16**) and 1-naphthyl$_3$SiH (**21**), were investigated.

Initial experiments investigated the effect of the pyrolysis temperature, morphology and particle size on the cycling behaviour. In analogy to the precursor materials, electrodes were prepared with 4%wt binder and carbon black. However, the insoluble particles required adapting a different electrode preparation method: the materials were ground in a mortar and subsequently mixed with dissolved PVdF in NMP, carbon black as well as graphite and homogenised *via* ball-milling. In these experiments, an equal amount of graphite and pyrolysed silane were employed. The resulting curves for **33a** and **b,** pyrolysed at different temperatures, predetermined by TGA/DSC are shown in Figure 59.

Among the tested substances, compound **33b** pyrolysed at 800 °C (with 20 °C min^{-1} heating rate, 2 L min^{-1} gas flow, 2h dwell time) displays a remarkably high average specific capacity of 440 mAh g^{-1}. It exceeds the accordingly prepared graphite blank by 100%. These promising results mirror the high currents observed in the CV experiment for this sample (*cf.* Figure 55, a)).

The other samples show capacities similar to the one of the respective graphite blank prepared by method **A**. However, a tendency towards higher capacity may be noted for both the four- and five-membered silicon ring systems pyrolysed at 850 °C for **33a** and 800 °C for **33b**, respectively. This may be caused by remaining aryl groups abstracted from the silicon atoms during the pyrolysis process, which are trapped in the bulk and thus not able to evaporate. These residual aryl moieties are likely to arrange in a symmetrical order allowing for the storage of lithium ions during charging of the battery (*cf.* section 3.4). This assumption is further reinforced by the fact that the pyrolysed samples show a noteworthy cycle stability with coulombic efficiencies ranging between 97 and 99%.

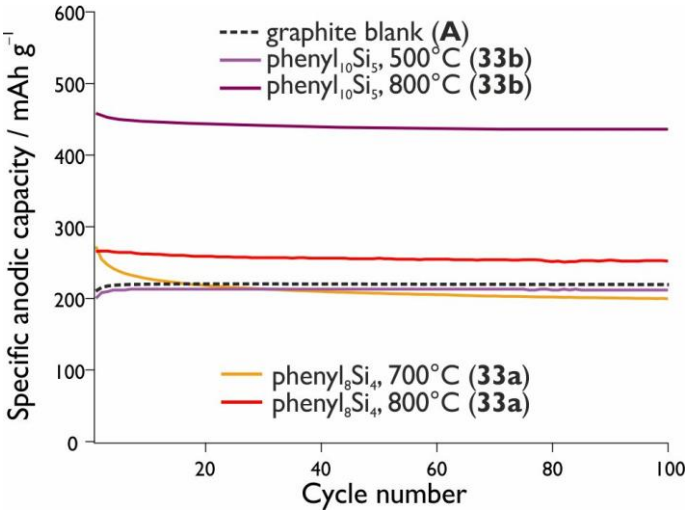

Figure 59 Specific anodic capacities determined by GCPL experiments of $phenyl_{2n}Si_n$ samples pyrolysed at different temperatures. 46%wt silane, 46%wt graphite, 4%wt binder/carbon black, each. Electrodes used in these experiments were prepared with a pyrolysed silanes to graphite ratio 46:46%wt (preparation method **H**, *cf.* Figure 51). (**A**) represents a blank with 92%wt graphite. Residual percentages consisted of equal part of carbon black and binder.

3.6.4.1.2 Pyrolysed Materials without Graphite

Encouraged by the high capacities of the pyrolysed five-membered ring (**33b**, at 800 °C), the interest in the capacity of the pure material without the influence of graphite arose.

However, the first electrodes with 92% silane prepared according to method **J** showed capacities of averagely 205 mAh g^{-1} (Figure 60, red line). This unsatisfactory result is explained by insufficient adhesion of the active material to the surface of the current collector. This led to optically detectable uncovered patches on the electrode where the active material lost contact during cycling. All subsequent experiments were therefore carried out with 10% binder and carbon black, each, to ascertain adhesion between the active material and the current collector (method **K**).

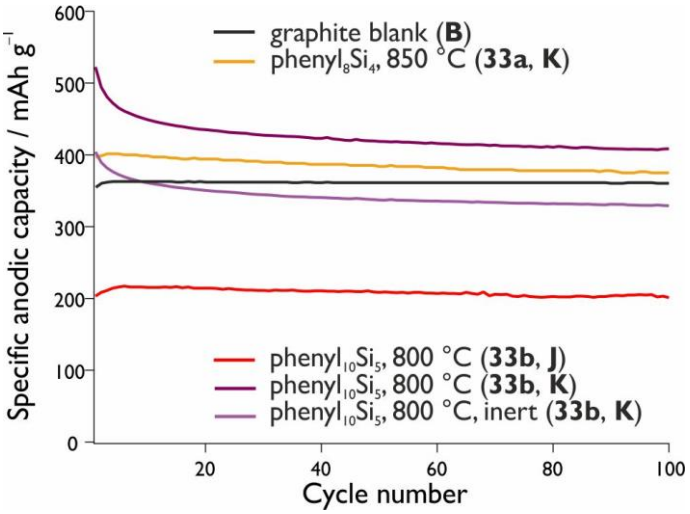

Figure 60 Specific anodic capacities determined by GCPL experiments, showing effects of air-exposure of the pyrolysed phenyl$_8$Si$_4$/phenyl$_{10}$Si$_5$ samples during electrode preparation. 80%wt silane, 10%wt binder/carbon black, each (preparation method **K**, *cf.* Figure 51). The sample prepared according to method **J** consisted of 92%wt of the pyrolysed silane.

With this new method, compound **33b** pyrolysed at 800 °C showed the highest measured capacities of 425 mAh g^{-1} in average. This corresponds to an improvement of 17% compared to the respective graphite blank. Similar results were obtained for the pyrolysed four-membered ring (**33a** at 850 °C) with capacities of averagely 387 mAh g^{-1} over the first 100 cycles. Along with the reduced amount of carbon in the sample, a rapid capacity decay was anticipated. However, the samples contained enough carbon to mediate the volume expansion of the silicon during the charging step and show coulombic efficiencies of 98.7% (**33b**) and 98.9% (**33a**), respectively.

The pyrolysed silane samples are prone to adsorption of oxygen when stored under air (*cf.* section 3.4). The influence of this adsorption was investigated by preparing a series of electrodes under strictly inert conditions. Details for this procedure are discussed in section 4.3.1 (page 92). Thereby created electrodes showed a similar progression as the ones created under air, however, at lower capacities of averagely 352 mAh g^{-1} and thus falling below the graphite blank by 3%. The lowered capacities are most likely caused by the complicated electrode preparation under inert conditions. Therefore, the following experiments were carried out under ambient conditions.

3.6.4.1.3 Interdependence between Pyrolysis Conditions, Morphology and Performance

Further experiments focused on the effects of different pyrolysis procedures and thereby resulting morphologies on the performance of the particles in Li-ion battery anodes.

Initial investigations focused on the morphologies obtained when the sample is placed in a cold oven (**I**), in an oven pre-heated to 800 °C (**II**) or in an oven pre-heated to 450 °C with subsequent heating to 800 °C (**III**). The latter two approaches resulted in similar specific anodic capacities of 290 and 266 mAh g^{-1}, respectively (Figure 61, orange and red lines). These values are well below the average capacity of the sample prepared according to the first approach (440 mAh g^{-1}).

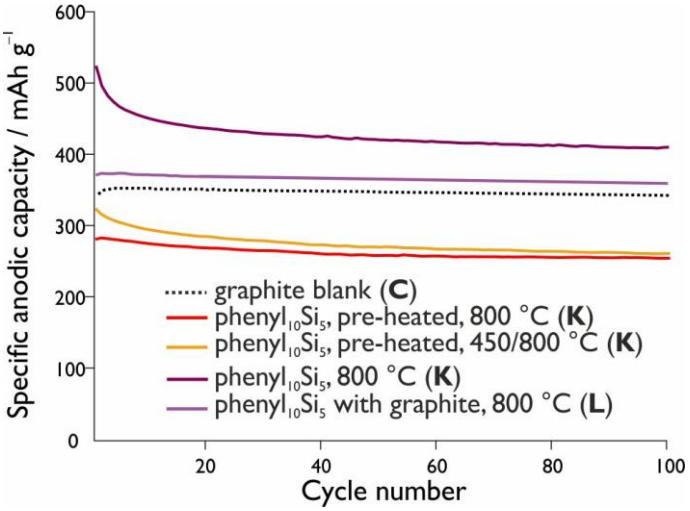

Figure 61 Specific anodic capacities of pyrolysed phenyl$_{10}$Si$_5$ (**33b**) samples following different pyrolysis protocols. Measurements were carried out in $LiPF_6$ in EC:DMC 1:1 (vol.) *vs.* Li. The electrodes were prepared with 80%wt pyrolysed silane (method **K**, *cf.* Figure 51). Electrodes prepared according to method **J** consisted of 80%wt of **33b** pyrolysed together with graphite. (**C**) represents a blank of pyrolysed graphite.

This lower capacity is possibly caused by the morphology of the amorphous particles. In contrast to the usual procedure, which results in edged particles, the sudden change in temperature upon placing the samples in the pre-heated oven leads to spherical particles covering the usual edged ones (*cf.* section *3.4*). These are likely to encapsulate partially cleaved silanes and thereby offer less intercalation sites for lithium ions during charging. Another explanation might be related to the binder efficiency, which could be significantly lower for particles with a smoother surface. An example of a silane electrode prepared by step-wise heat treatment was imaged by SEM spectroscopy (*cf.* Figure 62). The uncycled electrode (a) displays the edged particles covered by the much smaller spherical particles mixed with carbon black and gives an idea of the course nature of the particles. Figure 62, b) shows the electrode recovered after the GCPL experiments. The volume expansion caused by lithium intercalation into silicon leads to a smoothening of the particle edges as well as a more homogeneous surface morphology.

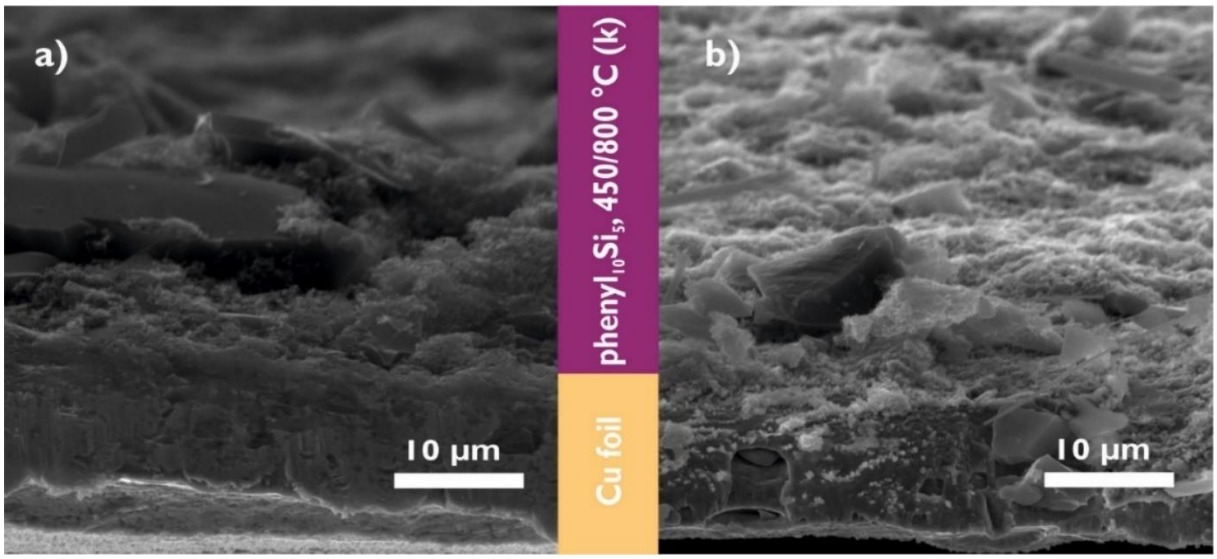

Figure 62 SEM images of cross-sections of an anode (80:10:10%wt) of step-wise pyrolysed phenyl$_{10}$Si$_5$ (450/800 °C). a) uncycled, b) after cycling (GCPL).

The next series of experiments was devoted to investigate the distribution of the pyrolysed silane. To this end, a mixture of graphite and silane was pyrolysed. Therefore, the precursor silane was

dissolved in THF, mixed with graphite in a mass ratio of 1:1, dried *in vacuo* and subsequently pyrolysed at 800 °C using the standard parameters (heating rate: 20 °C min^{-1}, gas flow: 2 L min^{-1}, dwell time: 60 min). The resulting bulk was mixed with 10%wt binder and carbon black, each. Electrodes prepared by this method yielded stable capacities of 370 mAh g^{-1} and are therefore 3% above the capacities of the respective graphite blank (Figure 63). The latter was prepared from graphite pyrolysed at the same conditions, yielding an average specific capacity of 351 mAh g^{-1}.

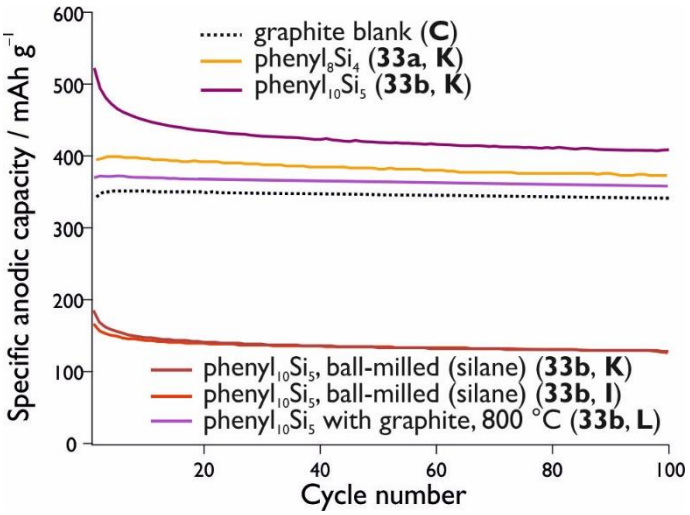

Figure 63 Specific anodic capacities of pyrolysed silanes in milled and unmilled form. Measurements were carried out in $LiPF_6$ in EC:DMC 1:1 (vol.) *vs.* Li. The respective electrons were prepared according to preparation methods **I** (40%wt pyrolysed silane and graphite, each), **K** (80%wt pyrolysed silane) and **L** (80%wt of a pyrolysed silane/graphite mixture). Details are given in Figure 51. (**C**) represents a blank of pyrolysed graphite.

The graphite seems to be only minimally affected by the thermal treatment, which was also confirmed by SEM spectroscopy (Figure 64, a)). The overall effect of the silane on the pyrolysed graphite may be seen in SEM images of the sample (Figure 64, b)).

Compared to the pure pyrolysed graphite, the silane containing composite material prepared according to method **J** shows agglomerations of larger graphite flakes, most likely adhered by the silane component. Considering the performance of the materials, the capacities for the latter exceed the respective blank by 6%. However, they are still outperformed by samples prepared according to the first approach.

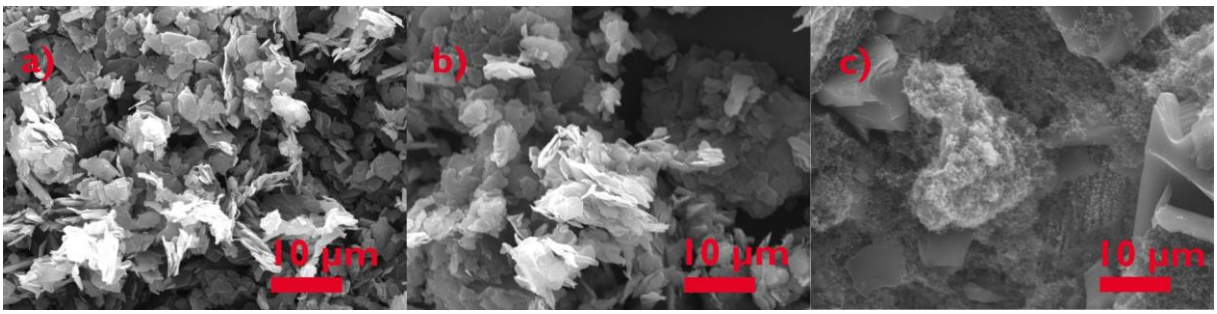

Figure 64 SEM images of a) graphite and b) graphite mixed with $phenyl_{10}Si_5$. c) surface of a neat pyrolysed $phenyl_{10}Si_5$ electrode. All samples were pyrolysed at 800 °C with a heating rate of 20 °C min^{-1}, a gas flow of 2 L min^{-1} and a dwell time of 60 min.

Another way to force intermixing of silane and graphite is ball-milling. Therefore, either the plain silane particles (**K**) or a mixture of silane particles with graphite (1:1 wt, **J**) were ball-milled in a tungsten carbide beaker before adding the remaining ingredients. Both of these samples surprisingly result in almost the same curves, regardless of the amount of graphite added to the mixture (Figure 63). The average anodic capacity amounts to 156 mAh g^{-1} in both samples.

This behaviour indicates that an essential structure for the interaction between lithium ions and silicon was destroyed by the mechanical stress applied by the ball-mill. Originally, the physical appearance of the pyrolysed silanes could be compared to a pumice or an amorphous sponge. It is very likely that the residual aromatic groups in the samples, regardless if attached to the silicon atom or not, are forming a structure allowing for intercalation of lithium ions as well as a contact to the silicon atom. The surrounding organic structure seems to be able to mitigate the volume expansion and contact loss. The ball-milling destroys the (layered) structure, which is vital for Li-ion storage.

These findings are further corroborated by cyclic voltammetry (Figure 65), which allows to follow the intercalation and deintercalation of lithium ions into/from the active material. The intercalation steps are best seen at the example of a graphite blank: the step-wise lithiation of the graphite is seen by plateaus in voltage, which correspond to the LiC_x phases already discussed for cyclic voltammetry experiments.[203] Regarding the pyrolysed samples (purple line), broad shoulders hint at a similar intercalation behaviour, however less defined. The ball-milled, pyrolysed sample (orange line) lacks any indication of staged intercalation.

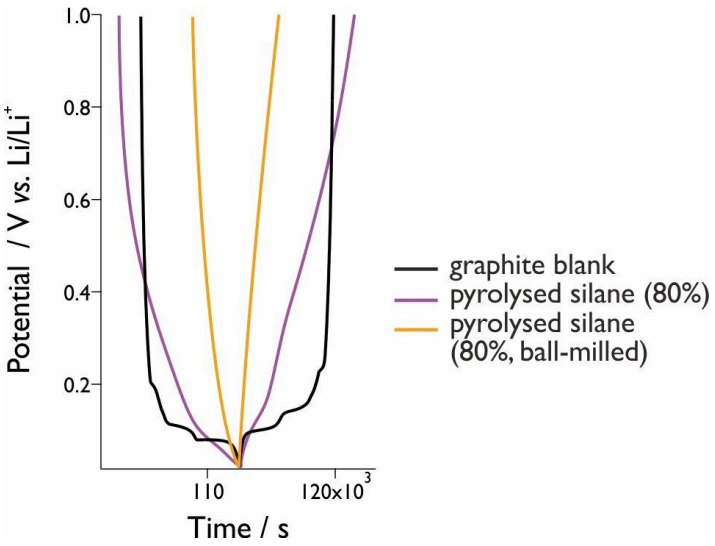

Figure 65
Lithium intercalation potentials of graphite and pyrolysed silanes.

To study the varying silicon content, other silanes, *i.e.* pyrolysed 1-naphthyl$_2$SiH$_2$ (**16**, 42%wt Si[1]) and 1-naphthyl$_3$SiH (**21**, 30%wt Si[1]) were tested; their cycling behaviour is shown in Figure 66. For these samples a higher capacity was expected due to the overall higher silicon content with for compound **16** and for compound **21** as compared to the phenylated silane rings (28%wt). However, for both samples rather low anodic capacities were determined, amounting to 229 mAh g^{-1} (**16**) and 128 mAh g^{-1} (**21**), respectively. This indicates that in samples containing 1-naphthyl moieties, a structure necessary for lithium (de-)intercalation is formed, however not as efficiently as with the smaller phenyl residues. Nevertheless, despite the unsatisfying performance of pyrolysed monosilanes, all samples displayed a remarkable cycle stability and may thus be interesting for further research.

[1] Determined by elemental analysis of the respective samples.

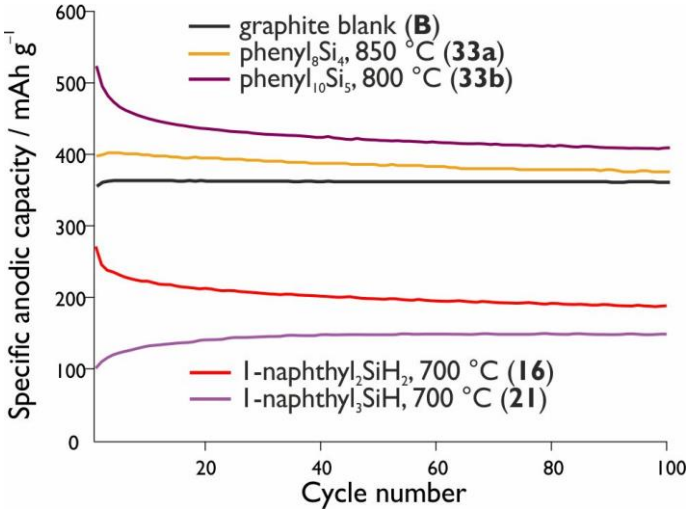

Figure 66 Specific anodic capacities of pyrolysed aryl silanes (80:10:10) determined by GCPL experiments. Measurements were carried out in $LiPF_6$ in EC:DMC 1:1 (vol.) *vs.* Li. All electrodes were prepared with 80%wt of the respective pyrolysed silane. (**B**) represents a blank with 80%wt graphite.

In summary, it was found that the morphology has a much larger influence on the cycling performance than the overall silicon content. The morphology provides intercalation sites for lithium ions, which could not be enhanced by pyrolysis of the silane directly in a graphite matrix. The structures vital for the lithium intercalation are destroyed by ball-milling and are directly influenced by the pyrolysis protocol, especially by the heating and gas flow rate (*cf.* section 3.4).

3.6.5 Summary of Li-Ion Batteries

Electrochemical characterisation of the precursor aryl silanes as well as of pyrolysed particles derived from aryl silanes was carried out by cyclic voltammetry and constant current cycling (GCPL) experiments in Li-ion battery half-cells. Different electrode preparation methods as well as different compositions were tested. Composite anodes created with the precursor materials and graphite resulted in broader oxidation/reduction peaks in CV experiments and lower specific anodic capacities compared to a respectively prepared graphite blank. This is most likely caused by coating of the graphite component by the silane, partially inhibiting lithium ion (de)intercalation during charge/discharge.
Similar to the behaviour observed in cyclic voltammetry of the pure silanes in MeCN, the oxidation peaks shift towards lower potentials along with the successive exchange of a phenyl substituent on the silicon atom by a 1-naphthyl group.

The highest specific anodic capacities of averagely 440 mAh g^{-1} were achieved by composite anodes containing pyrolysed phenyl$_{10}$Si$_5$ (46%wt) equal amounts of graphite (46%wt) and 4%wt binder/carbon black, each. The pyrolysis of the silanes was carried out at 800 °C with a heating rate of 20 °C min^{-1}, gas flow of 2 L min^{-1} and a dwell time of 60 min. Capacities in the same range could also be obtained from electrodes prepared with 80%wt of the same pyrolysed silane and 10%wt, each, of binder/carbon black, amounting to 425 mAh g^{-1}. The electrochemical performance does not solely depend on the effective silicon content. Instead, it strongly depends on the structure/morphology of the pyrolysed silane. Additionally, the structure enables contact of the lithium ions to the silicon while mitigating the volume expansion of the latter upon lithiation. This leads to a stable cycling behaviour with coulombic efficiencies of 98-99% and the comparatively high capacities.

3.7 Summary of Silanes

The present work aimed for the synthesis and comprehensive characterisation of novel or incompletely characterised, literature-known aryl silanes, as well as for the investigation of their reactivity and prospective applications.

Therefore, several mono-, di- and triaryl(chloro)silanes were synthesised with varying steric bulk of the aromatic system. The employed aryl groups consisted of phenyl, 1-naphthyl or 2,5-xylyl moieties. Depending on the number of desired aryl-substituents on the silicon atom, the aryl(chloro)silanes could be synthesised either *via* reaction of the corresponding chlorosilane $SiCl_4$ or $phenyl_nSiCl_{4-n}$ (n = 1-2) with arylMgBr or arylLi reagents. With respect to di- and triarylated compounds, a focus was set on species with mixed substituents, *i.e.* 1-naphthyl and phenyl. The aryl(chloro)silanes were used as educts for the preparation of either 1) the respective hydrogen-rich aryl silanes (compounds **10**-**21**), 2) triaryl(allyl)silanes (compounds **22**-**25**) or 3) mixed-substituent tetraarylsilanes and cyclic phenylated silanes (compounds **30**-**33**). All compounds were characterised by ^{29}Si NMR, showing trends of the chemical shift corresponding to the substituents. Crystal structures of these compounds displayed Si–C bond lengths in the expected range of 1.844-1.889 Å, which is in agreement with values reported in literature.[6] Stabilising effects like of Van-der-Waals (C–H···Cl or Si–H···Si), edge to face and/or π-π stacking interactions were found in mono-, di- and triaryl silanes. The latter, however, are much less likely to occur with increasing numbers of aryl substituents.

Furthermore, the reactivity of triaryl(allyl)silanes (**22**-**25**) was investigated *via* iEDDA reactions with tetrazines in THF. These resulted in novel silanes, where the terminal olefin of the allyl group is implemented into the ring system of the pyridazine under nitrogen abstraction. The products (**26**-**29**) could be identified using ^{1}H, ^{13}C and ^{29}Si NMR spectroscopy, as well as with 2D HSQC and HMBC spectra. A single crystal of compound **29** elucidated the structure of the products. Additionally, UV-Vis kinetic measurements in toluene assessed their first order reaction rates (k) to be in the same range as the ones of styrene with $k_{26\text{-}29} = 3.95 \times 10^{-3}$ - 9.01×10^{-4} $M^{-1}\ s^{-1}$ and $k_{styrene} = 3 \times 10^{-3}\ M^{-1}s^{-1}$. The found reactivity of triaryl(allyl)silanes with tetrazines opens new application possibilities in the field of surface functionalisation or polymerisation.

For the planned application in Li-ion batteries, aryl silanes were electrochemically characterised by cyclic voltammetry in a non-aqueous system using MeCN as solvent in a purpose-built CV cell. The oxidation potentials of the aryl silanes are located around 2 V *vs.* the non-aqueous Ag/AgCl reference electrode and decrease along with increasing substituent bulk-size. No reduction potentials could be detected within the electrochemical stability window of the solvent reaching to –2.0 V *vs.* non-aqueous Ag/AgCl. Along with the increasing number of aryl substituents on the silicon atom, the response of the 20 μm Pt working electrode diminished due to fast passivation of its surface.

Silicon-enriched Si/C materials were gained by the bulk pyrolysis of di- and triaryl silanes as well as of perphenylated cyclic silanes under different pyrolysis conditions. Pyrolysis protocols were established for each compound, considering the corresponding TGA/DSC curves. Materials gained by pyrolysis were characterised by SEM/EDX as well as CHN elemental analysis and displayed layered structures consisting of 19-32%wt silicon and 68-81%wt carbon. The silicon content in the Si/C material is tuneable not only by adjusting the pyrolysis protocol, but also by number and nature of the aryl substituents. Tuning of the pyrolysis conditions as well as

employing larger aromatic residues such as anthracene or pyrene is likely to lead to the formation of pure nano-structured silicon.

Electrochemical characterisation was carried out for the pure arylsilane precursor compounds mixed with graphite as well as for the respective pyrolysed materials in Li-ion battery half-cells. Therefore, several electrode preparation methods were tested, resulting in insightful and reproducible data. While the graphite composite anodes with precursor compounds mostly lowered the capacity of graphite itself, the pyrolysed samples displayed a different behaviour in cyclic voltammetry as well as in constant current cycling experiments. With respect to the GCPL experiments, overall best results could be obtained by employing Si/C materials from $phenyl_{10}Si_5$ (**33b**) pyrolysed at 800 °C in combination with graphite (46%wt, each), binder and carbon black (4%wt, each), resulting in average capacities of 440 mAh g^{-1} (22% above the graphite blank at 360 mAh g^{-1}) and Coulombic efficiencies between 98-99% over 100 cycles.

Stannanes

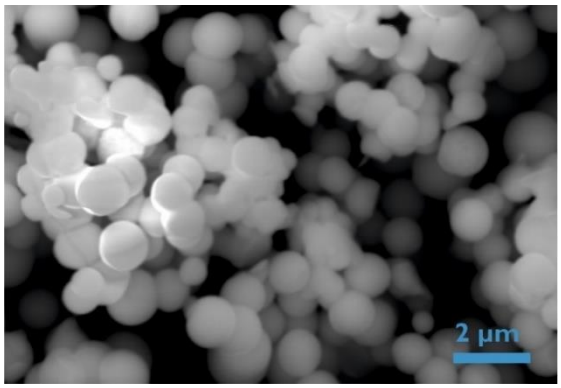

4 Results and Discussion

4.1 Synthesis

Over the course of this work a series of known aryl-substituted tin hydrides were synthesised *via* routes already discussed in literature and tested for their electrochemical behaviour.[19] The whole reaction path is depicted in Scheme 6. In all cases, the synthesis was started with a conversion of the commercially available aryl bromide into a Grignard reagent which was subsequently treated with tin tetrachloride ($SnCl_4$) in order to generate either the diaryldichloro stannane ($aryl_2SnCl_2$) or the tetraarylstannane ($aryl_4Sn$). The latter was reacted with stoichiometric amounts of $SnCl_4$ to generate the aryltin trichloride ($arylSnCl_3$) according to the Kozeshkov equilibrium.[204] Finally, the chloride species were hydrogenated using an excess of $LiAlH_4$ as described in literature.[19] In general, the thermal stability of tin hydrides was reported to decrease when a replacing organic substituents by a hydrogen atom; trihydride species being the most labile.[30] Therefore, purification of the liquid aryltin hydrides was carried out by distillation *in vacuo* at the lowest possible temperatures according to their boiling point. The solid hydride 1-naphthyl_2SnH_2 could be recrystallized from Et_2O at –30 °C.

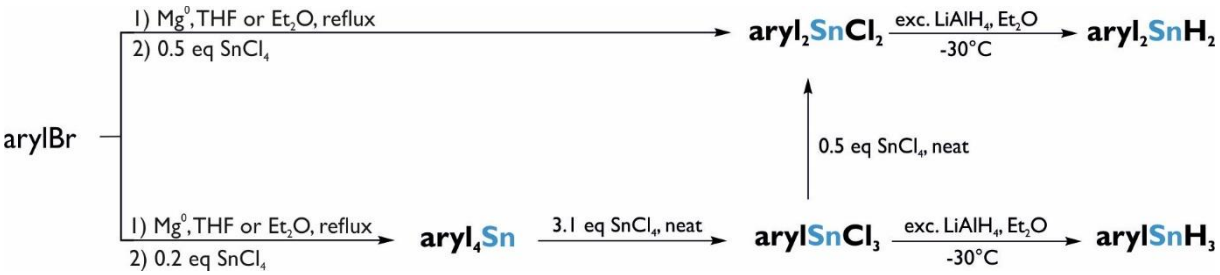

Scheme 6 Synthetic routes to aryltin hydrides.

Phenyl, *o*-tolyl, 1-naphthyl and mesityl were selected as aromatic substituents in order to determine the influence of the number and the steric demand of the ligands on the electrochemical properties of this compound class (see Figure 67). Since the investigated aryltin trihydrides were known in literature, the material characterization was confined to ^1H and ^{119}Sn NMR. Additional information on morphology was obtained by SEM/EDX and SAXS measurements, electrochemical properties were determined by cyclic voltammetry.

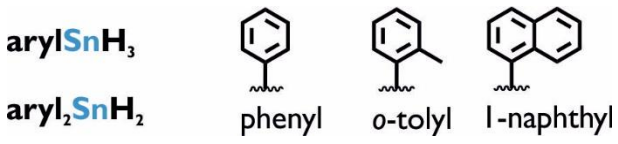

Figure 67 Aromatic substituents used for organotin hydrides.

4.1.1 Dehydrogenative Coupling

The formation of oligo- and polystannanes from diaryltin dihydrides and aryltin trihydrides may be approached by a dehydrogenative coupling reaction promoted by the labile Sn–H bond and has been extensively studied by Uhlig and co-workers.[67,72,205] The properties of the tin particles, insoluble in usual organic solvents, are particularly interesting: Zeppek reported that the nature of the solvent as well as reaction time influences both, size and morphology of the resulting particles.[72] The use of toluene, for example, leads to nano rods whereas donating solvents such as Et_2O or DME lead to spherical particles. It was found that these particles consist of spherical superstructures exhibiting diameters of approximately 1 µm and are furthermore composed of smaller spherical subunits which display a size range of 7-30 nm These spherical substructures are usually formed very quickly upon addition of the amine base and display a strong propensity towards agglomeration, finally leading to the described superstructures (Figure 68).[72]

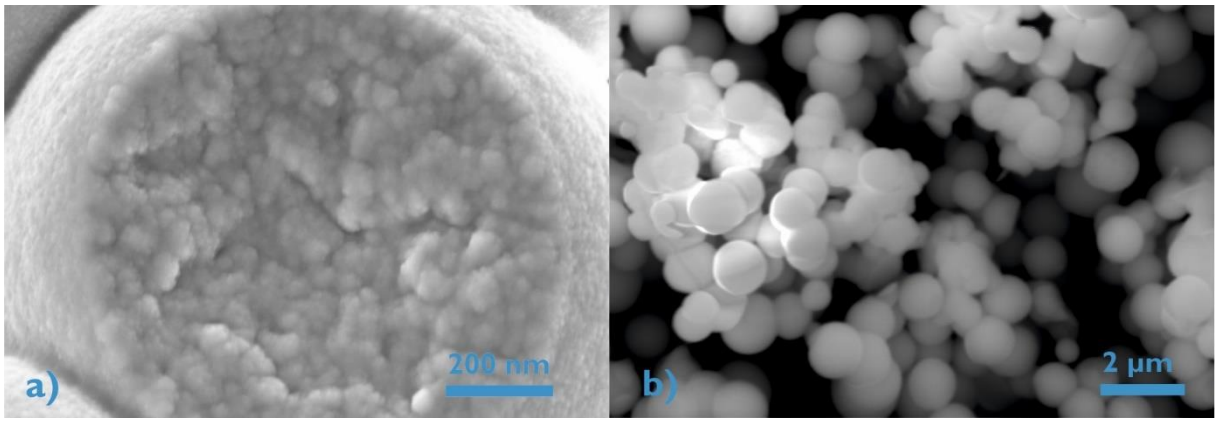

Figure 68 FESEM and SEM pictures of a) subunits[72] and b) superstructures of Sn@o–tolyl from Et_2O. EDX: Sn 84%wt (36%at), C 15%wt (64%at).

All experiments towards (nano)particles were carried out according to the work of Zeppek.[72] In a typical reaction a 0.8 M solution of the pure aryltin trihydride in a dried, degassed solvent (toluene, Et_2O, DME or cyclohexane) was treated with an equimolar amount of TMEDA and was stirred at room temperature under inert atmosphere. The initially clear, colourless solution immediately turned yellow and hydrogen formation could be observed. Over the course of a few minutes the colour darkened over orange to brown and finally reddish-black as insoluble precipitates were formed (Sn@aryl). This colour change indicates the formation of Sn–Sn bonds allowing for σ–σ^* and σ–π transitions as has been reported for poly(diaryl)stannanes.[59] The precipitate was filtered off subsequently dried. Due to high susceptibility of the black solids to oxidation when exposed to trace-amounts of oxygen leading to off-white stannoxanes, the products were further handled under inert atmosphere.

4.1.1.1 Ultrasonication Experiments

Sn@aryl particles formed *via* dehydrogenative coupling are interesting not only due to their high tin and low carbon content, but also due to the size of their substructures (*cf.* Figure 68). Considering a possible application in Li-ion batteries *i.e.* a Sn nanoparticle graphite composite to be used for anodes, homogeneous sizes in the range of the substructures are desirable. In order to decrease the sizes of the superstructures/agglomerates, ultrasonication experiments were carried out with *o*-tolylSnH$_3$. This compound was chosen due to its extensive characterisation carried out by Zeppek.[72] As stated before, the size and shape of the resulting particles remain the same when the polymerisation is carried out in Et$_2$O or DME;[72] due to its higher boiling point, DME was used for the presented ultrasonication experiments. Therefore, a probe-type ultrasonicator was placed in a Schlenk flask under inert atmosphere, filled with dried, degassed DME and 1 mL of a 0.8 M stock solution of *o*–tolylSnH$_3$ (170 mg, compound **42**) in the same solvent. The probe was immersed 1–2 cm deep into the solution; the amount of solvent was adjusted to the size of the Schlenk flask. In all experiments the treatment consisted of a sequence of 0.5 s of sonication at 40 W followed by a 1.5 s pause. Upon start of the ultrasonication 1 equivalent of TMEDA (0.12 mL) was added to the solution and the conditions were maintained during a defined amount of time. Since a considerate amount of solvent evaporated due to local heating at the ultrasonicator probe in addition to the flowing nitrogen in the open setup, the flask was ice-cooled upon repetition of the experiments. During the ultrasonication the expected change in colour of the solution was observed. Within 30 seconds of the treatment the mixture turned from colourless over orange, red and brown to the eventual black that was reached after approximately 2 min of overall sonication time. After the experiment the probe was replaced by a stopper and the Schlenk flask was set aside in order to allow the particles to precipitate. This, however, did not take place even after 4 days. Therefore, the particles were collected by careful evaporation of the solvent under reduced pressure. A collection by filtration *via* a Por. 4 frit with additional filter paper had failed beforehand, despite this being the established gathering method for the untreated particles. The dried particles were subjected to SAXS measurements, performed by Dr. M. Kriechbaum, from which correlation lengths in the range of 1.52-1.64 nm could be calculated. Upon repetition of the experiment samples of the suspension were taken after 2, 5, 10 and 15 min of overall ultrasonication time.

In order to determine the influence of the ultrasonication an *in-situ* SAXS experiment without the ultrasonic treatment was set up to follow the sizes and form of the formed particles over time. These experiments were designed and performed in cooperation with Dr. A. Chemelli. Therefore, the reaction was carried out using the same concentrations while stirring at room temperature. The suspension was transported from the flask into the flow-cell *via* a Teflon® tube stuck through a septum, aided by the pressure of the gas evolution during the reaction. The system was held airtight by fixing a nitrogen-flooded syringe on the opposite end of the tubing, thereby providing a deposit for both, the flowed through suspension as well as the hydrogen gas (Figure 69). By using this closed system no further sample preparation was necessary and the formation process could be monitored by measurements taken every minute.

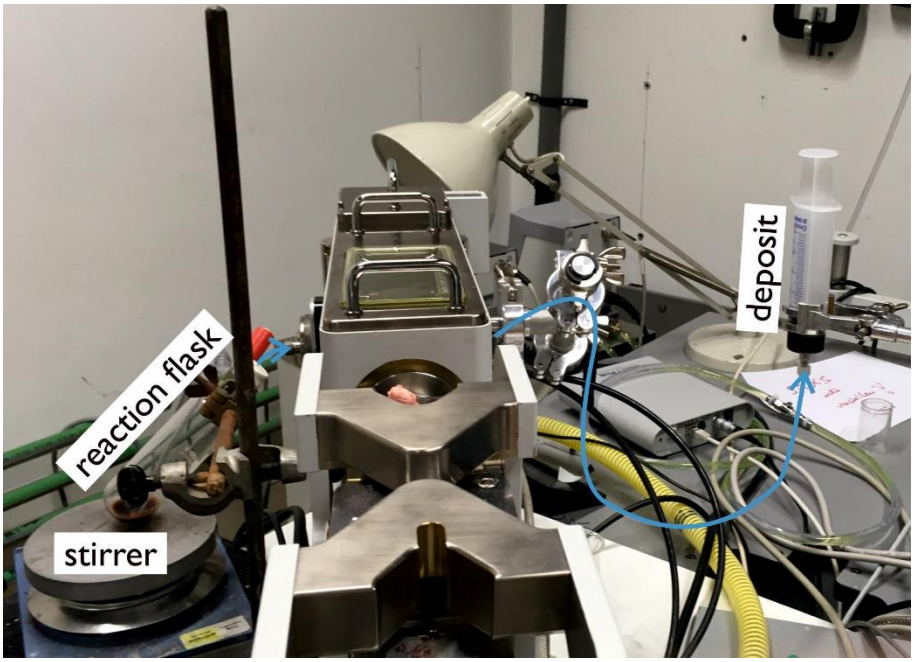

Figure 69 Flow-cell setup for SAXS measurements. Teflon® tubing is depicted in blue.

An evaluation of the SAXS data of particles taken from the ultrasonicated (u.s.) suspension gave two main peaks which may be associated with particle radii of 0.6 nm and 2.3-2.6 nm for samples taken after a total of 2, 5, 10 and 15 min of ultrasonication treatment, respectively (Figure 70). In order to compare the data of the different experiments, the intensity of all obtained curves was normalized with respect to the first peak. The intensity distribution is therefore given in arbitrary units (a.u.). For the *in-situ* measurements with the flow cell samples were measured at comparable times with respect to the time needed for sample preparation (*e.g.* measurements for 2 min u.s. corresponds to 18 min of stirring (8 min treatment + 10 min sample preparation)). The resulting curves display two maxima, again at average radii of 0.65 and 2.2 nm. Judging from the position and appearance of the curves two different sizes are superimposing each other, indicating either the presence of two differently sized spherical particles as main components in the sample or one elongated particle as seen from different angles resulting in the difference of length. Assuming monodispersity in the sample and a cylindrical shape with a width of 0.7 nm and a length of 5 nm a simulation was carried out resulting in a curve remarkably close to the experimental data (Figure 70, right). The experimental curves for both, the ultrasonicated and stirred samples display a less steep decline than the simulation, which indicates the presence of particles with different lengths. Considering these data, it is not yet clear if the particles present are solely spherical and agglomerate along one dimension forming rods or if a formation of wholly cylindrical particles is taking place under the given conditions.

These results are only one step into the full characterization of the Sn@*o*–tolyl particles and needs to be further reinforced by variations of the reaction conditions, *e.g.* concentrations or solvent as well as with theoretical investigations, which lies not in the scope of this work.

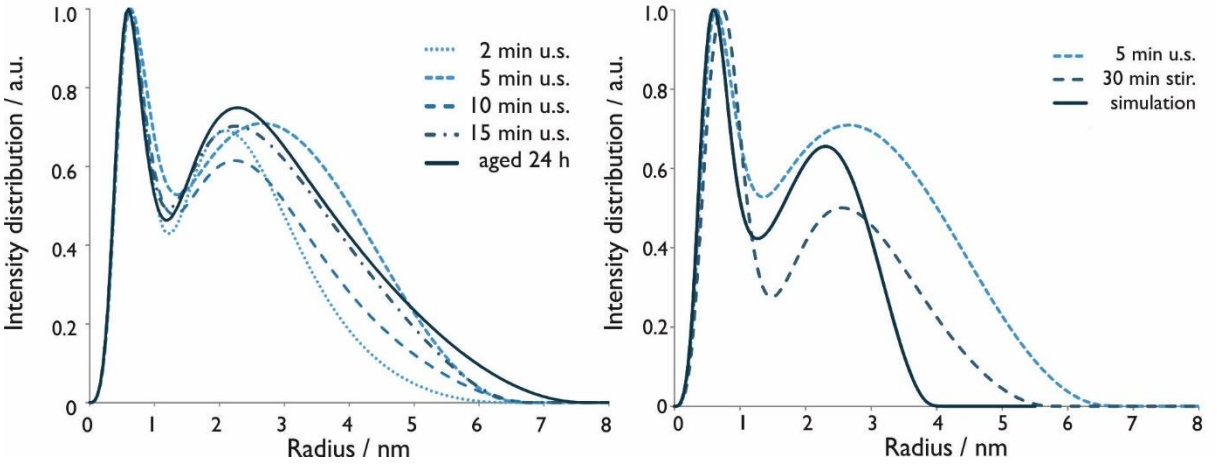

Figure 70 SAXS measurements of particle formation from *o*-tolylSnH$_3$ during ultrasonication (u.s.) treatment (left); comparison of ultrasonicated and stirred particle formation with a simulated curve for cylindrical particles (0.7 nm x 5 nm) (right).

4.1.1.1.1 Summary of Ultrasonication Experiments

In summary it may be stated that a treatment with ultrasonication of the reaction solution resulted in no significant difference of neither the size range of the formed (nano)particles nor their shape. Also, an influence on the agglomeration caused by ultrasonication may be excluded. However, considering the aspect of using the Sn@aryl particles for composite anodes in Li-ion batteries, ultrasonication might provide a useful way to introduce Sn@aryl particles homogeneously into graphite in the future by simultaneously exfoliating the graphite sheets to form graphene and assisting in the distribution of the *in-situ* formed particles on its surface.

4.1.2 Pyrolysis Experiments

The spherical particles formed by arylSnH$_3$ when reacted with TMEDA in ethereal solutions have shown indications on existing as layered core–shell particles with an organic core wrapped in a Sn layer and decorated with the aryl moieties as the outer shell as reported by Zeppek.[72] In order to in cleave some of the aryl substituents from the Sn cores and thereby enhance the concentration of Sn within the sample pyrolysis experiments were carried out. Therefore, *o*-tolyl@Sn particles were prepared *via* the usual reaction with 1 equivalent of TMEDA in Et$_2$O, dried *in vacuo* and were subsequently pyrolysed under argon atmosphere. Here, Et$_2$O was chosen due its low boiling point resulting in fast evaporation after the polymerisation. SEM investigations on the influence of the treatment at elevated temperatures are displayed in Figure 71, the respective details to weight and atomic percentages of Sn and C determined by EDX are summarized in Table 19. The first pyrolysis experiment was carried out at 250 °C and therefore close to the melting point of elemental tin (232 °C). Treatment of the samples at this temperature resulted in a partial melting of the structures to some larger agglomerates, yet the carbon to tin ratio remained largely unaltered in comparison to the untreated particles (Table 19; Figure 71, a) and b)). When treated at temperatures above the melting point, namely 400 °C, however, the Sn content rose rapidly to an average of approximately 95%wt.

In addition to the frayed surface structures of the particles, large lumps of elemental Sn with a diameter of approximately 1-2 mm were detected (Figure 71, d)). These findings further provide indication on the core-shell nature of the spherical particles.

Table 19 Weight (wt) and atomic (at) percentages of Sn and C in Sn@*o*-tolyl particles determined by EDX.

Sn@o–tolyl	*Untreated*		*250 °C*		*400 °C*	
	%wt	*%at*	*%wt*	*%at*	*%wt*	*%at*
Sn	85	36	79	31	97	76
C	15	64	21	69	3	24

The pyrolysis experiments showed that temperatures above the melting point of tin are necessary in order to cleave a Sn–C bond, yet the main structure remains in frayed form. Furthermore, the particles treated at higher temperatures are interesting candidates for additives in anodes for Li-ion batteries, due to their elevated, nanostructured tin content and a possibility to form into a graphite-Sn nanocomposite when created *in-situ*.

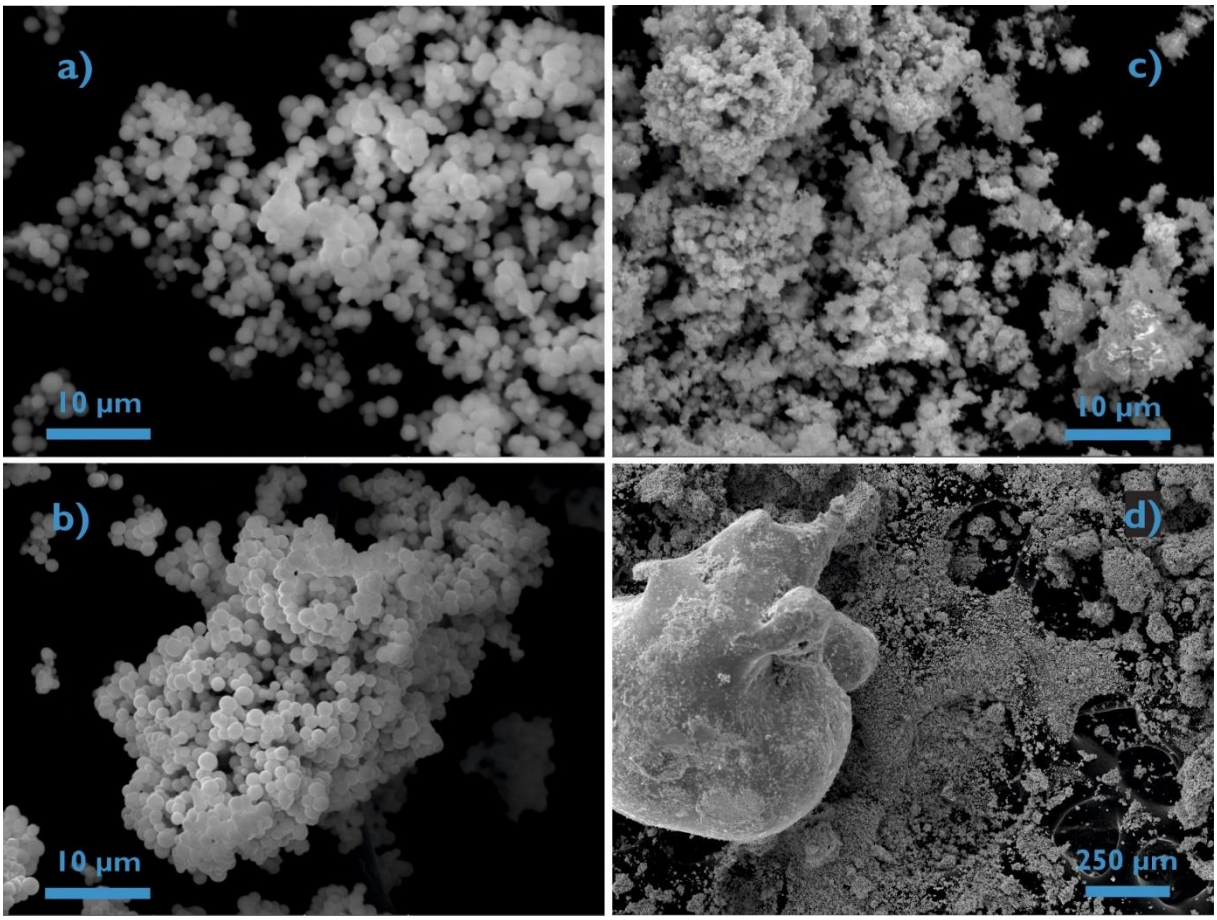

Figure 71 SEM pictures of Sn@*o*–tolyl particles from Et_2O; a) untreated, b) pyr. at 250 °C, c) pyr. at 400 °C, d) lump of Sn^0 formed during pyrolysis at 400 °C.

4.2 Electrochemical Characterisation of Aryltin Hydrides by Cyclic Voltammetry

As stated above, to the best of our knowledge, very little and imprecise information on electrochemical properties of aryltin hydrides is available. Similarly as for their silicon counterparts, the focus of research laid mostly on the electrochemical generation of organotin hydrides starting from the respective halides rather than on their characterization.[206] One reason for this lack of information stems from the sensitive nature of aryltin hydrides posing several challenges for even the simplest cyclic voltammetry measurements: the pure compounds are highly sensitive towards oxygen, temperatures above –35 °C and, in some cases, even towards visible light. Similar to their silicon counterparts, electrochemical reduction and oxidation processes have to be expected at comparatively high/low potentials, thus requiring of a solvent with a sufficiently large electrochemical stability window. Additionally, a high reactivity towards several chemicals, including solvents or supporting electrolyte salts, drastically restrict the choice of experimental conditions. Following some long-term exposure NMR studies of different solvents and supporting electrolyte salts, the combination of either tetrahydrofuran (THF) or acetonitrile (MeCN) with tetrabutylammonium hexafluorophosphate (TBAF) appear as the most suitable ones from the chemical stability point of view.

All of the above-mentioned reasons immensely complicate not only the design of a suitable cell but also the preparation of the samples needed for CV measurements, since for the transfer into an argon-filled glovebox the compounds will inevitably be warmed up. In the case of phenyltin trihydride, for example, the initially colourless, clear liquid turned yellow and finally orange within the few minutes necessary for transferring the sample into the glovebox and exact weighing in, indicating the dehydrogenative coupling reaction leading to insoluble particles. By minimizing the timeframe between the interruption of the cooling and the dilution of the aryltin hydride in the pre-cooled electrolyte solution (0.1 M TBAF in MeCN) by means of omitting the weighing step, the samples could be prepared fast enough to prevent polymerisation. The diluted samples were stored in tightly sealed vials immersed in liquid nitrogen outside of the glovebox. In order to slow down the reactions taking place during the CV measurements, all parts of the *Swagelok*® cell were cooled with liquid nitrogen before use, only warming up during the assembly. The measurements were carried out at 0 °C in a thermostatic cabinet, doubling as a faraday cage. Even though this preparation method came at the cost of quantitative results, useful qualitative information could be obtained.

By comparing differently substituted arylSnH$_3$ compounds measured at 100 mV s^{-1} an oxidation is visible for all tested trihydrides at potentials of 1.8 – 1.9 V *vs.* non-aqueous Ag/AgCl (Figure 72). The absence of any oxidation/reduction processes at the same potentials under the same conditions of the blank (Figure 72, black line) proves that the peaks are not to be assigned to instability of the supporting electrolyte solution and that the measured potentials lie within its stability window. In case of the 1-naphthyl species, a second oxidation peak is evident at 1.3 V, suggesting a multi-step reaction.

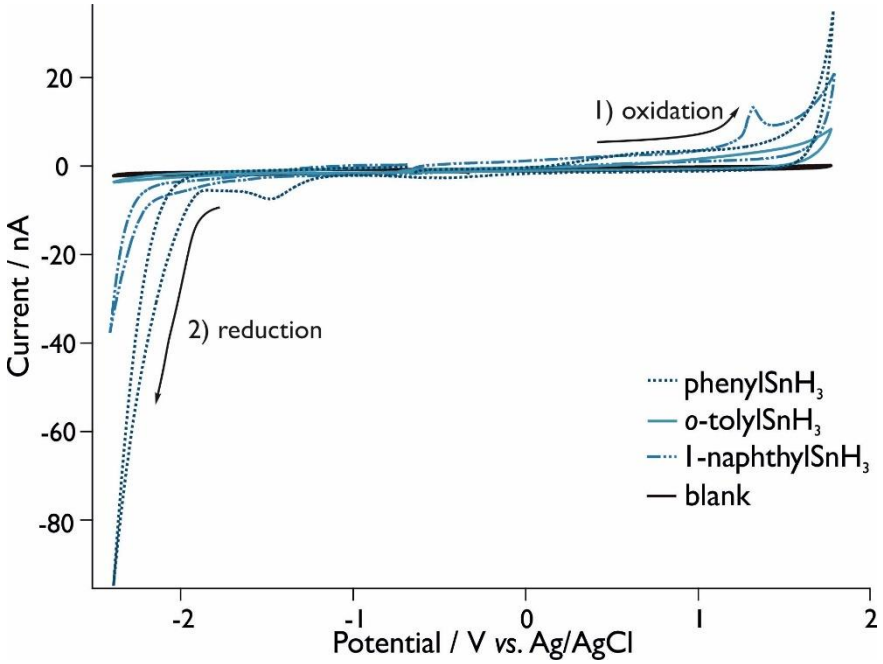

Figure 72 Cyclic voltammetry response of differently substituted aryltin trihydrides (aryl = phenyl, *o*–tolyl, 1-naphthyl) in 0.1 M TBAF in MeCN *vs.* Ag/AgCl (saturated, in MeCN) at 100 mV s^{-1} on a 20 µm Pt microelectrode. The direction of the CV experiments is indicated by arrows. All experiments were carried out equally.

All of the observed oxidation steps appear highly irreversible due to the lack of according reduction signals. A comparable behaviour was also observed for the comparable silicon derivatives shown in section 3.5.1, Figure 38. However, the oxidation potentials of the respective aryl moieties are further lowered by the presence of tin than by silicon. Thus, it may be possible that a 2 e^- transfer also takes place for the silanes, albeit outside of the measurable range. Similar to the oxidation of the tin hydrides also some reduction reactions are observed for the compounds substituted with phenyl and 1-naphthyl again close to the limit of the measurable range lying at –2.2 V each. In case of the phenylSnH$_3$ (**41**) also a second reduction step is visible at –1.3 V *vs*. Ag/AgCl whereas for its *o*–tolyl counterpart no reduction may be detected at all. This could indicate an effect caused by the methyl–group in α–position of the aromatic residue, shifting the reduction peaks towards lower potentials. In the following cycles a gradual loss in intensity of the peaks was observed indicating a passivation of the electrode which is most probably caused by a deposition of possibly electrically insulating Sn@aryl particles on the electrode surface.

Although the mechanism/reaction is not very well understood, an electrodeposition/ -polymerisation is presumed to take place during the measurements. This is further backed up by a change in colour of the solution from colourless to dark orange as well as the observation of black particles on the working electrode upon opening the cell after cycling. The electrochemical reactions taking place are very likely coupled with other chemical reactions leading to the observed particles; passivation could also occur due to hydrogen gas evolution leading to insulating bubbles that obstruct the electrode. An influence of the temperature on the reactions cannot be excluded, yet with the presently available cell investigations in this direction could not be performed.

The influence of the number of substituents was investigated for both the phenyl and 1-naphthyl moieties. Since both showed similar behaviours, only the example of 1-naphthyl is displayed in Figure 73. Contrary to the trihydride species the dihydrides do not show any reduction peaks, possibly due to a shift towards lower potentials caused by the additional aromatic system attached to the tin centre. The main difference between one and two aryl groups is seen in the region between 1.2 and 2.0 V, where in case of one aromatic ring system on the tin two distinct peaks are visible whereas for two ring systems these peaks seem to merge closer to each other, forming a shoulder. Very similarly to the arylSnH$_3$ a colour-change of the electrolyte solution of the aryl$_2$SnH$_2$ species could be detected, albeit less distinct. An optical determination of particle size was not possible.

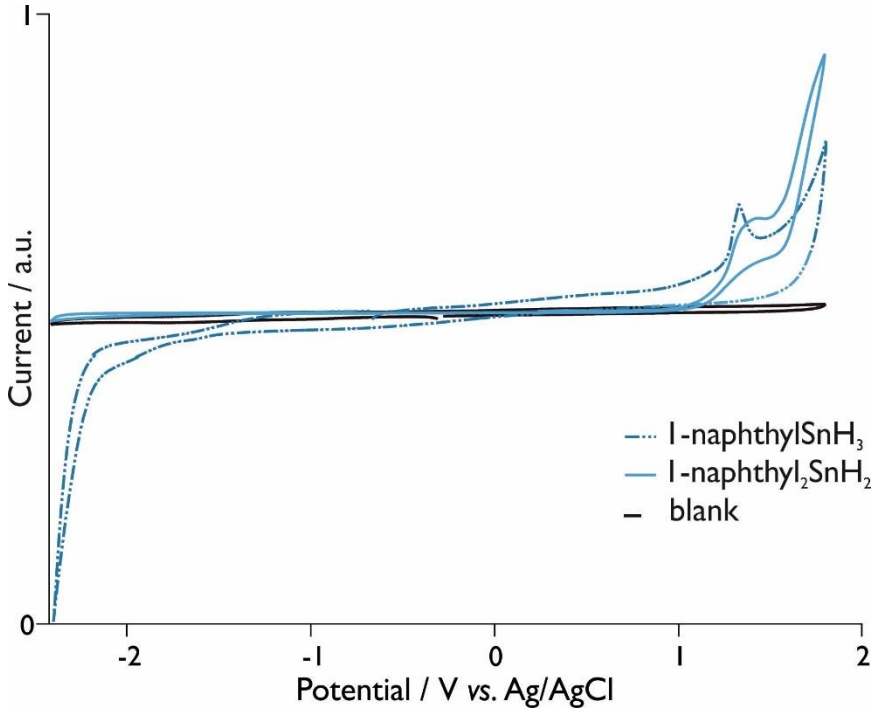

Figure 73 CV of 1-naphthyltin di- and trihydride in 0.1 M TBAF in MeCN *vs.* Ag/AgCl at 100 mV s^{-1}.

4.2.1 Summary of the Electrochemical Characterisation of Aryltin Hydrides

In conclusion it may be stated that for both, aryltin trihydrides as well as diaryltin dihydrides, irreversible oxidation processes could be observed which lead to a colour change of the sample solution. Electrochemical reactions occurring in the cell are likely to be coupled with a chemical reaction, leading to the formation of oligo- or polymeric particles on the surface of the working electrode and thus accounting well for the irreversibility. The particles show similarities to Sn@aryl particles formed by thermal or base–induced polymerisation reported for the aryltin trihydrides which in turn consist of a covalently bound Sn–Sn core/chain decorated by aryl moieties. Aryltin trihydrides display additional reduction peaks. However, the exact mechanisms of the reactions occurring during cyclic voltammetry are not yet completely understood. Future investigations should include NMR and FT-IR spectroscopy as well as SEM/EDX for the determination of the products formed. Finally, adaptions to the CV cell should be made, possibly by a change of the body–material, by designing a cooling mantle for the device, as well as the introduction of a septum for the possibility to fill the cell also outside of an argon-filled glovebox if necessary.

4.3 Li-Ion Batteries

Encouraged by the redox processes of aryltin trihydrides seen in cyclic voltammetry experiments and the comparatively high theoretical capacity of tin (990 mAh g^{-1}) further investigations in direction of an application of these compounds in Li-ion batteries were carried out. Thereby the Sn@aryl particles resulting from $arylSnH_3$ were especially interesting due to their high tin contents and particle sizes in the nanometre range.

4.3.1 Electrode Preparation

Particles based on aryltin trihydrides were tested as composite anode materials in Li-ion batteries. Therefore, several approaches for their incorporation were tested. A summary of the routes used towards the electrodes is displayed in Figure 74.

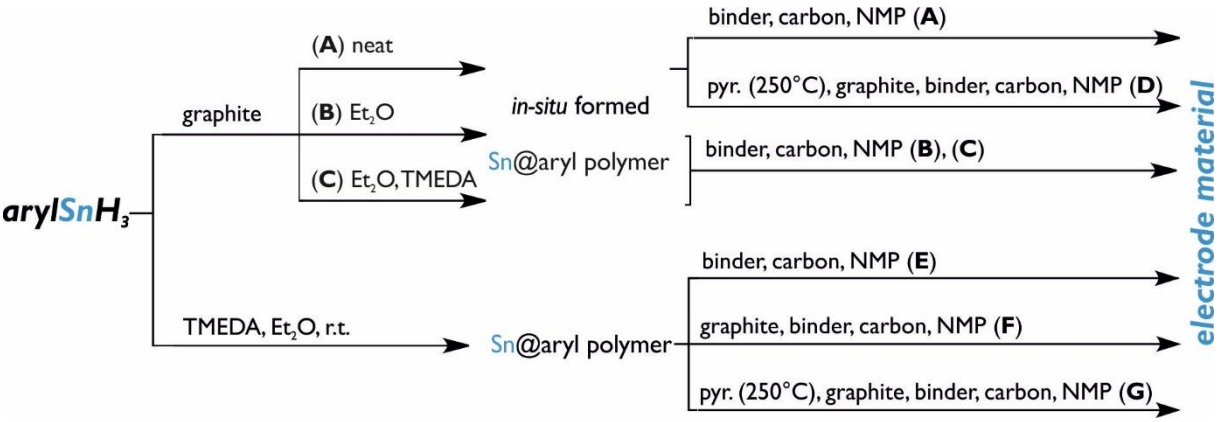

Figure 74 Routes towards electrode materials with $arylSnH_3$ as starting material. Hereafter, the preparation methods are referred to this figure and indicated with the respective letters.

The electrode preparation was challenging as, in contrast to their silicon analogues, none of the steps could be carried out at ambient conditions and therefore certain equipment could not be used. All slurries were prepared in an argon filled glovebox with dried and (in case of solvents) degassed chemicals. Routes **A**-**D** included an *in-situ* formation of the Sn@aryl particles, either carried out by stirring the neat aryltin trihydride with graphite **A**, stirring a mixture of graphite and tin trihydride in Et_2O **B**, or by addition of aryltin trihydride along with a few droplets of TMEDA to a suspension of graphite in Et_2O at room temperature **C**. Subsequently, a solution of polyvinylidene difluoride (PVdF) as binder in N-methyl pyrrolidone (NMP) and carbon black were added to the mixture.

The slurries were homogenised either by stirring for approximately 72 h or by using a ball-mill with stabilised ZrO_2 balls at 300 rpm for 45 min. In both, **B** and **C** the solvent was evaporated after 30 min of stirring and the remaining solids were used for the slurry production. As a variation of path **C**, the $arylSnH_3$ was added along with a few droplets of TMEDA onto a previously prepared graphite blank electrode. In case of **D**, the solid obtained by route **A** was pyrolysed under argon atmosphere at 250 °C for 30 min before use. In routes **E** to **G** the Sn@aryl particles were formed before their addition to the respective mixtures; for **E** the particles were tested without the addition of graphite, for **F** they were used as composite materials and finally for **G** they were mixed with graphite and pyrolysed at 250 °C.

Importance of the Casting Step during Electrode Preparation

As stated before, the casting step is crucial for the reproducibility of battery data. Ideally, the slurry is distributed homogeneously over the current collector (*i.e.* Cu foil with a thickness of 20 µm) in meticulous evenness and thickness. In reality, different problems are encountered as depicted in Figure 75. The film thickness may be reduced by crumples in the Cu foil, which in turn may lead to insufficient covering of small areas, resulting in contact loss to the current collector (**1**). This issue may be tackled by using a casting table with vacuum suction, where the current collector may be smoothed and held in place during the casting. Other factors to influence the film thickness are the viscosity of the slurry and the casting speed; if both of these aspects are too high, bubbles may be provoked on the substrate surface, resulting again in a thinning of the film (**2**). Therefore, an appropriate slurry texture and casting speed have to be determined. The latter may be managed by using the aforementioned casting table with an adjustable speed rate for the casting blade.

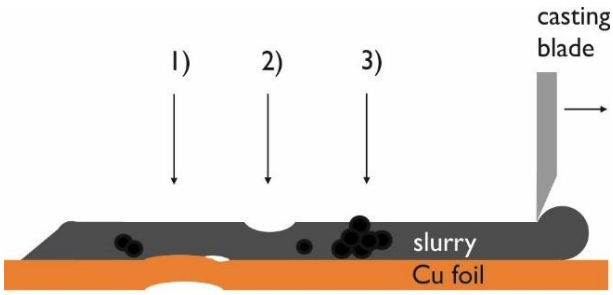

Figure 75 Possible complications during the casting step.

Complications in the homogeneous distribution of the samples were encountered especially with the investigated Sn@aryl (nano)particles. Since these compounds are prone to agglomeration (*cf.* section 4.1.1), a particle distribution similar to the one depicted in Figure 75, 3) occurred, leading to parts of the cast foil containing bundles of Sn@aryl on graphite whereas on other parts no Sn species could be found at all, evidenced by their performance in Li-ion battery cells.

Inside the argon-filled glovebox no casting table with vacuum suction was available and the procedure hence was carried out manually. The most effective way of keeping the current collector flat during the casting was by attaching the copper foil to a glass plate by using the adhesive effect of an ethanol film. Subsequent fixation with adhesive tape was followed by evaporation of the ethanol film lead to a flat foil. Even though this procedure could not prevent every imperfection in flatness, it provided a stable underground for casting. The constant casting speed could only be approximated when moving the casting blade manually. By applying the mentioned methods, areas wide enough for the cutting of the actual electrodes with 10 mm diameter used in Li-ion battery cells as well as even film thicknesses were made available. Cycling data showed a maximum deviation of the specific anodic capacities of 15%.

The agglomeration of the Sn@aryl particles, however, is still a challenging issue. Different approaches were tried in order to avoid this matter. One consisted of an *in-situ* formation of the particles on the graphite by mixing *o*-tolylSnH$_3$ (**42**) with graphite and TMEDA in ethereous

environment while stirring vigorously in order to obtain a homogeneous distribution of the forming particles and possibly even avoid an agglomeration altogether as in Figure 74, **B**/**C**. A visualization of this effect, however, was not yet possible with SEM.

In another attempt ultrasonication was used to prevent the agglomeration to superstructures (*cf.* 4.1.1.1), which unfortunately did not lead to the desired effects. In a physical approach, ball-milling in a planetary mill using stabilised ZrO_2 balls for a total of 45 minutes at 300 rpm was chosen for homogenisation instead of stirring. Hereby a more homogeneous distribution of the Sn@aryl particles in the electrodes could be achieved, as again evidenced by their performance in galvanostatic cycling experiments in Li-ion battery cells which is further described in section 4.3.3.

4.3.2 Cyclic Voltammetry with Sn@aryl Anodes

The electrochemical characterization of Sn@aryl particles by cyclic voltammetry in a classical setup is restricted by the insolubility of the materials in common organic solvents. Alternatively, the electrochemical properties of these materials could be determined by means of building anodes in Li-ion battery half-cells with particles formed from $arylSnH_3$ in Et_2O. The dehydrogenative coupling reaction was either carried out by stirring the mixture at room temperature (Figure 74, route **B**) or by acceleration *via* the addition of TMEDA (Figure 74, route **C**).

The CV measurements conducted in Li-ion battery half-cells were carried out in an electrolyte containing 1 M lithium hexafluorophosphate ($LiPF_6$) in an ethylene carbonate (EC):dimethyl carbonate (DMC) 1:1 (vol.) solution as electrolyte. A potential range of 0 to 2 V *vs.* Li^+/Li reference electrode was applied and the anodes were cycled at different scan rates. A typical experiment was started with two scans at a sweep rate of 1 mV s^{-1} followed by a 12 h resting period at open circuit voltage (OCV) and subsequent cycling at rates of 0.05, 0.1, 0.2, 0.5, 1, 2 and 5 mV s^{-1} with two scans each. A comparison between the different scan rates showed only insignificant differences in shape of the curves. Therefore, the data derived from measurements at 1 mV s^{-1}, including the first cycles were chosen as displayed in Figure 76 are used for discussion. Each CV is compared directly to a graphite blank prepared according to the respective preparation routes, replacing the tin compounds with graphite.

The graphite blank displays lithium intercalation steps during the reduction process at potentials of 0.6 and 0.2 V (black line at negative currents) while the de-intercalation takes place over a broader step at 0.3 V during the oxidation (black line at positive currents). As seen in the highlighted area (shaded with blue) of a), the Sn@aryl samples display additional peaks during both, reduction and oxidation steps, which broaden upon further cycling of the samples, yet do not vanish. They may be assigned to multistep electrochemical reduction reactions of tin with lithium to form various Li_xSn alloys, as described in literature.[207] Three discrete peaks, plus a shoulder at 0.5 V, are visible between 0.6 and 0.8 V in the anodic scan and may be assigned to the extraction of lithium from the formed alloys. The remaining peaks that appear at lower potentials result from (de)lithiation of the graphite. These curves indicate a formation of nanostructured Sn^0 in the electrode.

When focusing on the experiment where the Sn@aryl particles were used without the addition of graphite (Figure 76 b)), it is seen that all intercalation steps occur over an enormously broadened

potential range during the first cycle (solid line). The three discrete Sn^0 peaks seen in Figure 76, a) (inset) have merged into one broad shoulder possibly due to a much higher concentration of the tin (overall being 88%wt in comparison to 20%wt **F**) and the lack of graphite as a supporting matrix. However, the intercalation of lithium into the Sn particles seems to occur only during the first cycle as in the following cycle (Figure 76, b), dotted line), the oxidation and reduction curves are minimized to one peak each, lying at 0.2 V for the reduction and at approximately 0.5 V for the oxidation process. These peaks indicate that after the first cycle only the carbon in the samples, be it the additive carbon black or the aryl substituents "decorating" the tin particles, are electrochemically active.

A loss of contact due to swelling of the tin during the intercalation as well as incomplete tin delithiation is likely the reason for that. The broadening of the peaks during both processes indicates that the formation and the delithiation of Li_xSn alloys occur over less defined stages than the intercalation of lithium into a graphite lattice. This is most likely caused by the non-symmetrical array of the particles as well as some free spaces between the agglomerated spheres. These are generated by the hydrogen evolution during the dehydrogenative coupling reaction leading to the particles. Therefore, those particles are possibly not soaked completely by the electrolyte upon the first cycles and thus suffer an initial lack of contact to lithium ions.

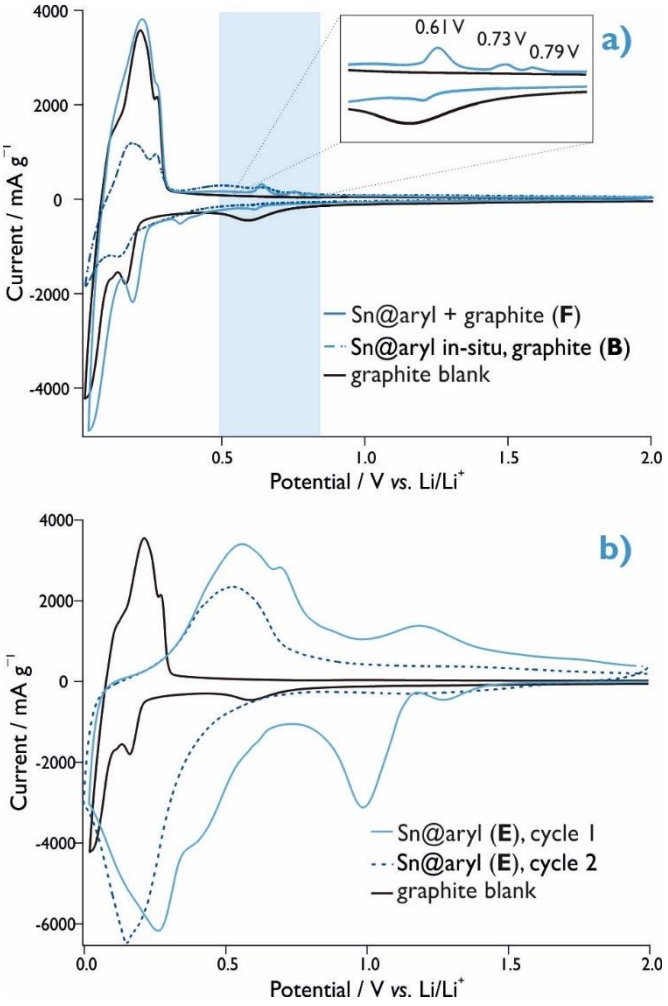

Figure 76 a) CV of Sn@aryl particles (blue line: *ex-situ* prepared particles (**F**); dashed line: *in-situ* in graphite prepared particles (**B**) as composite anodes with graphite in Li-ion batteries at 1 mV s^{-1}. b) CV of Sn@*aryl* particles as anodes without graphite (92%wt) Cyclic voltammetry was measured in $LiPF_6$ in EC:DMC 1:1 (vol.) *vs.* Li.

In conclusion the CV measurements of Sn@aryl particles in Li-ion battery half-cells have shown reduction and oxidation processes. These are most pronounced during the first cycle and fade quickly over the course of a few cycles, caused by swelling of the tin within the electrodes leading to contact loss or by incomplete delithiation of the tin particles. The swelling was shown to be mitigated by the use of graphite.

4.3.3 Galvanostatic Cycling with Potential Limitation (GCPL)

The redox processes seen in cyclic voltammetry experiments in addition to the high theoretical capacity of tin encouraged further investigations in direction of an application of the materials in Li-ion batteries. Therefore, constant current cycling experiments (GCPL) were performed with which the specific anodic capacities could be determined.

A usual experiment consisted of cycling a half-cell within the range of 0.02 to 1 V at a C-rate of C/2, always calculated with respect to the mass of active material contained in each electrode, usually Sn@aryl and graphite combined. At least three electrodes of the respective series were tested in order to assure the reproducibility of any given effect and exclude malfunctions of the cells. Regular experiments recorded 100 cycles to determine the long-term stability of the specific capacities reached. Despite possible inhomogeneities of the films resulting from manual casting of the air-sensitive samples, reproducibility could be achieved by the casting method described above. In order to compare the resulting capacity, an accordingly prepared blank, containing only graphite, conductive carbon and binder was used for reference in each procedure.

4.3.3.1 Sn@aryl as Anodes

Initial experiments aimed for the investigation of specific anodic capacities of the particles without addition of graphite to the mixture (Figure 74, route **E**). Additionally the influence of the amount of binder and carbon black on the performance was tested at two different ratios of active material:carbon black:binder of 92:4:4 (w/w; dark blue line, Figure 77) and 80:10:10 (w/w; light blue line, Figure 77). The overall Sn content accounted to 76 and 66%wt, respectively. From the cycling performance determined by GCPL measurements starting from 550 mAh g^{-1} or 285 mAh g^{-1} a rapid capacity fading is observed within the first cycles. This behaviour evidences the contact loss of the active material since the nature and overall content of carbon in the active material is not suitable for mediating the volume expansion stemming from the elemental tin. Cross-sections of both, uncycled and cycled, electrodes were acquired by SEM. The resulting images further prove a swelling of the active material during the GCPL experiments loosening its structure and thereby provoking a loss of contact compared to uncycled samples (Figure 78).

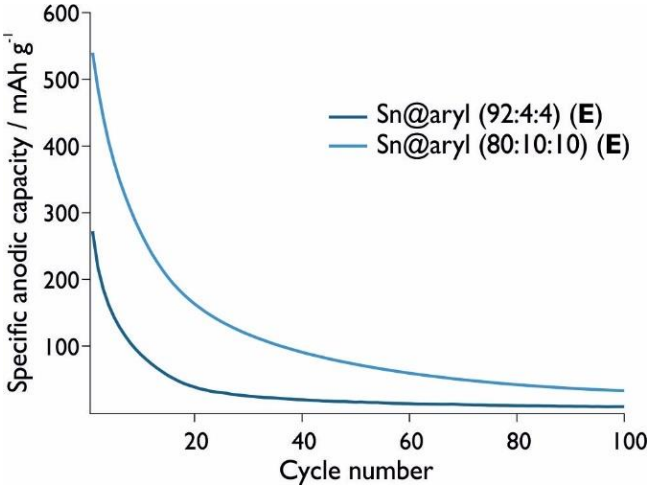

Figure 77 GCPL of "neat" anodes of Sn@aryl particles formed with TMEDA in Et_2O employing different carbon black/binder to active material ratios. Measurements were carried out in $LiPF_6$ in EC:DMC 1:1 (vol.) *vs.* Li.

The influence of the carbon amount used as conductive agent carbon black is clearly seen as well: in the light blue curve in Figure 77 the decay advances slower than its counterpart, indicating that the remaining capacity stems solely from the conductive agent rather than the tin (nano)particles. The initially high specific anodic capacities of the Sn@aryl particles, however, encouraged further investigations on these materials as composite materials with graphite in Li-ion anodes. For these experiments, the ratio of binder and carbon black was reduced to 4%wt in order to minimise the contribution of carbon black to the overall capacity.

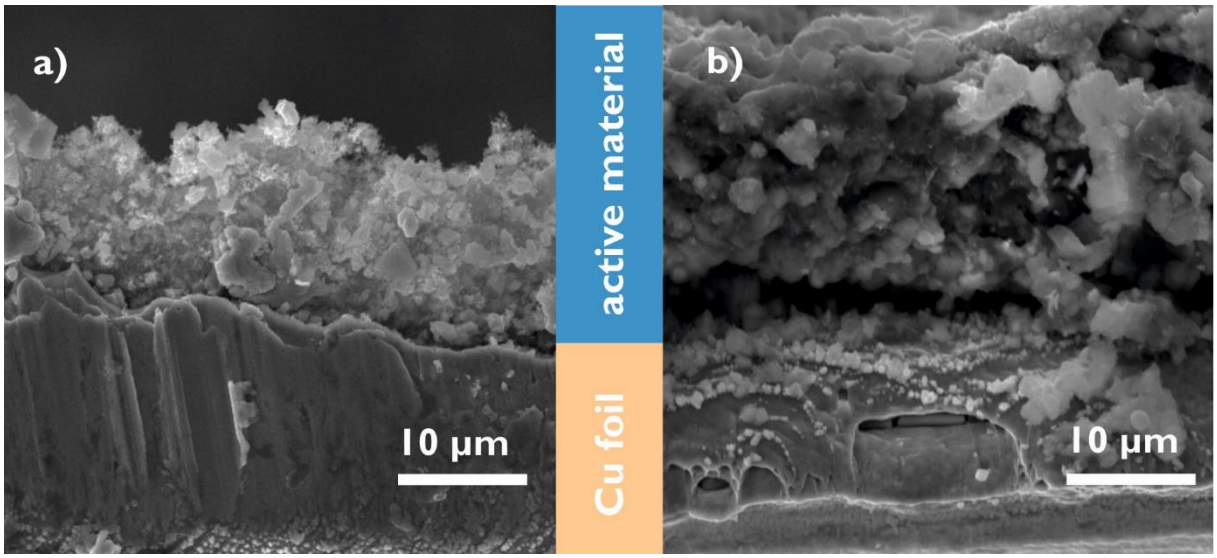

Figure 78 SEM images of cross-sections of Sn@aryl (92:4:4) electrodes. a) uncycled, b) after cycling (GCPL).

4.3.3.2 Composite Anodes – Graphite and Sn@aryl

Different aspects have to be considered when introducing Sn@aryl particles into graphite for the creation of composite anodes: on one hand the ratio of carbon to tin is relevant, on the other a homogeneous distribution of the chosen tin content, preferably within the graphite layers as intercalation compounds is important. However, first of all it was necessary to verify if the introduction into graphite could mitigate the swelling of the anodes as seen in the cyclic voltammetry (Figure 76) also over the course of 100 cycles. Hence, a ratio of 25%wt of the tin containing material was chosen, applying the afore determined amounts of 4%wt binder and

carbon black, each, leaving the remaining 67%wt of the active material to graphite. Electrode preparation was carried out by mixing an *ex-situ* prepared Sn@aryl polymer with the remaining ingredients and stirring the slurry for 72 h. Galvanostatic cycling of these samples is compared to the neat Sn@aryl sample and an accordingly prepared graphite blank in Figure 79 a). Clearly, the stabilisation of the specific anodic capacity is seen as after the first cycle, an average capacity of 205 mAh g^{-1} of active material is maintained over the course of 100 cycles. However, judging by the graphite blank displaying an average specific anodic capacity of 275 mAh g^{-1}, the Sn@aryl particles inhibit the lithiation of the graphite rather than enhance the capacity. This could be caused by coverage of the graphite surface by adsorption or (partial) clogging of the attack sites on the graphite by the inorganic material thus leading to a loss of possible lithium intake. The absence of a decay in capacity and the stability of the cycle curves leading to a coulombic efficiency of overall 97%, however, indicate close to no contact loss. This might indicate a decreased formation of Li_xSn and thus less volume expansion. The transport of lithium ions into the particles could be hindered by an irregular array of aryl–residues "decorating" the tin core. Another aspect to be considered is the (in)homogeneity of the particle distribution within the active material. Most electrodes containing *ex-situ* prepared Sn@aryl particles were afflicted with the issue of strong accumulation of particle agglomerates on certain points of the electrode as described in section 4.3.1.

Therefore, in a next step, an introduction of the samples *via in–situ* polymerisation of the $arylSnH_3$ was studied. It was already shown by Zeppek[72] that a dehydrogenative coupling reaction of aryltin trihydrides may be initiated by either temperature or by the addition of a Lewis base, *i.e.* TMEDA. Therefore, both of these methods were tested by the addition of the trihydride to graphite while stirring for at least 2 h (Figure 74). Preparation methods were varied into three different approaches carried out at room temperature: **A** neat $arylSnH_3$, **B** a solution of $arylSnH_3$ in Et_2O and **C** a solution of $arylSnH_3$ in Et_2O + 1.0 eq TMEDA. Representative results from galvanostatic experiments are shown in Figure 79, b). All samples showed a stable behaviour over the course of 100 cycles with coulombic efficiencies between 97 and 98%. Compared to the *ex-situ* prepared anode material with an average specific anodic capacity of 205 mAh g^{-1}, samples prepared according to approach **B** and **C** performed at average capacities of 167 mAh g^{-1} and 121 mAh g^{-1}, respectively. In case of approach **C,** a possible reason for the low capacity may be the high reaction speed induced by TMEDA which leads to an equally fast formation as well as agglomeration of the particles. An influence of the base on the electrochemical behaviour of graphite could be excluded as graphite blanks soaked with a few droplets of TMEDA did not show any differences in capacity when compared to the untreated ones. The lowest capacity was observed for the samples prepared in the ether solution. An agglomeration of the particles formed by temperature could possibly be affected by a slow evaporation of the solvent in combination with stirring: while the particles themselves are insoluble in common organic solvents their suspension during the polymerization process is still quite mobile. Once fixed to any position of the graphite it provides a target for agglomeration with particles suspended in the ether, accelerated by the movement of the suspension allowing for an agglomerate growth until complete evaporation of the solvent. By such a mechanism a passivation of the graphite surface as discussed before could take place.

The electrodes providing the highest capacities of an average of 303 mAh g^{-1} were prepared by mixing the pure $arylSnH_3$ with graphite at room temperature (Figure 74, a)). By this approach the reaction rate was fast enough to distribute particles homogeneously over the graphite while

being slow enough not to allow the formation of larger agglomerates. The tin distribution over the surface of an electrode was mapped using SEM/EDX showing a largely improved homogeneity (Figure 80).

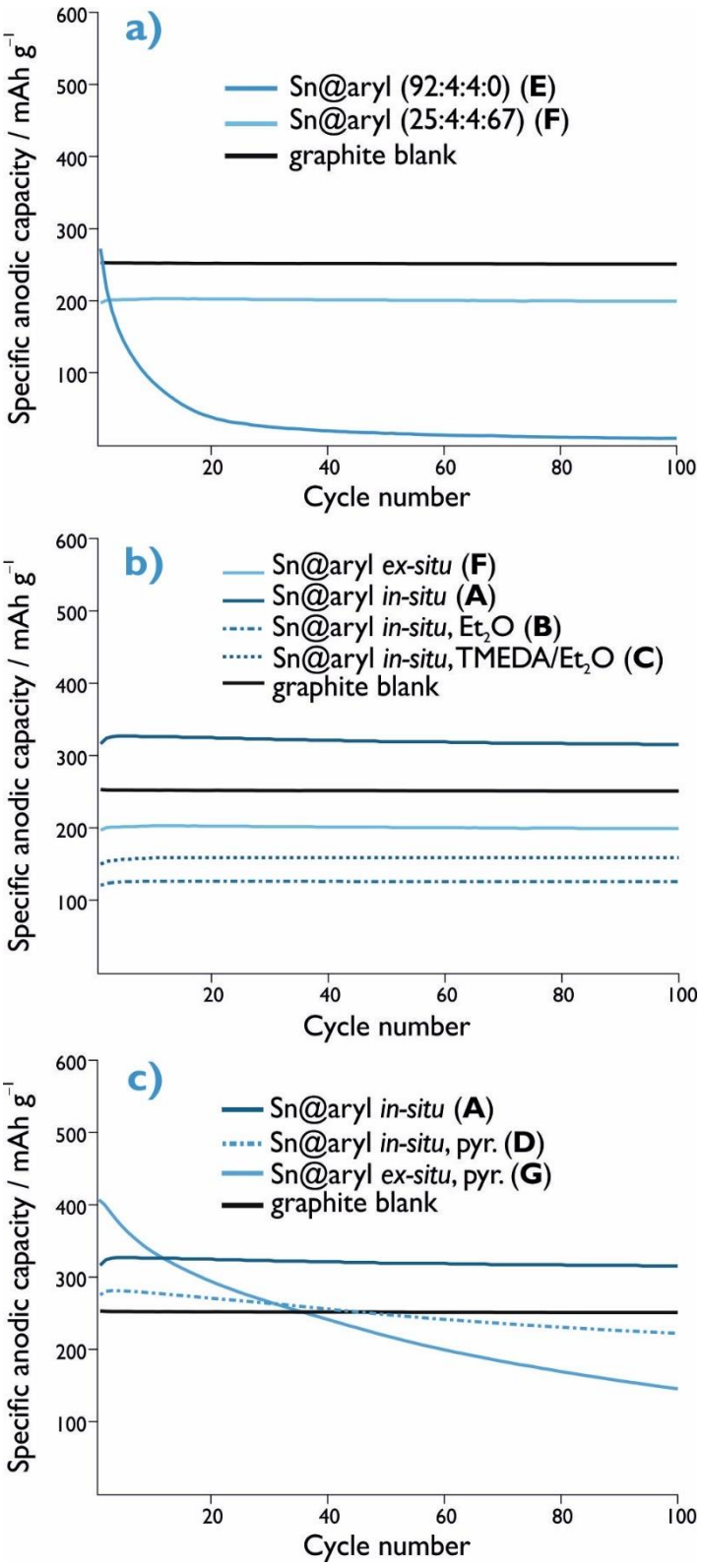

Figure 79 Specific anodic capacities determined by GCPL experiments. a) "neat" Sn@aryl electrodes (**E**) *vs.* Sn@aryl composite anodes with graphite (**F**). b) *ex-situ* (**F**) *vs.* differently *in-situ* prepared Sn@aryl composite anodes (**A**, **B** and **C**). c) untreated (**a**) *vs.* pyrolyzed *in-situ* (**D**) and *ex-situ* (**G**) prepared Sn@aryl anodes. All experiments were carried out applying a C–rate of C/2. Measurements were carried out in $LiPF_6$ in EC:DMC 1:1 (vol.) *vs.* Li.

Further experiments included the pyrolysis of the neatly *in-situ* prepared composites consisting of tin trihydride and graphite at 250 °C. Since preliminary SEM/EDX measurements confirmed only a morphological change for the trihydride particles at this temperature and no visible graphite change, electrodes with a ratio of trihydride:graphite:carbon black:binder of 46:46:4:4 (w/w) were prepared, with the expectation of a higher capacity resulting from additional 20%wt of the tin species. However, the resulting specific anodic capacities revealed quite the opposite effect: despite a minimally higher initial capacity of 285 mAh g^{-1} a continuous decay of the capacity is evident (Figure 79, c)). This effect is most likely caused by a combination of the elevated tin content of overall 36%wt as compared to the 20%wt investigated before and a slight alteration of surface. In case of the at 400 °C pyrolysed samples from *ex-situ* prepared composites (**g**) the decay of capacity is much more pronounced. Reason for this is the melting of the Sn in the particle agglomerates to large lumps, suffering all negative effects from lithiation.

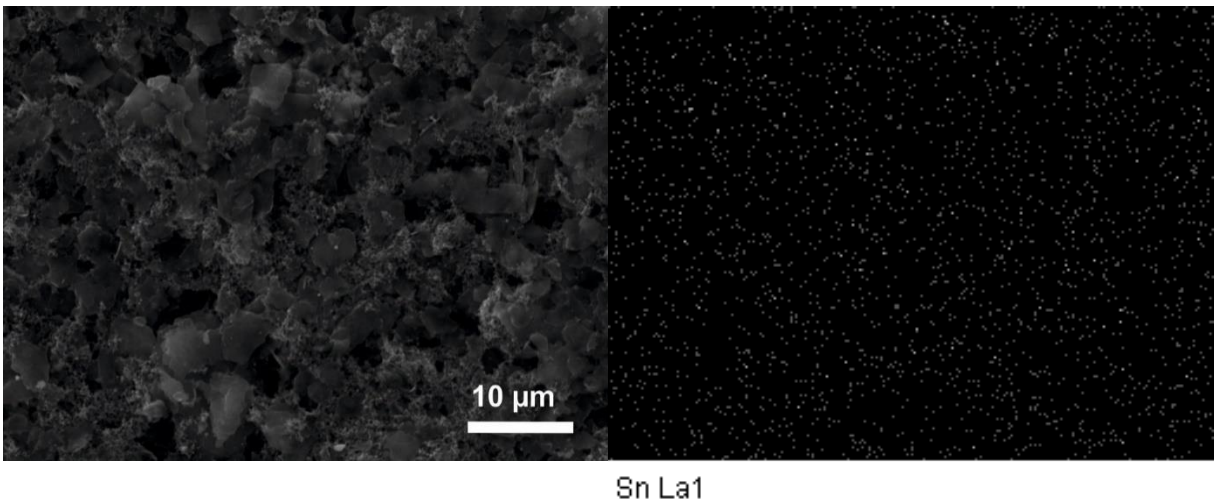

Figure 80 SEM/EDX (left) and EDX mapping (right) of the tin distribution in composite anodes containing tin prepared according to (**a**) (solvent free).

4.3.4 Summary of Li-Ion Batteries

In conclusion, the electrochemical behaviour of Sn@aryl particles in Li-ion batteries was investigated using cyclic voltammetry and constant current cycling as characterization methods. For this purpose, a method of carrying out the electrode preparation under inert atmosphere was developed and optimised. A need for graphite in the use as composite material became evident as it is required for the mitigation of the volume expansion of the tin particles occurring during the lithiation step proved in both, CV and GCPL, experiments. Furthermore, the presence of Sn^0 in the material was visualised using CV. The specific anodic capacities of Sn@aryl particles in graphite composite materials were determined by GCPL giving the best results when the pure arylSnH_3 was polymerised *in-situ* into the graphite. Thereby created electrodes yielded stable capacities reaching 303 mAh g^{-1}, hence being approximately 20% higher than the capacity reached by identically prepared graphite blanks (250 mAh g^{-1}).

4.4 Summary Stannanes

Aryltin di- and trihydrides were synthesised and the latter were polymerised *via* base-assisted dehydrogenative coupling according to literature procedures.[72] The pure aryltin hydrides were electrochemically characterised in a purpose-built CV cell under non-aqueous conditions. The oxygen-, temperature- and light-sensitive compounds displayed irreversible one or two electron oxidation processes, which led to a colouring of the sample solution to orange. This is most likely the result of a polymerisation reaction on the 20 μm Pt working electrode, covering its surface with insulating materials not unlike the polymers obtained by base-assisted dehydrogenative coupling (Sn@aryl).

In order to apply the latter in Li-ion batteries, several methods for introducing them into graphite were developed and tested under inert conditions. These methods included mixing of Sn@aryl materials with graphite and *in-situ* preparation of the Sn@aryl materials in graphite. The former resulted in inhomogeneous distribution of tin on the electrode surface due to strong agglomeration. Cyclic voltammetry experiments of *in-situ* generated Sn@aryl particles in composite anodes with graphite showed three distinct oxidation peaks, indicating the presence of Sn^0. The highest capacities could be gained by the same electrodes, yielding stable capacities of 303 mAh g^{-1}, being approximately 21% higher than the capacity reached by identically prepared graphite blanks (250 mAh g^{-1}).

These positive results could possibly be further enhanced by employing different aryl-substituents or *in-situ* generation of Sn@aryl materials in graphite or on graphene sheets *via* ultrasonication.

Experimental & Appendix

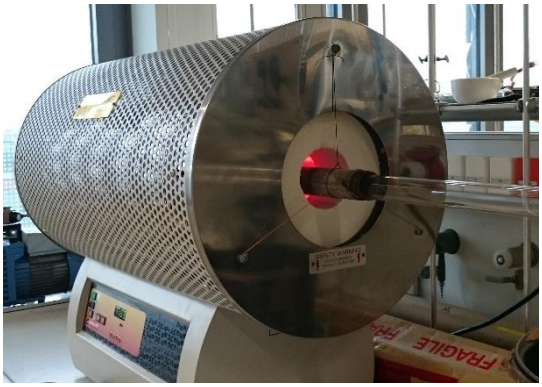

5 Experimental

5.1 Materials and Methods

NMR Spectroscopy

^{1}H (300.2 MHz), ^{13}C (75.5 MHz) and ^{29}Si (59.6 MHz) NMR spectra were recorded on a Mercury 300 MHz spectrometer from Varian at 25 °C. Chemical shifts are given in parts per million (ppm) relative to either TMS (δ = 0 ppm) or $CDCl_3$ (7.26 ppm for ^{1}H or 77.0 ppm for ^{13}C). Coupling constants (J) are reported in Hertz (Hz).

GC-MS Measurements

GCMS measurements were performed on an Agilent Technologies 7890A GC system with a HP–SMS column and a mass selective detector Type Agilent 5975C using electron impact ionisation (EI) at 70 eV.

Crystal Structure Determination

All crystals suitable for single crystal X–ray diffractometry were removed from a vial or a Schlenk and immediately covered with a layer of silicone oil. A single crystal was selected, mounted on a glass rod on a copper pin, and placed in the cold N_2 stream provided by an Oxford Cryosystems cryostream. XRD data collection was performed for compounds **1**, **3**, **4**, **7–9**, **14**, **18–25**, **29**, on a Bruker APEX II diffractometer with use of an Incoatec microfocus sealed tube of Mo Kα radiation (λ= 0.71073 Å) and a CCD area detector. Empirical absorption corrections were applied using SADABS or TWINABS.[208,209] The structures were solved with use of the intrinsic phasing option in SHELXT and refined by the full-matrix least-squares procedures in SHELXL.[210–212] The space group assignments and structural solutions were evaluated using PLATON.[213,214] The solvent of crystallization for compound 1-naphthyl$_2$phenyl$_2$Si (toluene) (**31**) was removed from the refinement by using the "squeeze" option available in the PLATON program suite.[215,216]

Non-hydrogen atoms were refined anisotropically. Hydrogen atoms bonded to silicon atoms were located in a difference map and refined isotropically. All other hydrogen atoms were located in calculated positions corresponding to standard bond lengths and angles and refined using a riding model. Disorder was handled by modeling the occupancies of the individual orientations using free variables to refine the respective occupancy of the affected fragments (PART).[217]

In compound **29**, the similar-ADP restraint SIMU and the rigid-bond restraint RIGU, were used to make the ADP values of problematic atoms in one of the naphthyl residues more reasonable. The distances between the atom pairs were restrained to possess the same value using the SADI instruction. Anisotropic U^{ij}-values of one naphthyl carbon atom was restrained (ISOR) to behave more isotropically. Additional restraints to afford optimized geometries (FLAT) were used.

Electrostatic non–covalent intermolecular interactions,[218–221]Van-der-Waals contacts (C–H···X),[222–224] Si–H···Si contacts,[225] for presented and published compounds were based on a Cambridge Structural Database[225] search and fall within expected ranges. Centroids and planes were

determined by features of the programs Mercury[226] and Diamond.[227] All crystal structures representations were made with the program Diamond. Tables containing crystallographic data and details of measurements and refinement for compounds may be found in the Appendix.

SEM/EDX

Scanning electron microscopy (SEM) analysis was performed on a Vega 3 SBU SEM with a tungsten hair-pin cathode. Non-conductive samples were sputtered with gold for topographic characterisation. Qualitative and quantitative analysis of the layers and particles was performed via energy dispersive X–ray microanalysis (EDX) (Oxford Instruments, model INCA X-act).

Small Angle X-Ray Scattering (SAXS)

The SAXS equipment consisted of a SAXSess camera (Anton–Paar, Graz, Austria). The X–ray source was a sealed tube X–ray generator (DebyeFlex3000) operating at 40 kV and 50 mA. The divergent polychromatic X–ray beam was focused into a line shaped beam of Cu Kα radiation (λ = 0.154 nm) with a Goebel mirror. A 1 D–Diode detector (Mythen 1K, Dectris, Swizerland) was used to record the two–dimensional scattering patterns. It has 1280 pixels each having a size of 50 μm. The scattering patterns were edited by correcting the cosmic X-ray impacts. The samples were filled into a capillary or a flow-through cell for *in-situ* measurements. Ten times 60 seconds measurements were recorded and averaged. In case of *in-situ* measurements they were recorded for 60 seconds without delay. All measurements were performed at 20 °C. The absolute scale calibration was achieved by using water as a secondary standard.[228] All SAXS data have been evaluated by an indirect Fourier transform (IFT) method,[229,230] using a model-free determination of P(Q) or a size distribution of spheres weighted by intensity[231] was calculated.

Complementary Techniques

Elemental analysis was performed on a VARIO micro cube (Elementar) with a CHN detector at 1200°C. All CHN contents were verified by threefold determination.

Melting point measurements were carried out by threefold determination with a Stuart Scientific SMP 50 (up to 400 °C).

Infrared spectra were recorded on a Bruker ALPHA FT-IR spectrometer with platinum-diamond top. For air-sensitive samples measurements took place in a glove-box.

TGA/DSC measurements were performed on a NETZSCH STA 409 under argon atmosphere at a heating rate of 10 °C min^{-1} up to 1500 °C.

5.2 Synthesis

5.2.1 Organosilicon Compounds

For arylsilicon chlorides from commercial sources only characterization is given below.

phenylSiCl$_3$: ^{1}H (CDCl$_3$, 300 MHz): δ = 7.91 (d, 2H, $^3J_{H–H}$ = 7.3 Hz), 7.67–7.54 (m, 3H) ppm. ^{13}C (CDCl$_3$, 75.5 MHz): δ = 133.2, 132.8, 131.6, 128.7 ppm, ^{29}Si (CDCl$_3$, 59.64 MHz): δ = –0.6 ppm. EA: 34.07% C, 2.38% H (calc.), 33.97% C, 2.29% H (found).

phenyl$_2$SiCl$_2$: ^{1}H (CDCl$_3$, 300 MHz): δ = 7.81 (d, 2H, $^3J_{H–H}$ = 7.5 Hz), 7.59–7.47 (m, 3H) ppm. ^{13}C (CDCl$_3$, 75.5 MHz): δ = 134.1, 132.0, 131.8, 128.4 ppm, ^{29}Si (CDCl$_3$, 59.64 MHz): δ = 6.21 ppm. EA: 56.92% C, 3.98% H (calc.), 56.87% C, 3.99% H (found).

phenyl$_3$SiCl: ^{1}H (CDCl$_3$, 300 MHz): δ = 7.66 (d, 6H, $^3J_{H–H}$ = 6.7 Hz), 7.52–7.40 (m, 9H) ppm. ^{13}C (CDCl$_3$, 75.5 MHz): δ = 135.2, 132.9, 130.7, 128.1 ppm, ^{29}Si (CDCl$_3$, 59.64 MHz): δ = 1.19 ppm. EA: 73.32% C, 5.13% H (calc.), 73.46% C, 4.76% H (found).

Preparation of $R_xSiCl_{4–x}$

$RSiCl_3$

The arylsilicon trichlorides were prepared by reaction of the respective Grignard reagent with a 4 to 6-fold excess of SiCl$_4$ in THF at 0 °C. In a typical reaction, a three–necked flask equipped with reflux condenser, dropping funnel and gas inlet was charged with Mg and Et$_2$O or THF. The dropping funnel was charged with an ethereal solution of the respective aryl bromide of which 10% were added to the Mg. The reaction was started with careful heating of the reaction mixture or by addition of 0.15 mL 1,2-dibromoethane. The aryl bromide solution was added slowly and upon complete addition the reaction was refluxed for 2-12 hours, until complete consumption of the Mg. The reaction mixture was allowed to warm to room temperature and was stirred for approximately 4 hours. The solvent was evaporated *in vacuo* and the solid residue dissolved in boiling toluene. The insoluble salts were filtered over Celite® and washed with hot toluene. The solvent of the resulting clear solution was evaporated under reduced pressure to give the product in form of a colourless liquid or solid. Purification was in all cases carried out by distillation.

Special care has to be directed at the evaporated THF, as, due to their similar boiling points, a separation of SiCl$_4$ and solvent is not possible. Therefore, the SiCl$_4$/THF solution has to be carefully quenched with alcohol and water.

2,5-xylylSiCl$_3$ (**1**): 2.67 mL 1-bromo-2,5-xylene (19.5 mmol, 1.0 eq) in 50 mL THF, 0.5 g Mg (21 mmol, 1.05 eq). 5.6 mL SiCl$_4$ (48.9 mmol, 2.5 eq). Yield: 72 % (3.3 g, 14 mmol). mp: 44 °C. ^{1}H (CDCl$_3$, 300 MHz): δ = 7.66 (s, 1H, *ortho*–H), 7.29 (d, 1H, $^3J_{H–H}$ = 8.3 Hz), 7.18 (d, 1H, $^3J_{H–H}$ = 7.7 Hz), 2.61 (s, 3H, C**H$_3$**), 2.37 (s, 3H, C**H$_3$**) ppm, ^{13}C (CDCl$_3$, 75.5 MHz): δ = 140.7, 135.3, 135.2, 133.9, 131.4, 129.3, 22.2, 21.1 ppm, ^{29}Si (CDCl$_3$, 59.64 MHz): δ = –0.91 ppm. GC-MS: t_r = 9.45 min, m/z = 238.0 (M^+). EA: 40.10% C, 3.79% H (calc.), 40.55% C, 3l87% H (found).

1-naphthylSiCl$_3$ (**2**): 24.3 mL 1-bromonaphthalene (173.5 mmol, 1.0 eq) in 80 mL THF, 4.64 g Mg (191 mmol, 1.1 eq) in 100 mL THF. 119.5 mL $SiCl_4$ (1.041 mol, 6.0 eq). Yield: 65 % (29.85 g, 114 mmol). mp: 46 °C. ^{1}H ($CDCl_3$, 300 MHz): δ = 8.45 (d, 1H, $^3J_{H–H}$ = 8.4 Hz), 8.17 (d, 1H, $^3J_{H–H}$ = 7.1 Hz, $^4J_{H-H}$ = 0.9 Hz), 8.08 (d, 1H, $^3J_{H–H}$ = 8.2 Hz), 7.95 (d, 1H, $^3J_{H–H}$ = 7.8 Hz), 7.68–7.50 (m, 3H) ppm, ^{13}C ($CDCl_3$, 75.5 MHz): δ = 135.6, 134.5, 134.2, 133.7, 129.5, 128.0, 127.6, 127.2, 126.7, 124.7 ppm, ^{29}Si ($CDCl_3$, 59.64 MHz): δ = –0.87 ppm. GC-MS: t_r = 11.9 min, m/z = 260.0 (M^+). EA: 80.97% C, 4.76% H (calc.), 80.99% C, 4.84% H (found).

R_2SiCl_2

Diarylsilicon dichlorides were prepared *via* a lithiation reaction with *n*–butyl lithium.

2,5-xylyl$_2$SiCl$_2$ (**3**): 6.9 mL 1-bromo-2,5-xylene (50 mmol, 2.0 eq) in 40 mL Et_2O, 34.7 mL *n*-BuLi (1.6 M, 55 mmol, 2.2 eq). 2.87 mL $SiCl_4$ (25 mmol, 1.0 eq). Yield: 57 % (8.8 g, 28.5 mmol). mp: 63 °C. ^{1}H ($CDCl_3$, 300 MHz): δ = 7.7 (s, 1H, *ortho*–H), 7.25 (d, 1H, $^3J_{H–H}$ = 8.2 Hz), 7.22–7.08 (m, 1H), 2.35 (s, 3H, C**H$_3$**), 2.29 (s, 3H, C**H$_3$**) ppm, ^{13}C ($CDCl_3$, 75.5 MHz): δ = 140.6, 135.8, 135.1, 132.8, 131.7, 130.8, 22.4 (*meta*–CH3), 22.3 (*ortho*–CH_3) ppm, ^{29}Si ($CDCl_3$, 59.64 MHz): δ = 6.4 ppm. GC-MS: t_r = 14.4 min, m/z = 308.1 (M^+). EA: 62.13% C, 5.87% H (calc.), 62.26% C, 5.76% H (found).

1-naphthyl(phenyl)SiCl$_2$ (**4**): 70 mL 1-bromonaphthalene (500 mmol, 1.0 eq) in 250 mL Et_2O, 220 mL *n*-BuLi (1.6 M, 550 mmol, 1.1 eq). 160 mL phenylSiCl$_3$ (1 mol, 2.0 eq). Yield: 44 % (67.4 g, 222 mmol). mp: 72 °C. ^{1}H ($CDCl_3$, 300 MHz): δ = 8.17 (d, 1H, $^3J_{H–H}$ = 7.7 Hz), 8.01 (t, 2H, $^3J_{H–H}$ = 8.8 Hz), 7.90 (d, 1H, $^3J_{H–H}$ = 8.1 Hz, $^4J_{H-H}$ = 1.6 Hz), 7.77 (d, 2H, $^3J_{H–H}$ = 6.8 Hz), 7.54–7.42 (m, 6H) ppm, ^{13}C ($CDCl_3$, 75.5 MHz): δ = 136.4, 135.4, 134.0, 133.5, 133.1, 131.7, 129.1, 128.6, 128.4, 127.9, 126.8, 126.1, 124.8 ppm, ^{29}Si ($CDCl_3$, 59.64 MHz): δ = 6.89 ppm. GC-MS: t_r = 19.9 min, m/z = 302.2 (M^+). EA: 63.37% C, 3.99% H (calc.), 63.72% C, 3.78% H (found).

1-naphthyl$_2$SiCl$_2$ (**5**): 14 mL 1-bromonaphthalene (100 mmol, 1.0 eq) in 100 mL Et_2O, 57.1 mL *n*-BuLi (1.8 M, 105 mmol, 1.05 eq). 5.74 mL $SiCl_4$ (50 mmol, 0.5 eq). Yield: 59 % (20.8 g, 59 mmol). mp: 150 °C. ^{1}H ($CDCl_3$, 300 MHz): δ = 8.27 (d, 2H, $^3J_{H–H}$ = 8.2 Hz), 8.12 (d, 2H, $^3J_{H–H}$ = 7.1 Hz), 8.06 (d, 2H, $^3J_{H–H}$ = 8.2 Hz), 7.92 (d, 2H, $^3J_{H–H}$ = 7.9 Hz), 7.56–7.43 (m, 6H) ppm, ^{13}C ($CDCl_3$, 75.5 MHz): δ = 136.2, 135.6, 133.7, 133.2, 129.7, 129.3, 128.1, 127.0, 126.4, 125.2 ppm, ^{29}Si ($CDCl_3$, 59.64 MHz): δ = 7.34 ppm. GC-MS: t_r = 21.6 min, m/z = 352.1 (M^+). EA: 67.99% C, 3.99% H (calc.), 68.21% C, 4.07% H (found).

R_3SiCl

An oven–dried Schlenk flask was charged with a solution of the aryl bromide in Et_2O, cooled to –78 °C and *n*–butyl lithium was added dropwise using a syringe. The reaction solution was stirred for 1 h and allowed to warm to room temperature. In a second flask, the educt chlorosilane was dissolved in Et_2O and cooled to 0°C. The lithiated species was transferred slowly *via* a cannula, the resulting suspension was stirred for 1 h at room temperature. The solvent was evaporated *in vacuo*, the colourless solid residue taken up in hot toluene and the insoluble salts filtered over Celite®. The solvent was evaporated and the resulting product recrystallized from toluene, THF or ethyl acetate.

2,5-xylyl$_3$SiCl (**6**): 10.3 mL 1-bromo-2,5-xylene (75 mmol, 3.0 eq) in 150 mL Et_2O, 45.0 mL *n*-BuLi (2.0 M, 90 mmol, 3.6 eq). 2.86 mL $SiCl_4$ (25 mmol, 1.0 eq). Yield: 52 % (4.9 g, 13 mmol). mp: 110 °C. ^{1}H ($CDCl_3$, 300 MHz): δ =7.26 (d, 3H, $^3J_{H–H}$ = 2.4 Hz), 7.19 (d, 3H, $^3J_{H–H}$ = 8.1 Hz), 7.09 (d, 3H, $^3J_{H–H}$ =

8.1 Hz), 2.28 (s, 9H, C**H**$_3$), 2.25 (s, 9H, C**H**$_3$) ppm, ^{13}C ($CDCl_3$, 75.5 MHz): δ = 141.7, 137.0, 135.0, 134.5, 132.7, 131.7, 131.6, 130.8 ,130.6 ppm, ^{29}Si ($CDCl_3$, 59.64 MHz): δ = 2.9 ppm. GC-MS: t_r = 17.7 min, m/z = 378.2 (M^+). EA: 76.06% C, 7.18% H (calc.), 76.11% C, 7.26% H (found).

1-naphthyl(phenyl)$_2$SiCl (**7**): 4.05 mL 1–bromonaphthalene (1.0 eq, 29 mmol) in 50 mL Et_2O, 19.9 mL *n*-BuLi (1.1 eq, 31.8 mmol), 6.1 mL Ph_2SiCl_2 (1.0 eq, 29 mmol) in 30 mL Et_2O. Yield: 80 % (9.2 g, 23.2 mmol) of colourless crystals. mp: 111°C, ^{1}H NMR ($CDCl_3$, 200 MHz): δ 8.10 (d, 1H, $^3J_{H-H}$ = 8.5 Hz), 8.0 (d, 1H, $^3J_{H-H}$ = 8.1 Hz), 7.90 (d, 1H, $^3J_{H-H}$ = 8.1 Hz), 7.67 (d, 4H, $^3J_{H-H}$ = 7.7 Hz), 7.62 (d, 1H, $^3J_{H-H}$ = 7.0 Hz), 7.50-7.35 (m, 9H) ppm. ^{13}C NMR ($CDCl_3$, 75.5 MHz): δ 137.48, 136.56, 135.39, 133.54, 130.83, 130.37, 129.09, 128.32, 126.42, 126.04, 125.04 ppm. ^{29}Si NMR ($CDCl_3$, 59.64): δ 2.43 ppm. GC-MS: t_r = 18.99, m/z = 344.1. EA: 79.07% C, 4.85% H (calc.). 78.6% C, 4.94% H (found).

1-naphthyl$_2$(phenyl)SiCl (**8**): 7.08 mL 1–bromonaphthalene (2.0 eq, 50.6 mmol) in 50 mL Et_2O, 34.8 mL *n*-BuLi (2.1 eq, 55.6 mmol), 4.06 mL $PhSiCl_3$ (1.0 eq, 25.3 mmol) in 30 mL Et_2O. Yield: 87 % (8.7 g, 22.0 mmol) of colourless crystals. mp: 171°C. ^{1}H NMR ($CDCl_3$, 300 MHz): δ = 8.21 (d, 2H, $^3J_{H-H}$ = 8.6 Hz), 7.99 (d, 2H, $^3J_{H-H}$ = 8.4 Hz), 7.91 (d, 2H, $^3J_{H-H}$ = 8.4 Hz), 7.67 (t, 4H, $^3J_{H-H}$ = 7.1 Hz), 7.50-7.46 (m, 3H), 7.43 (m, 6H) ppm, ^{13}C NMR ($CDCl_3$, 75.5 MHz): δ = 137.18, 136.42, 135.44, 133.57, 132.03, 130.73, 128.99, 128.21, 126.28, 125.89, 124.97 ppm, ^{29}Si NMR ($CDCl_3$, 59.64 MHz): δ = 3.12 ppm. GC-MS: t_r = 21.9 min, m/z = 394.1. EA: 79.07% C, 4.85% H (calc.), 78.92% C, 4.92% H (found).

1-naphthyl$_3$SiCl (**9**): 24.8 mL 1-bromonaphthalene (3.0 eq, 177 mmol) in 200 ml Et_2O, 73.5 mL *n*-BuLi (3.1 eq, 183 mmol), 6.75 ml $SiCl_4$ (1.0 eq, 59 mmol) in 200 ml Et_2O. Yield: 71 % (18.6 g, 41.8 mmol) of colourless crystals. mp: 207°C. ^{1}H ($CDCl_3$, 300 MHz): δ = 8.34-8.31 (d, 3H, $^3J_{H-H}$ = 8.5 Hz), 8.02-8.00 (d, 3H, $^3J_{H-H}$ = 8.3 Hz), 7.94-7.91 (d, 3H, $^3J_{H-H}$ = 8.1 Hz), 7.75-7.73 (d, 3H, $^3J_{H-H}$ = 6.6 Hz), 7.49 (t, 3H, $^3J_{H-H}$ = 7.5 Hz), 7.39-7.26 (m, 6H) ppm, ^{13}C ($CDCl_3$, 75.5 MHz): δ = 137.6, 136.6, 133.8, 132.2, 130.9, 129.3, 129.1, 126.4, 126.0, 125.2 ppm, ^{29}Si ($CDCl_3$, 59.64 MHz): δ = 3.69 ppm. GC-MS: t_r = 26.5 min, m/z = 444.2. EA: 80.97% C, 4.76% H (calc.), 80.32% C, 5.01% H (found).

Preparation of R_xSiH_{4-x}

Method ***A***: An oven-dried Schlenk flask was charged with the triarylchloro silane dissolved in Et_2O and THF (vol 1:1). The solution was cooled to 0 °C and the $LiAlH_4$ was carefully added portion-wise.

Method ***B***: An oven–dried three–necked flask, equipped with a dropping funnel, was charged with a suspension of $LiAlH_4$ in dry Et_2O and cooled to 0 °C. A solution of the educt arylchlorosilane in dry Et_2O was added dropwise.

Upon complete addition, the reaction mixture was stirred for 1 h and allowed to warm to room temperature. To quench the excess of $LiAlH_4$ the greyish suspension was cooled to 0°C and diluted, degassed H_2SO_4 (10%) was added. The phases were separated *via* cannula, and the aqueous phase washed with THF or Et_2O twice. The combined organic phases were extracted with saturated potassium tartrate in degassed, deionised water and the resulting organic phase dried over $CaCl_2$. After filtering off and washing the drying agent twice with Et_2O, the solvent was evaporated *in vacuo* and the resulting colourless product recrystallised from toluene, THF or ethyl acetate.

$RSiH_3$

The arylsilicon trihydrides were prepared according to Method ***A*** and occur as liquids.

phenylSiH$_3$ (10): 2.96 mL phenylSiCl$_3$ (18.5 mmol, 1.0 eq) in 20 mL Et$_2$O, 0.84 g LiAlH$_4$ (22.2 mmol, 1.2 eq). Yield: 80% (1.6 g, 14.8 mmol). ^{1}H (CDCl$_3$, 300 MHz): δ = 7.63 (d, 2H, $^1J_{H-H}$ = Hz), 7.4 (m, 3H), 4.24 (s, 3H, $^1J_{Si-H}$ = 200.7 Hz) ppm. ^{13}C (CDCl$_3$, 75.5 MHz): δ = 135.9, 134.2, 129.9, 128.3 ppm. ^{29}Si (CDCl$_3$, 59.64 MHz): δ = –59.2 ppm. GC-MS: t_r = 7.59 min, m/z = 108.1. EA: 80.02% C, 6.19% H (calc.), 80.01% C, 6.15% H (found).

2,5-xylylSiH$_3$ (11): 4.8 g 2,5-xylylSiCl$_3$ (20 mmol, 1.0 eq) in 20 mL Et$_2$O, 0.91 g LiAlH$_4$ (24 mmol, 1.2 eq). Yield: 83% (2.26 g, 16.6 mmol). ^{1}H (CDCl$_3$, 300 MHz): δ = 7.46 (s, 1H, *ortho*–H), 7.21 (d, 1H, $^3J_{H-H}$ = 8.0 Hz), 7.14 (d, 1H, $^3J_{H-H}$ = 7.8 Hz), 4.25 (s, 3H, $^1J_{Si-H}$ = 200.15 Hz), 2.46 (s, 3H, C**H$_3$**), 2.38 (s, 3H, C**H$_3$**) ppm, ^{13}C (CDCl$_3$, 75.5 MHz): δ = 141.8, 138.4, 135.1, 131.8, 129.7, 128.5, 22.6, 21.4 ppm, 29Si (CDCl3, 59.64 MHz): δ = –62.9 ppm. GC-MS: t_r = 8.61 min, m/z = 136.1. EA: 70.51% C, 8.88% H (calc.), 70.54% C, 8.99% H (found).

1-naphthylSiH$_3$ (12): 25 g 1-naphthylSiCl$_3$ (95.6 mmol, 1.0 eq) in 200 mL Et$_2$O, 5.0 g LiAlH$_4$ (133.8 mmol, 1.4 eq). Yield: 80% (12.23 g, 76.4 mmol). ^{1}H (CDCl$_3$, 300 MHz): δ =8.06 (d, 1H, $^3J_{H-H}$ = 7.8 Hz), 8.0 (d, 1H, $^3J_{H-H}$ = 8.3 Hz), 7.95–7.90 (t, 2H, $^3J_{H-H}$ = 7.1 Hz), 7.66–7.50 (m, 3H), 4.59(s, 3H, $^1J_{Si-H}$= 201.3 Hz) ppm, ^{13}C (CDCl$_3$, 75.5 MHz): δ = 137.5, 136.9, 133.1, 131.0, 128.9, 127.9, 127,4., 126.5, 126.0, 125.4 ppm, ^{29}Si (CDCl$_3$, 59.64 MHz): δ = –61.7 ppm. GC-MS: t_r = 9.08 min, m/z = 158.1. EA: 75.89% C, 6.37% H (calc.), 74.35% C, 6.08% H (found).

R_2SiH_2

The diarylsilicon dihydrides compounds were prepared according to Method ***B***.

phenyl$_2$SiH$_2$ (13): 2.3 mL phenyl$_2$SiCl$_2$ (8.5 mmol, 1.0 eq) in 25 mL Et$_2$O, 0.49 g LiAlH$_4$ (13 mmol, 1.2 eq). Yield: 78% (0.72 g, 6.6 mmol). ^{1}H (CDCl$_3$, 300 MHz): δ = 7.66 (d, 4H, $^3J_{H-H}$ = 7.1 Hz), 7.47–7.25 (m, 6H), 4.99 (s, 2H, $^1J_{Si-H}$ = 199.6 Hz) ppm, ^{13}C (CDCl$_3$, 75.5 MHz): δ =135.7, 131.6, 129.9, 128.2 ppm, ^{29}Si (CDCl$_3$, 59.64 MHz): δ = –33.4 ppm. GC-MS: t_r = 9.74 min, m/z = 184.2. EA: 78.20% C, 6.56% H (calc.), 78.12% C, 6.56% H (found).

2,5-xylyl$_2$SiH$_2$ (14): 5 g 2,5xylyl$_2$SiCl$_2$ (16.1 mmol, 1.0 eq) in 25 mL Et$_2$O, 0.74 g LiAlH$_4$ (19.4 mmol, 1.2 eq). Yield: 77% (2.98 g, 12.4 mmol). mp: 63 °C. ^{1}H (CDCl$_3$, 300 MHz): δ = 7.30 (s, 2H, *ortho*–H), 7.15 (d, 2H, $^3J_{H-H}$ = 7.8 Hz), 7.09 (d, 2H, $^3J_{H-H}$ = 7.9 Hz, $^4J_{H-H}$ = 1.8 Hz),4.93 (s, 2H, $^1J_{Si-H}$ = 197.12 Hz), 2.37 (s, 6H, *meta*–C**H$_3$**), 2.29 (s, 6H, *ortho*–C**H$_3$**) ppm, ^{13}C (CDCl$_3$, 75.5 MHz): δ = 141.5, 137.6, 134.6, 131.1, 130.7, 129.5, 22.1 (*meta*–**C**H$_3$) , 21.1 (*ortho*–**C**H$_3$) ppm, ^{29}Si (CDCl$_3$, 59.64 MHz): δ = –39.5 ppm. GC-MS: t_r = 12.7 min, m/z = 240.1 (M^+). EA: 79.93% C, 8.39% H (calc.), 79.98% C, 8.43% H (found).

1-naphthyl(phenyl)SiH$_2$ (15): 15.16 g 1-naphthyl(phenyl)SiCl$_2$ (50 mmol, 1.0 eq) in 25 mL Et$_2$O, 2.28 g LiAlH$_4$ (60 mmol, 1.2 eq). Yield: 74% (8.7 g, 37 mmol). ^{1}H (CDCl$_3$, 300 MHz): δ = 8.09 (m, 1H), 7.98 (d, 1H, $^3J_{H-H}$ = 8.3 Hz), 7.93–7.86 (m, 2H), 7.67 (d, 2H, $^3J_{H-H}$ = 7.1 Hz), 7.54–7.45 (m, 3H), 7.43–7.37 (m, 3H), 5.31 (s, 2H, $^1J_{Si-H}$ = 200.0 Hz) ppm, ^{13}C (CDCl$_3$, 75.5 MHz): δ = 137.0, 135.8, 131.1,

130.0, 129.0, 128.3, 128.1, 126.5, 126.0, 125.5 ppm ^{29}Si ($CDCl_3$, 59.64 MHz): δ = –35.9 ppm. GC-MS: t_r = 14.12 min, m/z = 234.1. EA: 82.00% C, 6.02% H (calc.), 81.36% C, 5.86% H (found).

1-naphthyl$_2$SiH$_2$ (**16**): 12 g 1-naphthyl$_2$SiCl$_2$ (33.9 mmol, 1.0 eq) in 25 mL Et_2O, 1.4 g $LiAlH_4$ (13 mmol, 1.1 eq). Yield: 81% (7.8 g, 27.4 mmol). mp: 100.5 °C. ^{1}H ($CDCl_3$, 300 MHz): δ = 8.16 (d, 2H, $^3J_{H–H}$ = 8.8 Hz), 7.97 (d, 2H, $^3J_{H–H}$ = 8.4 Hz), 7.92 (d, 2H, $^3J_{H–H}$ = 8.8 Hz), 7.80 (d, 2H, $^3J_{H–H}$ = 6.8 Hz), 7.55–7.44 (m, 6H), 5.60 (s, 2H,, $^1J_{Si–H}$ = 200.6 Hz) ppm, ^{13}C ($CDCl_3$, 75.5 MHz): δ = 137.6, 137.1, 133.3, 131.1, 129.8, 129.0, 128.1, 126.5, 126.0, 125.6 ppm, ^{29}Si ($CDCl_3$, 59.64 MHz): δ = –38.7 ppm. GC-MS: t_r = 18.11 min, m/z = 284.1. EA: 84.46% C, 5.67% H (calc.), 83.93% C, 5.56% H (found).

R_3SiH

The triarylsilicon hydrides were mostly prepared according to Method ***B***. Due to the low solubility of triarylsilicon chlorides carrying at least one 1-naphthyl moiety in Et_2O, THF and/or toluene were used as supporting solvents.

phenyl$_3$SiH (**17**): The compound was prepared according to literature. The spectroscopic data is in full agreement with literature data.[153] mp: 42 °C. ^{1}H ($CDCl_3$, 300 MHz): δ = 7.66 (d, 6H, $^3J_{H–H}$ = 7.4 Hz), 7.51–7.41 (m, 9H), 5.57 (s, 1H, $^1J_{Si–H}$ = 199.1 Hz) ppm. ^{13}C ($CDCl_3$, 75.5 MHz): δ = 135.9, 133.4, 130.0, 128.21 ppm, ^{29}Si ($CDCl_3$, 59.64 MHz): δ = –18.1 ppm. GC-MS: t_r = 14.5 min, m/z = 260.1(M^+). EA: 83.02% C, 6.19% H (calc.), 83.04% C, 5.64% H (found).

2,5-xylyl$_3$SiH (**18**): 2 g 2,5-xylyl$_3$SiCl (5.3 mmol, 1.0 eq) in 25 mL Et_2O, 0.24 g $LiAlH_4$ (6.3 mmol, 1.2 eq). Yield: 47% (0.86 g, 27.4 mmol). mp: 162 °C. ^{1}H ($CDCl_3$, 300 MHz): δ = 7.13 (s, 3H, *ortho*–H), 6.79–6.69 (m, 6H), 5.80 (s, 2H, $^1J_{Si–H}$ = 196.80 Hz), 2.12 (s, 9H, *meta*–C**H$_3$**), 1.70 (s, 9H, *ortho*–C**H$_3$**) ppm, ^{13}C ($CDCl_3$, 75.5 MHz): δ = 141.5, 137.6, 134.6, 131.1, 130.7, 129.5, 22.1 (*meta*–**C**H$_3$) , 21.1 (*ortho*–**C**H$_3$) ppm ^{29}Si ($CDCl_3$, 59.64 MHz): δ = –28.7 ppm. GC-MS: t_r = 16.6 min, m/z = 344.2. EA: 83.66% C, 8.19% H (calc.), 84.01% C, 8.25% H (found).

1-naphthyl(phenyl)$_2$SiH (**19**): 3 g **7** (8.7 mmol, 1.0 eq) in 20 mL Et_2O and 20 mL toluene, 0.66g $LiAlH_4$ (17.4 mmol, 2.0 eq) at 0 °C. Yield 33% (1 g, 2.9 mmol). mp: 92 °C. ^{1}H NMR ($CDCl_3$, 300 MHz): δ = 8.08 (d, 1H, $^3J_{H–H}$ = 8.5 Hz), 7.95 (d, 1H, $^3J_{H–H}$ = 8.2 Hz), 7.90 (d, 1H, $^3J_{H–H}$ = 8.4Hz), 7.64–7.59 (m, 5H), 7.49–7.36 (m, 9H), 5.93 (s, 1H, $^1J_{Si–H}$ = 199.0 Hz) ppm; ^{13}C ($CDCl_3$, 75.5 MHz): δ = 137.4, 136.9, 136.1, 133.3, 130.9, 129.9, 128.9, 128.3, 128.2, 126.3, 125.8, 125.4 ppm; ^{29}Si ($CDCl_3$, 59.64 MHz): δ = –20.7 ppm. GC-MS: t_r = 18.19 min, m/z = 310.1. EA: 85.11%C, 5.53% H (calc.), 86.29% C, 5.66% H (found).

1-naphthyl$_2$(phenyl)SiH (**20**): 1.5 g **8** (1.0 eq, 3.8 mmol) in 28 mL Et_2O and 12 mL toluene, 0.35 g $LiAlH_4$ (2.0 eq, 7.6 mmol). 10 mL H2SO4, 10 mL aqueous, degassed potassium tartrate solution (sat.). Yield: 60% (0.85 g, 2.3 mmol) of colourless crystals .mp: 169°C. ^{1}H NMR ($CDCl_3$, 300 MHz): δ = 8.12 (d, 2H, $^3J_{H–H}$ = 8.5 Hz), 7.96 (d, 2H, $^3J_{H–H}$ = 8.4 Hz), 7.929 (d, 2H, $^3J_{H–H}$ = 8.1 Hz), 7.61 (d, 2H, $^3J_{H–H}$ = 7.5 Hz), 7.57 (d, 2H, $^3J_{H–H}$ = 6.7 Hz), 7.53-7.35 (m, 9H), 6.38 (s, ^{1}H, $^1J_{SiH}$ = 196.5 Hz) ppm; ^{13}C ($CDCl_3$, 75.5 MHz): δ = 137.5, 137.2, 136.3, 133.4, 133.2, 131.3, 130.9, 129.9, 128.9, 128.4, 128.2, 126.3, 125.8, 125.4 ppm; ^{29}Si ($CDCl_3$, 59.64 MHz): δ = –24.5 ppm. GC-MS: tr = 21.31 min, m/z = 360.2. EA: 86.62% C, 5.59% H (calc.), 86.12% C, 5.53 % H (found).

1-naphthyl$_3$SiH (**21**): 10 g **9** (1.0 eq, 22.4 mmol) in 150 mL THF and 20 mL toluene 2.16 g $LiAlH_4$ (2.5 eq, 56,9 mmol). 50 mL H_2SO_4, 40 mL aqueous, degassed potassium tartrate solution (sat.). Yield: 78% (7.25 g, 17.6 mmol) of colourless crystals. mp: 237 °C. ^{1}H NMR ($CDCl_3$, 300 MHz): δ =

8.18 (d, 3H, $^{3}J_{H-H}$ = 8.3 Hz), 7.93 (t, 6H, $^{3}J_{H-H}$ = 9.2 Hz), 7.52-7.48 (m, 6H), 7.42-7.32 (m, 6H), 6.52 (s, 1H, $^{1}J_{SiH}$ = 196.6 Hz) ppm; ^{13}C ($CDCl_3$, 75.5 MHz): δ = 137.5, 133.5, 131.0, 19.0, 128.6, 126.3, 125.9, 125.6 ppm; ^{29}Si ($CDCl_3$, 59.64 MHz): δ = –28.9 ppm. GC-MS: tr = 25.3 min, m/z = 410.2. EA: 87.76% C, 5.40% H (calc.), 87.77% C, 5.50% H (found).

Preparation of R_3(allyl)Si

An oven–dried flask equipped with a reflux condenser was charged with Mg^0 and Et_2O. After the addition of approximately 10% of the allylchloride, the suspension was warmed up carefully to initiate the reaction. Upon complete addition, the reaction was stirred at room temperature for 1.5 to 24 h. The concentration of the Grignard reagent was determined by diluting a small volume of the solution with deionised water and titration with HCl, using phenolphthalein as indicator. In a second flask the chlorotriaryl silane was dissolved in THF and Et_2O (Vol. 1:1) and subsequently transferred drop–wise onto the Grignard reagent using a syringe. The reaction suspension was stirred overnight and the excess of Grignard reagent was quenched with deionised water. The phases were extracted twice, the combined organic phases dried over Na_2SO_4, filtered and the solvent was evaporated *in vacuo*. Purification of the product was carried out by crystallisation from either Et_2O or toluene.
Additionally, NMR were recorded in acetone d_6 for easier comparison to the sensitive dihydropyridazine products.

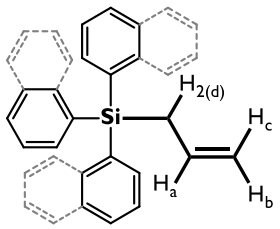

Scheme 7 Schematic representation of triaryl(allyl)silane for the assignment of coupling constants.

phenyl$_3$(allyl)Si (**22**): 0.5 g Mg (1.8 eq, 20.6 mmol) in 35 mL Et_2O, 1.60 mL allylchloride (1.7 eq, 19.6 mmol), 3.32 g phenyl$_3$SiCl (1.0 eq, 11.3 mmol) in 51 mL Et_2O. Yield: 73% (2.51g, 8.3 mmol) mp: 91 °C. ^{1}H NMR ($CDCl_3$, 300.2 MHz): δ 7.53 (d, 6H, $^{3}J_{H-H}$ = 6.5 Hz), 7.44-7.36 (m, 9H), 5.87 (ddt, 1H, C**H$_a$**=CH$_2$), 4.99 (dd, 2H, $^{3}J_{Ha-Hb}$ = 10.9 Hz CH=C**H$_b$**H$_c$, $^{3}J_{Ha-Hc}$ = 18.3 Hz, CH=C**H$_c$**H$_b$), 2.43 (d, 2H, $^{3}J_{Ha-Hd}$ = 7.8 Hz, C**H$_{2(d)}$**-CH=CH$_2$) ppm. ^{13}C NMR ($CDCl_3$, 75.5 MHz): δ 135.87, 134.69, 133.92, 129.67, 127.96, 115.21, 21.33 ppm. ^{29}Si NMR ($CDCl_3$, 59.64): δ –13.8 ppm GC-MS: t_r = 15.95 min, m/z = 300. 1.. EA: 83.94%C, 6.71%H (calc.), 83.94% C, 6.61% H (found).

^{1}H NMR (acetone d_6, 300.2 MHz): δ 7.54-7.51 (d, 6H), 7.44-7.34 (m, 9H), 5.91-5.77 (m, 1H, C**H**=CH$_2$), 4.96-4.81 (dd, 2H, CH=C**H$_2$**), 2.43 (d, 2H, C**H$_2$**-CH=CH$_2$) ppm. ^{13}C NMR (acetone d_6, 75.5 MHz): δ 136.2 (6C), 135.2 (q, 2C), 134.5 (q, 1C), 130.2 (3C), 128.5 (6C), 115.1 (1C), 21.3 (1C) ppm. ^{29}Si NMR (acetone d_6, 59.6 MHz): δ -13.8 ppm

1-naphthyl(phenyl)$_2$(allyl)Si (**23**): 0.89 g Mg (2.5 eq, 36.6 mmol) in 45 mL Et_2O, 2.84 mL allylchloride (2.4 eq, 34.9mmol). 5g **7** (1.0 eq, 14.5 mmol) in 15 mL THF and 15 mL Et_2O. Yield: 36% (1.8 g, 5.1 mmol). mp: 188 °C. ^{1}H NMR ($CDCl_3$, 300.2 MHz): δ 7.94 (d, 2H, $^{3}J_{H-H}$ = 7.2 Hz), 7.88 (d, 2H, $^{3}J_{H-H}$ = 9.3 Hz), 7.63 (d, 2H, $^{3}J_{H-H}$ = 7.5 Hz), 7.58 (d, 2H, $^{3}J_{H-H}$ = 7.2 Hz), 7.46-7.33 (m, 9H), 5.85 (ddt, 1H, C**H$_a$**=CH$_2$), 4.96 (d, 1H, $^{3}J_{Ha-Hc}$ = 16.8 Hz, CH=C**H$_c$**H$_b$), 4.85 (d, 1H, $^{3}J_{Ha-Hb}$ = 10.2 Hz,

CH=C**H**$_b$H$_c$), 2.57 (d, 2H, $^3J_{Ha–Hd}$ = 7.6 Hz, C**H**$_{2(d)}$-CH=CH$_2$) ppm. ^{13}C NMR ($CDCl_3$, 75.5 MHz): δ 137.34, 137.00, 135.90, 135.30, 133.59, 130.83, 129.63, 129.31, 129.03, 128.03, 125.82, 125.63, 125.26, 115.21, 22.58 ppm. ^{29}Si NMR ($CDCl_3$, 59.64): δ –12.9 ppm. GC-MS: t_r = 19.14 min, m/z = 350.2. EA: 85.66% C, 6.33% H (calc.), 84.64% C, 6.19% H (found).

^{1}H NMR (acetone d_6, 300.2 MHz): δ 7.99-7.87 (m, 3H), 7.66-7.53 (m, 5H), 7.46-7.31 (m, 9H), 5.91-5.77 (m, 1H, C**H**=CH$_2$), 4.93 (d, 1H, CH=C**H**$_2$), 4.76 (d, 1H, CH=C**H**$_2$), 2.58 (d, 2H, C**H**$_2$-CH=CH$_2$) ppm. ^{13}C NMR (acetone d_6, 75.5 MHz): δ 137.5(1C), 137.1 (2C), 135.9 (4C), 135.6 (q, 1C), 134.6 (q, 1C), 134.1 (q, 1C), 131.2 (1C), 130.0 (2C), 129.5 (1C), 129.4 (1C), 128.4 (4C), 126.0 (2C), 125.6 (1C), 115.0 (1C), 22.4 (1C) ppm. ^{29}Si NMR (acetone d_6, 59.6 MHz): δ –13.1 ppm.

1-naphthly$_2$(phenyl)(allyl)Si (**24**): 0.5 g Mg (2.7 eq, 20.6 mmol) in 35 mL Et_2O. 1.60 mL allylchloride (2.5 eq, 19.6 mmol). 3.05 g **8** (1.0 eq, 7.7 mmol) in 30 mL Et_2O and 30 mL THF. Yield 95% (3.0 g, 7.5 mmol). mp: 179 °C. ^{1}H NMR ($CDCl_3$, 300.2 MHz): δ 7.98 (d, 2H, $^3J_{H–H}$ = 8.4 Hz), 7.93 (d, 2H, $^3J_{H–H}$ = 8.1 Hz), 7.87 (d, 2H, $^3J_{H–H}$ = 8.2 Hz), 7.68 (d, 2H, $^3J_{H–H}$ = 6.9 Hz), 7.60 (d, 2H, $^3J_{H–H}$ = 7.1 Hz), 7.49-7.29 (m, 9H), 5.74 (ddt, 1H, C**H**$_a$=CH$_2$), 4.97 (d, 1H, $^3J_{Ha–Hc}$ = 16.8 Hz, CH=C**H**$_c$H$_b$), 4.77 (d, 1H, $^3J_{Ha–Hb}$ = 10.1 Hz, CH=C**H**$_b$H$_c$), 2.78 (d, 2H, $^3J_{Ha–Hd}$ = 7.9 Hz, C**H**$_{2(d)}$-CH=CH$_2$) ppm. ^{13}C NMR ($CDCl_3$, 75.5 MHz): δ 137.31, 136.83, 136.08, 135.73, 134.81, 133.50, 130.68, 129.59, 129.14, 128.98, 127.98, 125.83, 125.57, 125.33, 115.19, 23.64 ppm. ^{29}Si NMR ($CDCl_3$, 59.64): δ –11.5 ppm. GC-MS: t_r = 21.86 min, m/z = 400.2. EA: 86.87% C, 6.03% H (calc.), 85.76% C, 6.01% H (found).

^{1}H NMR (acetone d_6, 300.2 MHz): δ 8.00-7.90 (m, 6H), 7.70 (d, 2H), 7.58 (d, 2H), 7.47-7.19 (m, 9H), 5.72-5.60 (m, 1H, C**H**=CH$_2$), 4.95 (d, 1H, CH=C**H**$_2$), 4.67 (d, 1H, CH=C**H**$_2$), 2.79 (d, 2H, C**H**$_2$-CH=CH$_2$) ppm. ^{13}C NMR (acetone d_6, 75.5 MHz): δ 137.1 (q, 2C), 136.5 (2C), 135.7 (2C), 135.4 (q, 1C), 134.5 (1C), 134.2 (q, 2C), 131.5 (q, 2C), 130.4 (2C), 129.8 (1C), 129.5 (2C), 128.7 (3C), 126.4 (2C), 126.3 (2C), 125.9 (2C), 115.3 (1C), 23.7 (1C) ppm. ^{29}Si NMR (acetone d_6, 59.6 MHz): δ –11.3 ppm.

1-naphthyl$_3$(allyl)Si (**25**): 1.5 g Mg (6.4 eq, 61.7 mmol) in 100 mL Et_2O. 4.8 mL allylchloride (6.1 eq, 58.7mmol). 4.3 g **9** (1.0 eq, 9.7 mmol) in 30 mL Et_2O and 30 mL THF; Yield: 85% (3.7 g, 8.2 mmol). mp: 171 °C. ^{1}H NMR ($CDCl_3$, 300.2 MHz): δ 8.30 (d, 3H, $^3J_{H–H}$ = 8.6 Hz), 7.9 (t, 6H, $^3J_{H–H}$ = 8.5 Hz), 7.67 (d, 3H, $^3J_{H–H}$ = 6.4 Hz), 7.44 (t, 3H, $^3J_{H–H}$ = 7.6 Hz), 7.36 (d, 2H, $^3J_{H–H}$ = 7.5 Hz), 7.31 (d, 2H, $^3J_{H–H}$ = 5.0 Hz), 7.26 (d, 2H, $^3J_{H–H}$ = 6.8 Hz), 5.74 (ddt, 1H, C**H**$_a$=CH$_2$), 5.03 (d, 1H, $^3J_{Ha–Hc}$ = 16.7 Hz, CH=C**H**$_c$H$_b$), 4.76 (d, 1H, $^3J_{Ha–Hb}$ = 10.0 Hz, CH=C**H**$_b$H$_c$), 2.94 (d, 2H, $^3J_{Ha–Hd}$ = 8.1 Hz, C**H**$_{2(d)}$-CH=CH$_2$) ppm. ^{13}C NMR ($CDCl_3$, 75.5 MHz): δ 137.42, 135.44, 133.90, 133.68, 130.78, 129.71, 129.10, 125.86, 125.63, 125.47, 115.85, 24.88 ppm. ^{29}Si NMR ($CDCl_3$, 59.64): δ –7.6 ppm. GC-MS: t_r = 25.8 min, m/z = 450.2. EA: 87.95% C, 5.82% H (calc.), 87.92% C, 5.82% H (found)

^{1}H NMR (acetone d_6, 300.2 MHz): δ 8.05 (d, 3H), 7.99-7.91 (dd, 6H), 7.69 (d, 3H), 7.44-7.33 (m, 6H), 7.29-7.24 (t, 3H), 5.70-5.59 (m, 1H, C**H**=CH$_2$), 5.00 (d, 1H, CH=C**H**$_2$), 4.65 (d, 1H, CH=C**H**$_2$), 2.96 (d, 2H, C**H**$_2$-CH=CH$_2$) ppm. ^{13}C NMR (acetone d_6, 75.5 MHz): δ 138.1 (2C), 137.8 (q, 3C), 135.9 (q, 1C), 134.6 (q, 2C), 131.6 (q, 3C), 130.1 (4C), 129.9 (4C), 126.5 (4C), 126.5 (4C), 126.1 (3C), 115.9 (1C), 24.9 (1C) ppm. ^{29}Si NMR (acetone d_6, 59.6 MHz): δ –8.3 ppm.

Methyl$_3$(allyl)Si: ^{1}H NMR ($CDCl_3$, 300.2 MHz): δ 5.80 (ddt, 1H, C**H**$_a$=CH$_2$), 4.85 (d, 1H, $^3J_{Ha–Hc}$ = 7.5 Hz, CH=C**H**$_c$H$_b$), 4.81 (s, 1H, CH=C**H**$_b$H$_c$), 1.51 (d, 2H, $^3J_{Ha–Hd}$ = 8.0 Hz, C**H**$_{2(d)}$-CH=CH$_2$), 0.01 (s, 9H, Si-CH$_3$) ppm. ^{13}C NMR ($CDCl_3$, 75.5 MHz): δ 135.4 (1C), 112.7 (1C), 24.8 (1C), –2.0 (3C) ppm.

Methoxy$_3$(allyl)Si: ^{1}H NMR ($CDCl_3$, 300.2 MHz): δ 5.81 (ddt, 1H, C**H**$_a$=CH$_2$), 5.02 (d, 1H, $^3J_{Ha–Hc}$ = 16.9 Hz, CH=C**H**$_c$H$_b$), 4.94 (d, 1H, $^3J_{Ha–Hb}$ = 10.1 Hz, CH=C**H**$_b$H$_c$), 3.57 (s, 9H, O-CH$_3$), 1.67 (d, 2H,

$^{3}J_{Ha–Hd}$ = 7.8 Hz, C**H**$_{2(d)}$-CH=CH$_2$) ppm. ^{13}C NMR ($CDCl_3$, 75.5 MHz): δ 132.2 (1C), 115.1 (1C), 50.8 (3C), 17.1 (1C) ppm. ^{29}Si NMR ($CDCl_3$, 59.6 MHz): δ –46.8 ppm.

Preparation of R_3Si dihydropyridazines

All triarylsilyl pyridazines were prepared by mixing 3,6-(2-pyridinyl)$_2$-1,2,4,5-tetrazine (**pyTz**)[133,143] with allyltriaryl silane in a THF solution. The reaction mixture was stirred at room temperature, intermittently monitored by TLC with cyclohexane:ethyl acetate (10:1), until a complete reaction of the pyTz was evident. Complete conversion was also indicated by a colour change from brightly pink to yellow. The solvent was evaporated and the residual yellow solid or oil was purified by column chromatography with cyclohexane:ethyl acetate (10:1). Due to decomposition of the product in $CDCl_3$ the NMR were taken in acetone d_6 allowing for data interpretation without interfering solvent signals.

3,6-(2-pyridinyl)$_2$-1,2,4,5-tetrazine (**pyTz**): ^{1}H NMR (acetone d_6, 300.2 MHz): δ = 8.94 (d, 2H, $^{3}J_{HH}$ = 4.1 Hz), 8.69 (d, 2H, $^{3}J_{HH}$ = 7.9 Hz), 8.16 (dt, 2H, $^{3}J_{HH}$ = 7.8 Hz, $^{4}J_{HH}$ = 1.47 Hz), 7.71 (dt, 2H, $^{3}J_{HH}$ = 6.2 Hz, $^{4}J_{HH}$ = 1.05 Hz) ppm. ^{13}C NMR (acetone d_6, 75.5 MHz): δ = 165.1 (q, 2C), 152.0 (q, 2C), 151.8 (2C), 138.5 (2C), 127.4 (2C), 125.3 (2C) ppm.

3,6-(2-pyridinyl)$_2$-4-((phenyl$_3$silyl)methyl)pyridazine (**26**): 61.1 mg **9** (0.203 mmol, 1.2 eq, 40 mg) **pyTz** (0.169 mmol, 1.0 eq) in 2 mL THF. ^{1}H NMR (acetone d_6, 300.2 MHz): δ =9.46 (bs, 1H, NH), 8.67 (d, 1H, $^{3}J_{HH}$ = 4.5 Hz, Py), 8.52 (d, 1H, $^{3}J_{HH}$ = 4.5 Hz, Py), 8.13 (d, 1H, $^{3}J_{HH}$ = 8.1 Hz, Py); 7.77 (dt, 1H, $^{3}J_{HH}$ = 8.2 Hz, $^{4}J_{HH}$ = 1.8 Hz, Py), 7.73 (dd, 6H, $^{3}J_{HH}$ = 7.9 Hz, $^{4}J_{HH}$ = 1.4 Hz, Ph), 7.66 (dt, 1H, $^{3}J_{HH}$ = 7.6 Hz, $^{4}J_{HH}$ = 1.7 Hz, Py), 7.45–7.38 (m, 9H, Ph), 7.32–7.26 (m, 2H, Py), 6.88 (d, 1H, $^{3}J_{HH}$ = 8.0 Hz, Py), 5.06 (d, 1H, $^{3}J_{HH}$ = 6.5 Hz, Pz), 4.64–4.60 (m, 1H, Pz), 1.85–1.72 (m, 2H, CH$_2$) ppm. ^{13}C NMR (acetone d_6, 75.5 MHz): δ = 155.5 (q, 1C), 151.2 (q, 1C), 149.4 (1C), 149.1 (1C), 144.4 (q, 1C), 137.9 (q, 1C), 137.4 (1C), 137.0 (1C), 136.6 (9C), 130.3 (3C), 128.8 (6C), 123.9 (1C), 123.7 (1C), 121.5 (1C), 120.0 (1C), 100.7 (1C), 27.7 (1C), 18.6 (1C) ppm. ^{29}Si NMR (acetone d_6, 59.64): δ –13.2 ppm.

3,6-(2-pyridinyl)$_2$-4-((1-naphthyl(phenyl)$_2$silyl)methyl)pyridazine (**27**): 71.1 mg **10** (0.203 mmol, 1.2 eq, 40 mg **pyTz** (0.169 mmol, 1.0 eq) in 2 mL THF. ^{1}H NMR (acetone d_6, 300.2 MHz): δ = 9.52 (bs, 1H, NH), 8.67 (d, 1H, $^{3}J_{HH}$ = 4.0 Hz, Py), 8.45 (d, 1H, $^{3}J_{HH}$ = 4.4 Hz, Py), 8.10 (d, 1H, $^{3}J_{HH}$ = 7.6 Hz, py), 8.02 (d, 1H, $^{3}J_{HH}$ = 8.0 Hz), 7.97–7.11 (m, 20H, Naph, Ph, Py), 6.47 (d, 1H, $^{3}J_{HH}$ = 9.4 Hz, Py), 4.81 (d, 1H, $^{3}J_{HH}$ = 6.3 Hz, Pz), 4.67–4.60 (m, 1H, Pz), 1.78–1.74 (m, 2H, CH$_2$) ppm. ^{29}Si NMR (acetone d_6, 59.64): δ –12.4 ppm.

3,6-(2-pyridinyl)$_2$-4-((1-naphthyl$_2$(phenyl) silyl)methyl)pyridazine (**28**): 81.2 mg **11** (0.203 mmol, 1.2 eq, 40 mg **pyTz** (0.169 mmol, 1.0 eq) in 2 mL THF. ^{1}H NMR (acetone d_6, 300.2 MHz): δ = 9.55 (bs, 1H, NH), 8.64 (d, 1H, $^{3}J_{HH}$ = 4.4 Hz, Py), 8.46 (d, 1H, $^{3}J_{HH}$ = 4.4 Hz, Py), 8.13–7.08 (m, 24H, Naph, Ph, Py), 6.45 (d, 1H, $^{3}J_{HH}$ = 8.4 Hz, Py), 4.67–4.64 (m, 1H, Pz), 4.60–4.52 (m, 1H, Pz), 1.77–1.73 (m, 2H, CH$_2$) ppm. ^{29}Si NMR (acetone d_6, 59.64): δ –10.9 ppm.

3,6-(2-pyridinyl)$_2$-4-((1-naphthyl$_3$silyl)methyl)pyridazine (**29**): 91.6 mg **12** (0.203 mmol, 1.2 eq, 40 mg **pyTz** (0.169 mmol, 1.0 eq) in 2 mL THF. ^{1}H NMR (acetone d_6, 300.2 MHz): δ = 9.58 (bs, 1H, NH), 8.64—8.62 (m, 1H, Py), 8.58–8.56 (m, 1H, Py), 8.13 (t, 6H, $^{3}J_{HH}$ = 7.4 Hz, Naph), 8.05 (d, 1H, $^{3}J_{HH}$ = 7.9 Hz, Py), 7.99 (d, 3H, $^{3}J_{HH}$ = 8.2 Hz, Naph), 7.89 (d, 3H, $^{3}J_{HH}$ = 7.9 Hz, Naph), 7.72 (t, 1H, $^{3}J_{HH}$ = 8.1 Hz, Py), 7.60 (t, 1H, $^{3}J_{HH}$ = 7.6 Hz, Py), 7.4–7–19 (m, 11H, Naph), 6.74 (d, 1H, $^{3}J_{HH}$ = 7.9 Hz, Py), 4.69–4.67 (m, 1H, Pz), 4.43–4.36 (m, 1H, Pz), 2.59–2.50 (m, 1H, CH$_2$), 2.28–2.22 (m, 1H, CH$_2$) ppm. ^{13}C NMR (acetone d_6, 75.5 MHz): δ = 155.5 (q, 1C), 151.1 (q, 1C), 149.6 (1C), 149.3 (1C), 145.1 (q, 1C), 138.9 (q, 1C), 138.4 (2C), 138.1 (3C), 137.7 (1C), 137.0 (1C), 137.0 (1C), 135.3 (1C),

134.8 (1C), 131.7 (3C), 130.4 (3C), 130.0 (3C), 129.9 (2C), 129.2 (2C), 126.6 (3C), 126.5 (3C), 126.3 (3C), 124.0 (1C), 123.8 (1C), 121.6 (1C), 119.9 (1C), 99.7 (1C), 29.2 (1C), 20.9 (1C) ppm. ^{29}Si NMR (acetone d_6, 59.64): δ –9.1 ppm.

Preparation of R_4Si

Tetraaryl silanes were prepared, wherever possible, according to literature procedures *via* lithiation of the respective aryl halide.[137] The preparation of tetra–1-naphthyl silane, however, was attempted several times yet never resulted in the desired product. The attempts are summarized below.

(1-naphthyl)phenyl$_3$Si (**30**): A solution of 7.5 mL 1-bromonaphthalene (53 mmol, 1.5 eq) in 100 mL Et_2O was lithiated with 11 mL *n*-BuLi (2.5 M, 59 mmol, 1.65 eq) at –78 °C. The lithiated species was transferred onto a solution of 7.6 mL phenyl$_3$SiCl (36 mmol, 1.0 eq) in 100 mL Et_2O *via* cannula after approximately 1 h of stirring and allowing to warm up to room temperature. Reflux for 90 min was followed by filtration over Celite® and aqueous extraction of the product. The organic phases were dried over sodium sulphate, the solvent evaporated and the product recrystallised from THF. Yield: 43% (5.9 g, 15.5 mmol). mp: 177 °C. ^{1}H ($CDCl_3$, 300 MHz): δ = 7.95 (d, 1H, $^3J_{H-H}$ = 8.2 Hz), 7.89–7.81 (dd, 2H, $^3J_{H-H}$ = 8.4 Hz), 7.57 (d, 6H, $^3J_{H-H}$ = 8.6 Hz), 7.49 (d, 1H, $^3J_{H-H}$ = 7.5 Hz), 7.44–7.31 (m, 11H), 7.19 (t, 1H, $^3J_{H-H}$ = 7.3 Hz) ppm, ^{13}C ($CDCl_3$, 75.5 MHz): δ = 138.1, 136.6, 134.9, 133.6, 131.0, 130.2,129.6, 128.8, 128.0, 125.7, 125.4 ppm, ^{29}Si ($CDCl_3$, 59.64 MHz): δ = –13.7 ppm. EA: 87.00% C, 5.74% H (calc.), 86.91% C, 5.65% H (found).

(1-naphthyl)$_2$phenyl$_2$Si (**31**): A solution of 0.61 mL 1-bromonaphthalene (43 mmol, 1.5 eq) in 10 mL Et_2O was lithiated with 2.9 mL *n*-BuLi (1.6 M, 46 mmol, 1.6 eq) at –78 °C. The lithiated species was transferred onto a solution of 1 g 1-naphthyl(phenyl)$_2$SiCl (28 mmol, 1.0 eq) in 10 mL Et_2O and 10 mL toluene *via* cannula after approximately 2 h of stirring and allowing to warm up to room temperature. The solvent was evaporated, the residue dissolved in toluene and filtered over Celite®. The concentrated solution yielded in colourless crystals. Yield: 36% (4.3 g, 10 mmol). mp: 203 °C. ^{1}H ($CDCl_3$, 300 MHz): δ = 7.98 (d, 2H, $^3J_{H-H}$ = 8.2 Hz), 7.87 (d, 4H, $^3J_{H-H}$ = 8.6 Hz), 7.65 (d, 3H, $^3J_{H-H}$ = 7.0 Hz), 7.60 (d, 3H, $^3J_{H-H}$ = 7.4 Hz), 7.43–7.37 (t, 6H, $^3J_{H-H}$ = 7.5 Hz), 7.31 (t, 4H, $^3J_{H-H}$ = 7.5 Hz), 7.20–7.12 (dd, 2H, $^3J_{H-H}$ = 8.4 Hz) ppm, ^{13}C ($CDCl_3$, 75.5 MHz): δ = 137.7, 137.4, 136.5, 135.2, 133.6, 132.7, 130.8, 129,9, 129.4, 128.7, 127.9, 125,4 ppm, ^{29}Si ($CDCl_3$, 59.64 MHz): δ = –12.9 ppm. EA: 88.03% C, 5.54% H (calc.), 88.17% C, 5.60% H (found).

(1-naphthyl)$_3$phenylSi (**32**): 1.83 g of 1-naphthyl$_3$SiCl (4.1 mmol, 1.0 eq) was dissolved in 30 mL toluene and cooled to 0 °C. 3 mL of a phenyllithium solution (1.9 M in dibutylether, 4.5 mmol, 1.1 eq) was added dropwise *via* septum. The reaction mixture was allowed to warm to room temperature and was stirred overnight. The solvent was evaporated *in vacuo*, the residue dissolved in toluene and insoluble salts were filtered over Celite®. The product was obtained as brown powder. Recrystallisation attempts with toluene, ethyl acetate, THF and mixtures of the former with pentane failed. Yield (crude product): 58% (1.2 g, 2.3 mmol). mp: 192 °C. ^{1}H ($CDCl_3$, 300 MHz): δ = 7.93-7.80 (m, 12H), 7.60 (d, 2H, $^3J_{H-H}$ = 7.5 Hz), 7.41–7.23 (m, 9H), 7.05 (t, 3H, $^3J_{H-H}$ = 7.7 Hz) ppm, ^{13}C ($CDCl_3$, 75.5 MHz): δ = 137.7, 137.0, 133.7, 133.4, 131.0, 129.7, 128.9, 128.1, 125.7, 125.6 ppm, ^{29}Si ($CDCl_3$, 59.64 MHz): δ = –12.2 ppm. EA: 88.84% C, 5.38% H (calc.), 88.19% C, 5.50% H (found).

Attempts towards 1-naphthyl$_4$Si

In order to complete the row of homologues, the preparation of 1-naphthyl$_4$Si was attempted. Therefore, lithiation and Grignard-type reactions with different chlorosilane educts at different excesses of reagent were tested. Generally, the lithiation reactions were carried out by providing a solution of 1-bromonaphthalene in Et_2O or DME at –78 ° followed by the dropwise addition of an *n*-BuLi solution in hexanes. Work-up procedures for lithiation reactions consisted of evaporation of the used solvent, dissolving of the residues in toluene, filtering of the insoluble salts over Celite® and evaporation of toluene. For the Grignard reactions Mg was provided in THF and a solution of 1-bromonaphthalene was added dropwise to keep the exothermic reaction at reflux. Subsequently, the respective chlorosilanes were added to the lithiated or Grignard reagent or *vice versa*. For the work-up, the solvent was evaporated; the residue was taken up in aqua dest. and the silane was extracted with dichloromethane (DCM) before the solvent was evaporated again. The experiment protocols are summarised below. For all experiments ^{29}Si NMR shifts are given.

a) *1-naphthylLi + $SiCl_4$*

*4:*1 5.6 mL 1-bromonaphthalene (40 mmol, 4.5 eq) in approximately 50 mL Et_2O, 17.6 mL *n*-BuLi (2.5 M, 44 mmol, 4.9 eq). 1 mL $SiCl_4$ (8.7 mmol, 1.0 eq) was added *via* septum at –30 °C. ^{29}Si NMR (THF, D_2O): δ = 4.0 ppm.

6:1 7.3 mL 1-bromonaphthalene (52.3 mmol, 6 eq) in approximately 80 mL Et_2O, 23 mL *n*-BuLi (2.5 M, 57.5 mmol, 6.6 eq). 1 mL $SiCl_4$ (8.7 mmol, 1.0 eq) was added *via* septum at –20 °C. ^{29}Si NMR (toluene, D_2O): δ = 3.7, –5.7 ppm.

b) *1-naphthylMgBr + $SiCl_4$*

3.38 g Mg (137.5 mmol, 4.6 eq) provided in 250 mL Et_2O, 18.1 mL 1-bromonaphthalene (125 mmol, 4.17 eq) were added. The Grignard solution was replenished to a total of 800 mL Et_2O. 3.44 mL $SiCl_4$ (30 mmol, 1.0 eq) were added *via* Septum after filtration of the Grignard reagent. ^{29}Si NMR (C_6D_6): δ = 12.73, 4.10 (1-naphthyl$_3$SiCl), –1.15, -6.46 ppm.

c) *1-naphthylLi + 1-naphthyl$_3$SiCl*

0.95 mL 1-bromonaphthalene (1,40 g, 6.7 mmol, 3.0 eq) in 10 mL Et_2O, 3 mL *n*-BuLi (2.5 M, 7.5 mmol, 3.3 eq), 1 g 1-naphthyl$_3$SiCl (2.2 mmol, 1.0 eq).

Sample NMR taken after a) stirring for 2 days: ^{29}Si NMR (THF, D_2O) = 3.8 ppm and b) 14 d (336 h) reflux: ^{29}Si NMR (THF, D_2O) = 3.5, –9.6 ppm

The obtained NMR shifts indicate solely a conversion of 1-naphthyl$_3$SiCl to 1-naphthyl$_3$SiOH, possibly caused by a leak in the reaction apparatus.

d) *1-naphthylMgBr + 1-naphthyl$_3$SiCl*

0.58 g Mg (24 mmol, 12.0 eq) were provided in approximately 120 mL THF. 2.8 mL 1-bromonaphthalene (20 mmol, 10.0 eq) were added *via* septum. Reflux for 4 h. The Grignard reagent was transferred to a solution of 0.89 g 1-naphthyl$_3$SiCl in approximately 50 mL THF *via* filter cannula at 0 °C. Stirring at room temperature for 72 h. The Si containing species were extracted with DCM. ^{29}Si NMR (C_6D_6): δ = 4.0 ppm.

e) *1-naphthylLi + 1-naphthyl$_2$SiCl$_2$*
2.8 mL 1-bromonaphthalene (4.1 g, 20 mmol, 4.0 eq) in 30 mL Et$_2$O, 13.75 mL *n*-BuLi (1.6 M, 22 mmol, 4.4 eq). Addition of the lithiated species to a solution of 1.76 g 1-naphthyl$_2$SiCl$_2$ (5 mmol, 1.0 eq) in 60 mL Et$_2$O at 0 °C. Refluxing for 8 h at room temperature resulted in 1-naphthyl$_3$SiCl (^{29}Si NMR (Et$_2$O, D$_2$O): δ = 4.1 ppm.) The solvent was evaporated and exchanged for toluene. Refluxing of the reaction mixture for 8 h showed no signs of further conversion, either. ^{29}Si NMR (toluene, D$_2$O): δ = 4.1 ppm.

f) *1-naphthylLi + 1-naphthyl$_2$SiF$_2$*
0.65 mL 1-bromonaphthalene (0.97 g, 4.7 mmol, 3.0 eq) in 10 mL DME, 3.2 mL *n*-BuLi (1.6 M, 5.1 mmol, 3.3 eq). Addition to 0.5 g 1-naphthyl$_2$SiF$_2$ (1.5 mmol, 1.0 eq) in 10 mL DME at 0 °C. Stirring for 12h at room temperature. The obtained ^{19}F and ^{29}Si NMR data correspond to 1-naphthyl$_3$SiF. ^{29}Si NMR (DME, D$_2$O): δ = 8.5 ppm. ^{19}F NMR (DME, D$_2$O): δ = –153 ppm.

In all cases, ^{29}Si NMR showed 1-naphthyl$_3$SiX (X = Cl, F) as product.

phenyl$_8$Si$_4$/phenyl$_{10}$Si$_5$ (33a/b)
The perphenylated silane rings were prepared according to literature procedure *via* Wurtz-type coupling of phenyl$_2$SiCl$_2$ with Li in THF.[146] The spectroscopic data are in full agreement with literature values.[232] ^{29}Si NMR (CDCl$_3$): δ = –22.5 (phenyl$_8$Si$_4$), –34.7 (phenyl$_{10}$Si$_5$) ppm.

5.2.2 Organotin Compounds

The preparation of aryltin compounds was carried out according to literature-known procedures.[233] In the following, only ^{1}H and ^{119}Sn NMR shifts are provided.

R$_4$Sn

***o*-tolyl$_4$Sn (34)**: ^{1}H (CDCl$_3$, 300 MHz): δ = 7.53 (d, 4H, $^3J_{H\text{-}H}$ = 7.6 Hz, $^3J_{^{117}Sn\text{-}H}$ = 39.2 Hz, $^3J_{^{119}Sn\text{-}H}$ = 53.8 Hz ppm), 7.31-7.23 (m, 8H), 7.19-7.11 (m, 4H). ^{119}Sn (CDCl$_3$, 112 MHz): δ = –121.8 ppm.

1-naphthyl$_4$Sn (35): ^{1}H (CDCl$_3$, 300 MHz): δ = 8.44 (d, 4H, $^3J_{H\text{-}H}$ = 8.3 Hz), 8.23 (d, 4H, $^3J_{H\text{-}H}$ = 6.6 Hz, $^3J_{^{117}Sn\text{-}H}$ = 27.2 Hz, $^3J_{^{119}Sn\text{-}H}$ = 59.2 Hz ppm), 7.68 (dd, 8H, $^3J_{H\text{-}H}$ = 8.2 Hz), 7.20-7.09 (m, 8H), 6.94 (t, 4H, $^3J_{H\text{-}H}$ = 7.7 Hz) ^{119}Sn (CDCl$_3$, 112 MHz): δ = –117.2 ppm.

RSnCl$_3$

phenylSnCl$_3$ (36): ^{1}H (CDCl$_3$, 300 MHz): δ = 8.10-8.07 (m, 2H), 8.03-7.98 (m, 3H) ppm, ^{119}Sn (CDCl$_3$, 112 MHz): δ = –61.2 ppm.

***o*-tolylSnCl$_3$ (37):** ^{1}H (CDCl$_3$, 300 MHz): δ = 7.64 (d, 1H, $^3J_{H\text{–}H}$ = 7.55 Hz), 7.59–7.51 (m, 1H), 7.46-7.31 (m, 2H), 2.68 (s, 3H, CH$_3$) ppm, ^{119}Sn (CDCl$_3$, 112 MHz): δ = –60.3 ppm.

1-naphthylSnCl$_3$ (38): ^{1}H (CDCl$_3$, 300 MHz): δ = 7.99-7.91 (dd, 1H, $^3J_{H\text{–}H}$ = 7.59 Hz ppm), 7.52-7.32 (m, 3H), 7.15-7.04 (m, 2H), 6.95-6.87 (m, 1H), ^{119}Sn (CDCl$_3$, 112 MHz): δ = –54.2 ppm.

R_2SnCl_2

phenyl$_2$SnCl$_2$ (39): ^{1}H ($CDCl_3$, 300 MHz): δ = 7.72-7.69 (m, 4H), 7.55-7.51(m, 6H) ppm, ^{119}Sn ($CDCl_3$, 112 MHz): δ = –27.4 ppm.

1-naphthyl$_2$SnCl$_2$ (40): ^{1}H ($CDCl_3$, 300 MHz): δ = 8.09 (t, 2H, $^{3}J_{H-H}$ = 8.62 Hz ppm), 7.94 (t, 4H, $^{3}J_{H-H}$ = 6.28 Hz), 7.83 (dd, 2H, $^{3}J_{H-H}$ = 8.61 Hz), 7.64 (t, 2H, $^{3}J_{H-H}$ = 7.85 Hz), 7.58-7.48 (m, 2H), 7.41-7.35 (m, 1H), 7.14 (t, 1H, $^{3}J_{H-H}$ = 7.85 Hz) ^{119}Sn ($CDCl_3$, 112 MHz): δ = –8.8 ppm.

$RSnH_3$

In order to avoid a reaction with halogenated solvents due to weak Sn–H bonds, the following NMR spectra were taken in C_6D_6.

phenylSnH$_3$ (41): ^{1}H (C_6D_6, 300 MHz): δ = 7.30–7.25 (d, 2H, $^{3}J_{H-H}$ = 7.6 Hz, $^{3}J_{117Sn-H}$ = 43.8 Hz, $^{3}J_{119Sn-H}$ = 54.2 Hz ppm), 7.11–7.03 (m, 3H), 5.02 (s, 3H, $^{1}J_{119Sn-H}$ = 1925 Hz, $^{1}J_{117Sn-H}$ = 1839 Hz, Sn**H$_3$**) ppm, ^{13}C (C_6D_6, 75.5 MHz): δ = 138.0, 132.5, 129.2, 128.8 ppm, ^{119}Sn (C_6D_6, 112 MHz): δ = –344.4 ($^{1}J_{119Sn-H}$ = 1909 Hz) ppm. EA: 36.24% C, 4.06% H (calc.), 35.97% C, 4.01% H (found).

***o*-tolylSnH$_3$ (42):** ^{1}H (C_6D_6, 300 MHz): δ = 7.36 (d, 1H, $^{3}J_{H-H}$ = 7.2 Hz, $^{3}J_{117Sn-H}$ = 56.3 Hz, $^{3}J_{119Sn-H}$ = 70.3 Hz ppm), 7.08 (d, 1H, $^{3}J_{H-H}$ = 7.4 Hz), 6.99–6.93 (m, 2H), 4.91 (s, 3H, $^{1}J_{119Sn-H}$ = 1908 Hz, $^{1}J_{117Sn-H}$ = 1825 Hz, Sn**H$_3$**) ppm, ^{13}C (C_6D_6, 75.5 MHz): δ = 144.8, 139.0, 134.4, 129.8, 126.0, 25,8 (*ortho*–CH_3) ppm, ^{119}Sn (C_6D_6, 112 MHz): δ = –359.9 ($^{1}J_{119Sn-H}$ = 1914 Hz) ppm. EA: 39.50% C, 4.74% H (calc.), 39.09% C, 4.56% H (found).

1-naphthylSnH$_3$ (43): ^{1}H (C_6D_6, 300 MHz): δ = 7.69 (d, 1H, $^{3}J_{H-H}$ = 6.8 Hz), 7.67–7.56 (m, 2H), 7.50 (d, 1H, $^{3}J_{H-H}$ = 6.8 Hz), 7.26–7.21 (m, 2H), 7.12 (dd, 1H, $^{3}J_{H-H}$ = 7.4 Hz), 5.15 (s, 3H, $^{1}J_{119Sn-H}$ = 1935 Hz, $^{1}J_{117Sn-H}$ = 1849 Hz, Sn**H$_3$**) ppm, ^{13}C (C_6D_6, 75.5 MHz): δ = 139.2, 138.2, 134.5, 134.1, 130.4, 130.1, 129.2, 126.6, 126.0, 125.9 ppm, ^{119}Sn (C_6D_6, 112 MHz): δ = –353.8 ($^{1}J_{119Sn-H}$ = 1915 Hz) ppm. EA: 48.02% C, 4.05% H (calc.), 48.98% C, 3.99% H (found).

R_2SnH_2

phenyl$_2$SnH$_2$ (44): ^{1}H (C_6D_6, 300 MHz): δ = 7.41–7.39 (m, 4H), 7.14–7.10 (m, 6H), 6.07 (s, 3H, $^{1}J_{119Sn-H}$ = 1925 Hz, $^{1}J_{117Sn-H}$ = 1843 Hz, Sn**H$_2$**) ppm, ^{13}C (C_6D_6, 75.5 MHz): δ = 137.7, 135.5, 129.1, 128.9 ppm, ^{119}Sn (C_6D_6, 112 MHz): δ = –232.0 ($^{1}J_{119Sn-H}$ = 1929 Hz) ppm. EA: 52.42% C, 4.40% H (calc.), 52.18% C, 4.21% H (found).

1-naphthyl$_2$SnH$_2$ (45): ^{1}H (C_6D_6, 300 MHz): δ = 7.96 (d, 2H, $^{3}J_{H-H}$ = 7.3 Hz), 7.62 (dd, 6H, $^{3}J_{H-H}$ = 5.3 Hz, $^{3}J_{117Sn-H}$ = 58.6 Hz, $^{3}J_{119Sn-H}$ = 72.1 Hz ppm), 7.28–7.08 (m, 6H), 6.44 (s, 3H, $^{1}J_{119Sn-H}$ = 1938 Hz, $^{1}J_{117Sn-H}$ = 1851 Hz, Sn**H$_2$**)ppm, ^{13}C (C_6D_6, 75.5 MHz): δ = 139.2, 137.9, 136.7, 134.3, 130.5, 130.1, 129.1, 126.1, 125.9 ppm, ^{119}Sn (C_6D_6, 112 MHz): δ = –248.4 ($^{1}J_{119Sn-H}$ = 1951 Hz) ppm. EA: 64.05% C, 4.30% H (calc.), 64.18% C, 4.16% H (found).

5.3 Pyrolysis

Equipment and Sample Preparation

The pyrolysis experiments were carried out in a Carbolite GHA 12/600 single zone horizontal tube furnace. A schematic of the typical pyrolysis setup is given in Figure 81. The loosely heaped precursor sample were introduced into the quartz glass tube in an aluminium oxide shuttle under argon counter-flow and the tube was flooded for at least 15 min with argon before heating.

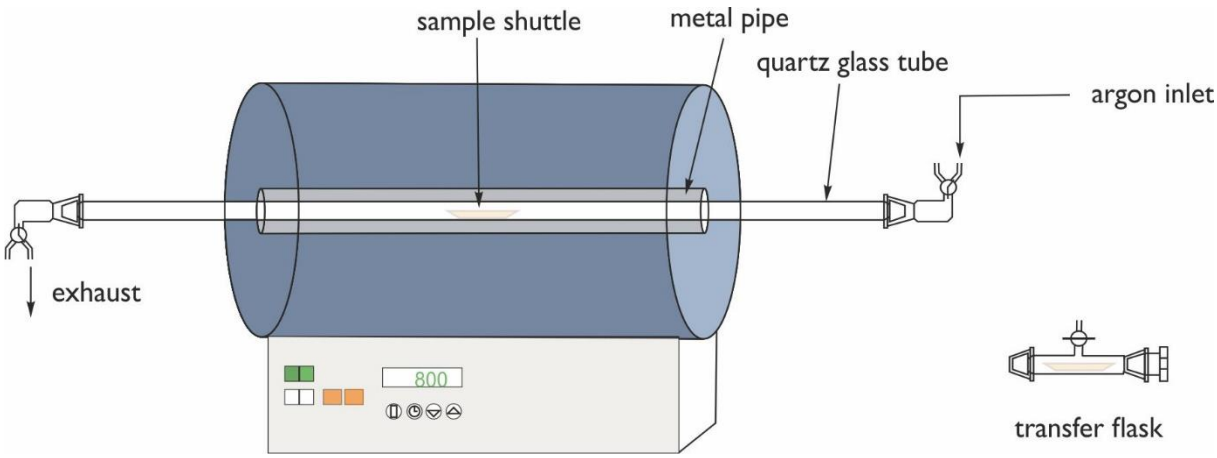

Figure 81 Schematic of the pyrolysis setup (horizontal tube furnace Carbolite GHA 12/600).

The heating process was adapted to each substrate; the three most frequently used procedures are summarised in Figure 82. Temperatures, heating rates, gas flow rates and dwell times suitable for the pyrolysis of the substrates were determined empirically.

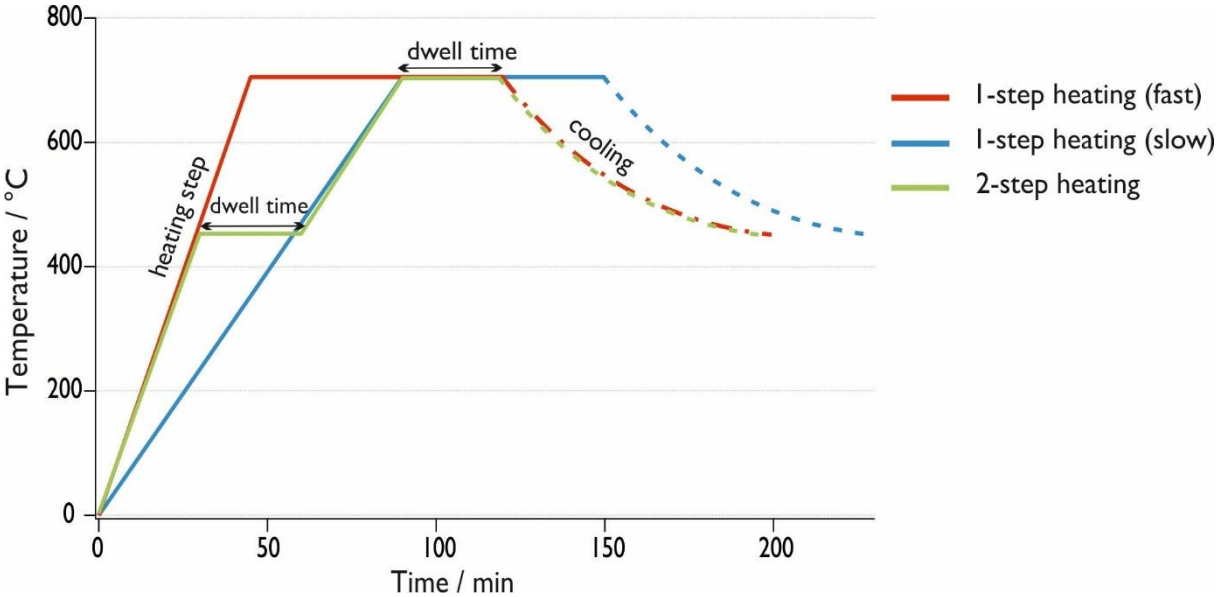

Figure 82 Typical heating procedures for pyrolysis.

After the pyrolysis, the samples were transferred into an Argon filled glovebox to avoid adsorption of oxygen onto the substrate surface. Characterization of the pyrolysed products was carried out by SEM/EDX. A summary of all conducted experiments is given in Table 20. Elemental analysis (CHN) results of the pyrolysed samples are summarised in Table 21. Measured nitrogen values stem from flooding of the transfer flask with the gas between two evacuation steps.

Table 20 Mass loss and experimental parameters for pyrolysis experiments.

Compound	*Initial Mass [mg]*	*Final Mass [mg]*	*Mass Loss [%]*	*Temp. [°C]*	*Pre-Heated*	*Rate [°C min⁻¹]*	*Gas Flow [L min⁻¹]*	*Dwell Time [min]*
1-naphthyl$_2$SiH$_2$	250	31	88	450/700	—	10	2	60/60
	231	26	89	700	—	10	2	120
1-naphthyl$_3$SiH	251	8	97	450/700	—	50	2	60/60
	230	2	99	700	—	50	0.1	30
	225	2	99	700	—	20	0.1	120
	227	32	86	700	—	50	0.1	60
	250	17	93	700	—	50	0.1	120
	262	23	92	700	✓	—	2	30
1-naphthyl$_2$(phenyl)SiH	245	1	99	400	—	50	0.1	30
	253	1	99	500	✓	—	0.1	10
	250	2	99	500	—	50	0.1	30
	247	1	99	700	—	10	0.1	30
	251	2	99	700	—	50	0.1	30
	261	35	87	700	—	50	2	30
1-naphthyl(phenyl)$_2$SiH	543	63	88	600	—	50	2	30
	511	4	99	700	—	50	2	30
phenyl$_8$Si$_4$	520	129	75	450	—	20	2	60
	556	122	78	700	—	20	2	60
	549	89	84	850	—	20	2	60
phenyl$_{10}$Si$_5$	493	133	72	500	—	20	0.1	120
	561	163	71	500	—	20	2	60
	521	99	81	800	—	20	2	120
	536	110	80	800	—	10	2	120
	551	89	84	800	—	50	2	120
	520	78	85	800	—	50	2	60
	531	69	87	800	—	50	2	360
	512	102	80	800	✓	—	0.1	60
	550	83	85	900	—	20	2	120
	587	88	85	450/800	✓	50	2	30/30
graphite	146	142	3	800	—	50	0.1	60
o–tolyl@Sn	98	48	51	250	—	50	0.1	30
	100	47	53	400	—	50	0.1	30
o–tolyl@Sn with graphite (in-situ)	311	309	1	250	—	50	0.1	30
o–tolyl@Sn with graphite (in-situ, Et$_2$O)	158	156	1	250	—	50	0.1	30

Table 21 Elemental analysis (CHN) of pyrolysed samples.

Compound	*Pyrolysis Temp. [°C]*	*Rate [°C min⁻¹]*	*Gas Flow [L min⁻¹]*	*Dwell Time [min]*	*%N*	*%C*	*%H*
1-naphthyl$_2$SiH$_2$	700	50	2	120	0.68	50.52	1.80
1-naphthyl$_3$SiH	700	20	0.1	120	0.92	69.12	1.55
	700	50	0.1	30	1.10	83.98	1.73
	700	50	0.1	60	0.68	67.83	1.21
	700	50	0.1	120	0.99	71.12	1.05
	700	—	0.1	120	0.70	74.48	2.20
phenyl$_8$Si$_4$	450	20	2	60	—	66.75	3.93
	700	20	2	60	0.29	71.47	1.30
	850	20	2	60	0.15	74.50	0.40
phenyl$_{10}$Si$_5$	500	20	2	120	0.26	70.66	3.80
	500	20	0.1	120	0.39	80.24	1.73
	800	10	2	120	0.30	74.85	0.56
	800	20	2	120	0.23	73.42	0.68
	800	50	2	120	0.39	74.78	0.76
	800	50	2	360	0.42	74.21	0.79
	800	20	0.1	120	0.18	73.13	0.87
	800	—	2	60	1.18	72.46	1.36
	450/800	—	2	30/30	1.13	72.83	1.10
	900	20	2	120	0.09	72.91	0.59

5.4 Electrochemistry

5.4.1 Cyclic Voltammetry

Swagelok®–Cell (Ag/AgCl Reference)

In order to measure small quantities of the sensitive aryl silanes and -stannanes, a CV cell was designed to fit their needs the best way possible. This cell corpus consisted of a *Swagelok®* PFA–620–3 tube fitting with a diameter of ⅜ inch, allowing the sample volumes to be as small as 0.5 mL. As working electrodes either a platinum microelectrode with a diameter of 20 µm using a sleeve of PTFE or glassy carbon or platinum disk electrodes with a diameter of 3 mm in a modified PEEK–body were used. The reference electrode was designed to be adaptable to different situations: on one hand the parts designed may be used in a redox-reference setup inspired by Compton et al.,[202] while on the other hand the parts may be realigned to build a Ag/AgCl reference including a container for the solid AgCl which is in contact with the platinum wire. Detailed description and pictures of the cell may be found in section 3.5.2.

Vial–Cell (Pseudo Silver Reference)

In other cyclic voltammetry experiments a cell consisting of a glass-vial with a PTFE lid, in which the electrodes were fit. In this setup, a glassy carbon electrode acted as working electrode, a platinum wire as a counter electrode and a silver wire as a pseudo-reference electrode was used. Ferrocene was added to the sample solutions as an internal reference. All measurements were carried out in an Argon-filled glove-box, using approximately 1.5 mL of a 0.1 M TBAF solution of the samples (2 mM, 5mM or approximately 10 mM) in either THF or MeCN.

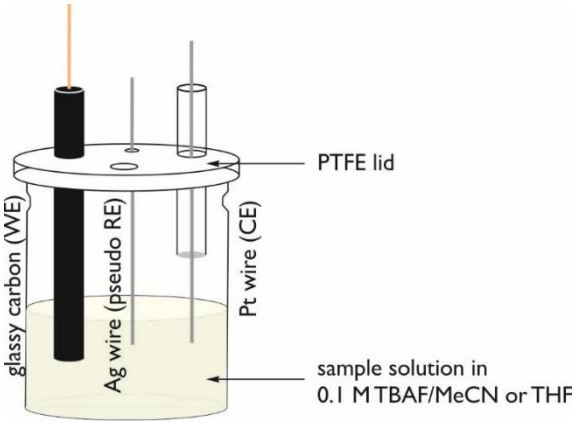

Figure 83 Vial-cell as used in the glove-box. Sample volume approximately 1.5 mL.

5.4.2 Li-Ion Half-Cells

The experiments in Li-ion half-cells were carried out in an airtight three electrode setup housed within a PFA–220–3–*Swagelok*® tube fitting with a diameter of ½ inch, using parts made of submarine steel for the electrodes. All test cells were assembled in argon filled glove-box. The reference and counter electrodes were covered with a layer of lithium (lithium ribbon, 0.38 x 23 mm, *Sigma-Aldrich*, AT), the working electrode, consisting of a copper foil coated with active material, was contacted with the corresponding steel part.

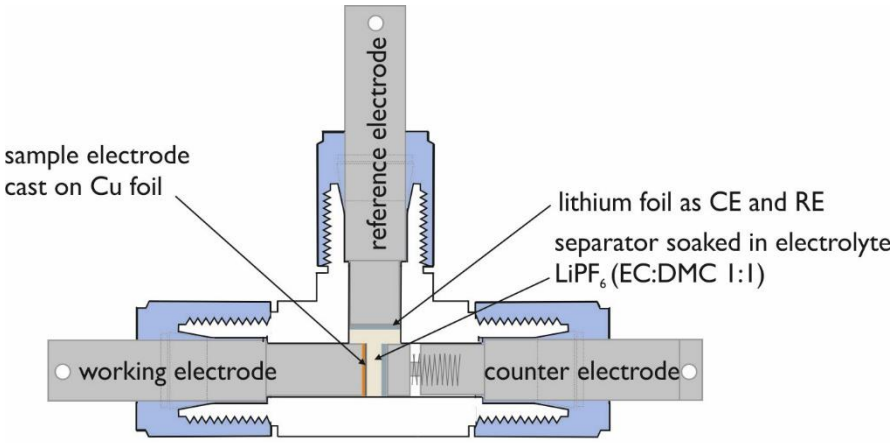

Figure 84 Scheme of a Li-ion half-cell used for CV and GCPL experiments *vs.* Li/Li^+.

Electrode Preparation

The typical preparation of electrodes mostly involved a set of standard chemicals, including a conductive additive in form of carbon black (*SuperC 65*, conductive carbon black, *Imerys Timcal C-NERGY*, CH) and a polymeric binding agent (*Kynar 761*, polyvinylidene difluoride, PVdF, *ARKEMA*, FR). *N*–methylpyrrolidone (NMP, *Sigma-Aldrich*, AT) was used as a solvent for the slurry preparation.

Graphite (KS 6L, *Imerys Timcal C-NERGY*, CH) was ground in a planetary rotary mill at 400 rpm for 1 h using a beaker and milling balls made from tungsten–carbide. As supporting metal and current collector, a copper foil with rough surface (*Goodfellow Cambridge Limited*, 99.9%, thickness 17.5 or 50 μm) was used.

The electrode compositions of silane samples with graphite are summarised in Table 22. A summary of samples prepared without the addition of graphite are given in Table 23. All electrode compositions containing stannanes are found in Table 24.

Table 22 Electrode compositions with silicon compounds incl. graphite.

	Silane [%wt]	*PVdF [%wt]*	*SuperC 65 [%wt]*	*Graphite [%wt]*
phenyl$_{10}$Si$_5$	30	4	4	62
phenyl$_{10}$Si$_5$ + graphene	25 + 5	10	10	50
phenyl$_{10}$Si$_5$, pyr. (500°C)	46	4	4	46
phenyl$_{10}$Si$_5$, pyr. (700°C)	46	4	4	46
phenyl$_{10}$Si$_5$, pyr. (800°C)	46	4	4	46
phenyl$_{10}$Si$_5$, pyr. (800°C), ball–milled (incl. solvent)	46	4	4	46
phenyl$_8$Si$_4$	30	4	4	62
phenyl$_8$Si$_4$, pyr. (700°C)	30	4	4	62
	46	4	4	46
phenyl$_8$Si$_4$, pyr. (800°C)	46	4	4	46
phenyl$_8$Si$_4$, pyr. (800°C), ball–milled (incl. solvent)	46	4	4	46
1-naphthyl(phenyl)SiH$_2$	25	4	4	67
	25	10	10	55
1-naphthyl$_2$SiH$_2$	25	4	4	67
	25	10	10	55
phenyl$_2$SiH$_2$	25	4	4	67
	25	10	10	55
1-naphthyl$_2$(phenyl)SiH	40	10	10	40
	25	10	10	55
1-naphthyl(phenyl)$_2$SiH	25	10	10	55

Table 23 Electrode compositions with silicon compounds ("neat").

	Silane [%wt]	*PVdF [%wt]*	*SuperC 65 [%wt]*
phenyl$_8$Si$_4$	80	10	10
phenyl$_{10}$Si$_5$, pyr. (800°C)	92	4	4
	80	10	10
phenyl$_{10}$Si$_5$, pyr. (800°C),ball–milled (dry)	80	10	10
phenyl$_{10}$Si$_5$, pyr. (800°C, preheated oven)	80	10	10
phenyl$_{10}$Si$_5$, pyr. (450/800°C, preheated oven)	80	10	10
phenyl$_{10}$Si$_5$ + graphite pyr. (800°C)	80	10	10
1-naphthyl$_2$SiH$_2$	80	10	10
1-naphthyl$_3$SiH	80	10	10

Table 24 Tin compounds (with and without graphite).

	Stannane [%wt]	*PVdF [%wt]*	*SuperC 65 [%wt]*	*Graphite [%wt]*
1-naphthyl@Sn (Et$_2$O)	25	10	10	55
1-naphthyl@Sn (DME)	25	10	10	55
1-naphthylSnH$_3$	25	10	10	55
1-naphthylSnH$_3$ + TMEDA	25	10	10	55
o-tolyl@Sn (Et$_2$O)	25	4	4	67
o-tolylSnH$_3$ + TMEDA	25	4	4	67
o-tolyl@Sn + graphite, pyr. (250 °C)	46	4	4	46
o-tolyl@Sn + graphite (in-situ, T), pyr. (250 °C)	46	4	4	46
o-tolyl@Sn + graphite (in-situ, T)	46	4	4	46

Exfoliation of Graphene from Graphite

The graphene sheets used in this work were prepared *in-situ* along the lines of the exfoliation of boron nitride nano-sheets optimised in our research group.[234] Therefore, natural graphite was treated with ultrasonication for 12 h at 10 °C. Therefore, organic solvents such as the established NMP and THF were tested.[235] Yields were determined by UV-Vis spectroscopy, applying Lambert-Beer's law. Generally, the experiments carried out in NMP resulted in higher yields of averagely 1.1 mg mL^{-1} while experiments in THF yielded 0.4 mg mL^{-1}. The comparatively high yield resulting from NMP is correlated with the viscosity of the solvent which enables better suspension than the less viscous THF. For the coupling experiments, however, THF was preferred over NMP, due to the solubility of the silanes involved.

Cyclic Voltammetry in Li-Ion Batteries

For the studies on reduction and oxidation processes occurring inside of a lithium-ion battery half-cell, Cyclic Voltammetry (CV) was conducted on a modular potentiostat/galvanostat/EIS (electrochemical impedance spectrometer) VMP3 from *Bio-Logic Science Instruments*. Data processing was carried out with the proprietary software *EC-Lab*, while plotting was done in *IGOR Pro*.

Galvanostatic Cycling with Potential Limitation (GCPL)

GCPL of Li-ion half-cells over the course of 100 cycles was performed using a MACCOR 40 cell tester with a charge and discharge current corresponding to a C-rate of $^{C}/_{2}$, calculated from the battery capacity according to Faraday's law (below). The C-rate is a measure of the rate at which a battery is charged or discharged in relation to its maximum capacity. In case of $^{C}/_{2}$ the necessary current is applied to or drained from the battery to charge or discharge it completely within two hours.

$$I = \frac{m \cdot F \cdot z}{t \cdot M}$$

I	current [A]	$z = \frac{1}{6}$	number of e^- exchanged per C atom
m	mass of electro–active material [g]	M	molar mass [g mol^{-1}]
F	Faraday's constant [96485 C mol^{-1}]		

Considering the discharge reaction in the test cell (reduction process)

$$Li^+ + e^- + 6C_{(graphite)} = LiC_6$$

the following calculation was done for each electrode used:

$$I\,[A] = \frac{m\,[g] \cdot 96485\,[C\,mol^{-1}] \cdot \frac{1}{6}}{7200[s] \cdot 12[g\,mol^{-1}]}$$

Data processing was carried out in *MIMS* (the proprietary software for processing MACCOR data files) followed by plotting in *IGOR Pro*.

6 Appendix

2D NMR Spectra

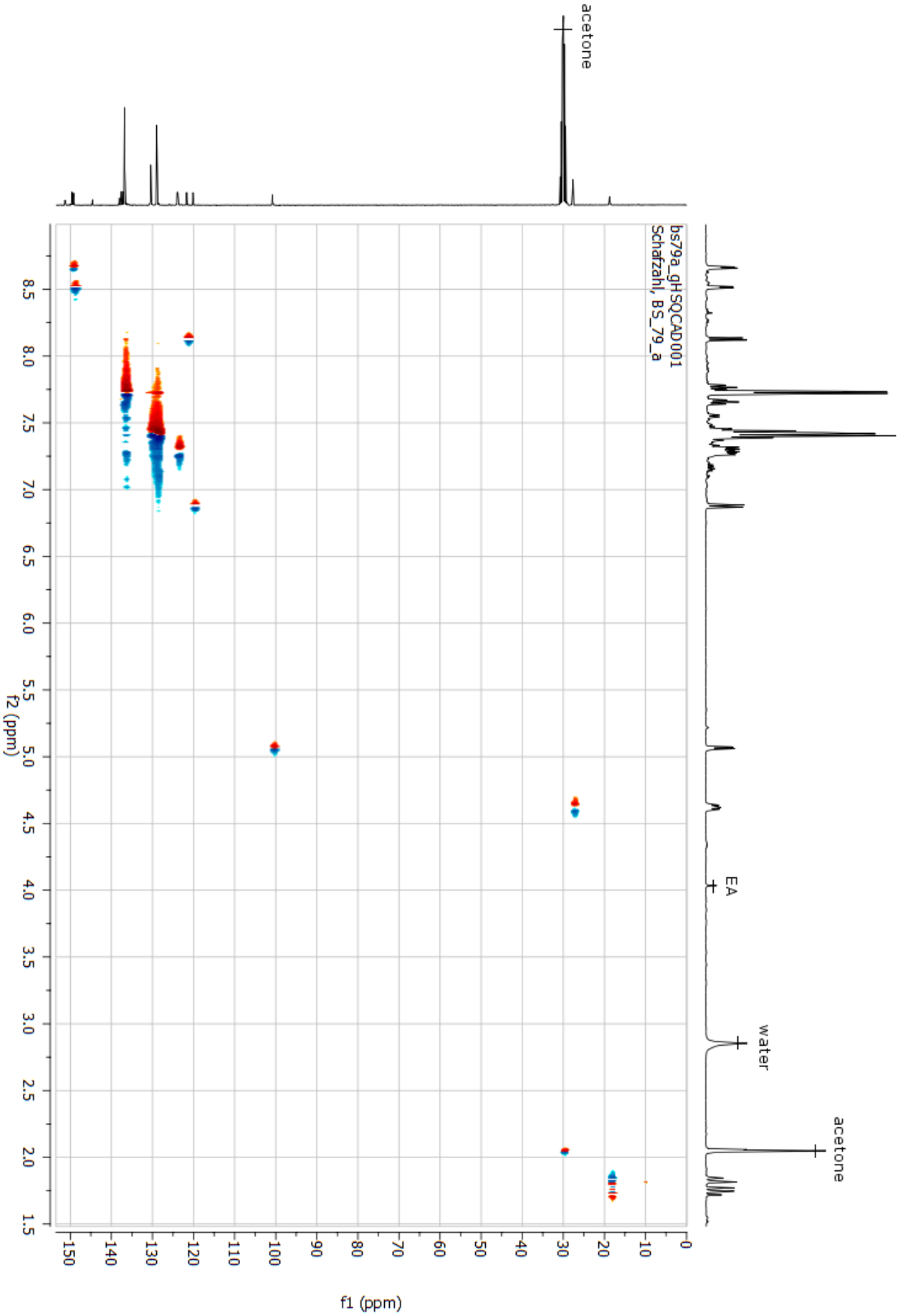

Figure 85 HSQC NMR spectrum of phenyl$_3$SipyPz (**26**) in acetone d_6.

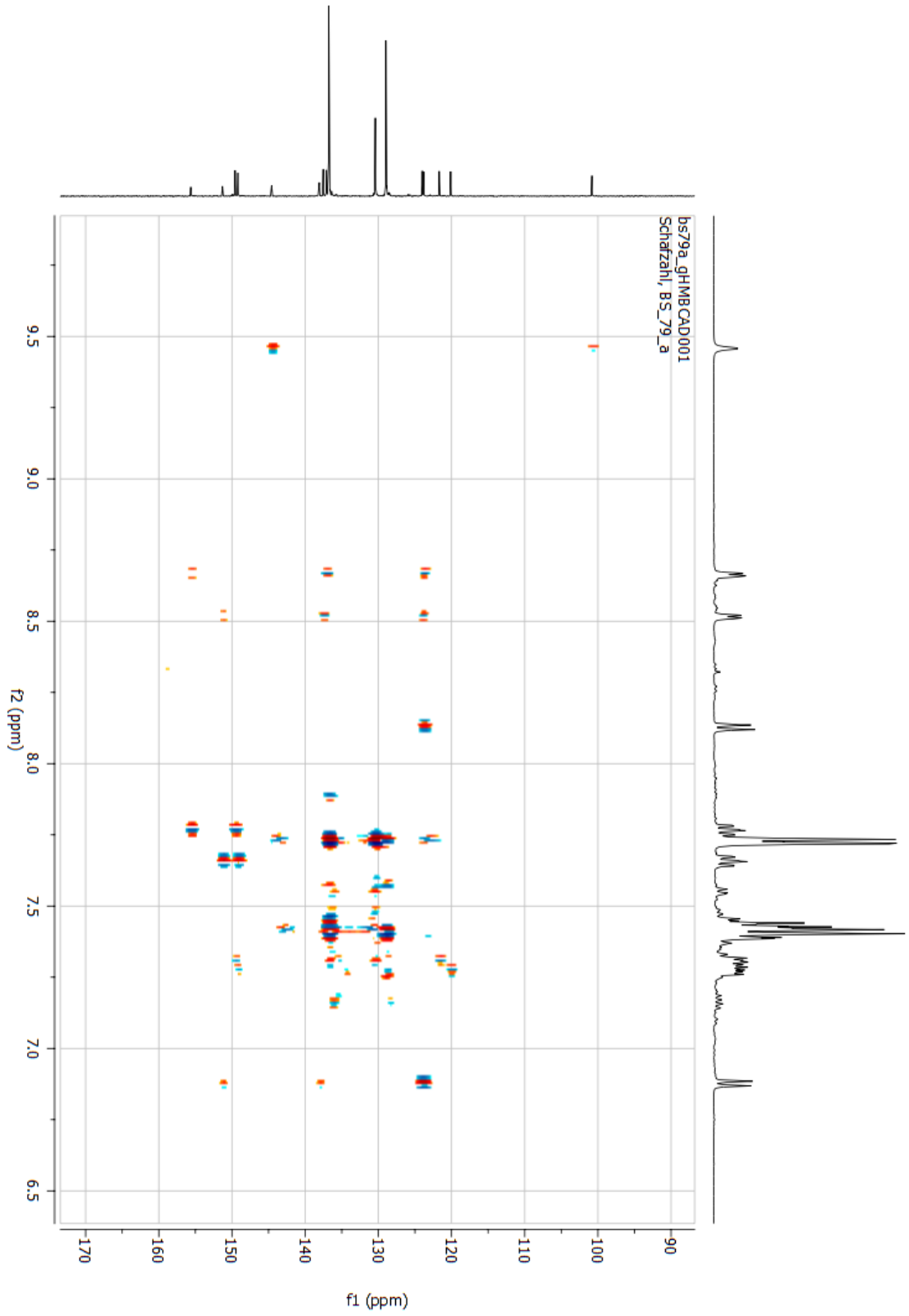

Figure 86 HMBC NMR spectrum of phenyl$_3$SipyPz (**26**) in acetone d_6 (aromatic region).

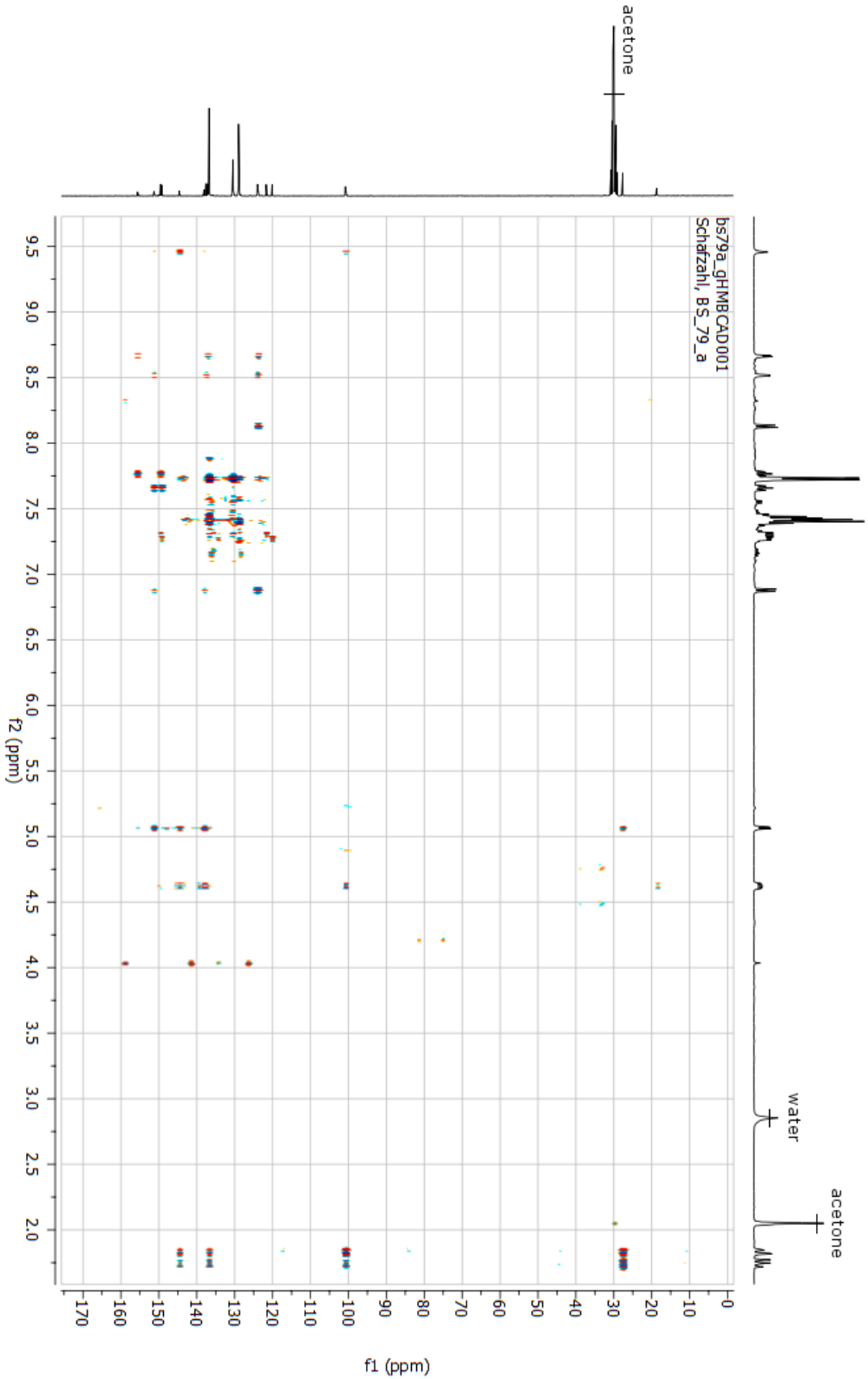

Figure 87 HMBC NMR spectrum of phenyl$_3$SipyPz (**26**) in acetone d_6 (aliphatic region)

Crystallographic data

Averaged Bond Lengths, Angles, Inter- and Intramolecular Interactions

Table 25 Selected bond lengths and angles for presented chlorosilanes.

N°	Compound	Space Group	Si–C_{aryl} [Å] (avg.)	Si–C_{Ph} [Å] (avg.)	Si–Cl [Å] (avg.)	C–Si–C [°] (avg.)	Cl–Si–Cl [°] (avg.)	C–Si–Cl [°] (avg.)
1	*2,5-xylylSiCl$_3$*	*P*2$_1$/*m*	1.844(12)		2.039(3)	—	106.39(7)	112.39(2)
	2,6-xylylSiCl$_3$[159]	*Pnma*	1.860(4)		2.048(4)	—	105.35(7)	113.37(7)
	1-naphthylSiCl$_3$[6]	*P*2$_1$/*c*	1.841(2)		2.034(8)	—	106.9(4)	111.9(7)
	2-naphthylSiCl$_3$[17]	*P*2$_1$/*n*	1.873(4)		2.034(10)	—	107.2(4)	111.7(9)
	2,4-xylyl$_2$SiCl$_2$[7]	*P*-1	1.858(3)		2.059(2)	118.15(9)	104.95(4)	108.24(9)
3	*2,5-xylyl$_2$SiCl$_2$*	*P*2$_1$/*c*	1.861(3)		2.063(3)	116.11(4)	104.667(5)	108.86(3)
	2,6-xylyl$_2$SiCl$_2$[7]	*P*-1	1.877(2)		2.069(2)	113.72(7)	102.66(3)	110.09(3)
4	*1-naphthyl(phenyl)SiCl$_2$*	*P*2$_1$/*c*	1.859(3)		2.0621(9)	113.03(12)	106.57(4)	109.24(9)
	1-naphthyl$_2$SiCl$_2$ [7]	*P*2$_1$/*n*	1.859(3)		2.063(2)	116.84(10)	106.18(4)	110.01(8)
	phenyl$_3$SiCl[168]	*P*2$_1$/*c*	—	1.861(2)	2.079(2)	111.57(3)	—	107.27(3)
6	*2,5-xylyl$_3$SiCl*	*P*2$_1$/*c*	1.871(17)	—	2.096(6)	112.31(7)	106.43(5)	1.871(17)
7	*1-naphthyl(phenyl)$_2$SiCl*	*P*2$_1$/*c*	1.868(2)	1.859(2)	2.079(2)	111.25(10)	—	107.61(8)
8	*1-naphthyl$_2$(phenyl)SiCl*	*P*-1	1.869(3)	1.863(2)	2.086(3)	110.86(9)	—	107.99(7)
	1-naphthyl$_3$SiCl[6]	*P*-1	1.874(3)	—	2.089(2)	111.23(6)	—	107.66(5)
9	*1-naphthyl$_3$SiCl · naph.*	*P*-1	1.872(2)	—	2.078(2)	110.78(9)	—	108.12(6)

N°	Compound	π-π Stacking [Å]		Edge to Face [Å]	$CH_3 \cdots \pi$ [Å]	C–H···Cl [Å]
		d	*R*			
1	*2,5-xylylSiCl$_3$*	—	—	—	2.95	3.02 – 3.20
	2,6-xylylSiCl$_3$[159]	—	—	—	2.94	3.07 – 3.22
	1-naphthylSiCl$_3$[6]	3.41	1.72	2.94	—	3.01 – 3.19
	2-naphthylSiCl$_3$[17]	—	—	2.78 – 2.87	—	—
	2,4-xylyl$_2$SiCl$_2$[7]	—	—	3.26	2.99	—
3	*2,5-xylyl$_2$SiCl$_2$*	—	—	2.73	3.17 – 3.38	3.08 – 3.33
	2,6-xylyl$_2$SiCl$_2$[7]	3.45	1.46	—	3.24	2.99
4	*1-naphthyl(phenyl)SiCl$_2$*	3.42	2.2	2.73, 3.39	—	2.97 – 3.19
	1-naphthyl$_2$SiCl$_2$ [7]	3.58, 3.69	1.54, 1.23	2.95	—	2.91
	phenyl$_3$SiCl[168]	—	—	—	—	—
6	*2,5-xylyl$_3$SiCl*	—	—	3.08 – 3.35	2.51 – 3.29	—
7	*1-naphthyl(phenyl)$_2$SiCl*	—	—	2.87 – 3.37	—	2.95 – 3.15
8	*1-naphthyl$_2$(phenyl)SiCl*	—	—	2.69 – 3.39	—	3.10 – 3.12
	1-naphthyl$_3$SiCl[6]	3.45	1.61	2.79 – 3.20	—	3.08 – 3.19
9	*1-naphthyl$_3$SiCl · naph.*	3.67	2.92	2.59 – 3.38	—	—

Table 26 Selected bond lengths and angles as well as intermolecular interactions for presented silanes.

N°	Compound	Space Group	$Si–C_{Aryl}$ [Å] (avg.)	$Si–C_{Ph}$ [Å] (avg.)	Si–H [Å] (avg.)	C–Si–C [°] (avg.)	C–Si–H [°] (avg.)
	2,4-xylyl$_2$SiH$_2$[8]	$P2_1/c$	1.869(2)	—	1.389(2)	117.18(6)	—
14	*2,5-xylyl$_2$SiH$_2$*	$P\bar{1}$	1.8723(18)	—	1.426(18)	114.15(8)	108.8(8)
	2,6-xylyl$_2$SiH$_2$[8]	$P2_1/c$	1.885(2)	—	1.354(2)	114.05(7)	—
	1-naphthyl$_2$SiH$_2$[8]	*Pbca*	1.869(3)	—	1.385(2)	109.90(6)	—
	phenyl$_3$SiH[1]	$P2_1/c$	—	1.851(2)	1.490(2)	111.03(5)	107.87(5)
18	*2,5-xylyl$_3$SiH*	$P2_1/c$	1.889(2)	—	1.463(18)	110.1(9)	108.83(7)
19	*1-naphthyl(phenyl)$_2$SiH*	$P2_1/n$	1.884(3)	1.874(3)	1.437(3)	110.36(5)	108.57(5)
20	*1-naphthyl$_2$(phenyl)SiH*	*Pbca*	1.869(4)	1.874(4)	1.36(3)	109.69(17)	109.23(12)
21	*1-naphthyl$_3$SiH*	$Pna2_1$	1.872(6)	—	1.4200	111.07(3)	107.83(4)
	2,4,6-mesityl$_3$SiH[152]	Cc	2.02	—	—	105.23	—
	2,3,4,5,6-mesityl$_3$SiH[173]	$P\bar{1}$	1.963(4)	—	1.000(2)	105.87(2)	105.41(2)

N°	Compound	Edge to Face [Å]	$CH_3\cdots\pi$ [Å]	$Si–H\cdots Si$ [Å]
	2,4-xylyl$_2$SiH$_2$[8]	3.18	2.83	—
14	*2,5-xylyl$_2$SiH$_2$*	—	2.80	3.19
	2,6-xylyl$_2$SiH$_2$[8]	2.95	2.76	—
	1-naphthyl$_2$SiH$_2$[8]	2.79 – 2.83	—	—
	phenyl$_3$SiH[1]	2.82 – 3.09	—	—
18	*2,5-xylyl$_3$SiH*	—	2.76 – 3.01	3.78
19	*1-naphthyl(phenyl)$_2$SiH*	2.65 – 2.93	—	—
20	*1-naphthyl$_2$(phenyl)SiH*	2.88 – 3.18	—	3.63
21	*1-naphthyl$_3$SiH*	2.98 – 3.39	—	3.49 – 3.51
	2,4,6-mesityl$_3$SiH[152]	—	—	—
	2,3,4,5,6-mesityl$_3$SiH[173]	—	2.82 – 3.32	—

Table 27 Selected average bond lengths of triaryl(allyl)silanes.

N°	Compound	Si–C_{Naph} [Å] (avg.)	Si–C_{Ph} [Å] (avg.)	Si–$C_{1'}$ [Å] (avg.)	$C_{1'}$–$C_{2'}$ (Allyl) [Å]	$C_{2'}$–$C_{3'}$ (Allyl) [Å]
22	*phenyl*$_3$(allyl)*Si*	—	1.872(3)	1.892(3)	1.494(2)	1.325(2)
23	*1-naphthyl(phenyl)*$_2$(allyl)*Si*	1.891(3)	1.881(3)	1.899(3)	1.492(2)	1.317(3)
24	*1-naphthyl*$_2$*(phenyl)* (allyl)*Si*	1.890(3)	1.881(3)	1.920(3)	1.483 (2)	1.323(2)
25	*1-naphthyl*$_3$(allyl)*Si*	1.892(3)	—	1.918(3)	1.506(2)	1.326(2)
	1-naphthyl(2,4,6-mesityl)(phenyl)(allyl)*Si*[151]	1.873(2)	1.877(2)	1.888(2)	1.491(2)	1.305(2)
	2,4,6-mesityl$_3$(allyl)*Si*[152]	—	1.909(2)	1.919(3)	1.454(3)	1.351(8)

N°	Compound	C_{aryl}–Si–C_{aryl} [°] (avg.)	C_{aryl}–Si–C_{allyl} [°] (avg.)	Si–$C_{1'}$–$C_{2'}$ (Allyl) [°]	$C_{1'}$–$C_{2'}$–$C_{3'}$ (Allyl) [°]
22	*phenyl*$_3$(allyl)*Si*	110.01(6)	108.93(6)	115.14(9)	125.56(13)
23	*1-naphthyl(phenyl)*$_2$(allyl)*Si*	110.21(7)	108.69(7)	117.49(12)	125.62(19)
24	*1-naphthyl*$_2$*(phenyl)* (allyl)*Si*	109.00(6)	109.89(6)	117.21 (10)	126.20 (16)
25	*1-naphthyl*$_3$(allyl)*Si*	108.61(5)	110.32(6)	118.00(9)	125.11(14)
	1-naphthyl(2,4,6-mesityl)(phenyl) (allyl)*Si*[151]	109.65(6)	109.26(2)	114.52(1)	125.53(1)
	2,4,6-mesityl$_3$(allyl)*Si*[152]	112.87(1)	105.81(2)	124.71(2)	124.82(3)

Table 28 Inter- and intramolecular interactions of triaryl(allyl)silanes.

N°	Compound	Edge to Face [Å]	$CH_3 \cdots \pi$ [Å]	CH_2(allyl) $\cdots \pi$ [Å]	$CH{=}CH_2(\pi)$ (allyl) $\cdots H$ [Å]	
					intra	inter
22	*phenyl*$_3$*(allyl)Si*	2.81 – 3.34	3.28 (methylene-pi)	—	2.92 edge to face	2.94, 3.02 edge to face
23	*1-naphthyl(phenyl)*$_2$*(allyl)Si*	2.81 – 3.41	—	—	2.90, 3.31 edge to face	2.95, 3.34 edge to face
24	*1-naphthyl*$_2$*(phenyl) (allyl)Si*	3.21 – 3.74	—	—	2.72 edge to face	2.89 edge to face
25	*1-naphthyl*$_3$*(allyl)Si*	2.66 – 3.28	—	—	2.65 edge to face	2.82 edge to face
	1-naphthyl(2,4,6-mesityl) (phenyl)(allyl)Si	2.84 – 2.94	2.85	3.25	2.81 edge to face	2.96, 3.09 edge to face
	2,4,6-mesityl$_3$*(allyl)Si*[152]	—	3.12 – 3.31	3.49	3.23 methyl	3.29 methyl

Table 29 Crystallographic data and details of measurements for compounds **1**, **3**, **4**. Mo Kα (λ=0.71073 Å). $R_1 = \sum / |F_o| - |F_c| / \sum |F_d|$; $wR2 = [\sum_w (F_o^2 - F_2^2)^2 / \sum_w (F_o^2)^2]^{1/2}$.

Compound	*2,5-xylylSiCl$_3$ (**1**)*	*2,5-xylyl$_2$SiCl$_2$ (**3**)*	*1-naphthyl(phenyl)SiCl$_2$ (**4**)*
Formula	$C_8H_9Cl_3Si$	$C_{16}H_{18}Cl_2Si$	$C_{16}H_{12}Cl_2Si$
Fw (g mol^{-1})	239.59	309.29	303.25
a [Å]	8.9210(7)	9.3063(4)	8.9439 (6)
b [Å]	7.2244(6)	15.4212(7)	8.9911 (6)
c [Å]	9.3319(7)	11.4517(6)	17.4880 (11)
α [°]	90	90	90
β [°]	118.142(2)	110.085(1)	91.733 (2)°
γ [°]	90	90	90
V (Å^3)	530.33(7)	1543.53(13)	1405.66 (16)
Z	2	4	4
Crystal size (mm)	0.12 × 0.10 × 0.08	0.08 × 0.04 × 0.04	0.10 × 0.09 × 0.06
Crystal habit	Blocks, colourless	Block, colourless	Block, colourless
Crystal system	Monoclinic	Monoclinic	Monoclinic
Space group	*P*2$_1$/*m*	*P*2$_1$/*c*	*P*2$_1$/*c*
d_{calc} (mg m^{-3})	1.500	1.331	1.433
μ (mm^{-1})	0.92	0.48	0.53
T (K)	100(2)	100(2)	100(2)
2θ range [°]	2.5–33.3	2.3–33.2	3.2–33.2
F(000)	244	648	624
R_{int}	0.060	0.054	0.059
independent reflns	2197	5921	2457
No. of params	72	244	172
R1, wR2 (all data)[a]	R1 = 0.0289 wR2 = 0.0722	R1 = 0.0367 wR2 = 0.0857	R1 = 0.0442 wR2 = 0.1020
R1, wR2 (>2σ)[b]	R1 = 0.0244 wR2 = 0.0686	R1 = 0.0294 wR2 = 0.0798	R1 = 0.0402 wR2 = 0.0999

Table 30 Crystallographic data and details of measurements for compounds **7**–**9**.
Mo Kα (λ=0.71073 Å). $R_1 = \sum / |F_o| - |F_c| / |\sum |F_d$; $wR2 = [\sum_w (F_o^{2-}F_2^2)^2 / \sum_w (F_o^2)^2]^{1/2}$.

Compound	*1-naphthyl(phenyl)$_2$SiCl (**7**)*	*1-naphthyl$_2$(phenyl)SiCl (**8**)*	*1-naphthyl$_3$SiCl Naph (**9**)*
Formula	$C_{22}H_{17}ClSi$	$C_{26}H_{19}ClSi$	$C_{30}H_{21}ClSi \cdot 0.5(C_{10}H_8)$
Fw (g mol^{-1})	344.89	394.95	509.09
a [Å]	11.0731(5)	9.4897(7)	9.4283(5)
b [Å]	8.9778(4)	9.5015(7)	12.1949(7)
c [Å]	18.1359(8)	12.3469(10)	12.5213(7)
α [°]	90	110.360(3)	96.162(2)
β [°]	98.594(2)	93.101(3)	108.914(2)
γ [°]	90	104.691(3)	99.300(2)
V (Å^3)	1782.68(14)	997.09(13)	1324.21(13)
Z	4	2	2
Crystal size (mm)	0.07 × 0.07 × 0.05	0.10 × 0.09 × 0.08	0.09 × 0.08 × 0.08
Crystal habit	Block, colourless	Block, colourless	Block, colourless
Crystal system	Monoclinic	Triclinic	Triclinic
Space group	*P*2$_1$/*c*	*P*-1	*P*-1
d_{calc} (mg m^{-3})	1.285	1.315	1.277
μ (mm^{-1})	0.28	0.26	0.21
T (K)	100(2)	100(2)	100(2)
2θ range [°]	2.5–27.9	2.6–28.1	2.4–33.2
F(000)	720	412	532
R_{int}	0.053	0.048	0.114
independent reflns	3427	4789	4652
No. of params	286	329	334
R1, wR2 (all data)[a]	R1 = 0.0643 wR2 = 0.1073	R1 = 0.0616 wR2 = 0.1042	R1 = 0.0506 wR2 = 0.1097
R1, wR2 (>2σ)[b]	R1 = 0.0490 wR2 = 0.1017	R1 = 0.0443 wR2 = 0.0962	R1 = 0.0397 wR2 = 0.1033

Table 31 Crystallographic data and details of measurements for compounds **14** and **18**. Mo Kα (λ=0.71073 Å). $R_1 = \sum / |F_o| - |F_c| / |\sum |F_d|$; $wR2 = [\sum_w (F_o^2 - F_2^2)^2 / \sum_w (F_o^2)^2]^{1/2}$.

Compound	*2,5-xylyl$_2$SiH$_2$ (**14**)*	*2,5-xylyl$_3$SiH (**18**)*
Formula	$C_{16}H_{20}Si$	$C_{24}H_{28}Si$
Fw (g mol^{-1})	240.41	344.55
a [Å]	4.9753(4)	5.2443(6)
b [Å]	11.4103(8)	33.820(3)
c [Å]	12.4601(8)	11.1289(12)
α [°]	96.895(4)	90
β [°]	96.562(3)	95.673(4)
γ [°]	94.975(3)	90
V (Å^3)	694.01(9)	1964.2(4)
Z	1	4
Crystal size (mm)	0.03 × 0.001 × 0.001	0.04 × 0.001 × 0.001
Crystal habit	Needle, colourless	Needle, colourless
Crystal system	Triclinic	Monoclinic
Space group	*P–1*	*P2$_1$/c*
d_{calc} (mg m^{-3})	1.15037	1.165
μ (mm^{-1})	0.15	0.12
T (K)	100(2)	100(2)
2θ range [°]	1.6–28	2.2–25.8
F(000)	260	744
R_{int}	0.068	0.102
independent reflns	3329	3453
No. of params	166	236
R1, wR2 (all data)[a]	R1 = 0.0681 wR2 = 0.1233	R1 = 0.0586 wR2 = 0.1110
R1, wR2 (>2σ)[b]	R1 = 0.0457 wR2 = 0.1114	R1 = 0.0438 wR2 = 0.1015

Table 32 Crystallographic data and details of measurements for compounds **19**–**21**. Mo Kα (λ=0.71073 Å). $R_1 = \sum / |F_o| - |F_c| / |\sum |F_d$; $wR2 = [\sum_w (F_o^2 - F_2^2)^2 / \sum_w (F_o^2)^2]^{1/2}$.

Compound	*1-naphthyl(phenyl)$_2$SiH (**19**)*	*1-naphthyl$_2$phenylSiH (**20**)*	*1-naphthyl$_3$SiH (**21**)*
Formula	$C_{22}H_{18}Si$	$C_{26}H_{20}Si$	$C_{30}H_{22}Si$
Fw (g mol^{-1})	310.45	360.51	410.56
a [Å]	9.9345(16)	11.1928(9)	9.7302(9)
b [Å]	9.8379(16)	9.9036(8)	37.050(3)
c [Å]	17.532(3)	34.006(3)	17.7365(15)
α [°]	90	90	90
β [°]	97.198(6)	90	90
γ [°]	90	90	90
V (Å^3)	1700.0(5)	3769.5(5)	6394.1(10)
Z	4	8	12
Crystal size (mm)	0.09 × 0.08 × 0.07	0.20 × 0.06 × 0.02	0.10 × 0.08 × 0.07
Crystal habit	Block, colourless	Block, colourless	Block, colourless
Crystal system	Monoclinic	Orthorhombic	Orthorhombic
Space group	*P*2$_1$/*n*	*Pbca*	*Pna*2$_1$
d_{calc} (mg m^{-3})	1.213	1.270	1.279
μ (mm^{-1})	0.14	0.13	0.13
T (K)	100(2)	100(2)	100(2)
2θ range [°]	2.4–35.3	2.2–25.0	2.2–23.4
F(000)	656	1520	2592
R_{int}	0.050	0.149	0.127
independent reflns	2996	3250	5814
No. of params	280	248	838
R1, wR2 (all data)[a]	R1 = 0.0305 wR2 = 0.0788	R1 = 0.1271 wR2 = 0.1586	R1 = 0.0827 wR2 = 0.1265
R1, wR2 (>2σ)[b]	R1 = 0.0291 wR2 = 0.0776	R1 = 0.0593 wR2 = 0.1243	R1 = 0.0574 wR2 = 0.1181

Table 33 Crystallographic data and details of measurements for compounds **22**–**25**. Mo Kα (λ=0.71073 Å). $R_1 = \sum / |F_o| - |F_c| / |\sum |F_d$; $wR2 = [\sum_w(F_o^2-F_2^2)^2/\sum_w(F_o^2)^2]^{1/2}$.

Compound	*phenyl$_3$(allyl)Si* (**22**)	*1-napthyl(phenyl)$_2$(allyl)Si* (**23**)	*1-napthyl$_2$(phenyl)(allyl)Si* (**24**)	*1-naphthyl$_3$(allyl)Si* (**25**)
Formula	$C_{21}H_{20}Si$	$C_{25}H_{22}Si$	$C_{29}H_{24}Si$	$C_{33}H_{26}Si$
Fw (g mol^{-1})	300.46	350.51	400.57	450.63
a [Å]	9.4416(4)	9.8889(4)	10.0602(12)	10.0156(4)
b [Å]	9.5596(4)	10.0106(4)	10.1861(12)	11.7046(4)
c [Å]	10.0151(4)	30.6810(13)	11.3942(14)	11.7835(4)
α [°]	90.465(2)	84.358(2)	75.617(6)	111.075(1)
β [°]	110.968(2)	87.240(2)	69.312(6)	102.357(1)
γ [°]	99.629(2)	72.797(2)	84.092(6)	92.698(1)
V (Å^3)	829.92(6)	2886.7(2)	1057.9(2)	1247.39(8)
Z	2	6	2	2
Crystal size (mm)	0.12 × 0.10 × 0.07	0.10 × 0.09 × 0.08	0.13 × 0.11 × 0.09	0.08 × 0.07 × 0.06
Crystal habit	Block, colourless	Block, colourless	Block, colourless	Block, colourless
Crystal system	Triclinic	Triclinic	Triclinic	Triclinic
Space group	*P*-1	*P*-1	*P*-1	*P*-1
d_{calc} (mg m^{-3})	1.202	1.210	1.257	1.200
μ (mm^{-1})	0.14	0.13	0.12	0.11
T (K)	100(2)	100(2)	100(2)	100(2)
2θ range [°]	2.4–30.4	2.2–33.2	2.4–35.2	2.5–33.1
F(000)	320	1116	424	476
R_{int}	0.070	0.075	0.050	0.032
independent refIns	4394	10099	3689	4339
No. of params	279	703	271	411
R1, wR2 (all data)[a]	R1 = 0.0500 wR2 = 0.0910	R1 = 0.0433 wR2 = 0.0942	R1 = 0.0378 wR2 = 0.0924	R1 = 0.0384 wR2 = 0.1129
R1, wR2 (>2σ)[b]	R1 = 0.0383 wR2 = 0.0840	R1 = 0.0376 wR2 = 0.0901	R1 = 0.0334 wR2 = 0.0887	R1 = 0.0347 wR2 = 0.1084

Table 34 Crystallographic data and details of measurements for compounds **29** and **31**. Mo Kα (λ=0.71073 Å). $R_1 = \sum / |F_o| - |F_c| / |\sum |F_d$; $wR2 = [\sum_w(F_o^2 - F_2^2)^2 / \sum_w(F_o^2)^2]^{1/2}$.

Compound	*Naph$_3$SiPyPz (**29**)*	*1-naphthyl$_2$(phenyl)$_2$Si (**31**)*
Formula	$C_{45}H_{34}N_4Si$, C_7H_8	$C_{32}H_{24}Si$
Fw (g mol^{-1})	750.66	436.60
a [Å]	9.8642(4)	18.2253(14)
b [Å]	11.3904(5)	7.4874(6)
c [Å]	18.7421(9)	19.1104(14)
α [°]	74.315(2)	90
β [°]	88.009(2)	93.889(3)
γ [°]	79.822(2)	90
V (Å^3)	1995.30(15)	2601.8(3)
Z	2	4
Crystal size (mm)	0.09× 0.06 × 0.08	0.09 × 0.06 × 0.06
Crystal habit	Block, colourless	Block, colourless
Crystal system	Triclinic	Monoclinic
Space group	P–1	$P2_1/c$
d_{calc} (mg m^{-3})	1.249	1.115
μ (mm^{-1})	0.10	0.11
T (K)	100(2)	100(2)
2ϑ range [°]	2.3–32.8	2.2–32.1
F(000)	792	920
R_{int}	0.0578	0.097
independent refIns	7032	4569
No. of params	519	298
R1, wR2 (all data)[a]	R1 = 0.0578 wR2 = 0.1009	R1 = 0.0499 wR2 = 0.0988
R1, wR2 (>2σ)[b]	R1 = 0.0398 wR2 = 0.0886	R1 = 0.0368 wR2 = 0.0908

Bibliography

1. Feigl, A., Bockholt, A., Weis, J. & Rieger, B. in *Advances in Polymer Science* 1–31 (2009). doi:10.1007/12_2009_1
2. Sacarescu, L., Mangalagiu, I., Simionescu, M., Sacarescu, G. & Ardeleanu, R. Polysilanes. A new route toward high performance EL devices. *Macromol. Symp.* **267,** 123–128 (2008).
3. Malandrino, G. Chemical Vapour Deposition. Precursors, Processes and Applications. Edited by Anthony C. Jones and Michael L. Hitchman. *Angew. Chemie Int. Ed.* **48,** 7478–7479 (2009).
4. Zard, S. Z. *Radical Reactions in Organic Synthesis*. (Oxford University Press, 2003).
5. Davies, A. G. Recent advances in the chemistry of the organotin hydrides. *J. Chem. Res.* **2006,** 141–148 (2006).
6. Binder, J. Synthesis, Characterization and Reactivity of novel Arylsilanes - steps towards new materials. (Graz University of Technology, 2015).
7. Binder, J., Fischer, R. C., Flock, M., Torvisco, A. & Uhlig, F. Novel Aryl Substituted Silanes Part I: Synthesis and Characterization of Diaryl Silicon Dichlorides. *Phosphorus. Sulfur. Silicon Relat. Elem.* **190,** 1980–1993 (2015).
8. Binder, J. *et al.* Novel aryl-substituted silanes Part II: Synthesis and characterization of diaryl silicon dihydrides. *Phosphorus. Sulfur. Silicon Relat. Elem.* **191,** 478–487 (2016).
9. McDowell, M. T., Lee, S. W., Nix, W. D. & Cui, Y. 25th anniversary article: Understanding the lithiation of silicon and other alloying anodes for lithium-ion batteries. *Adv. Mater.* **25,** 4966–4985 (2013).
10. Obrovac, M. N. & Chevrier, V. L. Alloy negative electrodes for Li-ion batteries. *Chem. Rev.* **114,** 11444–11502 (2014).
11. Yang, J., Winter, M. & Besenhard, J. O. Small particle size multiphase Li-alloy anodes for lithium-ionbatteries. *Solid State Ionics* **90,** 281–287 (1996).
12. Crafts, J. M. & Friedel, C. Ueber das Siliciummethyl und die Kieselsäure-Methylather. *Ann. der Chemie und Pharm.* **136,** 203–212 (1865).
13. Grignard, V. Mixed organomagnesium combinations and their application in acid, alcohol, and hydrocarbon synthesis. *Ann. Chim. Phys.* **24,** 433–490 (1901).
14. Kipping, F. S. Organic derivatives of silicon. Preparation of alkylsilicon chlorides. *Proc. Chem. Soc.* **19,** 15–16 (1904).
15. Dilthey, W. & Eduardoff, F. Ueber die Darstellung von Phenylsiliciumverbindungen. *Berichte der Dtsch. Chem. Gesellschaft* **37,** 1139–1142 (1904).
16. Clayden, J., Greeves, N., Warren, S. & Wothers, P. *Organic Chemistry*. (Oxford University Press, 2001).
17. Wiesinger, T. Synthesis and Characterization of Novel Chloroarylsilanes with Sterically Demanding Aryl Substituents and Their Applications Master Thesis Master of Science. (2012).
18. Hollemann, A. F., Wiberg, E. & Wiberg, N. *Lehrbuch der Anorganischen Chemie*. (Walter de Gruyter & Co., 10785 Berlin, 2007).
19. Finholt, E., Bond, C., Wilzbach, K. E. & Schlesinger, H. I. The Preparation and Some Properties of Hydrides of Elements of the Fourth Group of the Periodic System and of their Organic Derivatives. *J. Am. Chem. Soc.* **69,** 2692–2696 (1947).
20. Trost, B. M. & Ball, Z. T. Addition of Metalloid Hydrides to Alkynes: Hydrometallation with Boron, Silicon, and Tin. *ChemInform* **36,** (2005).
21. Jones, G. R. & Landais, Y. The oxidation of the carbon-silicon bond. *Tetrahedron* **52,** 7599–7662 (1996).
22. Gevorgyan, V., Rubin, M., Benson, S., Liu, J.-X. & Yamamoto, Y. A Novel $B(C_6F_5)_3$ -Catalyzed Reduction of Alcohols and Cleavage of Aryl and Alkyl Ethers with Hydrosilanes. *J. Org. Chem.* **65,** 6179–6186 (2000).
23. Fernandes, A. C. & Romão, C. C. A novel method for the reduction of imines using the system silane/MoO_2Cl_2. *Tetrahedron Lett.* **46,** 8881–8883 (2005).
24. Sato, Y., Saito, N. & Mori, M. Asymmetric Cyclization of ω-Formyl-1,3-dienes Catalyzed by a

Zerovalent Nickel Complex in the Presence of Silanes. *J. Org. Chem.* **67,** 9310–9317 (2002).
25. Penso, M., Albanese, D., Landini, D. & Lupi, V. Biaryl formation: palladium catalyzed cross-coupling reactions between hypervalent silicon reagents and aryl halides. *J. Mol. Catal. A Chem.* **204–205,** 177–185 (2003).
26. Sano, H., Torres, N. M. & Maleczka, R. E. in *Encyclopedia of Reagents for Organic Synthesis* **1,** 1–6 (John Wiley & Sons, Ltd, 2007).
27. Sarkar, T. K. in *Science of Synthesis; Category 1, Organometallics* (eds. Fleming & Ley) 873–925 (Georg Thieme Verlag, 2002). doi:10.1055/sos-SD-004-00909
28. Voronkov, M. G. & Egorochkin, A. N. in *The Chemistry of Organic Germanium, Tin and Lead Compounds* 131–168 (John Wiley & Sons, Ltd, 2003). doi:10.1002/0470857188.ch2
29. Schumann, H. & Schumann, I. in *Gmelin Handbuch der Anorganischen Chemie, Band 35, Teil 4* (Springer-Verlag, 1976).
30. Dillard, C. R., McNeill, E. H., Simmons, D. E. & Yeldell, J. B. Synthesis and Properties of Some Tin Alkyls. *J. Am. Chem. Soc.* **80,** 3607–3609 (1958).
31. Paneth, F. & Furth, K. Tin hydride. I. *Berichte der Dtsch. Chem. Gesellschaft Abteilung B Abhandlungen* **52B,** 2020–9 (1919).
32. Paneth, F., Johanssen, A. & Matthies, M. Preparation of gaseous metal hydrides from alloys and solution. *Berichte der Dtsch. Chem. Gesellschaft Abteilung B Abhandlungen* **55B,** 769–75 (1922).
33. Paneth, F. & Rabinowitsch, E. Über die Gewinnung des Zinnwasserstoffs durch kathodische Reduktion. *Berichte der Dtsch. Chem. Gesellschaft (A B Ser.* **57,** 1877–1890 (1924).
34. Davies, A. G. *Organotin Chemistry*. (Wiley-VCH Verlag GmbH & Co. KGaA, 2004). doi:10.1002/3527601899
35. Clark, A. J. in *Category 1, Organometallics* (eds. Moloney, M. G. & Thomas, E. J.) 205 (Georg Thieme Verlag, 2003). doi:10.1055/sos-SD-005-00189
36. Kipping, F. S. & Sands, J. E. XCIII.-Organic derivatives of silicon. Part XXV. Saturated and unsaturated silicohydrocarbons, Si_4Ph_8. *Journal of the Chemical Society, Transactions* **119,** 830 (1921).
37. Kipping, F. S. CCC.—Organic derivatives of silicon. Part XXVIII. Octaphenyldiethylsilicotetrane. *J. Chem. Soc., Trans.* **123,** 2598–2603 (1923).
38. Burkhard, C. A. Polydimethylsilanes. *J. Am. Chem. Soc.* **71,** 963–964 (1949).
39. Kumada, M. & Tamao, K. in *Advances in Organometallic Chemistry* 19–117 (Elsevier B.V., 1968). doi:10.1016/S0065-3055(08)60587-0
40. Boberski, W. G. & Allred, A. L. Properties of Long-Chain Permethylpolysilanes. *J. Organomet. Chem.* **88,** 65–72 (1975).
41. Hague, D. N. & Prince, R. H. Proceedings of the Chemical Society. September 1962. *Proc. Chem. Soc.* 300 (1962). doi:10.1039/ps9620000289
42. Gilman, H., Atwell, W. H. & Schwebke, G. L. Ultraviolet properties of compounds containing the silicon-silicon bond. *J. Organomet. Chem.* **2,** 369–371 (1964).
43. West, R. Electron delocalization and 'aromatic' behavior in cyclic polysilanes. *Pure Appl. Chem.* **54,** 1041–1050 (1982).
44. Carberry, E. & West, R. Cyclic Polysilanes. III. The Preparation of Permethylcyclopolysilanes by Coupling, Pyrolysis, and Redistribution Reactions. *J. Am. Chem. Soc.* **223,** 5440–5446 (1969).
45. Hengge, E. & Janoschek, R. Homocyclic Silanes. *Chem. Rev.* **95,** 1495–1526 (1995).
46. L.F. Brough, K. Matsumura, R. W. Homologe Reihe cyclischer Polysilane von (Me2Si)s bis (Me2Si)35[**1. *Angew. Chem.* **91,** 1022–1023 (1979).
47. L.F. Brough, R. W. Cyclic Polysilanes XIX. A Temperature Study of Redistribution Equilibria between Permethylcyclopolysilanes. *J. Organomet. Chem.* **194,** 139–145 (1980).
48. Gilman, H. & Schwebke, G. L. Decaphenylcyclopentasilane. *J. Am. Chem. Soc.* **85,** 1016–1016 (1963).
49. H.J.S. Winkler, A.W.P. Jarvie, D.J. Peterson, H. G. Preparation and characterization of Dodecaphenylcyclohexasilane. 4089–4093 (1961). doi:10.1016/j.jfluchem.2014.06.008
50. Kinstle, T. H., Haiduc, I. & Gilman, H. Mass spectrometry of cyclopolysilanes. *Inorganica Chim.*

Acta **3,** 373–377 (1969).
51. Hengge, E. in *Topics in Current Chemistry* 1–127 (Springer Berlin Heidelberg, 1974). doi:10.1007/BFb0111403
52. Hengge, E. & Kovar, D. Darstellung und Charakterisierung eines neuen cyclischen Siliciumchlorides Si4Cl8. *Zeitschrift für Anorg. und Allg. Chemie* **458,** 163–167 (1979).
53. Hengge, E., Gspaltl, P. & Pinter, E. Si-H-containing cyclosilanes and their behaviour in the dehydrogenative polymerization reaction. *J. Organomet. Chem.* **521,** 145–155 (1996).
54. Kira, M., Bock, H. & Hengge, E. Radical ions. XXVI. Radical anions of perphenylcyclopolysilanes. *J. Organomet. Chem.* **164,** 277–280 (1979).
55. Binder, J. Thermolysestudien an perphenylierten Cyclosilanen. *Diplomarbeit* (2011).
56. Fuchsbichler, B., Stangl, C., Kren, H., Uhlig, F. & Koller, S. High capacity graphite-silicon composite anode material for lithium-ion batteries. *J. Power Sources* **196,** 2889–2892 (2011).
57. Choffat, F., Smith, P. & Caseri, W. Polystannanes: Polymers of a molecular, jacketed metal-wire structure. *Adv. Mater.* **20,** 2225–2229 (2008).
58. Adams, S. & Dräger, M. Polystannanes Ph_3Sn-$SnPh_3$(n= 1–4): A Route to Molecular Metals? *Angew. Chemie Int. Ed. English* **26,** 1255–1256 (1987).
59. Trummer, M., Solenthaler, D., Smith, P. & Caseri, W. Poly(dialkylstannane) and poly(diarylstannane) homo- and random copolymers synthesized in liquid ammonia. *RSC Adv.* **1,** 823 (2011).
60. Rogers, J. A. & Bao, Z. Printed plastic electronics and paperlike displays. *J. Polym. Sci. Part A Polym. Chem.* **40,** 3327–3334 (2002).
61. Caseri, W. Polystannanes: processible molecular metals with defined chemical structures. *Chem. Soc. Rev.* **45,** 5187–5199 (2016).
62. Okano, M., Matsumoto, N., Arakawa, M., Tsuruta, T. & Hamano, H. Electrochemical synthesis of dialkylsubstituted polystannanes and their properties. *Chem. Commun.* 1799–1800 (1998). doi:10.1039/a804299c
63. Okano, M. & Watanabe, K. Electrochemical synthesis of stannane – silane and stannane – germane copolymers. *Electrochem. Commun.* **2,** 471–474 (2000).
64. Choffat, F., Smith, P. & Caseri, W. Facile synthesis of linear poly(dibutylstannane). *J. Mater. Chem.* **15,** 1789 (2005).
65. Bukalov, S. S., Leites, L. A., Lu, V. & Tilley, T. D. Order−Disorder Phase Transition in Poly(di- n -butylstannane) Observed by UV−Vis and Raman Spectroscopy. *Macromolecules* **35,** 1757–1761 (2002).
66. Sharma, H. K., Arias-Ugarte, R., Metta-Magana, A. J. & Pannell, K. H. Dehydrogenative dimerization of di-tert-butyltin dihydride photochemically and thermally catalyzed by iron and molybdenum complexes. *Angew. Chemie - Int. Ed.* **48,** 6309–6312 (2009).
67. Schittelkopf, K., Fischer, R. C., Meyer, S., Wilfling, P. & Uhlig, F. Catalytic dehydrogenative coupling of diorganotindihydrides by lanthanide diamide complexes. *Appl. Organomet. Chem.* **24,** 897–901 (2010).
68. Lechner, M. L. *et al.* From poly(dialkylstannane)s to poly(diarylstannane)s: Comparison of synthesis methods and resulting polymers. *Appl. Organomet. Chem.* **25,** 769–776 (2011).
69. Neumann, W. P. Neue Synthesen im Gebiet der Organozinn-Verbindungen (Über Zinn-dialkyle). *Angew. Chemie* **74,** 122–122 (1962).
70. Sindlinger, C. P. & Wesemann, L. Hydrogen abstraction from organotin di- and trihydrides by N-heterocyclic carbenes: a new method for the preparation of NHC adducts to tin(ii) species and observation of an isomer of a hexastannabenzene derivative [R_6Sn_6]. *Chem. Sci.* **5,** 2739 (2014).
71. Sindlinger, C. P., Stasch, A., Bettinger, H. F. & Wesemann, L. A nitrogen-base catalyzed generation of organotin(ii) hydride from an organotin trihydride under reductive dihydrogen elimination. *Chem. Sci.* **6,** 4737–4751 (2015).
72. Zeppek, C. Amine Base Induced Polymerization of Aryltin Hydrides: Mechanistic Insights & Nanomaterial Characterization. (2015).

73. Colombo, P. in *Polymer Derived Ceramics: From Nanostructure to Applications.* (eds. Colombo, P., Riedel, R., Sorarù, G. D. & Kleebe, H.-K.) 1–13 (DEStech Publications Inc., 2009).
74. Colombo, P., Mera, G., Riedel, R. & Sorarù, G. D. Polymer-Derived Ceramics: 40 Years of Research and Innovation in Advanced Ceramics. *J. Am. Ceram. Soc.* no-no (2010). doi:10.1111/j.1551-2916.2010.03876.x
75. Miller, R. D. & Michl, J. Polysilane high polymers. *Chem. Rev.* **89,** 1359–1410 (1989).
76. Fritz, G. Bildung siliciumorganischer Verbindungen. IV. Das thermische Verhalten von $C_2H_5SiH_3$, $(C_2H_5)_2SiH_2$ und $(C_2H_5)_3SiH$. *Zeitschrift für Anorg. und Allg. Chemie* **273,** 275–285 (1953).
77. Fritz, G. Bildung und Eigenschaften von Carbosilanen. *Pure Appl. Chem.* **13,** 281–296 (1966).
78. Paquin, D. P., O'Connor, R. J. & Ring, M. A. The pyrolysis of trimethylgermane and trimethylsilane. *J. Organomet. Chem.* **80,** 341–348 (1974).
79. Coleman, N. R. B. *et al.* Synthesis and Characterization of Dimensionally Ordered Semiconductor Nanowires within Mesoporous Silica. *J. Am. Chem. Soc.* **123,** 7010–7016 (2001).
80. Scott, B. A., Plecenik, R. M. & Simonyi, E. E. Kinetics and mechanism of amorphous hydrogenated silicon growth by homogeneous chemical vapor deposition. *Appl. Phys. Lett.* **39,** 73–75 (1981).
81. O'Brien, J. J. & Atkinson, G. H. Role of silylene in the pyrolysis of silane and organosilanes. *J. Phys. Chem.* **92,** 5782–5787 (1988).
82. Alyev, I. Y., Rozhkov, I. N. & Knunyants, I. L. Anode chemistry of organosilanes. Oxidative replacement of alkyl group by fluoride ion. *Tetrahedron Lett.* **17,** 2469–2470 (1976).
83. Zhang, Z.-R., Becker, J. Y. & West, R. Electrochemical oxidation of cyclic polysilanes under 'oxygen-free' and 'water-free' conditions. *J. Electroanal. Chem.* **455,** 197–204 (1998).
84. Grogger, C., Loidl, B., Stueger, H., Kammel, T. & Pachaly, B. Electrochemical Synthesis of Functional Organosilanes II: Direct Electrochemical Formation of Si-C Bonds. *J. Electrochem. Soc.* **160,** G88–G92 (2013).
85. Geniès, E. . & El Omar, F. Etude electrochimique de quelques phenylsilanes en milieu organique. *Electrochim. Acta* **28,** 547–556 (1983).
86. Geniès, E. M. & El Omar, F. Electrochimie des composes organiques du silicium. Revue bibliographique. *Electrochim. Acta* **28,** 541–546 (1983).
87. Boberski, W. G. & Allred, A. L. Electrochemical Reduction of Chloropermethylpolysilanes. *J. Organomet. Chem.* **88,** 73–77 (1975).
88. West, R. The polysilane high polymers. *J. Organomet. Chem.* **300,** 327–346 (1986).
89. Becker, J. Y., Shakkour, E. & West, R. Preparative electrochemical oxidation of cyclic peralkylsilanes. *Tetrahedron Lett.* **33,** 5633–5636 (1992).
90. Watanabe, H. & Nagai, Y. *Organosilicon and Bioorganosilicon Chemistry [Proc. Int. Symp. Organosilicon Chem.].* (Ellis Horwood, 1985).
91. Diaz, A. Electro-Oxidation of Substituted Silane High Polymers. *J. Electrochem. Soc.* **132,** 834 (1985).
92. Minge, O. & Naturwissenschaften, D. Der. ARYLSILANE.
93. Dhiman, A., Becker, J. Y., Minge, O., Schmidbaur, H. & Müller, T. A Simple Correlation of Anodic Peak Potentials of Silylarenes and Their Vertical Ionization Energies. *Organometallics* **23,** 1636–1638 (2004).
94. Bock, H. Fundamentals of Silicon Chemistry: Molecular States of Silicon-Containing Compounds. *Angew. Chemie Int. Ed. English* **28,** 1627–1650 (1989).
95. Yoshida, J. in *Topics in Current Chemistry* (ed. Steckhan, E.) 39–81 (Springer, Berlin, Heidelberg, 1994). doi:10.1007/3-540-57729-7_2
96. Giordan, J. C. Negative ions: effect of .alpha.- vs. .beta.-silyl substitution on the negative ion states of .pi. systems. *J. Am. Chem. Soc.* **105,** 6544–6546 (1983).
97. Wan, Y.-P., O'Brien, D. H. & Smentowski, F. J. Anion radicals of phenylsilanes. *J. Am. Chem. Soc.* **94,** 7680–7686 (1972).
98. Nagaura, T., Nagamine, M., Tanabe, I. & Miyamoto, N. in *Progress in Batteries and Solar Cells*

84–88 (JEC Press Inc., 1989).
99. Nagaura, T. & Tozawa, K. in *Progress in Batteries and Solar Cells* 209–212 (JEC Press Inc., 1990).
100. Mizushima, K., Jones, P. C., Wiseman, P. J. & Goodenough, J. B. LixCoO2 (0<x<-1): A new cathode material for batteries of high energy density. *Mater. Res. Bull.* **15,** 783–789 (1980).
101. Megahed, S. & Scrosati, B. Lithium-ion rechargeable batteries. *J. Power Sources* **51,** 79–104 (1994).
102. Scrosati, B. Recent advances in lithium ion battery materials. *Electrochim. Acta* **45,** 2461–2466 (2000).
103. Feng, K. *et al.* Silicon-Based Anodes for Lithium-Ion Batteries: From Fundamentals to Practical Applications. *Small* **1702737,** 1702737 (2018).
104. Armand, M. & Touzain, P. Graphite intercalation compounds as cathode materials. *Mater. Sci. Eng.* **31,** 319–329 (1977).
105. Nishi, Y. The development of lithium ion secondary batteries. *Chem. Rec.* **1,** 406–413 (2001).
106. Tobishima, S., Arakawa, M., Hirai, T. & Yamaki, J. Ethylene carbonate-based electrolytes for rechargeable lithium batteries. *J. Power Sources* **26,** 449–454 (1989).
107. McMillan, R. S. A Report on the Development of a Rechargeable Lithium Cell for Application in Autofocus Cameras. *J. Electrochem. Soc.* **138,** 1566 (1991).
108. Ko, M. *et al.* Scalable synthesis of silicon-nanolayer-embedded graphite for high-energy lithium-ion batteries. *Nat. Energy* **1,** 16113 (2016).
109. Sharma, R. A. & Seefurth, R. N. Thermodynamic Properties of the Lithium-Silicon System. *J. Electrochem. Soc.* **123,** 1763 (1976).
110. Wen, C. J. & Huggins, R. A. Chemical diffusion in intermediate phases in the lithium-silicon system. *J. Solid State Chem.* **37,** 271–278 (1981).
111. Wilson, A. M. & Dahn, J. R. Lithium Insertion in Carbons Containing Nanodispersed Silicon. *J. Electrochem. Soc.* **142,** 326 (1995).
112. Obrovac, M. N. & Christensen, L. Structural Changes in Silicon Anodes during Lithium Insertion/Extraction. *Electrochem. Solid-State Lett.* **7,** A93 (2004).
113. Chevrier, V. L. & Dahn, J. R. First Principles Model of Amorphous Silicon Lithiation. *J. Electrochem. Soc.* **156,** A454 (2009).
114. Li, J. & Dahn, J. R. An In Situ X-Ray Diffraction Study of the Reaction of Li with Crystalline Si. *J. Electrochem. Soc.* **154,** A156 (2007).
115. Hatchard, T. D. & Dahn, J. R. In Situ XRD and Electrochemical Study of the Reaction of Lithium with Amorphous Silicon. *J. Electrochem. Soc.* **151,** A838 (2004).
116. Liu, X. H. & Huang, J. Y. In situ TEM electrochemistry of anode materials in lithium ion batteries. *Energy Environ. Sci.* **4,** 3844 (2011).
117. Crosnier, O., Brousse, T. & Schleich, D. M. Tin based alloys for lithium ion batteries. *Ionics (Kiel).* **5,** 311–315 (1999).
118. Idota, Y., Kubota, T. & Matsufuji, A. Tin-Based Amorphous Oxide : A High-Capacity Lithium-Ion – Storage Material. *Science* **276,** 1395 (1997).
119. I. A. Courtney, J. R. D. Electrochemical and In Situ X-Ray Diffraction Studies of the Reaction of Lithium with Tin Oxide Composites. *J. Electrochem. Soc.* **144,** 2045–2052 (1997).
120. Brousse, T., Retoux, R., Herterich, U. & Schleich, D. M. Thin-Film Crystalline SnO_2-Lithium Electrodes. *J. Electrochem. Soc.* **145,** 1 (1998).
121. Winter, M. & Besenhard, J. O. Electrochemical lithiation of tin and tin-based intermetallics and composites. *Electrochim. Acta* **45,** 31–50 (1999).
122. Guler, M. O. *et al.* Freestanding nano crystalline Tin@carbon anode electrodes for high capacity Li-ion batteries. *Appl. Surf. Sci.* **Ahead of p,** (2018).
123. Zhu, Z. *et al.* Ultrasmall Sn nanoparticles embedded in nitrogen-doped porous carbon as high-performance anode for lithium-ion batteries. *Nano Lett.* **14,** 153–157 (2014).
124. Wang, C. *et al.* Three-dimensional Sn–graphene anode for high-performance lithium-ion batteries. *Nanoscale* **5,** 10599 (2013).
125. Li, H., Wang, Z., Chen, L. & Huang, X. Research on advanced materials for Li-ion batteries.

Adv. Mater. **21,** 4593–4607 (2009).
126. Knall, A.-C. & Slugovc, C. Inverse electron demand Diels–Alder (iEDDA)-initiated conjugation: a (high) potential click chemistry scheme. *Chem. Soc. Rev.* **42,** 5131 (2013).
127. Knall, A. C., Hollauf, M. & Slugovc, C. Kinetic studies of inverse electron demand Diels-Alder reactions (iEDDA) of norbornenes and 3,6-dipyridin-2-yl-1,2,4,5-tetrazine. *Tetrahedron Lett.* **55,** 4763–4766 (2014).
128. Kolb, H. C., Finn, M. G. & Sharpless, K. B. Click Chemistry: Diverse Chemical Function from a Few Good Reactions. *Angew. Chemie Int. Ed.* **40,** 2004–2021 (2001).
129. Prokhorov, A. M. & Kozhevnikov, D. N. Reactions of triazines and tetrazines with dienophiles (Review). *Chem. Heterocycl. Compd.* **48,** 1153–1176 (2012).
130. Wan, Z.-K., Woo, G. H. C. & Snyder, J. K. Dienophilicity of imidazole in inverse electron demand Diels–Alder reactions: cycloadditions with 1,2,4,5-tetrazines and the structure of zarzissine. *Tetrahedron* **57,** 5497–5507 (2001).
131. Rahanyan, N., Linden, A., Baldridge, K. K. & Siegel, J. S. Diels–Alder reactions of 3,6-disubstituted 1,2,4,5-tetrazines. Synthesis and X-ray crystal structures of diazafluoranthene derivatives. *Org. Biomol. Chem.* **7,** 2082 (2009).
132. Grumm, B. Inverse Electron Demand Diels-Alder Reactions (iEDDA) of 1,2,4,5-Tetrazines and Cyclic Enols. (Graz University of Technology, 2014).
133. Knall, A.-C. *et al.* Inverse electron demand Diels–Alder (iEDDA) functionalisation of macroporous poly(dicyclopentadiene) foams. *Chem. Commun.* **49,** 7325 (2013).
134. Devaraj, N. K., Thurber, G. M., Keliher, E. J., Marinelli, B. & Weissleder, R. Reactive polymer enables efficient in vivo bioorthogonal chemistry. *Proc. Natl. Acad. Sci.* **109,** 4762–4767 (2012).
135. Hansell, C. F. *et al.* Additive-Free Clicking for Polymer Functionalization and Coupling by Tetrazine–Norbornene Chemistry. *J. Am. Chem. Soc.* **133,** 13828–13831 (2011).
136. Pöschl, U., Siegl, H. & Hassler, K. Synthesis, spectroscopy and structure of phenylated cyclopentasilanes. *J. Organomet. Chem.* **506,** 93–100 (1996).
137. Gilman, H. & Brannen, C. G. Some 1-Naphthylsilicon Compounds. *J. Am. Chem. Soc.* **73,** 4640–4644 (1951).
138. Rosenberg, S. D., Walburn, J. J. & Ramsden, H. E. Preparation of Some Arylchlorosilanes with Arylmagnesium Chlorides. *J. Org. Chem.* **22,** 1606–1607 (1957).
139. Fleming, I., Dunoguès, J. & Smithers, R. The Electrophilic Substitution of Allylsilanes and Vinylsilanes. *Org. React.* **1948,** 57–575 (2004).
140. Knölker, H.-J. Cycloadditions of allylsilances. Part 10. Stereoselective Construction of Ring Systems by Cycloaddition Reactions of allyltriisopropylsilance. *J. für Prakt. Chemie/Chemiker-Zeitung* **339,** 304–314 (1997).
141. Knölker, H.-J., Jones, P. G. & Wanzl, G. Cycloadditions of Allylsilanes, Part 11. Stereoselective Synthesis of Hydroxycyclopentanes and Hydroxymethylcyclobutanes by Titanium Tetrachloride-Promoted [3+2] and [2+2] Cycloadditions of Sterically Hindered Allylsilanes and Subsequent Oxidative Cleavag. *Synlett* **1998,** 613–616 (1998).
142. Vrabel, M. *et al.* Norbornenes in inverse electron-demand diels-alder reactions. *Chem. - A Eur. J.* **19,** 13309–13312 (2013).
143. Bakkali, H. *et al.* Functionalized 2,5-Dipyridinylpyrroles by Electrochemical Reduction of 3,6-Dipyridinylpyridazine Precursors. *European J. Org. Chem.* **2008,** 2156–2166 (2008).
144. Gilman, H., Brannen, C. G. & Ingham, R. K. Some Tetrasubstituted Naphthyl- and Tolylsilanes. *J. Am. Chem. Soc.* **77,** 3916–3919 (1955).
145. Winkler, H. J. S., Jarvie, A. W. P., Peterson, D. J. & Gilman, H. Preparation and Characterization of Dodecaphenylcyclohexasilane. *J. Am. Chem. Soc.* **83,** 4089–4093 (1961).
146. Jarvie, a. W. P., Winkler, H. J. S., Peterson, D. J. & Gilman, H. Preparation and Characterization of Octaphenylcyclotetrasilane. *J. Am. Chem. Soc.* **83,** 1921–1924 (1961).
147. Thorshaug, K., Swang, O., Dahl, I. M. & Olafsen, A. An Experimental and Theoretical Study of Spin–Spin Coupling in Chlorosilanes. *J. Phys. Chem. A* **110,** 9801–9804 (2006).
148. Ernst, C. R., Spialter, L., Buell, G. R. & Wilhite, D. L. Silicon-29 Nuclear Magnetic Resonance.

Chemical Shift Substituent Effects. *J. Am. Chem. Soc.* **96,** 5375–5381 (1974).
149. Rofouei, M. K., Lawless, G. A., Morsali, A. & Hitchcock, P. B. Synth. and characterization of novel sterically demanding amido ligand derivatives and their alkali metal ion complexes, crystal structures of [SiH_2Mes_2], [$NH(SiHMes_2)_2$] and [$Na\{N(SiHMes_2)_2$. *Inorganica Chim. Acta* **359,** 3815–3823 (2006).
150. Grajewska, A. & Oestreich, M. Base-Catalyzed Dehydrogenative Si-O Coupling of Dihydrosilanes: Silylene Protection of Diols. *Synlett* **2010,** 2482–2484 (2010).
151. Popp, F., Nätscher, J. B., Daiss, J. O., Burschka, C. & Tacke, R. The 2,4,6-Trimethoxyphenyl Unit as a Unique Protecting Group for Silicon in Synthesis and the Silylation Potential of (2,4,6-Trimethoxyphenyl)silanes. *Organometallics* **26,** 6014–6028 (2007).
152. Lambert, J. B. *et al.* Torsional distortions in trimesitylsilanes and trimesitylgermanes. *J. Organomet. Chem.* **568,** 21–31 (1998).
153. Milbradt, M., Marsmann, H., Heine, T., Seifert, G. & Frauenheim, T. in *Organosilicon Chemistry Set* 324–328 (Wiley-VCH Verlag GmbH, 2008). doi:10.1002/9783527620777.ch54d
154. Schäfer, A., Saak, W., Haase, D. & Müller, T. Silyl Cation Mediated Conversion of CO_2 into Benzoic Acid, Formic Acid, and Methanol. *Angew. Chemie Int. Ed.* **51,** 2981–2984
155. Rofouei, M. K., Lawless, G. A., Morsali, A. & Hitchcock, P. B. Crystal Structure of [SiH2Mes2] (Mes = 2,4,6-trimethylphenyl). *Anal. Sci. X-ray Struct. Anal. Online* **21,** x103–x104 (2005).
156. Schröck, R., Angermaier, K., Sladek, A. & Schmidbaur, H. 9,10-Disilylanthracene; synthesis, structure and fluorescence. *J. Organomet. Chem.* **509,** 85–88 (1996).
157. Bolte, M. No Title. *CSD Commun.* (2010).
158. Constantine, S. P., Hitchcock, P. B. & Lawless, G. A. No Title. *CSD Commun.* (1995).
159. Hurkes, N., Spirk, S., Belaj, F. & Pietschnig, R. At the Edge of Stability - Preparation of Methyl-substituted Arylsilanetriols and Investigation of their Condensation Behavior. *Zeitschrift für Anorg. und Allg. Chemie* **639,** 2631–2636 (2013).
160. Jones, P. G. & Dix, I. No Title. *CSD Commun.* (2004).
161. Jutzi, P., Kanne, D., Hursthouse, M. & Howes, A. J. Mono- und Bis(η1-pentamethylcyclopentadienyl)silane – Synthese, Struktur und Eigenschaften. *Chem. Ber.* **121,** 1299–1305 (1988).
162. Danilenko, T. N., Tatevosyan, M. M. & Vlasenko, V. G. A study of the electronic structure of phenylsilanes by X-ray emission spectroscopy and quantum chemical calculation methods. *J. Struct. Chem.* **53,** 876–884 (2012).
163. V. Motsarev, G., R. Rozenberg, V., T. Inshakova, V. & I. Kolbasov, V. Halogenation of Aromatic Silanes. XXIX. Preparation of Chloro and Bromo Derivatives of 2,5-Dimethylphenyltrichlorosilane. *Zhurnal Obs. Khimii* **7,** (1976).
164. Alikhanov, P. P., Kalinachenko, V. R., Motsarev, G. V., Temnova, I. S. & Yakimenko, L. M. Reactivity of methyl derivatives of phenyltrichlorosilane and benzyltrichlorosilane during electrophilic deuterium exchange in a solution of liquefied hydrogen bromide. *Zhurnal Obs. Khimii* **47,** 365–368 (1976).
165. Chernyshev, E. A., Mironov, V. F. & Petrov, A. D. New method of preparation of organosilicon monomers by high temperature condensation of alkenyl chlorides, aryl chlorides, and olefins with hydrosilanes. *Izv. Akad. Nauk SSSR, Seriya Khimicheskaya* 2147–2156 (1960).
166. Metras, F., Plazanet, J. & Valade, J. Organosilicon compounds with amine groups. II. Syntheses, stabilities, and properties of primary dialkyldiaminosilanes $R_2Si(NH_2)_2$. *Bull. Soc. Chim. Fr.* **7,** 2155–2166 (1966).
167. V. Motsarev, G., R. Rozenberg, V., T. Inshakova, V. & I. Kolbasov, V. Halogenation of Aromatic Silanes. XXIX. Preparation of Chloro and Bromo Derivatives of 2,5-Dimethylphenyltrichlorosilane. *Zhurnal Obs. Khimii* **7,** (1976).
168. Lobkovskii, E. B., Fokin, V. N. & Semenenko, K. N. Crystal and molecular structure of triphenylsilicon chloride. *Zhurnal Strukt. Khimii* **22,** 152–155 (1981).
169. Liew, S. K. *et al.* Expanding the Steric Coverage Offered by Bis(amidosilyl) Chelates: Isolation of Low-Coordinate N -Heterocyclic Germylene Complexes. *Inorg. Chem.* **51,** 5471–5480 (2012).

170. Hayase, S., Onishi, Y., Suzuki, S. & Wada, M. Photopolymerization of cyclohexene oxide by the use of photodecomposable silyl peroxide. Aluminum complex/arylsilyl peroxide catalyst. *Macromolecules* **19,** 968–973 (1986).
171. Corriu, R. J. P., Dabosi, G. & Martineau, M. Kinetic and stereochemical evidence for nucleophilic assistance in the nucleophilic hydrolysis of chlorosilanes. *J. Chem. Soc. Chem. Commun.* 649 (1977). doi:10.1039/c39770000649
172. Allemand, J. & Gerdil, R. Triphenylsilane, $C_{18}H_{16}Si$. *Cryst. Struct. Commun.* **8,** 927–932 (1979).
173. Schäfer, A. *et al.* A New Synthesis of Triarylsilylium Ions and Their Application in Dihydrogen Activation. *Angew. Chemie Int. Ed.* **50,** 12636–12638 (2011).
174. Yamanoi, Y., Taira, T., Sato, J., Nakamula, I. & Nishihara, H. Efficient Preparation of Monohydrosilanes Using Palladium-Catalyzed Si−C Bond Formation. *Org. Lett.* **9,** 4543–4546 (2007).
175. Tokoro, Y., Sugita, K. & Fukuzawa, S. Synthesis of Silaphenalenes by Ruthenium-Catalyzed Annulation between 1-Naphthylsilanes and Internal Alkynes through C À H Bond Cleavage. 13229–13232 (2015). doi:10.1002/chem.201502746
176. Jin, W., Makioka, Y., Kitamura, T. & Fujiwara, Y. Selective synthesis of monohydrosilanes by the reactions of organoytterbium iodides with dihydrosilanes Monohydrosilanes can be prepared selectively in high yields from the reaction of various aryl and alkyl iodides with ytterbium metal followed by the re. 955–956 (1999).
177. Harland, J. J., Payne, J. S., Day, R. O. & Holmes, R. R. Steric Hindrance in Pentacoordinated Fluorosilicates. Synthesis and Molecular Structure of the Diphenyl-1-naphthyldifluorosilicate Anion and the Phenylmethyltrifluorosilicate Anion. *Inorg. Chem.* **26,** 760–765 (1987).
178. Brannen, C. G. Steric hindrance in arylsilicon compounds. *Retrosp. Theses Diss.* (1951).
179. Zakharkin, L. I., Okhlobystin, O. Y. & Bilevitch, K. A. Effect of solvents on reactions of organo-metallic compounds. *J. Organomet. Chem.* **2,** 309–313 (1964).
180. Zakharkin, L. I., Okhlobystin, O. Y. & Bilevitch, K. A. Effect of solvents on reactions of organo-metallic compounds. *J. Organomet. Chem.* **2,** 309–313 (1964).
181. Müller, E. & Martin, H. Nichtoxidkeramik aus siliciumorganischen Polymeren. *J. für Prakt. Chemie/Chemiker-Zeitung* **339,** 401–413 (1997).
182. Jones, A. C. & Hitchman, M. L. *Chemical Vapour Deposition*. (Royal Society of Chemistry, 2008). doi:10.1039/9781847558794
183. Fuchigami, T. in *The Chemistry of Organic Silicon Compounds* **2,** 1187–1232 (John Wiley & Sons, Ltd, 1998).
184. Martynov, B. I. & Stepanov, A. A. Electrochemical synthesis of fluoro-organosilanes. **85,** 127–128 (1997).
185. Hengge, E., Jammegg, C. & Kalchauer, W. Process for electrochemical synthesis of organic silicon compounds as well as an apparatus for carrying outsaid process and the use of said apparatus for preparing said organic silicon compounds. (1994).
186. Pons, P. *et al.* Electrosynthese en chimie organosilicique: preparation de phenyl- et benzyl-trimethylsilanes. *J. Organomet. Chem.* **321,** C27–C29 (1987).
187. Corriu, R. J. P., Dabosi, G. & Martineau, M. Electrochemical reduction of triorganohalo-silanes and -germanes. *J. Organomet. Chem.* **188,** 63–72 (1980).
188. Pitt, C. G., Carey, R. N. & Toren, E. C. Nature of the Electronic Interactions in Aryl-Substituted Polysilanes. *J. Am. Chem. Soc.* **94,** 3806–3811 (1972).
189. Kocieński, P. J. *Protecting Groups*. (Thieme, 1994).
190. Greene, T. W. & Wuts, P. G. W. *Greene's Protective Groups in Organic Synthesis*. (John Wiley & Sons, Inc., 2014). doi:10.1002/9781118905074
191. Gooding, J. J. & Ciampi, S. The molecular level modification of surfaces: from self-assembled monolayers to complex molecular assemblies. *Chem. Soc. Rev.* **40,** 2704 (2011).
192. Sioda, R. E. & Frankowska, B. Voltammetric oxidation of naphthalene derivatives. *J. Electroanal. Chem.* **612,** 147–150 (2008).
193. Okano, M. & Mochida, K. Electrochemical Halogenation of Trisubstituted Germanes and

Silanes. *Bull. Chem. Soc. Jpn.* **64,** 1381–1382 (1991).
194. Miller, R. D. & Michl, J. Polysilane High Polymers. *Chem. Rev.* **89,** 1359–1410 (1989).
195. Miller, R. D. *et al.* in *Materials for Nonlinear Optics: Chemical Perspectives (ACS Symposium Series)* (eds. Marder, S. R., Stucky, G. D. & Sohn, J. E.) 636–660 (American Chemical Society, 1991). doi:10.1021/bk-1991-0455.ch043
196. Boudjouk, P. *New Approaches to the Synthesis of Novel Organosilanes*. (1983).
197. Kimata, Y., Suzuki, H., Satoh, S. & Kuriyama, A. Electrochemical Polymerization of Hydrosilane Compounds. *Organometallics* **14,** 2506–2511 (1995).
198. Becker, J. Y. Electrochemical oxidation of cyclic polysilanes. *J. Organomet. Chem.* **685,** 145–155 (2003).
199. Zhang, Z.-R., Becker, J. Y. & West, R. The effect of ring-size on the electrochemical oxidation of perethylcyclopolysilanes [(Et2Si)n]. *J. Organomet. Chem.* **574,** 11–18 (1999).
200. Watanabe, H., Aoki, M., Matsumoto, H., Nagai, Y. & Sato, T. The Electrochemical Behaviour of Mononitrophenyltrimethylsilanes and 2,4-Dinitrophenyltrimethylsilane. *Bull. Chem. Soc. Jpn.* **50,** 1019–1020 (1977).
201. Mousavi, M. P. S., Saba, S. A., Anderson, E. L., Hillmyer, M. A. & Bühlmann, P. Avoiding Errors in Electrochemical Measurements: Effect of Frit Material on the Performance of Reference Electrodes with Porous Frit Junctions. *Anal. Chem.* **88,** 8706–8713 (2016).
202. Baron, R., Kershaw, N. M., Donohoe, T. J. & Compton, R. G. Electrochemistry in tetrahydrofuran and at low temperature: Protocol, procedures and methods. *J. Phys. Org. Chem.* **22,** 1136–1141 (2009).
203. Levi, M. D., Levi, E. A. & Aurbach, D. The mechanism of lithium intercalation in graphite film electrodes in aprotic media. Part 2. Potentiostatic intermittent titration and in situ XRD studies of the solid-state ionic diffusion. *J. Electroanal. Chem.* **421,** 89–97 (1997).
204. Kozeschkow, K. A. Untersuchungen über metallorganische Verbindungen, I. Mitteilung: Eine neue Klasse von Arylzinnverbindungen: Phenyl-trihalogen-stannane. *Berichte der Dtsch. Chem. Gesellschaft (A B Ser.* **62,** 996–999 (1929).
205. Fischer, R., Schollmeier, T., Schuermann, M. & Uhlig, F. Syntheses of novel silylsubstituted distannanes. *Appl. Organomet. Chem.* **19,** 523–529 (2005).
206. McLafferty, J. *Electrochemical research in chemical hydrogen storage materials: Sodium borohydride and organotin hydrides*. (2009).
207. Jung, Y. S., Lee, K. T., Ryu, J. H., Im, D. & Oh, S. M. Sn-Carbon Core-Shell Powder for Anode in Lithium Secondary Batteries. *J. Electrochem. Soc.* **152,** A1452 (2005).
208. *Bruker APEX2 and SAINT*. (Bruker AXS Inc., Madison, Wisconsin, USA, 2012).
209. Blessing, R. H. An empirical correction for absorption anisotropy. *Acta Crystallogr. Sect. A Found. Crystallogr.* **51,** 33–38 (1995).
210. Sheldrick, G. M. Phase annealing in SHELX-90: direct methods for larger structures. *Acta Crystallogr. Sect. A Found. Crystallogr.* **46,** 467–473 (1990).
211. Sheldrick, G. M. A short history of SHELX. *Acta Crystallogr. Sect. A Found. Crystallogr.* **64,** 112–122 (2008).
212. Sheldrick, G. M. Crystal structure refinement with SHELXL. *Acta Crystallogr. Sect. C Struct. Chem.* **71,** 3–8 (2015).
213. Spek, A. L. Single-crystal structure validation with the program PLATON. *J. Appl. Crystallogr.* **36,** 7–13 (2003).
214. Spek, A. L. Structure validation in chemical crystallography. *Acta Crystallogr. Sect. D Biol. Crystallogr.* **65,** 148–155 (2009).
215. van der Sluis, P. & Spek, A. L. BYPASS: an effective method for the refinement of crystal structures containing disordered solvent regions. *Acta Crystallogr. Sect. A Found. Crystallogr.* **46,** 194–201 (1990).
216. Spek, A. L. PLATON SQUEEZE: a tool for the calculation of the disordered solvent contribution to the calculated structure factors. *Acta Crystallogr. Sect. C Struct. Chem.* **71,** 9–18 (2015).

217. Müller, P., Herbst-Irmer, R., Spek, A. L., Schneider, T. R. & Sawaya, M. R. *Crystal Structure Refinement: A Crystallographer's Guide to SHELXL*. (Oxford University Press, 2006). doi:10.1093/acprof:oso/9780198570769.001.0001
218. Janiak, C. A critical account on π–π stacking in metal complexes with aromatic nitrogen-containing ligands †. *J. Chem. Soc. Dalt. Trans.* 3885–3896 (2000). doi:10.1039/b003010o
219. Hunter, C. A. & Sanders, J. K. M. The nature of .pi.-.pi. interactions. *J. Am. Chem. Soc.* **112,** 5525–5534 (1990).
220. Meyer, E. A., Castellano, R. K. & Diederich, F. Interactions with Aromatic Rings in Chemical and Biological Recognition. *Angew. Chemie Int. Ed.* **42,** 1210–1250 (2003).
221. Nayak, S. K., Sathishkumar, R. & Row, T. N. G. Directing role of functional groups in selective generation of C–H···π interactions: In situ cryo-crystallographic studies on benzyl derivatives. *CrystEngComm* **12,** 3112 (2010).
222. Alvarez, S. A cartography of the van der Waals territories. *Dalt. Trans.* **42,** 8617 (2013).
223. Nelyubina, Y. V., Antipin, M. Y. & Lyssenko, K. A. Are Halide···Halide Contacts a Feature of Rock-Salts Only? *J. Phys. Chem. A* **111,** 1091–1095 (2007).
224. Willett, R. D. *et al.* Dimethylammonium Trichlorocuprate(II): Structural Transition, Low-Temperature Crystal Structure, and Unusual Two-Magnetic Chain Structure Dictated by Nonbonding Chloride−Chloride Contacts. *Inorg. Chem.* **45,** 7689–7697 (2006).
225. Allen, F. H. The Cambridge Structural Database: a quarter of a million crystal structures and rising. *Acta Crystallogr. Sect. B Struct. Sci.* **B58,** 380–388 (2002).
226. Macrae, C. F. *et al.* Mercury CSD 2.0 – new features for the visualization and investigation of crystal structures. *J. Appl. Crystallogr.* **41,** 466–470 (2008).
227. Putz, H. & Brandenburg, K. Diamond - Crystal and Molecular Structure Visualization.
228. Orthaber, D., Bergmann, A. & Glatter, O. SAXS experiments on absolute scale with Kratky systems using water as a secondary standard. *J. Appl. Crystallogr.* **33,** 218–225 (2000).
229. Glatter, O. A new method for the evaluation of small-angle scattering data. *J. Appl. Crystallogr.* **10,** 415–421 (1977).
230. Glatter, O. The interpretation of real-space information from small-angle scattering experiments. *J. Appl. Crystallogr.* **12,** 166–175 (1979).
231. Glatter, O. Determination of particle-size distribution functions from small-angle scattering data by means of the indirect transformation method. *J. Appl. Crystallogr.* **13,** 7–11 (1980).
232. Pöschl, U. Synthese, Spektroskopie und Struktur selektiv funktionalisierter Cyclopentasilane und Cyclotetrasilane. (Graz University of Technology, 1995).
233. Zeppek, C., Pichler, J., Torvisco, A., Flock, M. & Uhlig, F. Aryltin chlorides and hydrides: Preparation, detailed NMR studies and DFT calculations. *J. Organomet. Chem.* **740,** 41–49 (2013).
234. Goni, F. High-yield production and characterization of boron nitride nanosheets. (Graz University of Technology, 2017).
235. Shen, J. *et al.* Liquid Phase Exfoliation of Two-Dimensional Materials by Directly Probing and Matching Surface Tension Components. *Nano Lett.* **15,** 5449–5454 (2015).